CRANFIELD UNIVERSITY

WENYI LIANG

THE INVESTIGATION OF ELECTROMAGNETIC RADIAL FORCE AND ASSOCIATED VIBRATION IN PERMANENT MAGNET SYNCHRONOUS MACHINES

SCHOOL OF WATER, ENERGY AND ENVIRONMENT

PHD THESIS

CRANFIELD UNIVERSITY

SCHOOL OF WATER, ENERGY AND ENVIRONMENT

PHD THESIS

Academic Year 2014-2017

Wenyi Liang

The Investigation of Electromagnetic Radial Force and Associated Vibration in Permanent Magnet Synchronous Machines

Supervisor: Prof. Patrick Chi-kwong Luk

February 2017

Abstract

The rising public awareness of climate change and urban air pollution has been one of the key drivers for transport electrification. Such trend drastically accelerates the quest for high-power-and-torque-density electric drive systems. The rare-earth permanent magnet synchronous machine, with its excellent steady-state and dynamic characteristics, has been the ideal candidate for these applications. Specifically, the fractional-slot and concentrated-winding configuration is widely adopted due to its distinctive merits such as short end winding, low torque pulsation, and high efficiency. The vibration and the associated acoustic noise become one of the main parasitic issues of high-performance permanent magnet synchronous drives. These undesirable features mainly arise from mechanical connection failure, imperfect assembly, torque pulsation, and electromagnetic radial and axial force density waves. The high-power-and-torque-density requirement will only be ultimately fulfilled by the reduction of both electromagnetic active material and passive support structure. This results in inflated electromagnetic force density inside the electric machine. Besides, the stiffness of the machine parts can be compromised and the resultant natural frequencies are significantly brought down. Therefore, the vibration and acoustic noise that are associated with the electromagnetic radial and axial force density waves become a burden for large deployment of these drives.

This study is mainly dedicated to the investigation of the electromagnetic radial forced density and its associated vibration and acoustic noise in radial-flux permanent magnet synchronous machines. These machines are usually powered by voltage source inverter with pulse width modulation techniques and various control strategies. Consequently, the vibration problem not only lies on the permanent magnet synchronous machine but also highly relates to its drive and controller. Generally, the electromagnetic radial force density and its relevant vibration can be divided into low-frequency and high-frequency components based on their origins. The low-frequency electromagnetic radial force density waves stem from the magnetic field components by the permanent magnets and armature reaction of fundamental and phase-belt current harmonic components, while the high-frequency ones are introduced by the interactions between the main low-frequency and sideband high-frequency magnetic field components.

Both permanent magnets and armature reaction current are the main sources of magnetic field in electric machines. Various drive-level modeling techniques are

first reviewed, explored, and developed to evaluate the current harmonic components of the permanent magnet synchronous machine drive. Meanwhile, a simple yet effective analytical model is derived to promptly estimate the sideband current harmonic components in the drive with both sinusoidal and space-vector pulse width modulation techniques. An improved analytical method is also proposed to predict the magnetic field from permanent magnets in interior permanent magnet synchronous machines. Moreover, a universal permeance model is analytically developed to obtain the corresponding armature-reaction magnetic field components. With the permanent magnet and armature-reaction magnetic field components, the main electromagnetic radial force density components can be identified and estimated based on Maxwell stress tensor theory.

The stator tooth structure has large impacts on both electromagnetic radial force density components and mechanical vibration behaviors. The stator tooth modulation effect has been comprehensively demonstrated and explained by both finite element analysis and experimental results. Analytical models of such effect are developed for prompt evaluation and insightful revelation. Based on the proposed models, multi-physics approaches are proposed to accurately predict low-frequency and high-frequency electromagnetic radial vibration. Such method is quite versatile and applicable for both integral-slot and fractional-slot concentrated-winding permanent magnet synchronous machines. Comprehensive experimental results are provided to underpin the validity of the proposed models and methods.

This study commences on the derivations of the drive parameters such as torque angle, modulation index, and current harmonic components from circuit perspective and further progresses to evaluate and decouple the air-gap magnetic field components from field perspective. It carries on to dwell on the analytical estimations of the main critical electromagnetic radial force density components and stator tooth modulation effect. Based on the stator mechanical structure, the corresponding electromagnetic radial vibration and acoustic noise can be accurately predicted. Various analytical models have been developed throughout this study to provide a systematic tool for quick and effective investigation of electromagnetic radial force density, the associated vibration and acoustic noise in permanent magnet synchronous machine drive. They have all been rigorously validated by finite element analysis and experimental results. Besides, this study reveals not only a universal approach for electromagnetic radial vibration analysis but also insightful correlations from both machine and drive perspectives.

Acknowledgements

I would like to acknowledge everyone who has knowingly and unknowingly helped me and wished me the best in successfully accomplishing this research.

I would like to express particular thanks to my supervisor, Professor Patrick Chi-kwong Luk. His supportive encouragement and supervision over the whole study have been extremely helpful and essential. A special thank goes out to Doctor Weizhong Fei, for his valuable helps and discussions during the research. Thanks also to all my family and friends whose support and love have made the entire study possible.

I would also like to thank the Engineering & Physical Sciences Research Council (EPSRC) for thesis sponsorship of this research.

Contents

List of Figures

List of Tables

Nomenclature

All units are in SI unless otherwise stated

Alphanumeric

A_m	Amplitude of vibration displacement
A_z	Magnetic vector potential
b_{ad}, b_{aq}	d- and q-axis fundamental air-gap magnetic field of fundamental armature reaction
b_d, b_q	d- and q-axis air-gap magnetic field of fundamental armature reaction
$b_{d\_\omega_\mu}, b_{q\_\omega_\mu}$	d- and q-axis air-gap magnetic field with frequency ω_μ
b_p, b_υ	Fundamental and υ^{th} air-gap magnetic field of fundamental armature reaction
$b_{p\_\omega_\mu}, b_{\upsilon\_\omega_\mu}$	Fundamental and υ^{th} air-gap magnetic field with frequency ω_μ
b_r	Magnetic field of permanent magnet
b_s	Fundamental armature-reaction magnetic field
b_0	Overall fundamental magnetic field
b_ν	Armature-reaction magnetic field of ν^{th} phase-belt current
b_μ	Armature-reaction magnetic field with frequency ω_μ
B	Friction coefficient
B_b	Magnetic flux density of rotor magnetic bridge
B_d, B_q	Magnitude of d- and q-axis fundamental air-gap magnetic flux density introduced by fundamental armature reaction
B_p, B_υ	Magnitude of fundamental and υ^{th} air-gap magnetic flux density introduced by fundamental armature reaction
B_0	Magnitude of overall fundamental air-gap magnetic flux density
B_1, B_k	Fundamental and k^{th} air-gap magnetic flux density of permanent magnet
B_δ	Air-gap magnetic flux density
c	Speed of sound
f_m	The m^{th} order stator natural frequency
f_r	Permanent magnet magnetomotive force
f_s	Fundamental armature-reaction magnetomotive force
f_ν	ν^{th} harmonic current armature-reaction magnetomotive force
f_μ	Sideband armature-reaction magnetomotive force with frequency ω_μ
$F_{m\_\omega_k}$	Radial force of m^{th} order with frequency ω_k

f_t	Radial force acting on single tooth
F_{r_υ}	υ^{th} magnetomotive force of permanent magnet
F_{s_p}, F_{s_υ}	Fundamental and υ^{th} magnetomotive forces of fundamental armature reaction
F_{s_d}, F_{s_q}	d- and q-axis magnetomotive forces of fundamental armature reaction
F_{υ_ν}	υ^{th} magnetomotive force of ν^{th} harmonic current armature reaction
F_{υ_μ}	υ^{th} magnetomotive force of current harmonic armature reaction with frequency ω_μ
G	Transposed matrix of P
H_m	Height of permanent magnet
i	Current in each circuit
i_a, i_b, i_c	Current in three phase windings
$i_{a\nu}, i_{b\nu}, i_{c\nu}$	ν^{th} current harmonics in three phase windings
$i_{a\mu}, i_{b\mu}, i_{c\mu}$	Sideband current harmonics in three phase windings with frequency ω_μ
i_d, i_q	d- and q-axis stator current components in the rotor reference frame
i_{d_W}, i_{q_W}	d- and q-axis equivalent current in windings
i_{d_L}, i_{q_L}	d- and q-axis equivalent current in damping loops
$i_{d\_\omega_\mu}$, $i_{q\_\omega_\mu}$	d- and q-axis current harmonics with frequency ω_μ in the rotor synchronous reference frame
i_s	Amplitude of current space vector
$i_{s\_\omega_\mu}$	Stator current harmonic with frequency ω_μ in the stator stationary reference frame
i_L	Damping loop current matrix
i_M	Magnet equivalent current matrix
i_W	Winding current matrix
I_s	Magnitude of winding current
$I_{s\nu}$	Magnitude of ν^{th} winding current harmonic
$I_{s\mu}$	Magnitude of sideband current with frequency ω_μ
I_m	The radial sound pressure
I_0	The standard reference radial sound pressure
J	Current density of conductor
J_M	Rotor inertia moment
K	Coupling matrix
$K_{wp}, K_{w\upsilon}$	Fundamental and υ^{th} winding factor
L	The sound pressure level
L_b	The equivalent length of rotor magnetic bridge
L_{ef}	Axial effective machine length
L_{WW}	Winding self inductance matrix
L_{LL}	Damping loop self inductance matrix
L_{ad}, L_{aq}	d- and q-axis fundamental reaction inductance components
L_d, L_q	d- and q-axis synchronous inductance components
L_p, L_υ	Fundamental and υ^{th} mean components of fundamental reaction inductance components
L_σ	Leakage inductance of each circuit

m	Number of phases
M	Modulation index
M_{dq}	d-q mutual inductance
M_C	Overall mutual inductance matrix of winding and bar
M_{WL}	Mutual inductance matrix of winding to damping loop
M_{WM}	Mutual inductance matrix of magnet and winding
M_{LM}	Mutual inductance matrix of magnet and damping loop
M_s	The overall mass of stator system
N	Winding turns in series per phase
P	Stiffness matrix
p, p_0	Pole pairs of actual machine and unit machine
p_r	Electromagnetic radial force density
p_t	Radial force density acting on single tooth
$p_{m\_\omega_k}$	Electromagnetic radial force density with m^{th} spatial order and ω_k frequency
$P_{m\_\omega_k}$	Magnitude of radial force density of m^{th} order component with ω_k frequency
Q	Conductivity matrix
R	Overall resistance of each circuit
R_a, R_m	Flat top air gap and magnet slot reluctance
R_b, R_δ	Rotor magnetic bridge and air-gap reluctance
R_g, R_σ	Overall and flux leakage reluctance in the rotor
R_s	Resistance of stator phase winding
R_t	Air-gap reluctance under a single tooth
R_y	Radius of stator yoke
R_{y_0}	Stator and rotor yoke reluctance related to a single tooth
R_B	Damping bar resistance diagonal matrix
R_E	End ring resistance diagonal matrix
R_L	Damping bar additional matrix
R_W	Winding resistance diagonal matrix
R_0	Radius of air gap
T_{em}	Electromagnetic torque
T_L	Load torque
u	Terminal voltage of each circuit
u_a	Voltage of phase A
u_d, u_q	d- and q-axis stator voltages in rotor synchronous reference frame
$u_{d\_\omega_\mu}, u_{q\_\omega_\mu}$	d- and q-axis voltage harmonics with frequency ω_μ in rotor synchronous reference frame
u_s	Amplitude of voltage space vector
u_W	Winding voltage matrix
u_α, u_β	α- and β-axis stator voltages in stator stationary reference frame
U_{dc}	Direct current link voltage
W_b	Width of rotor magnetic bridge
W_{b_0}	Width of slot opening
W_m	Width of permanent magnet
W_t	Stator tooth pitch

Z, Z_0	Slot number of actual machine and unit machine

Greek Symbols

α, β, γ	Pole arc angle of one tooth, tooth shoe and tooth root
α_a, α_s	Inner and outer arc angle of magnet
α_p, α_v	Fundamental and v^{th} pole arc angle
β, β_b	Actual and equivalent arc angle of magnetic bridge
δ	Torque angle
δ_{ef}	Effective air gap distance
γ	Nonlinear voltage drop in external circuit
λ	Overall air-gap permeance
λ_r	Relative air-gap permeance of rotor
Λ_d, Λ_q	Magnitude of d- and q-axis permeance
Λ_p, Λ_v	Magnitude of fundamental and v^{th} average air-gap permeance
λ_s	Relative air-gap permeance of stator
$\Lambda_g, \Lambda_\delta$	Magnitude of rotor and air-gap band permeance
Λ_0	Magnitude of average air-gap permeance
Λ_{2n}	The n^{th} relative rotor saliency permeance
Λ_{nZ}	The n^{th} relative slot permeance
μ	Material permeability
μ_0	Permeability of free space
μ_b	Permeability of rotor magnetic bridge
ω_e	Rotor electrical angular frequency
ω_r	Rotor mechanical angular frequency
ω_s	Carrier wave angular frequency
ω_m	The m^{th} order stator natural angular frequency
ψ	Flux linkage of each circuit
ψ_f	Permanent magnet magnetic flux linkage
ψ_d, ψ_q	d- and q-axis stator flux linkage components in rotor synchronous reference frame
ψ_{ad}, ψ_{aq}	d- and q-axis fundamental armature-reaction flux linkage components in rotor synchronous reference frame
ψ_{md}, ψ_{mq}	d- and q-axis overall fundamental flux linkage components in rotor synchronous reference frame
ψ_W	Winding flux linkage matrix
ψ_L	Damping loop flux linkage matrix
ψ_{PM}	Overall mutual flux linkage matrix
ψ_{WM}	Winding mutual flux linkage of permanent magnet
ψ_{LM}	Damping loop mutual flux linkage of permanent magnet
ϕ_r	Internal equivalent magnetic flux of permanent magnet
ρ	Density of the medium
σ	Material conductivity
σ_M	Coefficient of coupling in mutual inductance
τ_p	Pole arc distance
τ_s	Magnet pole arc coefficient

θ_m	Mechanical angle
υ_m	Stator vibration velocity
φ_0	Initial phase of overall fundamental air-gap magnetic flux density
$\varphi_{m\_\omega_k}$	Initial phase of radial force density of m^{th} order component with frequency ω_k
φ_s	Initial phase of winding current
φ_μ	Initial phase of ω_μ frequency winding current harmonic
φ_ν	Initial phase of ν^{th} winding current harmonic
ζ	Mechanical modal damping ratio

Subscripts

12	$\omega_s \pm 2\omega_e$
13	$\omega_s \pm 3\omega_e$
14	$\omega_s \pm 4\omega_e$
20	$2\omega_s$
21	$2\omega_s \pm \omega_e$
25	$2\omega_s \pm 5\omega_e$
26	$2\omega_s \pm 6\omega_e$
27	$2\omega_s \pm 7\omega_e$
L, M, W	Components of damping loop, magnet and winding in multi-loop machine model
a, b, c	Associated variables of phase a, b and c
d, q	d- and q-axis components of associated vector in rotor synchronous reference frame
p, υ	Spatial distributed components with fundamental and υ^{th} spatial order
μ	Sideband associated component with frequency ω_μ
ν	Phase-belt harmonic component with frequency $\nu\omega_e$

Abbreviations

2-D	Two-dimensional
3-D	Three-dimensional
4-D	Four-dimensional
AC	Alternating current
BLDC	Brushless direct current
DC	Direct current
DTC	Direct torque control
EMF	Electromotive force
ERFD	Electromagnetic radial force density
ERV	Electromagnetic radial vibration
FEM	Finite element method
FEA	Finite element analysis
FFCR	Feed forward current regulator
FFT	Fast fourier transform

FSCW	Fractional slot concentrated winding
FW	Flux weakening
IM	Induction machine
MMF	Magnetomotive force
MEPA	Maximum efficiency per ampere
MOPA	Maximum output torque per ampere
MTPA	Maximum torque per ampere
PM	Permanent magnet
PMDC	Permanent magnet direct current
PMSM	Permanent magnet synchronous machine
PID	Proportional integral derivative
PWM	Pulse width modulation
RPWM	Random switching pulse width modulation
SMO	Sliding mode observer for sensorless estimation
SPWM	Sinusoidal pulse width modulation
STO	State observer for sensorless estimation
SVPWM	Space vector pulse width modulation
VSI	Voltage source inverter

Chapter 1

Introduction

This chapter first briefs the applications of PMSM and its drive, with corresponding advantages over its counterparts. The PMSM types, with their characteristics and typical applications are reviewed, followed by the main topologies of PMSM based on the rotor structure. Then, the common control strategies are illustrated, as well as PWM techniques and position detection schemes. Some of them will be involved in further practical investigations. Besides, the principal demerits of PMSM are also discussed. ERV and its associated acoustic noise, as one of the main issues, are further introduced from low frequency and high frequency sources. The outline and main contributions of this study are listed.

1.1 Background

PMSMs, which have exquisite performances, are recently becoming one of the main commodities in variable-frequency drive systems for various applications. On the other hand, PWM techniques with vector control and direct torque control strategies are widely employed in PMSM drive systems to accomplish excellent static and dynamic performances. However, the undesirable magnetic field harmonic components are inevitably generated in PMSMs by slot opening, rotor structure, winding arrangement, core saturation and further complications caused by the controller. They can manifest in the formation of cogging torque, torque ripple and ERFD, which are the main sources of ERV in PM machines [1, 2]. Such vibration, as one of the parasitic effects, is quite a common issue for PMSM drives in many applications such as electric vehicles and elevators, and hence needs to be addressed properly.

1.1.1 The Electrical Drive

The Adjustable Speed Drive

Nowadays, the ever-increasing development activities on electrical adjustable speed drives have been propelled by huge demands of mechanical motion automation, sustained development in power semiconductors and integrated circuits, as well as the advent of new magnetic materials. The trend from constant speed systems to adjustable speed systems mainly rests on the demands of energy efficiency, speed or position control and excellent dynamic performance [3]. The adjustable speed is widely employed in applications such as fans, pumps and compressors to improve the efficiency. Meanwhile, there are also vigorous demands on the drive to achieve speed or position control in applications such as industrial automation, elevator traction and household appliance. Excellent transient performances are quite essential in applications of electric propulsion, aerospace, aviation and wind power.

Generally, modern electrical drive system includes the following four distinct elements [3, 4]:

- coupler and load;
- electric machine;
- power electronic converter;
- controller.

The load device ultimately realises the purpose of the drive system. The coupler is the component which connects the electric machine to the load to deliver the power smoothly. In the case of direct-drive systems, such as the application of gearless traction machine in the elevator, the coupler normally does not exist. The electric machine is the prime device transferring power from the source into rotating motion to drive the load. The converter offers the electrical energy to the machine in an available form by power switch module following the reference signals from the controller. The control algorithms are embedded in the controller collecting corresponding system status by sensors and generating modulation signals. As a result, the drive accomplishes the target torque, speed, position or power.

There are various types of electrical drives available in industry. However, their basic structures remain unchanged. The electric machines generally determine the characteristics of the drive. The basic machine type can be divided into two main categories:

- DC commutator variable-speed drive;
- AC variable-speed drive.

Basically, two types of machine are available in the DC commutator drive system. One is DC commutator machine, the other is PMDC commutator machine. While

the AC drives can be further categorized into AC IM drive and PM brushless machine drive.

The DC Drives

DC machine has physically separated magnetic field and armature reaction circuit. The magnetic field is mainly introduced by excitation winding or PMs on the stator. The interaction between the armature and excitation winding field produces the electromagnetic torque. In electrically excited DC machines, the torque can be tuned by respective winding currents via corresponding variable DC voltage source. As a result, stable and excellent transient performance can be readily achieved by simple drive controller. However, the applications of DC drive are constrained. The requirement of routine maintenance on brushes and commutator bars is one of the main issues. The drive speed is also limited by the physical commutator due to radio frequency interference, commutator sparking and potential source of ignition. Moreover, the space for the commutator and brushes can be also considerable. Consequently, the conventional DC commutator drives have been gradually replaced by maintenance-free brushless three-phase vector-controlled AC drives in many applications. Such drives can boast quick response, compact structure, light weight and large continuous and peak torques [3, 4].

The Induction AC Drives

The IM is widely adopted for various AC drives. IM drive with simple constant voltage/frequency scalar control method suffices most unsophisticated machinery. By adjusting the voltage magnitude in proportion to the supply frequency, adjustable speed can be achieved. The voltage drop on the stator resistance has to be compensated for low frequency operation. The voltage amplitude saturates to the level in the case of operation speed above the base value. Field oriented vector control is developed to further improve the steady-state and transient performance of the drive. Such method emulates the IM to separately excited DC machines. Both magnetic field and torque components can be controlled independently in the rotating reference frame. Moreover, DTC scheme, based on magnetic flux and torque estimation, is also widely investigated for such drive to offer better robustness [5].

However, the ohmic losses in the rotor conductors can considerably reduce the efficiency of IM drive. The power factor of IM drive also deteriorates because of the magnetizing current in the stator winding. Distributed winding arrangement is common practice in IM to achieve sinusoidal MMF. It implies that the pole-pair number is somewhat restricted in IM. That limits its direct deployment for low-speed applications. As a result, mechanical transmissions such as gears are required for low-speed applications. The efficiency of the overall drive system can be compromised. In addition, the associated maintenance of the mechanical transmission can eventually jeopardise the system in some cases. All these shortages are moving

it away from high performance applications.

The PM Brushless Drives

The PM brushless machine normally has the armature reaction windings accommodated in the stator slots in the same way as IM. On the other hand, the PMs in the rotor provides constant rational magnetic field. As a consequence, an average electromagnetic torque is produced by the interaction of stator and rotor magnetic fields, when the current induced MMF is precisely synchronized in the same frequency of the rotor. The PMs in the construction of such electrical machines bring the following benefits [6]:

- energy saving as no excitation losses is required to build the magnetic field, and hence substantially increasing the drive efficiency;
- higher torque and power per volume;
- better dynamic performance than electrically excited counterparts due to higher associated magnetic flux density in the air gap and lower moment of inertia;
- more simplified construction and maintenance;
- versatile configuration and more topologies.

Compared with IMs, the PM brushless machines have become a more attractive option in variable-speed drives, due to the enhanced steady-state and dynamic performance, together with improved torque and power density. The advancements of semiconductor, microprocessor and digital techniques have made the control of such brushless machines easy to realize. The vector control scheme is much more straightforward to implement in PMSM drives in comparison with IM drives. This is facilitated by the fact that the PM magnetic field aligns with the d-axis of the rotor reference frame. Therefore the space angle of the PM magnetic field is same as the rotor angle, which can be directly detected by the position sensor. In contrast, the detection of magnetic field position is much more complicated in IM. Normally a magnetic flux model estimating the slip position is always required to derive the space angle, which is different from the rotor position [7]. The range of operational speed can be extended in PM brushless machines with relatively high efficiency. The PM brushless machine is also a more viable option than its induction counterpart in the applications with low-speed, high-efficiency, and easy-maintenance requirements. In particular, direct drive system can be developed based on large pole-pair structure with concentrated-winding configuration. All these merits have constantly pushed the industrial penetrations of PM brushless machine drives over the last decades.

1.1.2 The Types of PM Brushless Drives

The PM brushless motor drives can be mainly categorized into two principal types, namely square and sinusoidal wave machines [8, 6, 9]. The square wave excitation machine is essentially equivalent to PMDC commutator machine with a different reference frame. The main magnetic field is introduced by the rotating PMs. This explains the motor with square wave current are called brushless DC machines. Similar to the DC commutator machine, the currents in the stator windings reverse with alternating polarity of the magnetic field by power transistors, which are performed in synchronization with the rotor position angle. Hence, the electromagnetic torque keeps unidirectional, and the resultant characteristics are essentially identical to DC commutator machines mathematically.

The polarity alternation of PMs in the rotor requires square-wave AC excitation in the phase winding. Therefore the phase back EMF is normally designed as trapezoidal waveform to achieve smooth torque with minimum fluctuation. The BLDC machine can be driven by open-loop configuration. However, current surge can be introduced in the start process. Consequently, closed-current-loop, normally realized by chopper control, is employed to achieve square wave current in each phase.

Sinusoidal currents are normally employed in PM brushless machines with sinusoidal back EMF. This kind of machine is simply named as PMSM. The PMSM structure and associated controller hardware are physically the same to the BLDC drive, with the distinction of the difference in control algorithms being incorporated. Normally, the electromagnetic torque in PMSMs can be expressed in the form of the cross vectorial product of the fundamental stator flux linkage space vector and fundamental stator current space vector in the rotating reference frame. Consequently, the vector control can be simply implemented by tracking the d- and q-axis current references, which are determined by the speed or torque reference. The sinusoidal forms of the current from the inverter and back EMF of PMSM are essential to establish ideal stator current space vector with synchronous frequency and achieve smooth instantaneous torque.

PMSM drives possess distinctive advantages on efficiency, low-speed performance and case in implementation of control scheme over induction counterparts. The high performance PMSM drive has been successfully applied in various applications. In particular, high power and torque density, great efficiency, excellent dynamic performance are of prime interest. By eliminating the transition torque fluctuation caused by current commutation in windings, PMSM drives can offer superior torque quality over BLDC drives. Moreover, some harmful ERFD components can be avoided by optimizing sinusoidal air-gap magnetic field and armature-reaction components. Therefore, low torque ripple, low ERV and associated acoustic noise can be generally achieved in PMSM drives.

1.1.3 The Types of PMSM

Based on flux path pattern of the machine, there are mainly three types of PMSMs [10]:

- radial flux PMSM;
- axial flux PMSM;
- linear PMSM.

Each type can be applied for specific applications based on the characteristics. The radial flux structure is the dominant type, while the axial flux PMSM is particularly suitable for applications with special aspect ratio requirement. Linear PMSM is quite popular for high performance direct-drive linear motion systems.

Normally, there are two types of winding arrangements for PMSMs:

- distributed winding;
- concentrated winding.

The distributed winding configuration normally has the coils embracing several stator slot pitches, and is commonly implemented in the machine with slot per pole per phase larger than one. On the other hand, for concentrated winding configuration each coil covers only one stator tooth, which is widely employed in small fractional-slot machines. Concentrated winding configuration can achieve short end winding and high slot fill factor, and hence results in lower resistance and better copper wire usage. PMSMs with FSCW configuration can easily accommodate large number of rotor poles to achieve low-speed direct-drive applications. Moreover, FSCW configuration can increase the inductance significantly so that good flux weakening capability can be easily achieved. However, the FSCW configuration will reduce the machine saliency and hence reluctance torque. The interharmonic MMF components from such winding configuration can produce severe iron core losses and magnet eddy losses. The resultant interharmonic magnetic field components can introduce abundant harmful ERFD components, and aggravate the ERV and acoustic noise problem.

Radial Flux PMSM

The radial flux PMSM can be further classified into inner rotor and outer rotor configurations. The radial flux inner rotor structure is the most common form of PMSMs. The PMs allocated in the internal rotor, as depicted in Figure 1.1(a), introduce the PM magnetic flux, which crosses the air gap into the stator in the radial direction. The fundamental MMF produced by the stator armature interacts with PM magnetic field, and pulls the rotor in synchronisation with traveling speed of stator MMF.

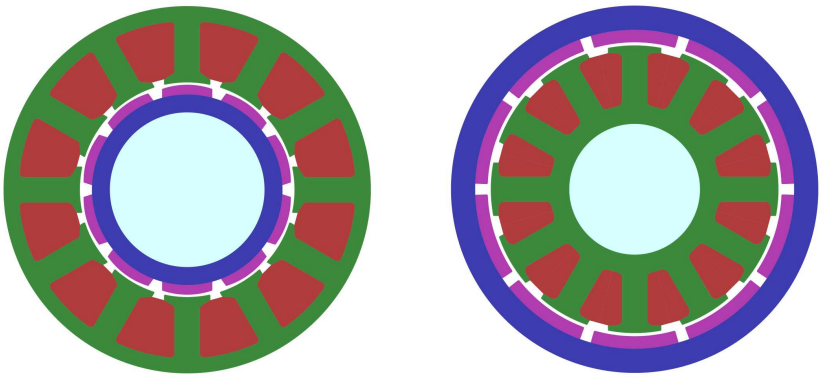

(a) (b)

Figure 1.1: Radial flux PMSM topologies: (a) inner rotor, (b) outer rotor.

As an alternative, the PM rotor can be placed outside the stator in a PMSM. Surface-mounted PM configuration is the most common among this type of PMSMs to achieve thin rotor yoke, as shown in Figure 1.1(b). The magnetic flux path of outer rotor PMSM is very similar to the inner rotor one. With the same machine envelope, outer rotor configuration can offer more circumferential space for PMs to generate the magnetic field so that the electromagnetic torque can be improved to some extent. The winding process can be significantly simplified as the stator openings are on the outer surface of stator core. However, the heat removal of the stator winding can be problematic since it is more difficult to implement an effective stator cooling system. The rotational inertia of the machine can be considerably increased from the inner rotor to out rotor structure. Consequently, outer rotor PMSMs are rarely employed for servo systems, which usually require excellent dynamic response. Normally, only one side of the rotor is mechanically supported in this type of machine. Thus the short axial length of outer rotor PMSM limits the deployment. Such machines are widely used as spindle motors for hard disk drives and ventilation fans for computer cooling. The large air-gap radius and hence high torque density make outer rotor PMSM an ideal contender for high torque direct-drive applications. They commonly appear in wheel hub drives of electric vehicles, gearless traction drives of elevators. It is noteworthy that the FSCW configuration is normally preferred for outer rotor PMSM to achieve large rotor pole number. The applications of outer rotor PMSMs in wind power generation have been intensively carried out. Mature commercial products are readily available for large direct-drive wind power applications [10].

Axial Flux PMSM

Different from its radial flux counterpart, the windings and PMs are arranged along the radial direction in axial flux PMSM, as illustrated in Figure 1.2(a). The magnetic flux travels axially in the air gap to generate electromagnetic torque. The axial flux PMSM is informally named as pancake motor due to its flat appearance. Single sided configuration as shown in Figure 1.2(a), has been employed for many

applications, such as small wind power systems. The unbalanced axial force in this structure, which can reduce the bearing service life significantly, is one of the most disadvantageous issues. The torque production capacity is low due to the relatively small air gap area. Therefore, double-sided configuration with either internal rotor or internal stator is more popular for axial flux PMSM. The axial force can be effectively balanced and the torque density is also significantly improved. Figure 1.2(b) depicts a typical double-sided axial flux PMSM with internal stator configuration. The disk type rotor results in large moment of inertia and compromises dynamic performance. However, it can improve stability against disturbance in return. Similar to outer rotor radial flux configuration, axial flux PMSM can facilitate large number of rotor poles. Hence, axial flux PMSMs are widely used for low-speed applications such as electromechanical traction drive, elevator hoist and wind generator. They are inherently of large aspect ratio and extremely attractive to the applications with stringent axial length constraint. It can be easily noticed that the laminated stator is rather difficult to construct and can increase the cost considerably. Soft magnetic composite material is employed instead to overcome the practical burden in stator manufacture. On the other hand, coverless stator configuration is widely implemented to eliminate the stator core. However, extensive PM material is required to offer competitive magnetic field and the resultant small winding inductance can bring new challenges to the power inverter [11].

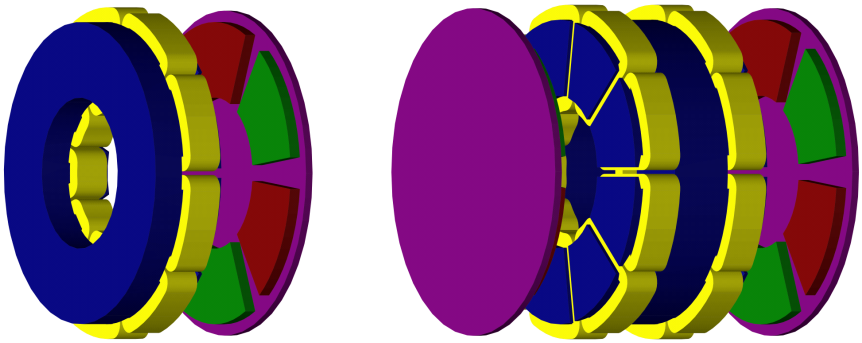

(a) (b)

Figure 1.2: Axial flux PMSM topologies: (a) single-sided, (b) double-sided.

Linear PMSM

In high-performance linear motion applications, the linear PMSM possesses inherent advantages. They can offer direct and accurate translation of speed and position without mechanical transmission. Therefore, better dynamic performance can be potentially accomplished. The mechanical speed of the translational motion synchronises with the armature-reaction magnetic field. As in axial flux PMSMs, both single-sided and double-sided configurations can be employed in linear PMSM. The structural diagrams of both types are depicted in Figure 1.3. Based on the applications, either the PMs or windings can be placed on the mover. By eliminating the intermediate mechanical transmission, high-precision control on translational

force, speed and position can be delivered in linear PMSM direct-drive systems. Therefore, linear PMSMs have been increasingly applied in various industrial applications. With the assistance of contactless magnetic suspension technique, linear PMSMs can be implemented on maglev train to achieve high efficient high-speed transport. It can deliver good safety, high reliability and low environmental impact. The applications on elevator hoisting and electromechanical actuation have also been investigated to improve the overall efficiency and minimize the package size. However, the cost of active material can be a challenging issue in such machines for long-stoke applications. A large amount of PMs or windings are required for the stationary part [12].

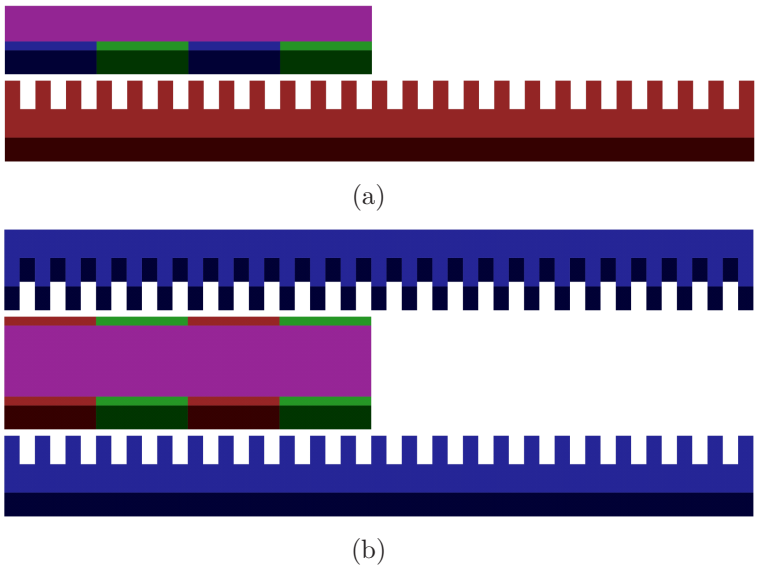

(a)

(b)

Figure 1.3: Linear PMSM topologies: (a) single-sided, (b) double-sided.

1.1.4 Rotor Topologies of Radial Flux PMSM

Despite of large variety of configurations, the radial flux PMSM is still the most common structure, without any doubt due to its overall distinctive merits. The inner rotor configuration has the absolute dominance in high-performance PMSM drives. Without loss of generality, this study is concentrated on the inner rotor radial flux PMSM only. The term of PMSM in the following sections generally means radial flux PMSM with inner rotor configuration.

Based on the position of PMs in the rotor, there are generally three basic types of PM rotor structures [6, 10]:

- surface-mounted PMSM;
- surface-inset PMSM;
- interior PMSM.

The typical depictions of these three types are shown in Figure 1.4 accordingly. In the surface-mounted PMSMs, the PMs are placed on the surface of the rotor as illustrated in Figure 1.4(a). The machine behaves like a constant air gap machine, in which the d- and q-axis synchronous inductances are equal. Sometimes the parallel-sided magnets are employed instead of the fan-shaped for easy assembly. The magnets with flat bottom can be another alternative. The resultant d- and q-axis inductances will be slightly different with relationship of $L_d < L_q$.

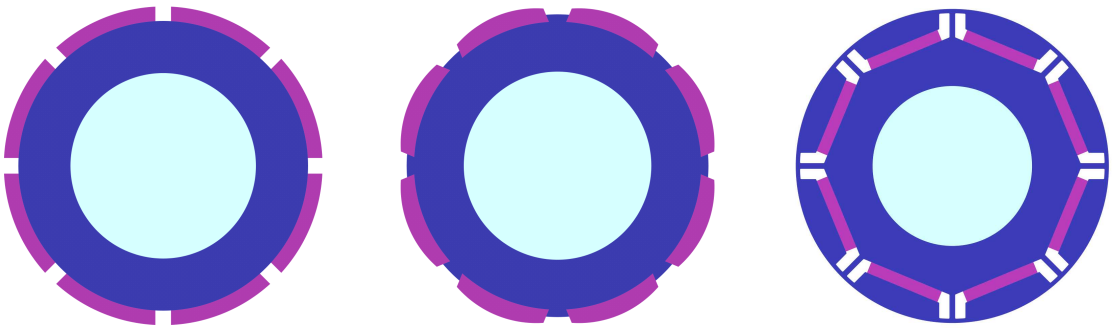

(a) (b) (c)

Figure 1.4: Rotor topologies of PMSM: (a) surface-mounted PM, (b) surface-inset PM, (c) interior PM.

For the surface-inset configuration, the magnets are allocated in the slots along the rotor surface as demonstrated in Figure 1.4(b). The variable air gap length brings magnetic saliency to the machine, which can produce additional reluctance torque. Therefore, the torque density of the machine can be improved with special control. The slot structure can be utilized to help the fixture of the magnets so that the PM assembly tolerance can be improved. The reluctance torque in such machine is quite mild due to the relatively large equivalent air gap.

The interior structure shown in Figure 1.4(c) is widely used due to its excellent torque capability and flux weakening performance. Large saliency ratio (L_q/L_d) can be achieved by allocating the magnet slots inside the rotor so that remarkable reluctance torque can be harnessed to improve the overall performance. Such structure can drastically reduce the equivalent air gap length and hence increase the inductances. As a result, great flux weakening capability can be realized. This configuration can be further subdivided into several types such as straight buried, V-shape buried, U-shape buried, spoke and multi-layer structure. This study only performs a thorough investigation on straight buried type. However, the methods proposed can be easily extended to cover other structures by updating the associated parameters.

1.1.5 Control of PMSM

Control Strategies of PMSM Drives

Based on the d- and q-axis inductances and PM flux linkage, the electromagnetic torque in PMSM can be expressed in the form of the d- and q-axis current vector components. A wide variety of control strategies based on the different d- and q-axis current combinations can be implemented in PMSM drive in order to achieve specific objectives [7, 13]. The non-saliency characteristics of surface-mounted PMSM make the corresponding electromagnetic torque proportional to the q-axis current component. Consequently, the $i_d = 0$ vector control strategy is widely implemented in such machine drive to achieve simple yet effective operation. Although it can also be employed in surface-inset and interior PMSMs, MTPA control strategy is preferred to harness the potential reluctance torque and hence maximize the electromagnetic torque for unit stator current. Normally, the real-time numerical derivations of d- and q-axis currents in MTPA control strategy are too complex and computationally intensive to realize. With minimal compromise, the reference current distribution can be efficiently derived from separate look-up tables instead. Such tables can be generated off-line based on numerical FEA or experimental results. The unity power factor control strategy is another option which can fully utilize the volt-ampere rating of the inverter by keeping the power factor as unity. Off-line look-up tables are also commonly involved in such strategy. As the upper limit of phase voltage is determined by the available DC link voltage, the maximum operational speeds under specific load conditions are restricted under normal vector control strategies due to the constant PM flux linkage. Flux weakening control strategy, which injects demagnetization current in d-axis, can be employed to extend the corresponding speed range with constant power operation. It is noteworthy that the maximum demagnetizing current should be restricted to avoid the irreversible demagnetization of PMs, particularly in ferrite PMSMs. By selecting optimal inverter switching modes, fast torque response can be effectively achieved based on the direct control of both overall flux linkage and electromagnetic torque in DTC strategy. The hysteresis band-band control algorithm is normally incorporated to carry out the switching selection so that high torque ripple can be potentially induced. The synergy of the SVPWM technique and DTC strategy can significantly improve the torque ripple characteristics associated with the switching process. Besides, there are other control strategies in PMSM drives such as maximum efficiency per ampere control. However they are only good candidates for particular applications rather than as a norm. Hence, only the most common control strategies, the $i_d = 0$ vector control, MTPA and flux weakening control, are employed in the investigation of ERFD associated ERV in this study.

Control Algorithms of PMSM Drives

The speed-current double-closed-loop control system is generally a universal solution for PMSM drives to achieve high performance. For some cases with position

control requirement, another closed-loop position controller should be implemented outside the double-closed loop to form a triple-closed-loop system [14]. The classic PI control algorithm is commonly employed for these closed-loop controllers. Various modern control algorithms such as sliding mode control [15], neural control and fuzzy logic control [16] are developed in PMSM drives, which may improve the dynamic response, stability or robustness. The vibration characteristics of PMSM during dynamic period can be very complex. However, the impacts of dynamic performance on ERV characteristics can be neglected for most cases. The investigations of ERV and associated acoustic noise are normally devoted to steady-state operations. Consequently, the common PI and wind-up PID control algorithms suffice the corresponding current and speed controllers in this study.

It is noteworthy that the tracking performance of the corresponding closed-loop controller is largely determined by the control algorithms. Hence, the control algorithms may have noticeable influences on the phase-belt harmonic components in some particular cases. As a result, evident phase-belt harmonic components may appear in the PMSM drive with large torque ripple or back EMF belt harmonic components. In practice, the PI parameters can exert big impacts on the phase-belt harmonic components as well. Nevertheless, the corresponding influences on the fundamental and sideband harmonic components are quite trivial.

PWM Techniques in PMSM Drives

VSI with PWM techniques are extensively used to power the PMSMs to achieve high performance. Thereinto, the SPWM and SVPWM techniques are the two most popular practices in PMSM drives [17, 18, 19]. By comparing the phase sinusoidal reference modulation wave with the triangular carrier wave, the switching sequence of all power modules can be obtained for the SPWM technique. The resultant simple and straight implementation makes it very popular for industrial inverters. On the other hand, the SVPWM technique is becoming the new formidable candidate for high-performance PMSM drives due to its advantageous features such as high utilization of DC link voltage and inherent vector control capability. The first sideband harmonic characteristics of SVPWM technique can also be improved so that it is more favorable in many applications.

Although excellent performance can be delivered by the PMSM drives with PWM techniques, significant sideband harmonic components, whose frequencies are around the multiple of the switching frequency, can be introduced. They will cause some undesirable parasitic effects such as ear-piercing acoustic noise, electromagnetic interference, and additional eddy losses. Particular emphasis is placed on the investigation of sideband harmonic components in PMSM drives with both SPWM and SVPWM techniques in this study.

The RPWM technique is usually implemented to mitigate the associated sideband harmonic problems in PMSM drives. With the randomly variable switching frequency, the frequency of each sideband harmonic component is distributed over a

wide spectrum range. As a result, the corresponding amplitude can be effectively reduced so that the associated electromagnetic interference and acoustic noise can be suppressed accordingly. Some new inverter topologies with multi-level configurations are investigated together with associated PWM techniques in order to attenuate the resultant harmonic distortion [18, 20, 21].

Rotor Position Detection of PMSM Drives

The instantaneous rotor position information is essential for the Park and inverse Park transformation of the voltage and current components in PMSM drive with vector control. The common practice of real-time rotor position detection is direct implementation of angular position sensor such as the encoder and resolver. The cost-effective hall-effect sensor, which can provide low-resolution position signal, is widely employed for the chopper control in BLDC drives. Such use can be extended to supply rotor position information for vector control in PMSM drive. The speed estimation is developed alongside the signals from the hall-effect sensors so that the rotor position information can be constantly updated to improve the resolution [22]. Sometimes, elimination of physical sensor is required in PMSM drive due to various accounts such as cost reduction. As a result, development of effective sensorless control approach becomes extremely important. The classic Luenberger state observer with phase-locked loop technique is widely employed to estimate rotor position based on the current and voltage feedbacks in PMSM drives. Sliding mode observer is introduced to improve the robustness of sensorless control by reconstructing the speed and position information [23]. The rotor position estimations based on both Luenberger stator observer and sliding mode observer can be achieved based on the back EMF. However, the back EMF at low-speed region is normally very small and hence it is practically impossible to measure it accurately for those cases. As a result, the corresponding sensorless control method is no longer feasible for low-speed operation of PMSM drive. Instead, high-frequency signal injection method with either voltage or current, is proposed in many interior PMSM drives to derive accurate position estimation in low-speed and even standstill conditions based on the saliency characteristics. The model reference adaptive system and extended Kalman filter are also introduced to improve the performance of sensorless control. In this study, sliding mode observer scheme is employed to achieve sensorless operation of Prototype I, while hall-effect sensors are employed to support the vector control of Prototype II. Furthermore, the standard Luenberger state observer with phase-locked loop technique is implemented for the sensorless controls of Prototype III and IV.

1.1.6 Disadvantages of PMSM

Besides the numerous advantages, PMSM possesses some inherent disadvantages such as cogging torque, low flux weakening capability, PM eddy current loss, and PM irreversible demagnetization. Those drawbacks have been extensively investigated

for various PMSMs. The vibration and acoustic noise problem, which is the common emphasis for all machine types, can be of particular interest in PMSMs with FSCW configuration especially. The tireless quests for high-power and high-torque PMSM have continuously pushed the boundaries of the design of machines and controllers. Generally, strong magnetic field is essential to boost the power and torque output while the reduction of the space envelope and passive material are always desirable. The combination of these factors makes the vibration and acoustic noise problem the most crucial criteria during the machine design stage.

Cogging Torque and Torque Ripple

Generally, low torque pulsation is an essential requirement in high-performance motion control system using PMSMs. There are two main types of electromagnetic torque fluctuation in PMSMs [24]:

- cogging torque: it is introduced by the interaction of PM magnet flux and reluctance variation with the rotor angular position.
- torque ripple: it is generated by the interaction of back EMF and armature current harmonic components.

The cogging torque has been thoroughly investigated and numerous reduction techniques have been comprehensively developed. The influences of various design parameters such stator slot and rotor pole combination, stator and rotor skewing angle, magnet pole arc width, auxiliary teeth, slot opening width, and magnet displacement, are investigated to mitigate the cogging torque [25, 26, 27, 28]. The FSCW configuration can be employed to achieve low cogging torque as well [29].

The on-load torque ripple can be generally minimized by proper machine design. Essentially sinusoidal back EMF waveform can be achieved by various design techniques such as magnet and rotor surface profiling, low high-order winding factor, sinusoidal slotless winding, stator and rotor skewing scheme, sinusoidal magnetization of PM. As a result, the on-load torque ripple can be effectively reduced. On the other hand, it can be also effectively mitigated by sophisticated machine control. Programmed PWM technique with predetermination of current harmonic injection can be employed to reduce the torque ripple in the drive [30, 31]. On-line compensation algorithms are also developed to minimize the torque pulsation in PMSMs [32, 33].

An analytical model of torque ripple in PMSMs is of particular importance to deliver insightful guidelines for machine and controller designs to achieve low-torque-ripple drives. An analytical expression of cogging torque based on the air-gap magnetic field distribution is proposed in [34]. An improved approach using the flux MMF diagram technique is presented in [35]. FEA method is normally employed to accurately predict the torque ripple in PMSMs by considering all the factors such as

magnetic saturation. As the magnetic saturation can impose impacts on both cogging torque and torque ripple, frozen permeability method can be employed in FEA model to decouple such impacts [36].

Flux Weakening Capability and PM Demagnetization

The poor flux weakening capability due to the constant PM magnetic field is one of the main disadvantages of PMSM. Especially the large equivalent air-gap length in surface-mounted PMSM makes the situation extreme. FSCW configuration can significantly increase the inductances and hence becomes essential to achieve wide constant power operational region in such machines [29]. The equivalent air-gap length can be effectively reduced in interior PMSMs. Therefore, the flux weakening capability can be ameliorated and expands the applications of interior PMSM. The rotor configuration of such machine has a huge impact on the reluctance torque components during flux weakening operation [37, 38]. Therefore, optimization of rotor structure in such machine can improve the flux weakening capability to some extent. However, the flux weakening capability of PMSM drive is still far from satisfactory when comparing with IM drive.

During flux weakening operation, the maximum allowable demagnetizing current should be accurately evaluated to avoid the irreversible demagnetization of PMs, especially in ferrite PMSMs. A reliable flux weakening control algorithm is developed for PMSM drives with the consideration of the protection against PM irreversible demagnetization [39]. The risk of PM irreversible demagnetization under harsh conditions can be effectively managed by assessing the PM magnetic flux density with consideration of the temperature factor. Various design techniques have been developed and investigated to minimize the chance of PM irreversible demagnetization in different types of PMSMs.

PM Eddy Current Losses

The stator armature reaction, even with ideal sinusoidal phase current, always produce abundant accessary air-gap magnetic field harmonic components, especially in FSCW PMSMs. These magnetic field harmonic components are generally introduced by the interaction of armature MMF harmonic components and air-gap permeance harmonic components. They can be further complicated by the effect of the severe core saturation under heavy load conditions. The rotational speeds of these components are normally different from the rotor synchronous speed so that eddy current effect occurs inside the PMs. Consequently, additional core losses and magnet eddy current losses are introduced and sometimes become quite excessive and will deteriorate overall performance. The peculiar FSCW configuration brings low-order interharmonic armature MMF components in PMSM. Such harmonic components can result in a remarkable hike of PM eddy current losses [40, 41]. The current harmonics, including the phase-belt and sideband components, can also

produce noticeable eddy losses in the magnets. Special attention is needed to achieve accurate performance prediction of PMSM drives [42]. Due to the shielding effect of the rotor core, the PM eddy current losses in interior PMSM is relatively small for most cases.

The existing research is mainly concentrated on the modeling techniques to predict such losses promptly and accurately. The analytical model of PM eddy current losses in surface-mounted PMSM is investigated under no-load [43] and load [44] conditions respectively. The method based on the magnetic equivalent circuit is proposed to predict PM eddy current losses for interior PMSMs [45]. On the other hand, FEA method is widely employed for accurate prediction in both surface-mounted [46] and interior [47] PMSMs. A hybrid method combining FEA with analytical models is developed to improve the computational efficiency with minimum compromise on prediction accuracy [48].

Vibration and Acoustic Noise

Vibration and acoustic noise are one of the common issues in all types of electric machine drives. Either long-term damage or immediate failure can be expected in the machine with severe vibration. The associated acoustic noise can be very unpleasant and can cause environmental concerns. Therefore, vibration and acoustic noise as the key parasitic effects become a critical concern during the design of PMSM drives. Generally, the frequency range of interest is from 0 to 1000Hz for mechanical vibration problem while acoustic noise issue covers the frequency over 1000Hz. However, the vibration and acoustic noise are highly associated and always coexist. For instance, the acoustic noise induced by ERFD components arises from the corresponding ERV of the machine. Hence, it is of particular importance to investigate acoustic noise in conjunction with the corresponding ERV in PMSM drive. Moreover, acoustic noise can also be introduced by mechanical frictions such as brush sliding contacts and not related to specific vibration in the machine body. There can be windage noise originating from the friction between the machine rotor and ambient air [49].

By comparisons with its induction and DC commutator counterparts, the special structure and associated magnetic field construction can bring some unique electromagnetic features in PMSMs. The cogging torque [50] and potential PM irreversible demagnetization [51] can exacerbate the torque ripple problem and result in extra torsional vibration in such machines. The popular FSCW configuration introduces low spatial order ERFD components with considerable amplitudes, and leaves the PMSM prone to vibration and acoustic noise [52]. The magnetic saliency and saturation can further complicate the ERV and its associated acoustic investigation in interior PMSMs, especially with FSCW configuration.

Diagnosis and reduction of vibration and acoustic noise have been widely investigated and implemented in PMSM drives. A novel black and white box method is proposed for identification and reduction of acoustic noise of the PMSMs [53, 54].

The black-box method is employed to diagnose the abnormal noise origins and the associated working conditions while the white-box method is used to validate the models for magnetic field, mechanical vibration and acoustic noise. Back EMF measurement based method is developed to determine the vibration intensity at no-load condition in PMSMs [55]. The source identification of vibration and acoustic noise becomes extremely important in PMSM drives for further performance optimization and vibration reduction.

1.1.7 Source of Vibration in PMSM Drive

The source of vibration and acoustic noise in electric machines can be basically categorized into three types as [49, 56]

- mechanical vibration and acoustic noise introduced by imperfect mechanical manufacture and assembly;
- aerodynamic vibration and acoustic noise stemming from the ventilation in the machine;
- electromagnetic vibration and acoustic noise induced by ERFD components, torque ripple, and magnetostrictive expansion of the core.

The mechanical vibration and acoustic noise can be easily triggered by the imperfect manufacture and assembly of the machine. The bearing and eccentricity are the principal causes accounting for a majority of mechanical vibration. The disequilibrium of the rotor due to the manufacture and assembly tolerances results in rotor dynamic imbalance and severe rotor vibration especially with high rotational speed. Misalignment can be another common source of vibration in the machine transmission [57]. The non-ideal mounting on foundation can also be an additional origin of such problem. All these mechanical problems lead to fatal damage and significantly curtail the lifespan of the machine. Various investigations have been conducted to detect these faults in the machine with either online or offline schemes [58, 59, 60, 61].

The aerodynamic source is normally more relevant to acoustic noise. The ventilation fan or siren effect of air duct in high speed machine can produce serious acoustic noise. Therefore, aerodynamical design is essential to optimize the airstream path so that the associated acoustic noise can be readily minimized [62].

The mechanical and aerodynamic vibration and acoustic noise are beyond the scope of this study and hence not included. This study only concentrates on the vibration and acoustic noise associated with ERFD components in PMSM drives.

Torque Pulsation

The torque pulsations in the machine can lead to severe torsional vibration. It implies that both cogging torque and torque ripple potentially introduce vibration and associated acoustic noise in PMSMs [63]. Consequently, reduction of these torque pulsations in PMSMs is commonly implemented to mitigate torsional vibration. By compensating the stator current with specific order harmonic components based on the vibration feedback, the torsional vibration can be effectively reduced [64]. Compensation based on the cogging torque and torque ripple information, the vibration behaviours of DTC controlled BLDC and PMSM drive systems are meliorated [65, 66]. Repetitive control together with online Fourier series expansion is developed to suppress torsional vibration [67]. The vibration signal is detected for the repetitive controller to produce corresponding compensation so that the torque ripple and associated vibration can be effectively attenuated. Online FFT on the signal provides vital information for the compensation.

The vibration induced by cogging torque is specifically introduced in some research [50]. Numerous design techniques are proposed for effective cogging torque reduction. Stator teeth pairing [68] and slot shift are two main stator design techniques. Indentations can be introduced in the rotor magnet poles to reduce cogging torque and acoustic noise. The discrete axial skewing technique is one of the most common practices in such machine [69]. The stator tooth shaping profile is also an effective way in the BLDC motor for cogging torque and associated noise reduction [70].

The investigations on torque pulsation, its related vibration and acoustic noise have been extensively carried out for PM brushless machines. There is an abundance of literature covering a huge amount of techniques to reduce them. Therefore, they are not included in this investigation for further discussion.

ERFD Components

The magnetic field harmonic components inhere in the air gap of PMSMs from the stator and rotor structure, winding arrangement and core saturation. These inevitable harmonic components together with the fundamental component will interact with each other to produce ERFD components in the machine. These ERFD components are found to be waves of different frequencies and spatial orders in the air gap around the air-gap periphery. Normally, the low-order components with large amplitude are susceptible to high mechanical response and hence cause severe vibration. The Maxwell stress tensor theory shows both radial and circumferential air-gap magnetic field components contribute ERFD items. The circumferential components have similar spatial and temporal order as their radial counterparts but normally much lower amplitudes. For the sake of simplicity, only the radial magnetic field components are considered in ERFD evaluations.

The characteristics of ERFD have been extensively investigated by various research studies. The ERFD characteristics with various field harmonic components in IMs

are revealed by analytical models [71]. While ERFD harmonic components of a surface-mounted PMSM are investigated based on the analytical expressions of the radial and circumferential air-gap magnetic field [52], an improved analytical model of air-gap magnetic field is proposed to enhance the accuracy of ERFD prediction [72]. Although the analytical models can provide insightful introduction for the spatial and temporal orders of the ERFD components, they are limited to only some special surface-mounted structure. It is nearly unattainable for the interior PMSMs due to the complex rotor structure and significant core saturation. Therefore FEA method is commonly employed to evaluate the ERFD components accurately in such machines [73, 74]. The ERFD characteristics including the spatial order, frequency and amplitude can be revealed.

The resultant vibration is the main by-product from ERFD components, and has been widely investigated based on structural analysis. A fully analytical model is developed for the vibration and acoustic noise behavior prediction in IM [75]. An analytical model is also introduced to determine the radial deformation of the stator teeth [76]. A statistical approach is employed to predict radiated acoustic noise especially for high-frequency cases [77]. It is noteworthy that the ERFD components involved in these analytical structural models are estimated by electromagnetic FEA method. Combination of analytical and numerical methods is developed to predict the stator radial displacement [78]. A mechanical FEA model is employed to obtain the corresponding stator modal matrix. The modal information is forwarded to the analytical equations so that the stator surface deflection can be derived. Full FEA method can be developed to accurately assess the mechanical deformation with consideration of the magnetostriction effect [79].

1.1.8 Low- and High-Frequency ERV

There are generally three types of current components existing in PMSM drives:

- fundamental current component;
- phase belt current harmonic components;
- sideband current harmonic components.

The phase-belt current harmonic components generally originate from the back EMF harmonic components. They are further influenced by the control strategies, controller parameters and discretized feedback. The sideband current harmonic components are produced by the PWM scheme due to the switching process in each cycle. Besides, the current-harmonic-injection method of the controller for the purpose of torque ripple reduction or sensorless control can directly introduce harmonic components in the drive system. The frequency of fundamental and phase-belt harmonic components are normally orders of magnitude lower than the sideband frequency. Therefore all these components are treated as low-frequency magnetic

field harmonic components. The associated ERFD components produced by the interaction between these low-frequency magnetic field components are also of low frequency. The ERFD components introduced by interaction between the sideband and low-frequency magnetic field harmonic components are normally of high frequency. They are named as high-frequency or sideband ERFD. Respective low-frequency and high-frequency ERV can be excited by these low-frequency and sideband ERFD components in electric machine drives. Corresponding acoustic noise will appear and become another issue.

Low-Frequency ERV

Investigations of low-frequency ERFD components and their associated ERV have been extensively carried out in electric machines based on various methods. Multi-physics approach is commonly implemented to predict ERV accurately. Electromagnetic and mechanical FEA methods are normally employed to estimate the ERFD components and ERV respectively. Such coupling method can offer reasonably good predictions of vibration characteristics related to low-frequency ERFD components. Therefore, this method is employed to analyze the low-frequency ERV of interior PMSMs [80]. The electromagnetic FEA model is constructed to evaluate the radial and circumferential magnetic field components in the air-gap of the machine. The associated ERFD components can be derived and applied in the mechanical FEA model to predict the ERV characteristics.

The spatial and temporal orders of ERFD components evaluated by the FEA method are sometimes quite difficult to reveal. Therefore 2-D FFT analysis on the ERFD results from comprehensive transient FEA models is essential to decouple the ERFD components based on their spatial and temporal orders [81]. The corresponding ERV components can be evaluated based on the mechanical harmonic response analysis. Such method can be quite versatile and hence employed to investigate ERV features of the machine under any specific operation [82]. One of the main drawbacks is the huge computational intensity. Based on magnetic field reconstruction and mechanical impulse response, a computationally efficient type of coupling method can be achieved to predict ERFD components and associated ERV [83]. An analytical model is developed to study the structural behavior of surface-mounted PMSM with an assistance from modal evaluation in FEA model [84].

Besides ERFD and ERV characteristics study, such a multi-physics method can be applied to improve low-frequency vibration behavior of PMSM. The effects of stator slot and rotor pole combination on low-frequency ERV features are revealed [85, 86]. The ERV behaviors of FSCW PMSMs with the same rotor but different stator slot numbers are investigated [87]. Whilst, such ERV characteristics are evaluated and compared for FSCW PMSMs with the same stator but different rotor poles [88]. The rotor magnet pole or stator tooth shape can have a huge impacts on the magnetic field harmonic components. Therefore, optimization of them can improve the vibration performance significantly in PMSMs [89]. The rotor pole parameters of spoke-type interior PMSMs are optimized to minimize the harmful

ERFD components and hence ERV [90].

Although the FEA methods are involved in the evaluations of ERFD and the associated ERV in the coupling model, large prediction error can still occur. The ERFD components with different spatial and temporal orders are evaluated based on the air-gap magnetic field with the consideration of slot opening effect. But the stator slots will have a great impact on the actual ERV production. In fact, the transmission of ERFD components through stator teeth toward the yoke can result in a modulation effect and change the spatial order. This effect is normally not included in most of the existing methods so that large error appears in the predictions. Consequently, new multi-physics methods are developed for accurate low-frequency ERV analysis in PMSMs by incorporating the stator tooth modulation phenomenon. The analytical model of the stator tooth modulation effect is developed as well.

High-Frequency ERV

Due to its ear-piercing frequencies, the sideband acoustic noise can be quite troublesome, though the amplitudes of the corresponding ERFD components are normally trivial. Such ERFD components mainly originate from the sideband voltage harmonic components introduced by PWM techniques. Numerical methods such as circuit simulation coupled with field FEA model can be employed to accurately predict such components in the drive with specific operational conditions. However, such methods are computationally intensive and hardly provide efficient design guidelines. Therefore an effective and simple analytical approach becomes practically attractive in order to reveal the insightful correlations between these harmonic components and design parameters. Double Fourier series expansion method is employed to derive the sideband voltage harmonic components from SPWM [91] and SVPWM [92] in closed-form formulae.

The complex magnetic structure of the machine including stator slots and rotor saliency makes the analytical derivations of the corresponding sideband current harmonic components quite burdensome. Therefore the existing studies merely concentrate on the analytical derivation of harmonic distortion index instead. It can be employed to evaluate the performance of corresponding PWM technique [93, 94]. On the other hand, the research on this subject is largely devoted on the optimization of sideband current harmonic components and their associated issues. Various techniques, such as multilevel inverter [95], hybrid PWM scheme [96] and random PWM techniques [97] are proposed and investigated to reduce or optimize the sideband parasitic effects.

As the analytical sideband current models are not readily available, the spatial and temporal orders especially the amplitudes of the corresponding ERFD components are not attainable. The investigations on high-frequency ERFD components and acoustic noise are quite limited and mainly focus on IM drives. However the mechanism of sideband ERV and acoustic noise in PMSM drives is more complex than IM drives due to the interactions stemming from the saliency effect. Thus a new analyt-

ical approach to predict the sideband current harmonic components and hence the corresponding ERFD and ERV characteristics is developed for PMSM drives with both SPWM and SVPWM techniques in this study. The proposed closed-form analytical models are of significant importance to offer insightful behavior analysis of high-frequency acoustic noise in PMSM drives. The direct revelation of the primary influence factors allows quick development of effective high-frequency acoustic noise mitigation techniques for specific applications.

1.2 Outline

The vibrations induced by both low-frequency and high-frequency ERFD components are comprehensively investigated for PMSM drives in this study. These ERFD components are introduced by the interactions between the corresponding magnetic field components, which are produced by the PMs and armature reactions. Besides the PM magnetic field, the accurate predictions of armature current harmonic contents are essential for the study. Consequently, the study starts with the modeling of PMSM and its drive with various controllers. The fundamental, phase-belt and sideband harmonic components of armature current can be estimated either analytically or numerically based on the proposed methods. The effective derivations of the magnetic field components from PM excitations and armature reactions are further provided by considering the rather complex rotor structure in interior PMSMs. As a consequence, the low-frequency and high-frequency ERFD components and their associated ERV are analytically derived and discussed. Comprehensive numerical simulations and experimental tests are carried out to validate the proposed analytical models.

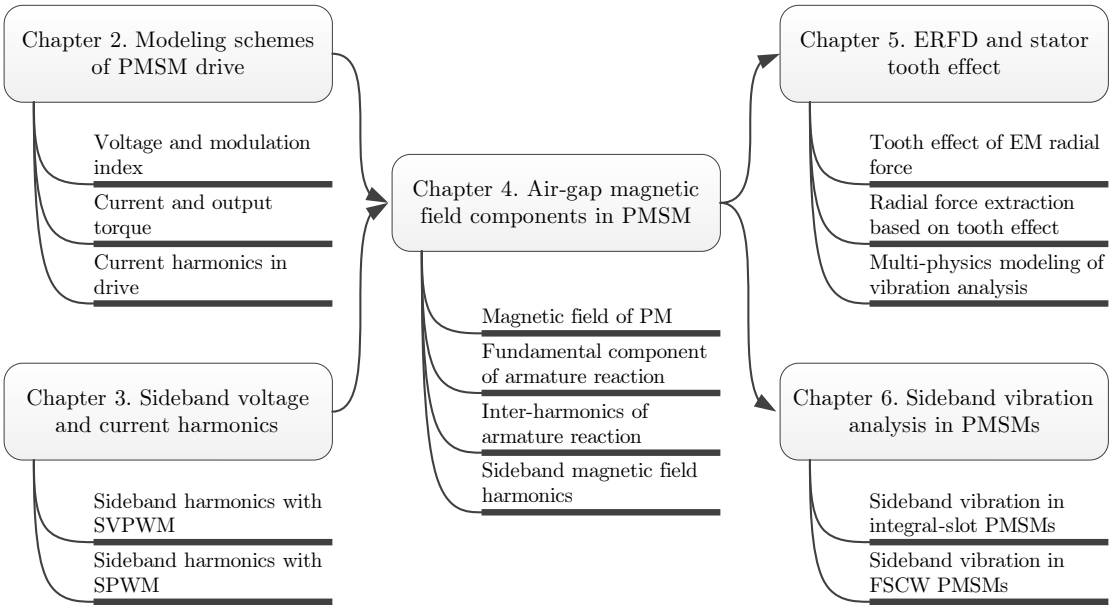

Figure 1.5: The outline of the study.

The work mainly comprises five parts and each part forms an individual chapter. The brief contents and relations of these chapters are depicted in Figure 1.5. The rationale of the study is clearly demonstrated in the flow chart above, and the summarizations of these chapters are outlined as:

Chapter 2 introduces the steady-state performance prediction of the PMSM drive. The voltage and current of PMSMs can be derived based on the circuit-field coupling technique. The co-simulation schemes and nonlinear modeling technique are investigated for accurate predictions of current harmonic components in the drive with different control strategies.

Chapter 3 presents new analytical derivations of sideband current harmonic components in PMSM drives with SPWM and SVPWM techniques. The analytical models are further extended to take into account the core saturation and crossing coupling effect in interior PMSMs. Comparison between SPWM and SVPWM techniques is carried out based on the analytical model. Comprehensive experimental results are employed to verify the validity of the proposed analytical models.

Chapter 4 focuses on the analytical model of air-gap magnetic field components induced by PMs and the armature reaction. A new and accurate method is developed to analytically predict the PM magnetic field in interior PMSMs. The rather complex permeance of interior PMSMs is also analytically approximated especially for the FSCW configuration. As a result, all the armature-reaction magnetic field components including the fundamental and interharmonic components can be analytically derived based on the magnetic field superposition technique.

Chapter 5 investigates the stator tooth modulation effect on the ERFD components and corresponding stator vibration characteristics. The analytical models based on the assumption of uniform and uneven distribution of radial force on the stator tooth shoe surface are developed to estimate the stator tooth modulation effect. Based on the stator tooth modulation effect model, novel multi-physics schemes are proposed to predict the stator vibration promptly without considerable compromise on the accuracy.

Chapter 6 proposes the analytical models of sideband ERFD components for both integral-slot and FSCW PMSMs. The analytical and experimental investigations of high-frequency ERV associated with corresponding sideband ERFD components are comprehensively carried out. The influence of rotational speed, armature reaction and PWM carrier frequency on the ERV characteristics of PMSMs are revealed and discussed. Besides, a new method to detect the damping ratios is developed based on the proposed sideband ERFD models.

They are followed by the conclusions and future work discussion in Chapter 7.

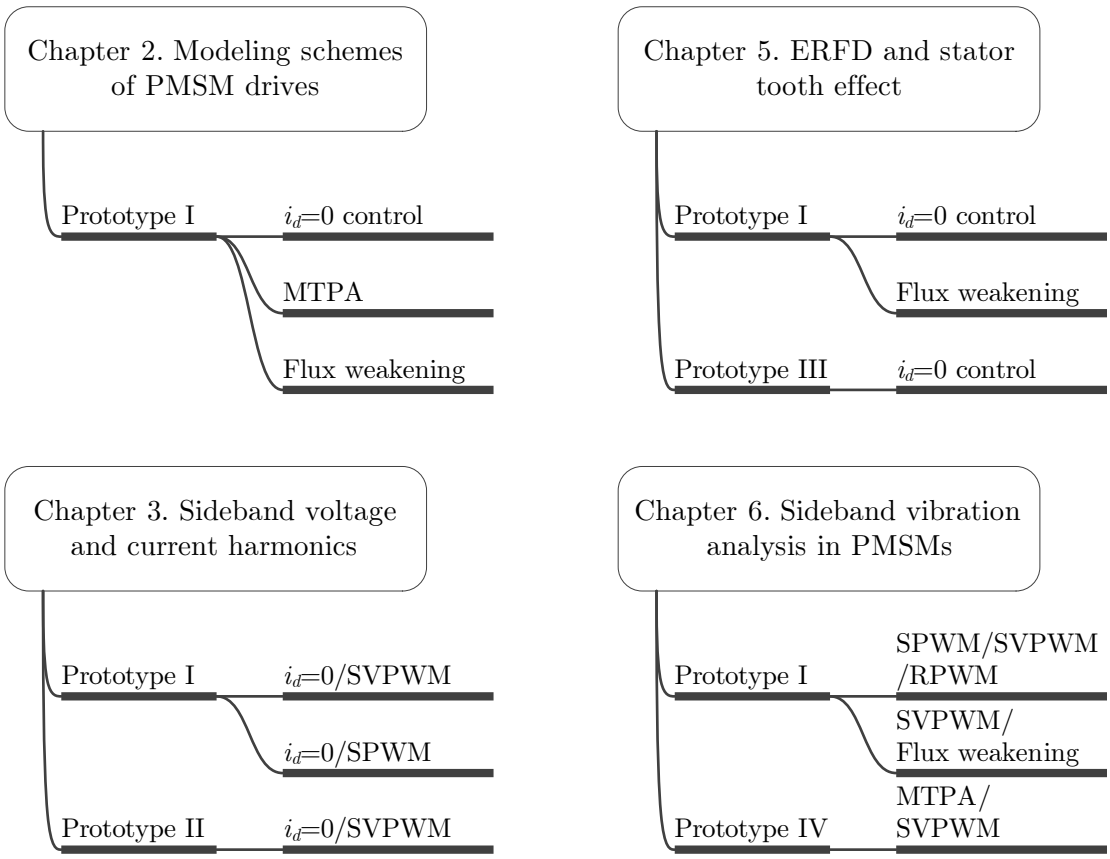

Figure 1.6: Experiments involved in the study.

Four prototype PMSM drives, detailed in Appendix A, are employed to experimentally underpin the validity of the proposed models either indirectly or directly in this study. The prototypes and control algorithms involved in experiments for all the validations throughout the study are demonstrated in Fig. 1.6.

Prototype I, a 10-pole 12-slot FSCW interior PMSM, is employed for the experimental validation in Chapter 2. As the machine experiences severe magnetic saturation under rated operational condition, the effectiveness of the proposed methods for severe saturation conditions can be thoroughly examined. The surface-inset PMSM, prototype II with 8-pole 30-slot configuration, is used to validate the analytical sideband current harmonic model in Chapter 3. The armature reaction in such surface-inset PMSM is generally small, thus the inductances of the machine can be assumed constant over the operational range. This makes Prototype II the right candidate to validate the linear analytical model. On the other hand, the validation of the improved nonlinear model rests on Prototype I. The comparison between SPWM and SVPWM techniques is carried out based on Prototype I as well.

It is practically very difficult to measure the magnetic field and ERFD components in PMSM. Therefore, the corresponding models in the study are validated by FEA results instead. The vibration measurements on Prototype III and IV are employed to indirectly underpin the validity of such magnetic field and ERFD models.

Prototype III is a surface-mounted ferrite PMSM with extremely large equivalent air gap and nearly closed slot openings. Therefore, the tooth harmonic components of the PMs and the armature-reaction magnetic field are trivial and hence can be ignored. This makes Prototype III the ideal candidate to demonstrate the stator tooth modulation effect on ERFD in Chapter 5. Besides, both no-load and flux weakening operations are implemented in the drive of Prototype I to study the proposed ERFD extraction method based on the stator tooth modulation effect. There are abundant interharmonic components in Prototype I with flux weakening operation due to its interior PM and FSCW configurations. Therefore it can be treated as large load condition so that the armature-reaction effects on the ERV characteristics can be investigated without potential interference from the mechanical transmission.

The Prototype IV with 6-pole 36-slot configuration, is driven by a two-level VSI with MTPA vector control in the sideband ERV investigation of integral-slot PMSM. Additionally, various modulation schemes including SPWM, SVPWM and RPWM techniques are applied to the PMSM drive of Prototype I so that the corresponding sideband ERV features of FSCW PMSM are revealed and compared.

Control algorithms such as SMO, stator observer and feed-forward current control are employed to guard the successful operation of these experimental platforms.

1.3 Main Contributions

The scientific contributions of this study are summarized in this section. Two generic modeling schemes of PMSM drive systems are proposed:

- A new transient-transient co-simulation technique is proposed for drive system simulation based on multi-loop theory of electrical machines.
- A new universal machine modeling scheme considering saturation effect and spatial harmonic components is proposed for transient simulation of drive system.

The air-gap magnetic field in all inner-rotor PMSMs is analytically discussed, and corresponding analytical models are derived. The main contributions of this part cover:

- A new analytical model of open circuit air-gap flux density distribution in single-layer interior PMSMs is presented by taking into account the impact of rotor flux barrier bridges. The harmonic characteristics are accordingly derived based on the proposed model.
- A new permeance model is analytically derived for the interharmonic magnetic field components evaluation. Meanwhile, the winding inductance model in FSCW PMSMs is improved accordingly.

- A new analytical model of air-gap armature-reaction interharmonic magnetic field components in FSCW PMSMs is proposed based on permeance model and superposition principle.

For the low-frequency ERFD and ERV investigation, the contributions mainly lie on the stator tooth modulation effect. They can be concluded as:

- The phenomenon of stator tooth modulation effect on the ERFD components is demonstrated and validated by combination of the structural simulation and experimental results.
- The analytical stator tooth modulation effect model of the ERFD components is proposed based on the assumption of both even and uneven distribution of radial force on the stator tooth shoe surface.
- Based on the proposed stator tooth modulation effect model, the new multi-physics vibration analysis procedure coupled with either analytical vibration model or numerical method is proposed.

Last but not least, the main contributions on the investigation of high-frequency ERV associated with PWM schemes include:

- An analytical sideband current harmonic model of PMSM drives fed by VSI with SVPWM scheme is proposed considering rotor saliency.
- An improved analytical sideband current harmonic model is further developed to cover the influences of magnetic saturation and cross coupling effects in interior PMSMs.
- The linear and nonlinear analytical sideband current harmonic models in PMSM drive system with SPWM technique are derived respectively.
- Novel sideband ERFD and ERV models are derived for integral-slot PMSMs fed by VSI with SVPWM. The impacts of speed and load on ERV characteristics are analytically and experimentally unveiled.
- The sideband ERFD and ERV models for FSCW PMSM are further developed and validated.
- The characteristics of sideband ERFD and ERV in FSCW PMSMs with SPWM technique are discussed with similar procedure.

Chapter 2

Modelling Schemes of PMSM Drives

The ERFD components are produced by the interaction of air-gap magnetic field components. The air-gap magnetic field is composed of PM introduced and armature-reaction components. The armature-reaction components are normally induced by the fundamental current component, which is mainly determined by the operational condition, and significantly affected by the control strategy. The current distortion, such as phase-belt and sideband harmonic components also introduce corresponding armature-reaction components, which are of particular importance in ERFD analysis. The fundamental and phase-belt harmonic current components can be accurately derived from FEA simulations or relevant equivalent models. However, the sideband current harmonic components are preferably evaluated in analytical methods due to potential computational intensity. More importantly, such characteristics can be insightfully reflected by an analytical model, which will be separately discussed in the next chapter.

This chapter illustrates the preliminary principle of PMSM drives. Both steady-state and transient models are introduced with consideration of the control algorithm impact. For the steady-state analysis, the traditional *d*-*q* model is employed to predict the drive performances under different control strategies. The nonlinear parameters involved in the model can be calculated by the FEA parametric sweeping with different *d*- and *q*-axis current combinations. The fundamental current component of the drive with certain control strategy under specific load can be obtained based on such nonlinear model. The model can be further employed for the armature reaction field analysis. For the transient model, a circuit-field coupling scheme is normally adopted to improve the prediction accuracy. Three time step schemes including fixed time step, variable time step and triggered time step are discussed for strong circuit-field coupling technique used in this study. The proposed trigger method is particularly suitable for the drives with PWM techniques by significantly improving the computational efficiency without compromise on the prediction accuracy. A generic weak-coupling scheme is also introduced based on the multi-loop machine model in order to flexibly develop the control model. Another new nonlin-

ear harmonic modeling technique is proposed to further improve the computational efficiency based on the multi-loop machine model. All these methods can be implemented to predict the dynamic behavior of drive, together with current harmonic characteristics. The derived current components will be further employed to evaluate the corresponding magnetic field and ERFD components. Both steady-state and transient modeling techniques are validated by experimental results.

2.1 The Linear *d*-*q* Model of PMSM

The linear *d*-*q* model is widely employed to predict the steady-state behavior of PMSM drives, by neglecting the core saturation impact of the machine over full operation range [98]. By involving the FE model and Fourier series expansion, the harmonic characteristics can be also taken into consideration [99]. In this part, the *d*-*q* model is used to promptly estimate the steady-state performance of PMSM drive. As the characteristics of VSI driven PMSMs are significantly affected by the control strategy, the control aspects are incorporated in the model. The most common strategies of $i_d = 0$ vector control, MTPA control and flux weakening control are investigated in the study. This model can be easily adapted for other control strategies, such as MEPA control and DTC by applying corresponding constraints. The variables such as fundamental current amplitude, modulation index and torque angle can be derived by the model. They will be employed for further armature-reaction field and sideband components analysis.

2.1.1 Traditional *d*-*q* Model

The *d*-*q* model of PMSMs can be expressed in electric-circuit form as

$$\begin{cases} u_d = R_s i_d + L_d \dfrac{\mathrm{d}i_d}{\mathrm{d}t} - \omega_e \psi_q \\ u_q = R_s i_q + L_q \dfrac{\mathrm{d}i_q}{\mathrm{d}t} + \omega_e \psi_d \end{cases} \tag{2.1}$$

where the winding flux linkage can be derived as

$$\psi_d = L_d i_d + \psi_f, \quad \psi_q = L_q i_q \tag{2.2}$$

The electromagnetic torque can be represented as

$$T_{em} = \frac{3}{2} p(\psi_d i_q - \psi_q i_d) = \frac{3}{2} p(\psi_f i_q + (L_d - L_q) i_d i_q) \tag{2.3}$$

and the associated mechanical model can be written as

$$T_{em} = T_L + J_M \frac{\mathrm{d}\omega_r}{\mathrm{d}t} + B\omega_r \tag{2.4}$$

These four equations represent the typical *d-q* dynamical model of PMSM. The parameters L_d, L_q and ψ_f are normally considered constant in the linear model. However, these parameters are actually variables due to the influences of slot opening, rotor saliency and core saturation. In such a model, all the spatial harmonic components except the fundamental component of the magnetic field are ignored. As a result, the corresponding voltage, current harmonic components and torque ripple are not included. As the saturation effect has not been taken into account, the application of such model to the variable-parameter condition can result in significant prediction errors. Normally, the rated parameters are only valid for the performance assessment of the drive near rated condition. For other conditions, the corresponding parameters need updates for accurate prediction.

This model is still very useful for some specific applications, such as quick performance appraisal at the initial stage of drive design. This model also can be employed for fast prediction of the steady-state performance of a PMSM drive. In the steady-state conditions, all the time-dependent components can be eliminated in the model. As a result, the circuit model can be rewritten as

$$u_d = R_s i_d - \omega_e \psi_q, \quad u_q = R_s i_q + \omega_e \psi_d \tag{2.5}$$

And the voltage amplitude can be accordingly calculated by

$$u_s = \sqrt{\left(R_s i_d - \omega_e \psi_q\right)^2 + \left(R_s i_q + \omega_e \psi_d\right)^2} \tag{2.6}$$

The maximum input voltage of the drive is limited by the DC link voltage of inverter. Consequently, the angular frequency is limited by the constraint formation as

$$\sqrt{\left(R_s i_d - \omega_e \psi_q\right)^2 + \left(R_s i_q + \omega_e \psi_d\right)^2} \leq u_{\max} \tag{2.7}$$

where, $u_{\max} = U_{dc}/\sqrt{3}$ and $u_{\max} = U_{dc}/2$ for SVPWM and SPWM techniques respectively. Meanwhile, the current amplitude is also restricted by

$$i_s = \sqrt{i_d^2 + i_q^2} \leq i_{\max} \tag{2.8}$$

The mechanical model can be updated as

$$T_{em} = T_L + B\omega_r \tag{2.9}$$

The other two important parameters involved in the PMSM drive, the modulation index and torque angle, are defined as

$$M = \frac{2u_s}{U_{dc}}, \quad \delta = \arctan\frac{-u_d}{u_q} \tag{2.10}$$

Different load conditions can be represented by these two parameters over the whole range. Hence, they will be employed as variables for performance evaluation of PWM techniques, and indices for output capability assessment in PMSM drive.

2.1.2 Output Capability Analysis

The steady-state performance is significantly influenced by control strategy applied. Such control strategy is determined by the requirement of drive system in specific applications. It is imperative to analyze the performance of a PMSM drive with the corresponding control strategy. The typical control methods, including $i_d = 0$ control, MTPA control and flux weakening control are discussed.

It can be seen from Equation (2.3) that the electromagnetic torque is determined by two variables i_d and i_q. For each torque, there are generally infinite combinations of i_d and i_q satisfying the equation. In order to obtain the specific current combination for specific torque, another constraint is required to solve the equation. The control strategy imposes an exact constraint to identify the relationship between the d- and q-axis components of current. For $i_d = 0$ control, the model can be simplified as

$$T_{em} = \frac{3}{2} p \psi_f i_q \tag{2.11}$$

Based on this model, the steady-state current with different output torque can be easily obtained. The parameters, such as the d- and q-axis voltages, modulation index and torque angle with different operational condition, including angular speed and torque load can be derived. The power factor and efficiency can be estimated as well.

For MTPA control, the extra constraint is [13]

$$\min i_s = \sqrt{i_d^2 + i_q^2} \tag{2.12}$$

In order to solve the torque equation with this constraint, the Lagrange method can be employed to construct the equations set. By solving the equation, it can be derived that [100, 101]

$$i_d = \frac{\psi_f - \sqrt{\psi_f^2 + 4(L_d - L_q)^2 i_q^2}}{2(L_q - L_d)} \tag{2.13}$$

It is noteworthy that this is only valid for PMSM with $L_d \neq L_q$. Substituting it into Equation (2.3), the electromagnetic torque can be represented as

$$T_{em} = \frac{3p\left(\psi_f + \sqrt{\psi_f^2 + 4(L_d - L_q)^2 i_q^2}\right) i_q}{4} \tag{2.14}$$

It is apparent that the exclusive variable i_q in Equation (2.14) can be solved for specific torque. Therefore i_d can be calculated by Equation (2.13). The voltage and torque can be derived accordingly.

Different from $i_d = 0$ and MTPA control, the voltage maintains its maximum value for flux weakening control. In order to obtain the maximum speed for a specific torque load, the currents are also constrained within its maximum, which is determined by both the converter and machine. Thus, the extra constraints for flux

weakening control are introduced from the voltage and current restrictions, and can be expressed as

$$\begin{cases} u_{\max} = \sqrt{(R_s i_d - \omega_e \psi_q)^2 + (R_s i_q + \omega_e \psi_d)^2}, \\ i_{\max} = \sqrt{i_d^2 + i_q^2} \end{cases} \tag{2.15}$$

Based on Equation (2.3) and (2.15), the output maximum speed capability can be derived for flux weakening vector control. Normally, the current needs to be examined by FEA to ensure that the PMs are not irreversibly demagnetized in flux weakening conditions.

2.1.3 Prompt Performance Prediction

The linear *d*-*q* PMSM model is implemented in this subsection to promptly predict the performance characteristics of Prototype I, an interior PMSM with FSCW configuration. It is quite difficult to analytically evaluate the electromagnetic parameters due to the severe magnetic saturation and flux leakage in the rotor flux barrier bridges in the machine. Therefore, 2-D FEA method is employed to accurately predict the necessary parameters for the model. The *d*- and *q*-axis inductances and PM flux linkage can be derived from the 2-D FEA model with no-load condition, and the resultant magnetic field flux density distribution is given in Figure 2.1(a). Based on the electromagnetic torque versus current capability model, the *d*- and *q*-axis current components can be derived for the machine drive with specific control strategy and torque output. The corresponding voltage components can be directly evaluated from Equation (2.5) while they are also constrained by Equation (2.7). This constraint generally determines the maximum achievable rotational speed for the drive with certain load condition.

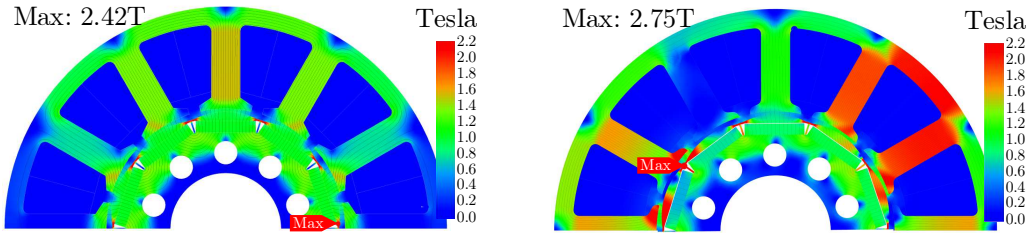

(a) (b)

Figure 2.1: Magnetic field distribution: (a) no-load condition, (b) load condition

The correlations between the *d*- and *q*-axis current components and electromagnetic torque for Prototype I with different control strategies such as i_d=0, MTPA and flux weakening vector controls revealed in Figure 2.2(a), while the corresponding maximum operational ranges are obtained and illustrated as Figure 2.2(b). The maximum obtainable electromagnetic torque is determined by the thermal and mechanical constraints of the machine, the current limitation and control strategy of

the drive. It can be directly observed from the figure that the MTPA control strategy provides larger electromagnetic torque than $i_d = 0$ control strategy as a result of effective utilization of reluctance torque. Meanwhile, the MTPA control strategy can generally deliver higher critical speed over the whole torque range available. However, the operational speed ranges for both control strategies are quite confined. On the other side, the flux weakening control strategy allows the machine achieve much wider operational speed range. In practice, the MTPA control strategy is implemented to achieve maximum electromagnetic torque up to the base rotational speed and the flux weakening control will kick in for the speed beyond.

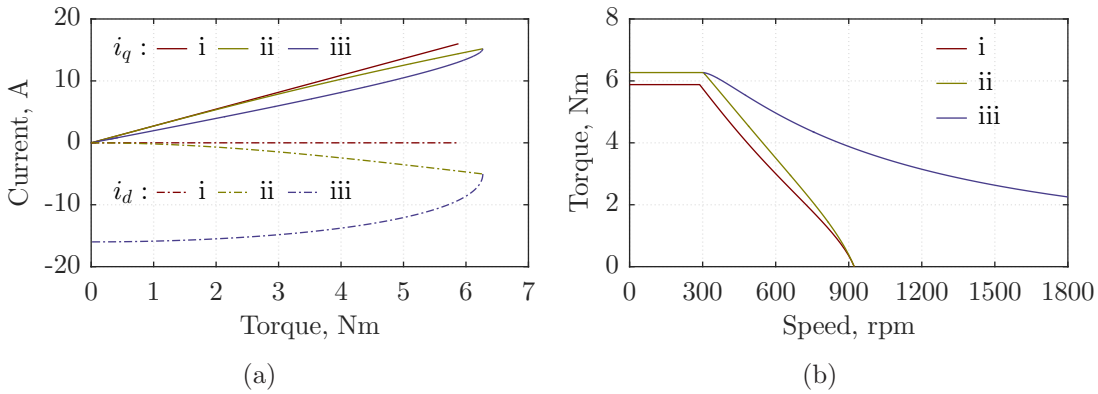

Figure 2.2: Output capability analysis in different control strategies: (a) *d*- and *q*-axis current components with output torque, (b) maximum operating range. (i - $i_d = 0$, ii - MTPA, iii - Flux weakening)

The performance analysis based on the linear model can be employed for the quick assessment of preliminary machine design and assistance of control strategy development. Therefore, such linear *d*-*q* model can be directly employed to facilitate fast but approximate initial design and optimization of PMSM drive. In practice, the additional armature-reaction magnetic field components can cause magnetic saturation in the machine and hence result in totally different parameters from the no-load condition. The magnetic field of Prototype I with i_q=15A under i_d=0 control strategy is evaluated by 2-D FEA and the resultant magnetic field flux density distribution is derived and illustrated in Figure 2.1(b). It can be observed that severe magnetic saturation occurs in the stator core due to the large armature-reaction magnetic field. Such saturation phenomenon significantly affects the *d*- and *q*-axis inductances and PM flux linkage and will ultimately abate the electromagnetic torque capability of the machine. As the combinations of *d*- and *q*-axis current components for the same electromagnetic torque are quite different, the level of magnetic saturation can be largely deviated with different control strategies. As a result, adoption of the parameter set from no-load condition in the model tends to overestimate the machine performance especially with large load conditions. The magnetic saturation brings nonlinear characteristics into the machine and hence introduces evident errors from the linear model. The inclusion of the influences of the magnetic saturation on the parameters is essential for the model to achieve accurate performance prediction. Therefore, the linear *d*-*q* PMSM model is further extended to take into account the

effect of magnetic saturation in the machine.

2.2 The Improved Nonlinear *d*-*q* Model

Besides the nonlinearity of *d*- and *q*-axis inductances and PM flux linkage, the magnetic saturation can bring cross-coupling effect between *d*- and *q*-axis, and hence introduces an extra mutual inductance term M_{dq} especially for interior PMSMs. Neglect of such nonlinearity and cross-coupling effects can result in significant prediction errors. The nonlinear characteristics of inductances and electromagnetic torque against *d*- and *q*-axis current components are considered for the model in order to improve the accuracy [102]. The equivalent magnetic circuit network method is developed to accurately evaluate the cross-coupling effect besides the nonlinear behavior of magnetic saturation in the machine [103]. The numerical curve-fitting method is implemented on the nonlinear electromagnetic parameters from common FEA methods in order to achieve reasonable accuracy and credible iteration convergence [104]. The method is employed to evaluate the drive performance of the machine with MTPA, MEPA and MOPA control strategies and accommodate further comparison and discussion. A resemblance is developed to accurately investigate the performance of PMSMs with different rotor topologies [38]. In this section, an extension on the aforementioned linear model is carried out by taking into account the nonlinear and cross-coupling effects. The characteristics of magnetic saturation are captured by comprehensive FEA parametric sweeping method. The frozen permeability technique is widely introduced in FEA model to decouple the nonlinear effects of magnetic saturation on armature-reaction and PM flux linkage components [105]. As a result, the matrices of the *d*- and *q*-axis self and mutual inductances and PM flux linkage over the whole operational range can be derived accordingly for the model. Therefore, the extended model can provide not only accurate prediction on steady-state performance but also quick assessment of dynamic transient characteristics. Instead, the *d*- and *q*-axis flux linkage and electromagnetic torque will suffice to accurately evaluate the steady-state performance.

2.2.1 Nonlinearity Extraction by FEA Parametric Sweeping

The FEA models with sweeping *d*- and *q*-axis current components are evaluated to obtain the nonlinear characteristics from magnetic saturation of the machine with different current combinations. Since the magnetic field model is somewhat involved in the circuit model, this extended nonlinear model is also named as circuit-field-coupled method. For Prototype I, the maximum overall current is defined as 16A and the maximum allowed demagnetizing current is 12A ($i_d \geq -12$A). The *d*- and *q*-axis flux linkage components, and electromagnetic torque of Prototype I with different combinations of *d*- and *q*-axis current components are evaluated by 2-D FEA models and the results are depicted in Figure 2.3. Instead of analytical models in Equation (2.2) and (2.3), look-up tables from FEA parametric sweeping together

with effective numerical curve-fitting algorithm are used to derive the flux linkage and electromagnetic torque in the extended nonlinear model.

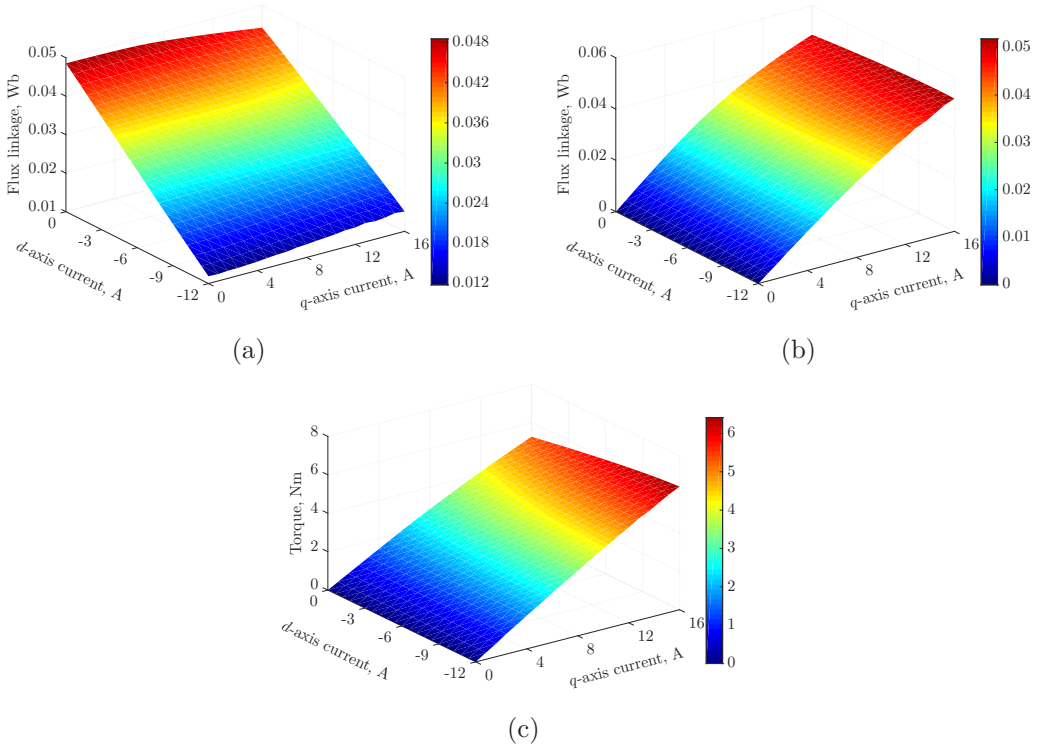

Figure 2.3: Electromagnetic parameters obtained from FEA parametric sweeping: (a) d-axis flux linkage, (b) q-axis flux linkage, (c) electromagnetic torque.

The d- and q-axis cross-coupling phenomenon can be easily observed from Figure 2.3(a) and 2.3(b). As a result, both the d- and q-axis flux linkage components will decrease as the respective orthogonal components increase. The results from FEA parametric sweeping in Figure 2.3 can be directly employed to evaluate the steady-state performances of Prototype I with different control strategies. The electromagnetic torque table illustrated in 2.3(c) can reveal the correlation between electromagnetic torque and current vector for different control strategies. By neglecting the temporal harmonic components of the magnetic field, the flux linkage tables can be employed to calculate the voltage vector so that the PWM modulation index and torque angle can be derived. Furthermore, these results can be used to evaluate the d- and q-axis self and mutual inductances with the assistance of frozen permeability technique. The d- and q-axis self and mutual inductances are involved in the sideband current harmonic calculation. Other performance characteristics such as efficiency and power factor can be easily derived based on the corresponding current, voltage, operational speed and electromagnetic torque [104].

As there are temporal harmonic magnetic field components in the machine from both PMs and armature reaction, all these electromagnetic parameters are normally position-dependant. The above FEA parametric sweeping method assumes them position-independent instead and only considers one rotor position. Therefore,

prediction errors are still inevitably introduced in the extended nonlinear model. The existences of the significant torque and flux linkage ripples, especially in the straight-slot machine, make the values from one rotor position largely deviate from the averages. On the other hand, the skewing-slot machine, such ripple components are nearly eliminated and the errors of the proposed method can be effectively reduced. Transient FEA models can be employed to derive the corresponding temporal components induced by such harmonic magnetic field components so that the machine performance can be evaluated more accurately.

2.2.2 Performance Evaluation

The counterpart of Figure 2.2 from the extended nonlinear *d*-*q* PMSM model can be directly derived based on the results in Figure 2.3 and shown as 2.4. It can be easily found that the maximum achievable electromagnetic torque of Prototype I with different control strategies depreciate noticeably. The corresponding magnetic saturation in the stator and rotor iron cores reduces the PM flux linkage and *q*-axis inductance component and hence the electromagnetic torque. Meanwhile, the rotational speed range from the improved model is expanded for Prototype I with both $i_d = 0$ and MTPA vector control strategies as the actual flux linkage components are smaller than those in the linear model. Moreover, the *q*-axis inductance is greatly reduced due to magnetic saturation and the corresponding gap between *d*- and *q*-axis inductance components shrinks significantly. As a result, the exploitable reluctance torque becomes quite small and the difference between the electromagnetic torque from $i_d = 0$ and MTPA vector control strategies narrows as shown in Figure 2.4(b). On the other hand, the large *d*-axis inductance from the FSCW configuration results in an excellent flux weakening capability, as demonstrated in Figure 2.4(b). The corresponding voltage, PWM modulation index and torque angle can be derived in the similar way as the linear method.

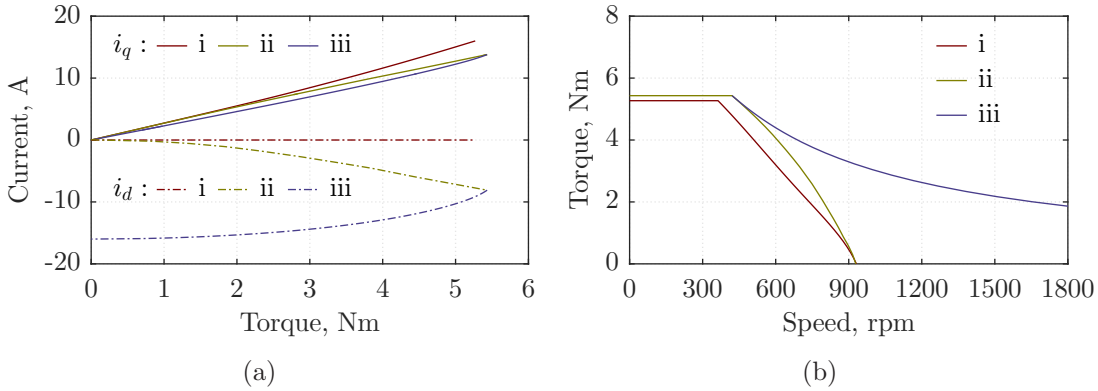

Figure 2.4: Circuit-field-coupled machine output analysis with different control strategies: (a) *d*- and *q*-axis current components with output torque, (b) maximum operating range. (i - $i_d = 0$, ii - MTPA, iii - Flux weakening)

Generally, the proposed circuit-field-coupled method can provide much more accu-

rate performance prediction over the linear model. However, the FEA parametric sweeping method needs extensive numerical iterations and results in computational burden. It is of particular importance to validate the machine performance by the extended nonlinear model during the design and evaluation stage of PMSM drive.

2.2.3 Experimental Validations

The experimental tests on the PMSM drive system of Prototype I with SVPWM technique are further carried out to validate the proposed circuit-field-coupled method. The modulation index can be directly obtained from the experiment and represents the voltage of the machine with certain operational speed and load. Therefore, it is employed as the validation index instead of voltage here. Figure 2.5(a) demonstrates the correlation between the modulation index and operational speed of the machine under no-load conditions. Very close agreements have been achieved between the results from the nonlinear model and experimental tests. During the no-load operations with speed over 900rpm, the flux weakening control strategy is implemented. The maximum operational speed of the machine with certain demagnetizing current under no-load condition can be easily derived by the proposed circuit-field-coupled model and experimental measurement. The corresponding flux weakening characteristics of the machine with no-load condition are revealed and compared in Figure 2.5(b). Again, the estimated values agree very well with the experimental results. The results have underpinned the validity of the proposed nonlinear model on the accurate predictions of voltage characteristics of the machine with no-load and flux weakening operations.

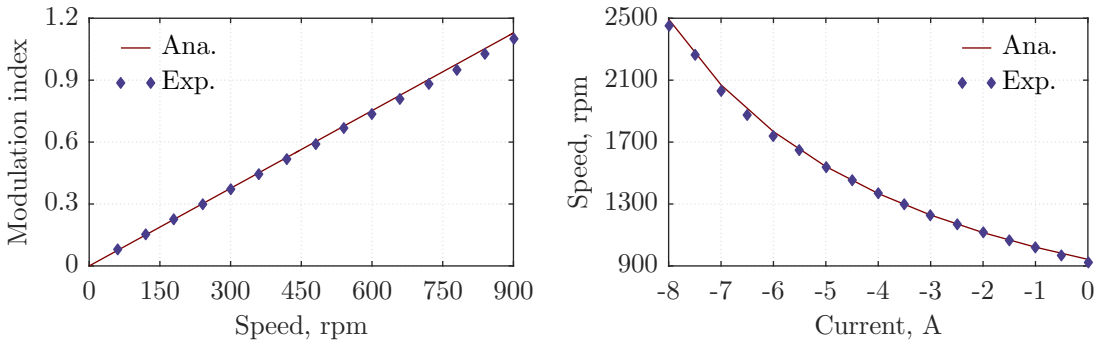

Figure 2.5: Experimental validation under no-load conditions: (a) modulation index in different speeds, (b) demagnetizing current in different speeds. (Ana. - Nonlinear model, Exp. - Experimental results)

The above experimental tests on the Prototype I with no-load and flux weakening operations all have very small and hence negligible q-axis current component. As a result, severe magnetic saturation in the machine has been avoided. It is always of particular interest to appraise the effectiveness of the extended nonlinear model for severe magnetic saturation circumstances. Therefore, comprehensive experimental

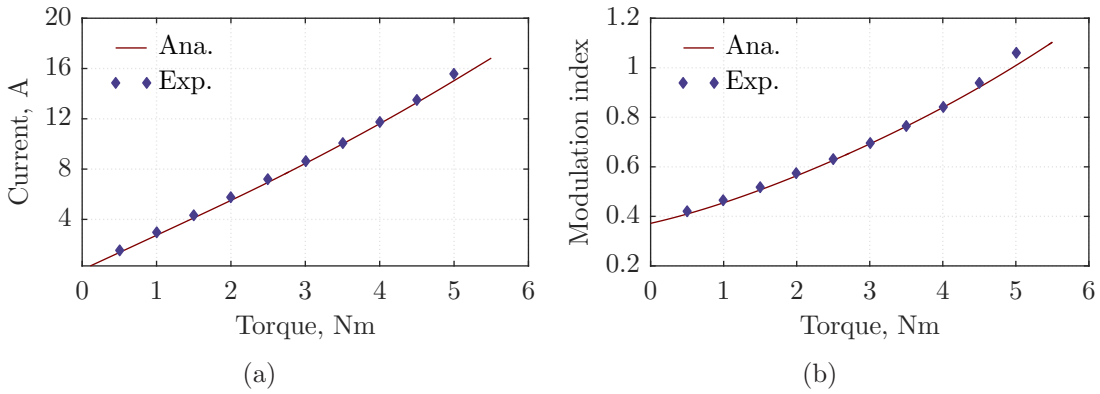

Figure 2.6: Experimental validation in loads condition with $i_d = 0$ control: (a) current with different output torque, (b) modulation index with different output torque. (Ana. - Nonlinear model, Exp. - Experimental results)

tests on Prototype I with different torque loads and constant rotational speed of 300rpm under both $i_d = 0$ and MTPA control strategies are conducted. The torque-current profiles and correlations between modulation index and torque load are compiled from both predicted and experimental results, and illustrated in Figure 2.6 and 2.7, respectively. Without loss of generality, the amplitude of the current vector is employed for the comparison and validation here instead of the d- and q-axis components. The torque and current characteristics of the machine with $i_d = 0$ and MTPA control strategies are shown in Figure 2.6(a) and 2.7(a). Excellent agreements between the predicted and experimental results have been demonstrated for both cases. The corresponding modulation index and torque profiles of the machine are also derived and compared in Figure 2.6(b) and 2.7(b). There are some noticeable deviations between the predicted and experimental results with high torque load conditions. The high torque load in the machine normally involves a large q-axis current component, which will induce severe magnetic saturation and distort the back EMF waveforms. Meanwhile, the winding temperature rises quickly during the high torque load tests. That imposes a quite large impact on the winding resistance and hence voltage drop. By taking to consideration all these factors, it can be concluded that the agreement between the results from the nonlinear model and experimental tests is reasonably good and acceptable. Therefore, the proposed nonlinear model can be employed to further investigations of the drive system performance. The modulation index and torque angle estimated from the nonlinear model are sufficient enough for further accurate predictions of sideband current harmonic components and effective ERFD investigation.

Despite the close agreements between the predicted and experimental results, the prediction errors still exist for the fundamental components. This is mainly caused by the neglect of the harmonic components in the proposed nonlinear model. Although the proposed circuit-field-coupled method cannot take into account these factors, it is still quite effective and sufficient to evaluate the steady-state performance of PMSM drive. In order to include the influences of these spatial components, transient field-circuit-coupled scheme is able to transform them from spatial

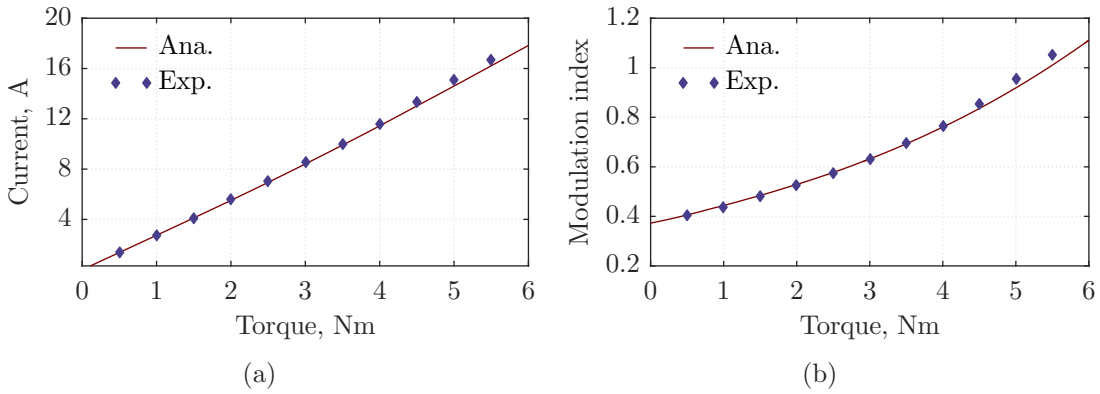

Figure 2.7: Experimental validation in loads condition with MTPA control: (a) current with different output torque, (b) modulation index with different output torque. (Ana. - Nonlinear model, Exp. - Experimental results)

domain into temporal domain. Furthermore, such scheme is capable to predict the phase-belt current harmonics as well as the fundamental component.

2.3 Transient Circuit-Field Co-Simulation Techniques

The FEA method can be employed to predict transient performance of electric machine accurately by coupling with a circuit solver. The practical characteristics of the machine such as material nonlinearity, peculiar winding arrangement, arbitrary complex geometry, eddy current effect and mechanical movement can be all taken into account in the magnetic field solver. On the other hand, external power electronic circuits including power converter, power source and passive components, together with sophisticated control algorithms, are becoming common practice for modern PMSM drive systems in order to achieve excellent performance. The physical circuit elements can significantly affect the performance of the drive by introducing extra current harmonic components. Therefore, only the magnetic field solver can no longer cope with the accurate transient performance analysis for such drive system as there is a strong coupling effect between circuit control unit and electric machine. The circuit-field co-simulation schemes, which numerically couples circuit simulation with magnetic field FEA solver, are commonly used to accurately evaluate the dynamic performance of electric machine drive system by considering machine magnetic field, electric circuit, control algorithm and their interactions simultaneously. There are generally two types of circuit-field co-simulation techniques for transient simulation of electric machine drive. One is called strong-coupling technique while the other is named weak-coupling technique[106]. They are also known as direct-coupling and indirect-coupling methods respectively [107].

In the strong-coupling numerical approach, the whole coupling problem is realized on solver matrix level. Normally, the circuit equations are directly appended to the

FEA matrix so that the magnetic field and external circuit involved can be solved simultaneously [108]. Several distinctive merits, such as credible convergence, outstanding computational efficiency and excellent accuracy, can be delivered by the strong-coupling technique. Normally, only one FEA model can be incorporated into the full coupled matrix, the strong-coupling method cannot deal with the cases involving multiple electric machine drive systems. Furthermore, the FEA solver mainly focuses on the magnetic field calculation and hence only basic circuit components are available for the controller modeling. As a result, the fidelity and complexity of the circuit model is quite limited in such method.

On the other hand, the weak-coupling technique separates circuit and field simulators. They are usually linked in cascade, and hence solved in successive steps. The coupling effect is realized by updating and exchanging a set of variables between the two simulators at each time step. In this method, the FEA field model of the electric machine is usually regarded as an equivalent lumped component by the circuit solver. Either Thevenin [109] or Norton [110] equivalent circuit method can be adopted to turn the electric machine into a controlled source in the circuit simulator. An one step time delay between the separate circuit and magnetic field solvers occurs due to the peculiar data update and transfer mechanism. This can potentially cause numerical instability and inaccuracy to the simulation, especially with severe magnetic saturation existing in the magnetic field simulator. However, the weak-coupling method is still widely used for sophisticated control algorithm development of advanced electric machine drive system thanks to its flexibility in the circuit modeling.

The advantages and disadvantages of the strong-coupling and weak-coupling techniques are briefly introduced above. It can be found that the strong-coupling method is more suitable for electric machine analysis and drive performance validation during the design stage. On the other hand, the weak-coupling method is preferred in the applications of the control power circuit and associated control algorithm research and development. Nonetheless, both transient circuit-field co-simulation schemes can be employed to evaluate the dynamic performance and associated harmonic feature of the electric machine drive system.

2.3.1 Circuit-Field Strong-Coupling Technique

The strong-coupling method has been extensively reported and investigated over the past decades. The direct-coupling approach, by involving Newton Raphson method to directly solve coupled matrix of the nonlinear electric circuit and electromagnetic field model equations, is presented and investigated in [111]. The nonlinear circuit component is simplified in another strong-coupling method as fixed parameter model during each time step by commutation and status predicted based on the previous time step [112]. Piecewise function is employed to model the nonlinear circuit components and the parameters involved are treated as constant for each status. This method is further extended to 3-D solver with the computational algorithm using the voltage induced to link the magnetic field and electrical circuit

models [113]. Meanwhile, a new coupling method with compensation is implemented between transient circuit solver and magnetic field simulator to eliminate the time step delay [114]. Thevenin equivalent circuit method is employed in this method by involving flux linkages and differential inductance parameters. The method is very similar to the conventional circuit-field strong-coupling technique. Furthermore, a control algorithm can be incorporated into the coupling method to deal with control strategies and PWM schemes in the electric machine drive system. Such a method is introduced for a linear induction machine [115] and a wound-field brushless starter generator [116] with vector control strategy. However, most of such control algorithms which are commonly accompanied with various PWM techniques require very small time steps for the coupling simulation and hence result in intensive computation.

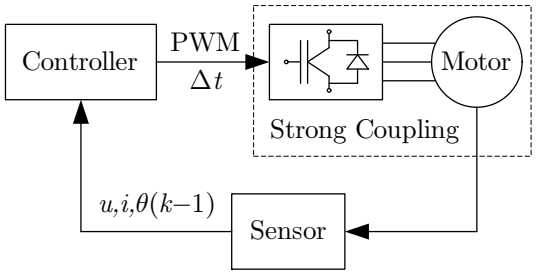

Figure 2.8: Scheme of strong coupling.

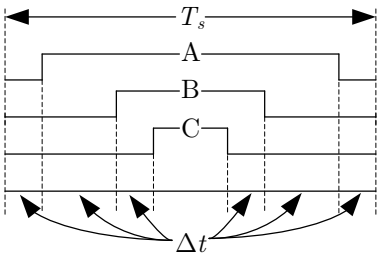

Figure 2.9: Trigger time step method.

The schematic block scheme for electric machine drive system is shown in Figure 2.8. The simulation model of the overall drive system usually comprises the electric machine, power electronics converter, sensors and controller. Generally, the fundamental equation of 2-D electromagnetic field problem of electric machine with associated boundary conditions and initial states can be expressed as

$$\nabla \times (\mu \nabla \times A_z) + \sigma \frac{\partial A_z}{\partial t} = J \tag{2.16}$$

In order to solve the problem numerically, the classical FEA method can be employed for further space discretization and the corresponding field result can be derived in the matrix form as

$$\left[K\right]\left[A_z\right] + \left[Q\right]\frac{\mathrm{d}}{\mathrm{d}t}\left[A_z\right] = \left[P\right]\left[i\right] \tag{2.17}$$

The terminal voltage of each circuit can be written as

$$u(t) = Ri(t) + L_\sigma \frac{\mathrm{d}i(t)}{\mathrm{d}t} + \frac{\mathrm{d}\psi(t)}{\mathrm{d}t} \tag{2.18}$$

As the electric machine windings are directly connected to the power inverter and other electric circuit elements, a nonlinear voltage drop occurs in the external circuit. In order to take into account this, the terminal voltage model in Equation (2.18) can be rewritten as

$$u(t) = Ri(t) + L_\sigma \frac{\mathrm{d}i(t)}{\mathrm{d}t} + \frac{\mathrm{d}\psi(t)}{\mathrm{d}t} + \gamma(i) \tag{2.19}$$

By combining Equation (2.16) and (2.19), the corresponding matrix form can be expressed as

$$[G]\frac{\mathrm{d}}{\mathrm{d}t}[A_z] + [R][i] = [u] - [L_\sigma]\frac{\mathrm{d}}{\mathrm{d}t}[i] - [\gamma] \tag{2.20}$$

The coupled model of electromagnetic field and circuit can be obtained by combining Equation (2.17) and (2.20) as

$$\begin{bmatrix} K & -P \\ 0 & R \end{bmatrix}\begin{bmatrix} A_z \\ i \end{bmatrix} = \begin{bmatrix} 0 \\ u \end{bmatrix} - \begin{bmatrix} Q & 0 \\ G & L_\sigma \end{bmatrix}\frac{\mathrm{d}}{\mathrm{d}t}\begin{bmatrix} A_z \\ i \end{bmatrix} - \begin{bmatrix} 0 \\ \gamma \end{bmatrix} \tag{2.21}$$

The backward Euler scheme can be employed to discretize the equation set and the Newton-Raphson algorithm can be applied to obtain the time stepping solution by numerical iterations. As the nonlinear voltage drop of external circuit component is included in the model, the resultant equation describing the relationship between voltage and current is integrated into the equation set for each component. It implies that the voltage drops in these nonlinear components are variables and need iterations with others during each time step.

The overall control algorithm including signal sampling, control strategy and PWM techniques can be easily realized in such model, as described in Figure 2.8. The values of all these parameters such as current and position are detected in every sampling instant, which are used by the machine controller to generate the PWM signals. The machine control algorithm is able to determine the switching sequence of the power switches each time for the following switch cycle. Therefore, the appropriate analytical model for corresponding switch state can be decided before coupling the circuit systems with the FEA equations for the next simulation step by the subprocess of the controller simulation.

There are generally two different types of time step approaches for such system simulation, fixed time step and variable time step methods. The fixed time step method is the most commonly used algorithm in the magnetic field FEA simulation. Normally, dozens of steps in one electrical period are required to achieve reasonable predictions from the time-stepping simulation of the electric machine supplied by the sinusoidal voltage. However, the supply voltage in PMSM drive is a series of square waveform generated by PWM techniques whose duty varies every switching cycle rather than sinusoidal as the machine is normally driven by VSI. As a result, at least 100 steps in each switch cycle are required for this method to capture the instant at which the switch states change so that accurate simulation can be achieved. In that case, the simulation time step should be set as at least 1 microsecond about for a drive system with 8kHz switch frequency. It is noteworthy that such small step for the strong-coupling simulation of a drive system is almost impractical due to the extensive numerical iterations.

As the fixed time step method can be quite time-consuming, a variable time step approach, which can remove the time steps based on the maximum error of system truncation, is proposed to save computational cost. The variable time step algorithm, as its name tells, will reduce the time step size to increase accuracy as the relative difference exceeds predefined value and increase the time step size to avoid

unnecessary steps as the relative difference is under the general value. The time step size needs to be computed at each time step. As a return, the overall simulation step number and hence the computational time can be potentially reduced. Although it sometimes can reduce computational load to some extent, the variable step method is still not quite practical for the strong-coupling system simulation of the PMSM drive as the minimum simulation step in microseconds is inevitable to accurately capture the step change instant of the voltage.

A new time step algorithm, namely trigger method, is proposed to reduce the computational load significantly to an acceptable level. In the machine drive system, the PWM switch sequence is normally generated by the controller and the time instant of switching on or off for each phase can be set as the simulation time step. The principle of the trigger method is demonstrated in Figure 2.9, which uses square waveforms for the PWM control signals of corresponding machine phases. The time steps are triggered and generated accordingly by the rising and falling edges of the PWM signals. It can be clearly observed that only six steps are required in every switch cycle for the common SVPWM technique. The proposed new method incorporates the state change of the switching devices from the control algorithm to trigger corresponding step of FEA simulation, while the conventional method would decide the step directly by FEA software itself without interaction with the controller. This close interaction during the strong-coupling simulation can minimize the overall simulation steps and hence reduce the computational time. In most normal circumstances, the switch period is much smaller than the fundamental electrical period of the phase voltage. Therefore, the time step generated by the proposed trigger method is small enough to guarantee sufficient step number for the simulation.

In order to validate that the new trigger method can significantly improve the computational efficiency without compromise on the prediction accuracy, a comparison between the results from the strong-coupling simulations with the conventional time step techniques and the new trigger method is carried out. The strong-coupling simulation models of PMSM drive system with Prototype I and i_d=0 vector control strategy, which is modulated by the SVPWM technique, are constructed with three different time step methods. The control algorithm is directly integrated into the FEA model in the software package. The controller consists of current and speed loop controller module, current and speed sample module, and coordinate transformation module including Park and Clark transformation, and SVPWM generation module. The power module in the system is a common two-level three-phase VSI built from six MOSFET switches and the DC-link voltage is 42V. The operational condition for the simulation is 3N·m at speed of 300rpm. The resultant 2-D mesh grid is composed of 8628 triangle elements for the FEA model of the machine. Only half of the machine is modeled in the FEA model with antiperiodic boundary condition to reduce the computational load.

The computer hardware configuration for these simulations is dual core Intel processor with 2.8GHz with 8GB RAM. As the carrier frequency of the SVPWM technique for the PMSM drive is set as 8kHz, the time for one switching period is 125 microsec-

onds. During the simulation, the instants of the square wave generations must be precisely detected to achieve accurate square wave voltages in each switching cycle. Assuming the required square wave width and time step size are T and Δt respectively, the actual square wave voltage width in the simulation will be between $(T - \Delta t)$ and $(T + \Delta t)$. With the maximum square wave voltage width error of $2\Delta t$, the time step sizes of 1 microsecond and 0.1 microsecond will result in minimum relative detection errors of 1.6% and 0.16% respectively for 8kHz PWM wave. Generally, the smaller the time step size, the higher accuracy of the prediction. Therefore, the time step size is preferably as small as possible. However, small time step size such as 0.1 microsecond in the conventional fixed and variable time step techniques can result in intensive computations and even impracticality. As a compromise, time step size of 1 microsecond is employed in the simulations with fixed and variable time step methods in this study. On the other hand, the computational load of the simulation is independent to the time step size for the proposed trigger method. Hence, minimum time step size of 0.1 microsecond, which can deliver high simulation accuracy, is adopted for the trigger method.

Table 2.1: Comparison of consumed time of three time step methods

Parameter	Fixed	Variable	Trigger	Unit
Simulation end time	60	60	60	ms
Switching cycle	125	125	125	μs
Minimum step size	1	1	0.1	μs
Consumed time	39.8	27.3	3.3	h

The main parameters for the three simulations are given and compared in Table 2.1. The fixed time step method takes more than one and a half days to finish 1.5 electrical periods simulations, while the variable time step method can reduce the simulation time by 20% but still requires more than one day. Normally, long transient processes such as the start up of the drive system and instant load changes require more than dozens of electrical periods. It can be expected that it will take more than one week for both constant and variable time step methods to analyze such processes. Above all, the trigger time step method can dramatically reduce the simulation time to just around 3 hours for proposed case. The computational efficiency has been significantly improved by the trigger method.

The electric machine parameters such as voltage and current vector, electromagnetic torque, can be obtained from the strong-coupling circuit-field co-simulations of the drive system. The simulations have considered all the nonlinearity of the devices and time delay of the digital control system. The influences of the controller parameters such as the proportional and integral coefficients can be accurately predicted. Besides the fundamental voltage and current harmonic components and average torque and speed, the phase-belt current harmonic components as well as torque and speed pulsations can be evaluated. The current and torque waveforms of PMSM drive system of Prototype I with 3N·m at speed of 300rpm from the strong-coupling circuit-field co-simulations based on three time step methods are given and

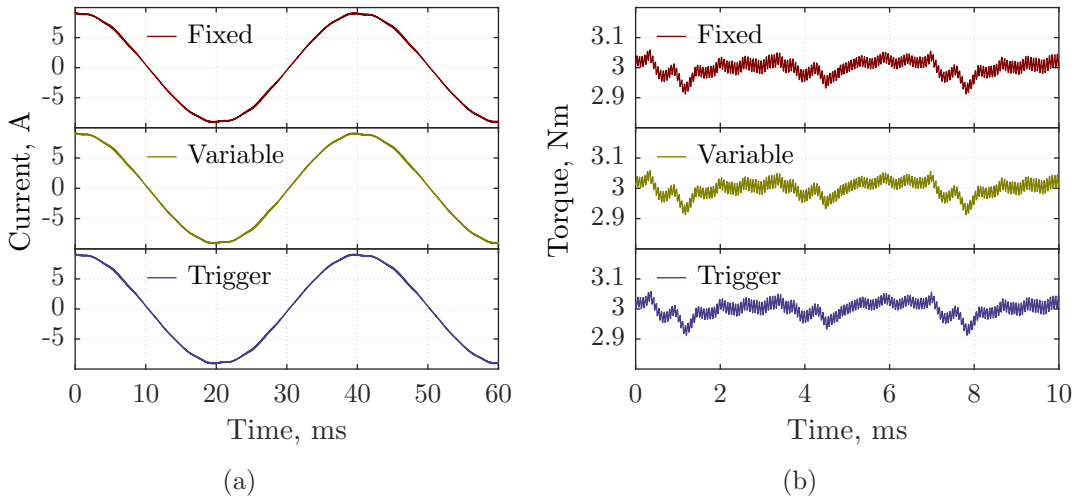

Figure 2.10: Comparison between different time step methods: (a) current response, (b) torque response.

compared in Figure 2.10. It can be directly observed from Figure 2.10(a) that the current response curve from the proposed trigger method is nearly identical to those from the fixed and variable time-step methods. Furthermore, the electromagnetic torque response curves from the same simulations are also obtained and compared accordingly. Again, extreme close agreements have been achieved from these three methods. The computational time can be effectively reduced by nearly one order of magnitude but with no notable compromise on the accuracy on the predictions of low-frequency harmonic components in the drive system.

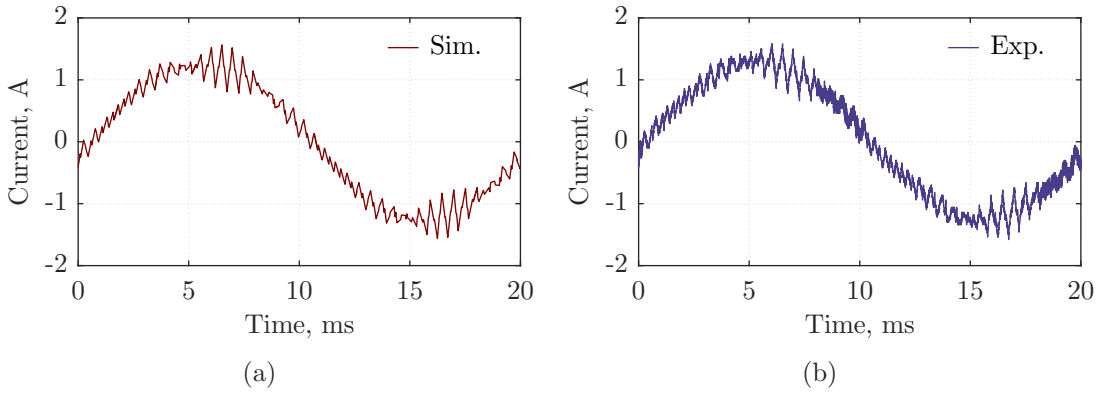

Figure 2.11: Comparison between predicted and experimental phase current waveforms: (a) predicted phase current from proposed trigger method, (b) experimental phase current. (Sim. - Simulation result, Exp. - Experimental result)

Besides the low-frequency harmonic components, high-frequency sideband harmonic components are inevitable in PMSM drive system with PWM techniques. It is of particular importance for the strong-coupling circuit-field co-simulation to accurately predict the sideband harmonic characteristics of the PMSM drive system. As aforementioned, the accuracy of the proposed trigger method on the predictions of

low-frequency characteristics of the drive has been validated. Experimental tests are carried out to underpin the validity of the trigger method on high-frequency sideband characteristics of the drive. In order to increase the sideband harmonic components, low carrier frequency of 2kHz and high rotational speed of 600rpm (large modulation index) are employed for PMSM drive system of Prototype I with SVPWM technique. Besides, i_d=0 vector control strategy and 0.5N·m torque load are implemented in both strong-coupling circuit-field co-simulation with trigger method and experimental tests. The phase current waveforms are derived from both simulation and experimental results and compared in Figure 2.11. It can be easily noticed from the figure that there are quite evident sideband current harmonic components in the drive system. The profiles of the phase current from the simulation and experimental results are almost identical with very close amplitude and ripple characteristics. A close agreement has been demonstrated between the predicted and experimental phase current waveforms in Figure 2.11. Therefore, the proposed trigger method can effectively capture the sideband characteristics from the PWM techniques in electric machine drive system. Overall, the proposed trigger method is much more practical than the conventional time-step approaches for the strong-coupling simulation of the machine drive system with PWM techniques.

2.3.2 Coupling Technique Based on Multi-Loop Model

Although reliable convergence and high accuracy can be achieved by the strong-coupling method in circuit-field co-simulation, the weak-coupling counterpart is still of great importance for controller modeling and development due to its merits of efficiency and flexibility on circuit components modeling. Hence, an abundance of research has been carried out on the numerical algorithm of indirect circuit-field co-simulation. The investigations of this aspect mainly focus on the commutation variable acquisition between the electric circuit and magnetic field solvers during each time step interval. A weak-coupling method for estimation of steady-state characteristics is proposed by employing an iterative approach based on state-space model with flux linkage and current variables of the machine [117, 118]. The inductance parameters involved in the matrix of electric circuit model are derived by FEA models. Another weak-coupling method, which combines the FEA model and the electric circuit simulator through parameters of mutual impedances or admittances, is developed to effectively predict the dynamic behavior of the electric machine drive system [119]. The parameters linking the two solvers among the conductors are evaluated by repeatedly solving the same FEA matrix equation with different right hand sides excitation in each time step. Thevenin equivalent circuit model of each phase is employed to accomplish the coupling approach [120]. In this method, the inductance and induced voltage are derived from FEA models for the circuit model matrix while the current excitations are extracted from the circuit simulator to field model in return. Another similar equivalent parameter extraction of coupled magnetic field model is presented [121]. Such method can take into account influences of eddy currents, internal circuits and mechanical motion based on the mathematical FEA formulation. To further improve the computational effi-

ciency of the circuit-field co-simulation, investigations on the numerical method itself are conducted. Temporary linearization of FEA models is implemented to extract equivalent lumped parameters of the electric machine so that the computational time can be significantly reduced by minimizing the FEA simulations [122]. Overall energy estimation method is also employed to optimize the variable time step of FEA models during the simulation [123]. Once the change of system energy exceeds the threshold value, the FEA model will be employed to calculate the corresponding machine parameters.

A coupling scheme established based on multi-loop theory is proposed in this study to further improve the flexibility of the drive system modeling and stability of the numerical computation. As its distinctive merit, such a method can easily deal with arbitrary circuit topology integrated with multiple FEA models. It can be employed for effective controller development and performance prediction of complex electric machine drive systems. The electric machine is considered as multiple circuit loops with relative movement in the multi-loop theory. In order to construct the generic PMSM model, it is assumed that

- The PMSM has M PMs in total;
- There are W sets of strand windings including armature coils and excitation coils in the PMSM;
- The PMSM also has L damping loops.

It is noteworthy that the multi-loop model can be established on the FEA model of minimum symmetry to simplify the parameter extraction and equation construction. The investigations on the fault conditions on single damping bar or parallel winding branch require the multi-loop model from the whole FEA model.

Therefore, the voltage and flux linkage equations for the windings can be written as,

$$\left[R_W\right]\left[i_W\right] + \frac{\mathrm{d}}{\mathrm{d}t}\left[\psi_W\right] = \left[u_W\right] \tag{2.22}$$

$$\left[L_{WW}\right]\left[i_W\right] + \left[M_{WL}\right]\left[i_L\right] + \left[M_{WM}\right]\left[i_M\right] = \left[\psi_W\right] \tag{2.23}$$

On the other hand, the voltage and flux linkage equations for the damping loops can be expressed as,

$$\left(\left[R_B\right] + \left[R_L\right] + \left[R_E\right]\right)\left[i_L\right] + \frac{\mathrm{d}}{\mathrm{d}t}\left[\psi_L\right] = 0 \tag{2.24}$$

$$\left[L_{LL}\right]\left[i_L\right] + \left[M_{LW}\right]\left[i_W\right] + \left[M_{LM}\right]\left[i_M\right] = \left[\psi_L\right] \tag{2.25}$$

where

$$\left[R_L\right] = \begin{bmatrix} R_{B\_L} & -R_{B\_1} & 0 & 0 & \cdots & 0 & -R_{B\_L} \\ -R_{B\_1} & R_{B\_1} & -R_{B\_2} & 0 & \cdots & 0 & 0 \\ 0 & -R_{B\_2} & R_{B\_2} & -R_{B\_3} & \cdots & 0 & 0 \\ \cdots & \cdots & \cdots & \cdots & \cdots & \cdots & \cdots \\ -R_{B\_L} & 0 & 0 & 0 & \cdots & -R_{B\_L-1} & R_{B\_L-1} \end{bmatrix} \tag{2.26}$$

The parameters in the equations for each damp loop are illustrated in a simple equivalent circuit in Figure 2.12. R_E for the k^{th} damp loop can be expressed as

$$R_{E\_k} = R_{E_1\_k} + R_{E_2\_k} \tag{2.27}$$

The inductances in Equation (2.23) and (2.25) are normally time-dependent due to the magnetic saturation of the stator and rotor cores and the relative movement between the stator and rotor. Therefore, these inductances should be evaluated in each time step.

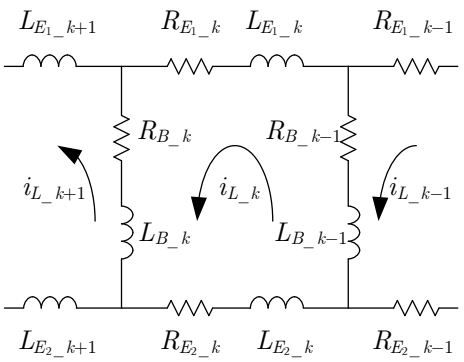

Figure 2.12: The damping loop diagram.

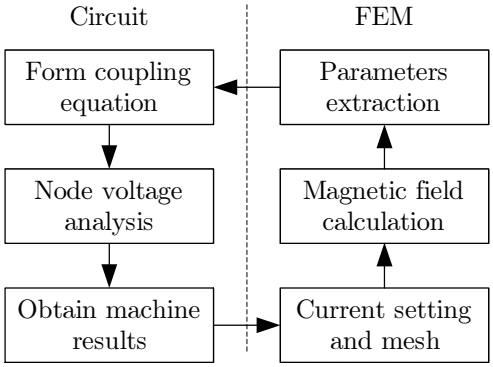

Figure 2.13: Coupling flow chart.

Since the equivalent excitation currents of PMs are considered constant, the corresponding circuit loops of PMs can be ignored in the model. The last term in the left side of Equation (2.23) and (2.25) can be replaced by time-dependent PM flux linkages in each loop. In PMSM, the resultant equation sets can be updated as

$$\left[L_{WW}\right]\left[i_W\right] + \left[M_{WL}\right]\left[i_L\right] + \left[\psi_{WM}\right] = \left[\psi_W\right] \tag{2.28}$$

$$\left[L_{LL}\right]\left[i_L\right] + \left[M_{LW}\right]\left[i_W\right] + \left[\psi_{LM}\right] = \left[\psi_L\right] \tag{2.29}$$

The corresponding electromagnetic torque can be obtained by

$$T_{em} = \frac{1}{2}\left[i\right]^{\mathrm{T}} \frac{\partial\left[M_C\right]}{\partial\theta_m}\left[i\right] + \left[i\right]^{\mathrm{T}} \frac{\partial\left[\psi_{PM}\right]}{\partial\theta_m} \tag{2.30}$$

The equation sets (2.28), (2.29) and (2.30) generally constitute the multi-loop model of PMSM in the circuit simulator. The Newton-Raphson approach with nodal voltage analysis method can be directly employed to promptly solve the overall drive system equations. It can be inspected that the multi-loop model allows accurate investigations including the spatial and temporal harmonic components, unbalanced operational conditions with right model parameters.

The time-variable parameters in the multi-loop model above, including resistance, inductance and flux linkage, can be directly extracted from the FEA model based on frozen permeability method for each time step. Whilst, the excitation currents of each loop in FEA model are provided by results from the circuit simulator. The

permeability of each element in FEA model will be frozen after the completion of electromagnetic field iterations for each time step. With the frozen permeability, one unit current is injected into each winding and damping loop in FEA model one by one with currents of the other windings and damping loops are kept zero so that the inductance matrix can be obtained. Similarly, by setting all excitations as zero except the PM excitation, the FEA model with frozen permeability technique can provide the resultant PM flux linkage for each loop. All the output parameters from the magnetic field simulation for the coupling model will be built in the electric circuit simulator as the system equations are defined and initialized.

For each time step in the electric circuit simulator, the node voltage method is commonly implemented to solve the system circuit and hence the current of each loop. The predicted results including the loop currents and mechanical movement will be further fed back into the FEA model for the new iterations. Furthermore, the partial derivatives between the FEA outputs and inputs are employed to determine the iterative convergence status between FEA and circuit simulators. It can be expected that several iterative processes of the FEA model may be required during each circuit simulation time step. Therefore, the computational time can be significantly increased and the resultant one time step delay between the electric circuit and magnetic field results can be eradicated by such iterative process. Consequently, the proposed coupling method is more like strong-coupling approach rather than weak-coupling method. It can deliver some distinct advantages over the common weak-coupling method, such as credible convergence and accuracy. The parameter extraction and iterative process of the proposed coupling method is depicted in Figure 2.13.

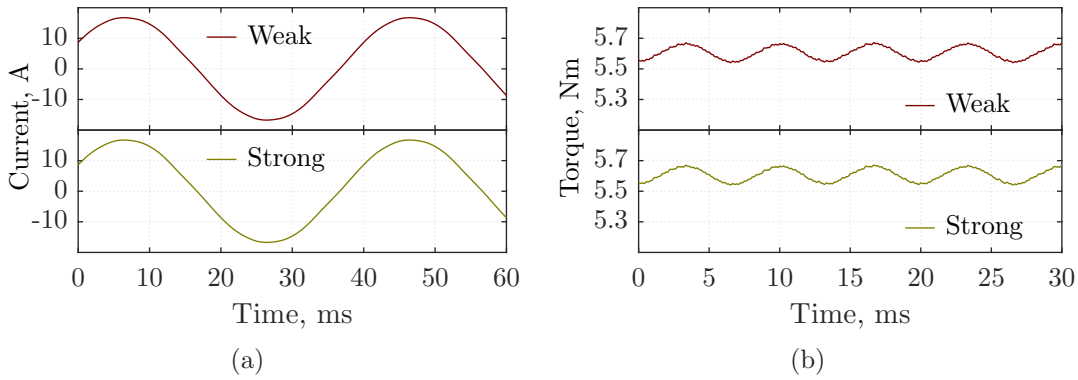

Figure 2.14: Comparison between strong and weak coupling method: (a) current response, (b) torque response.

In order to validate the proposed coupling method, the conventional strong-coupling simulation is employed to benchmark the results. The PMSM drive of Prototype I is employed for the validation. During the simulation, three-phase pure sinusoidal voltage with amplitude of 22V and frequency of 25Hz are fed into the phase windings of Prototype I so that relatively large time step of 1ms is employed for the FEA model. The power angle of the machine during the simulations is kept as 45°.

The current and torque responses from both coupling methods are shown and compared in Figure 2.14. It can be observed from the figure that both the current and torque waveforms are nearly identical between the two methods. There is apparently no time delay between the two results as the time delay in the conventional weak-coupling method has been eliminated by the iteration between the FEA and electric circuit simulators within each time step in the proposed method. Parameter prediction algorithm is also implemented in the proposed method to reduce the iteration numbers by setting the parameters appropriately in the equation initialization for each time step.

2.4 Nonlinear Harmonic Multi-Loop Model

Although the aforementioned coupling techniques can be employed to accurately investigate the PMSM drive performance, they are quite limited due to their extensively time-consuming characteristics for most applications. On the other hand, the equivalent circuit model is of great importance to improve efficiency of numerical calculation. The *d-q* linear dynamic model for PMSM drive is proposed to quickly examine the performance of the drive with vector control strategy [124]. The *d-q* linear dynamic model and three-phase variable model are developed for respective PMSM and PM brushless DC machine drives [125]. The ideal sinusoidal and trapezoidal phase back EMF are introduced for these two machine types respectively. Since only the fundamental component is considered in the linear dynamic model, the spatial harmonic components cannot be predicted. Therefore, an improved *d-q* dynamic model is developed based on an FEA model and harmonic analysis so that torque ripple characteristics of the machine can be accurately revealed [126]. However, significant prediction errors can be introduced by the linear dynamic model due to its neglect of magnetic saturation. A nonlinear *d-q* dynamic model of PMSM is proposed to improve the prediction accuracy, by taking into consideration the magnetic saturation of stator and rotor cores and spatial harmonic components of armature-reaction and PM magnetic field [127]. Another *d-q* dynamic model with the parameters extracted from FEA models can accurately predict the influences of magnetic saturation, *d*- and *q*-axis cross coupling effects, spatial harmonic components of armature-reaction and PM magnetic field, and core loss, on the performance of the drive [128]. In this study, a new nonlinear harmonic model based on a multi-loop method is proposed to further improve the generality of the modeling scheme. The influences of the magnetic saturation and spatial harmonic component of magnetic field are incorporated into the parameters of phase inductance and flux linkage. Such parameters can be directly extracted from FEA model to ensure the accuracy of the prediction. Besides PMSM drive, the proposed modeling method is quite versatile and can be employed for other drive types such as PM brushless DC machine drive, induction machine drive and synchronous reluctance machine drive.

As it is also based on the multi-loop concept, the proposed nonlinear machine model shares the same equation sets as the circuit-field coupling model expressed in Equation (2.28), (2.29) and (2.30). All the parameters in the equations, such as resis-

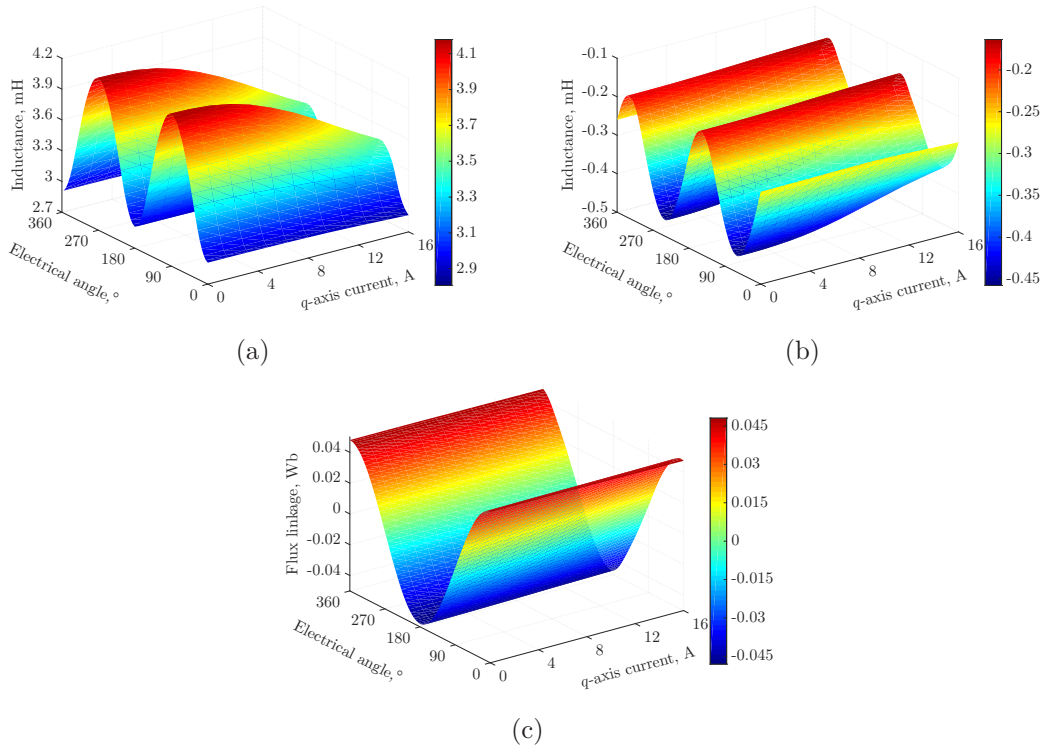

Figure 2.15: Model parameters extraction from FEM: (a) self inductance, (b) mutual inductance, (c) flux linkage of PM.

tance, inductance and PM flux linkage, are obtained from preestablished look-up tables instead of direct FEA simulations in this model. Normally, FEA models of the machine with different rotor position and current combinations can be employed to evaluate the electromagnetic parameters for the preestablished look-up table of each individual phase or damping loop in the model. Quite extensive computational load may be required for such FEA parametric sweeping, especially for some special machine such as line-start and multi-phase PMSMs. The current combinations of different phases and damping loops in such cases can simply overwhelm computational resource available. In practice, the current combinations are mainly applied to calculate the electromagnetic parameters with different saturated situations at specific position. Consequently, the equivalent current vector of overall stator winding can be employed to obtain the parameters instead of all phases and damping bars. As a result, only the combinations of i_d and i_q are sufficient enough to build up credible look-up tables so that the computational demand can be drastically suppressed. It implies that only i_d, i_q and position are involved as the sweeping variables in the PMSM nonlinear model. Figure 2.15 illustrates the electromagnetic parameters obtained by FEA sweeping under i_d=0A. It can be found from the figure that the self and mutual inductances, as well as PM flux linkage are affected by both rotor position and q-axis current. Similar FEA sweeping can be easily performed with different i_d to form the comprehensive look-up tables for the proposed nonlinear harmonic multi-loop model. Both spatial harmonic component and magnetic saturation are inherently included in the model parameters. Therefore, the proposed nonlinear harmonic multi-loop model strikes a right balance between the prediction

accuracy and computational efficiency.

With the extracted model parameters in each time step, the current of each loop can be quickly evaluated by the electric circuit model based on the multi-loop method. The equivalent vector components can be derived by Park transformations for each loop. For multi-phase machines with N_W windings, the Park transformation can be developed from Equation (B.11) and the d- and q-axis components can be derived as

$$\begin{cases} i_{d\_W} = \dfrac{2}{N_W} \displaystyle\sum_{k=0}^{N_W-1} \left(i_k \cos\left(\theta - \frac{2k\pi}{N_W} \right) \right) \\ i_{q\_W} = -\dfrac{2}{N_W} \displaystyle\sum_{k=0}^{N_W-1} \left(i_k \sin\left(\theta - \frac{2k\pi}{N_W} \right) \right) \end{cases} \tag{2.31}$$

For the damping loops, the corresponding d- and q-axis components can be expressed as

$$\begin{cases} i_{d\_L} = \dfrac{1}{pmNK_{wp}} \displaystyle\sum_{k=0}^{N_L-1} \left(i_k \cos\left(\theta - \frac{2k\pi}{N_L} \right) \right) \\ i_{q\_L} = -\dfrac{1}{pmNK_{wp}} \displaystyle\sum_{k=0}^{N_L-1} \left(i_k \sin\left(\theta - \frac{2k\pi}{N_L} \right) \right) \end{cases} \tag{2.32}$$

Therefore the equivalent d- and q-axis components of the machine can be obtained by simple synthesis as

$$i_d = i_{d\_W} + i_{d\_L}, \quad i_q = i_{q\_W} + i_{q\_L} \tag{2.33}$$

The correspondent parameters in the nonlinear model can be promptly evaluated based on the look-up tables with current vector components.

Simulations based on PMSM drive system of Prototype I are carried out with the conventional strong-coupling technique and proposed nonlinear harmonic multi-loop model for validation. The models are constructed to simulate the start-up process of the drive with 3N·m torque load and target speed of 300rpm. The current and mechanical speed response curves are derived from both simulations and compared in Figure 2.16. Owing to its interior PM configuration, the torque pulsation exists due to the rich harmonic components of the magnetic field and nonlinear characteristics appear as a result of severe magnetic saturation under large load conditions. All these phenomena can be captured by both simulation models and close agreement between results from the strong-coupling and nonlinear model have been achieved in Figure 2.16. The simulation of the start-up process takes around 6.5 hours by the strong-coupling circuit-field method even with trigger time step method. It only takes 1.5 minutes by the proposed model to accomplish the same process simulation, with two orders of magnitude improvement on the computational efficiency. Around two hours are required for the corresponding FEA sweeping to derive the look-up tables of the electromagnetic parameters. It is still worth constructing such a nonlinear model of PMSM for further performance analysis over the whole range of the drive and also design space exploration of control algorithms. Moreover, the utilization of distribution calculation and multi-threading scheme can be directly

implemented to speed up the parameter extraction of the model with minimum effort.

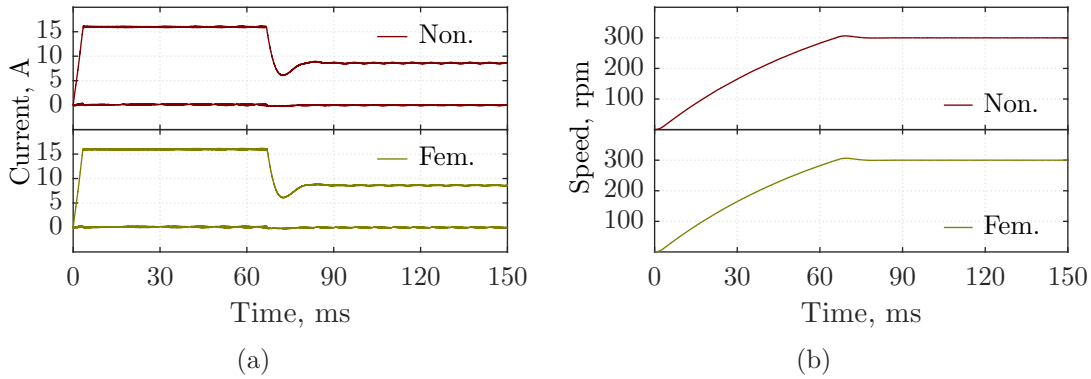

Figure 2.16: Validation of nonlinear harmonic model: (a) d- and q-axis Current components response, (b) mechanical speed response. (Non. - Nonlinear model, Fem. - Finite element model)

Despite the accuracy and computational efficiency the proposed nonlinear harmonic multi-loop model can achieve, the circuit-field co-simulation model still cannot be replaced completely for some occasions. Some numerical errors will still be introduced by the equivalent parameter construction and electromagnetic torque calculation in the proposed nonlinear model. Normally, the circuit-field coupled model can be employed for drive system performance validation of typical operation conditions due to its credible prediction accuracy. It can also be employed for accurate prediction of spatial and temporal harmonic components in the machine.

The generic model developed is also applicable to other types of machine drive. For the electrically excited synchronous machine, the DC excitation current in the rotor is normally employed as an extra sweeping variable. It will introduce a magnetic field difference from the i_d component. Furthermore, the damping loops in the machine, especially the induction machine, the slip frequency is another parameter for evaluations of the associated resistance and inductances. Numerical curve-fitting algorithms are implemented for all the derived parameters to improve the convergence quality of the simulation.

2.5 Applications of Simulation Schemes

Several basic control algorithms can be easily developed and integrated into the FEA software package with strong-coupling scheme. They can be directly employed for the PMSM and its drive performance evaluations during the machine design stage. The basic control block diagram of such scheme is illustrated in Figure 2.17. It includes $i_d = 0$ and MTPA vector control strategies, SVPWM technique, PID controller modules and coordinate transformation modules. It is noteworthy that

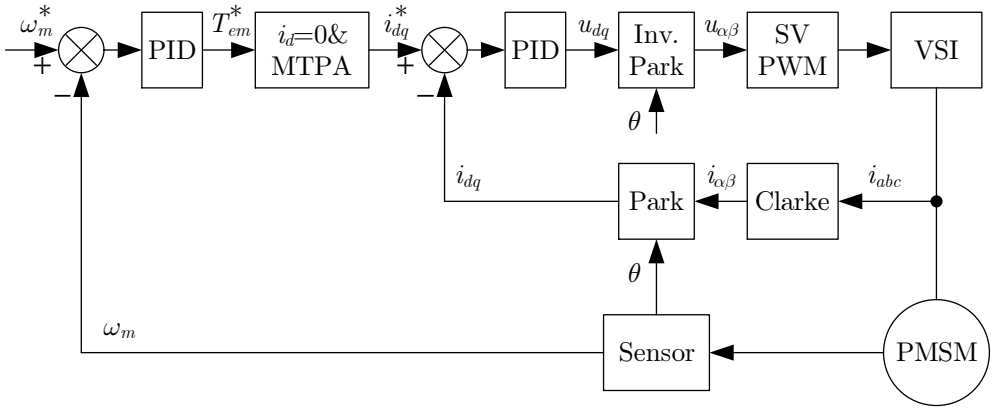

Figure 2.17: The PMSM drive model with strong co-simulation.

the MTPA control strategy employed here is based on a linear model. The reference current vector is derived by linear electromagnetic parameter model. Normally, the control algorithm can be also developed by the FEA interface with various scripting languages. It is quite inconvenient and cumbersome to develop the control algorithm in such way. Not only are the programming and modeling very inefficient in such a method, but also the simulation and debugging are very time-consuming and hence practically unacceptable.

It is still useful to employ the strong-coupling circuit-field co-simulation during the design stage as it can deliver accurate machine performance predictions with an integrated control algorithm before the prototype manufacture. The magnetic saturation of stator and rotor cores, temporal and spacial harmonic components of the magnetic field are all taken into account in such models. Therefore, the machine performance can be comprehensively and accurately evaluated to ensure that the specific requirements are met by the design.

In order to study the effects of control techniques on the ERFD in this study, various control algorithms are employed in PMSM drives as shown in Figure 2.18. Besides $i_d = 0$ vector control strategy, the MTPA and flux weakening vector control strategies will be covered. The MTPA control strategy here takes into account the nonlinear factor so that the linear model used in strong-coupling simulation needs improvement. On the other hand, different PWM techniques, such as SPWM, SVPWM and random SVPWM will also be investigated. The state observer of sensorless control, sliding mode observer control and feed-forward current control are employed to drive the corresponding prototypes with different configurations for experimental validations.

It is quite obvious that the strong-coupling circuit-field co-simulation is no longer suitable to model such a complex system. The time effort to debug the control parameters in different modules will become practically infeasible. However, the proposed nonlinear harmonic multi-loop model can cope with such complex cases conveniently and effectively with its great computational efficiency and accuracy. Therefore, the method is employed to investigate and optimize the control algorithm

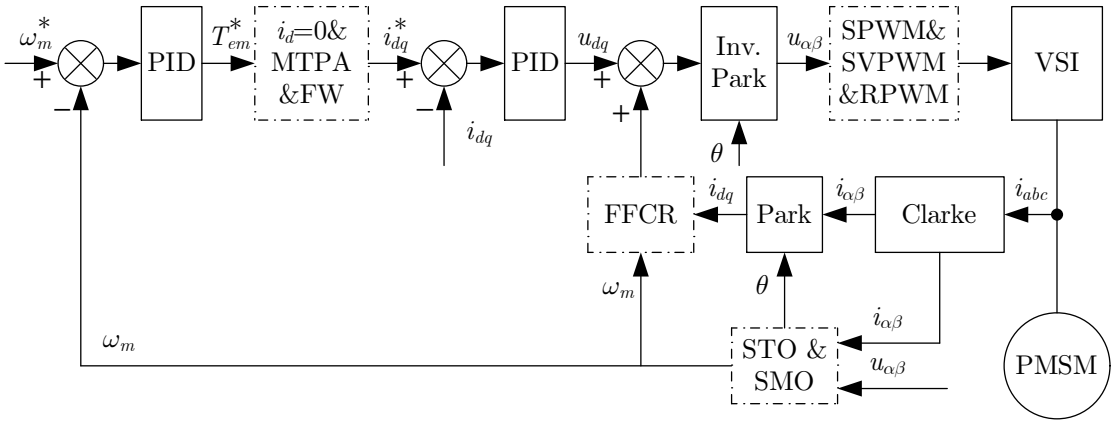

Figure 2.18: The PMSM drive model in circuit simulator.

of the PMSM drive systems. It is also very helpful for parameter debugging, such as the PI parameters in the control modules. Furthermore, the nonlinear model is also adopted for parametric analysis under different speed and torque conditions for sideband harmonic components.

The weak-coupling circuit-field co-simulation is employed for the simulation validation of the proposed nonlinear model with typical operational conditions. For these two methods, almost the same control model can be shared in circuit simulator with different machine models, one is an FEA model and the other is nonlinear model based on look-up tables. Such co-simulation results are employed to ensure the proposed nonlinear harmonic multi-loop model delivers credible estimations. The harmonic characteristics are also investigated by such methods to obtain the phase-belt current harmonic components in the drive for further ERFD investigations.

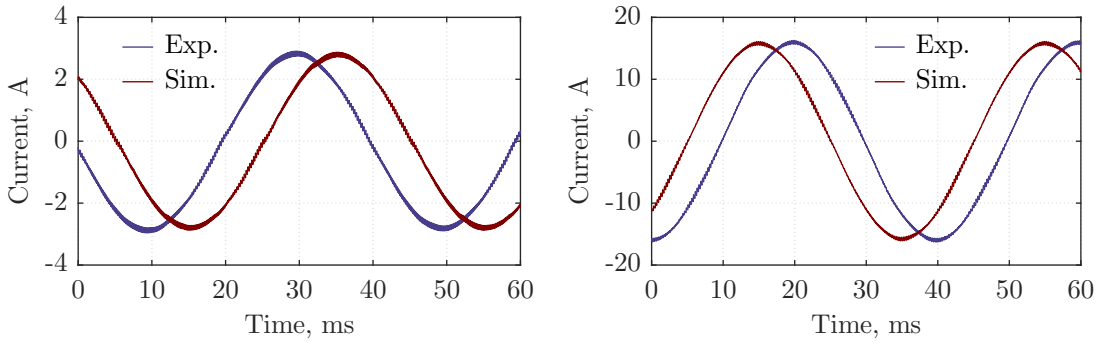

Figure 2.19: Current comparison between simulation and experiment results at 300rpm: (a) 1Nm, (b) 5Nm. (Exp. - Experimental results, Sim. - Simulation results.)

Finally, the experimental tests on the PMSM drive system of Prototype I are performed to validate the results from the proposed modeling schemes. The $i_d = 0$

vector control strategy and SVPWM technique are implemented in the drive system during the experimental tests. Different from aforementioned simulation model, the PWM carrier frequency is set as 4kHz instead to facilitate the investigations on sideband harmonic components. As a result, the sideband harmonic components, including the current and vibration components, can be more easily collected with a lower switching frequency. On the other hand, the switching frequency is set as 8kHz for the investigations associated with low-frequency harmonic components.

The phase current waveforms of Prototype I with 1N·m and 5N·m are measured from the experimental tests. They are given and compared with the results from the proposed nonlinear harmonic multi-loop model in Figure 2.19. The target speed of the drive system is set as 300rpm, and both simulations and experiments can trace the control instruction very well. It can be seen directly from the figure that excellent agreements have been achieved for phase current waveforms under both load conditions in terms of waveform shape and sideband harmonic components. The effect of magnetic saturation in the machine with heavy load of 5N·m can be effectively reflected. The corresponding current amplitude is about 16A while the current amplitude for 1N·m condition is only 2.85A. The nonlinear harmonic multi-loop model has been validated comprehensively by both strong-coupling circuit-field co-simulation and experiments. It will be employed for further drive analysis and development in this study.

2.6 Summary

This chapter mainly focused on the numerical modeling schemes of a PMSM drive system. With the consideration of control algorithm, the steady-state performance characteristics of the PMSM drive such as voltage, current and electromagnetic torque can be accurately predicted based on the electromagnetic parameters derived from FEA simulations. The obtained parameters such as the PWM modulation index, torque angle, d- and q-axis inductances can be further employed to evaluate the current harmonic components and their associated armature-reaction magnetic field and ERFD components. Furthermore, the transient circuit-field co-simulation scheme is also developed to accurately estimate the phase-belt current harmonic components from cogging torque, back EMF and current harmonic components. However, such schemes are extremely hungry for computational resource and sometimes very difficult to undertake in practice. Therefore, a nonlinear harmonic multi-loop model based on look-up tables from FEA parametric sweeping is further proposed to immensely improve the computational efficiency with minimum compromise on the prediction accuracy.

The corresponding experimental platform is employed to validate the proposed model:

- The experiments based on Prototype I is set up and conducted with both $i_d = 0$ and MTPA vector control strategy to validate the proposed modeling

schemes.

The main contributions of this part include:

- The steady-state performance prediction method with consideration of magnetic saturation in the stator and rotor cores as well as the impacts of control algorithm employed, is introduced and experimentally validated in Section 2.2;
- A novel variable time step technique, namely trigger method, is proposed to significantly reduce the computational time of strong-coupling circuit-field co-simulation in Section 2.3.1;
- A new transient circuit-field co-simulation technique based on multi-loop method is proposed for drive performance analysis in Section 2.3.2;
- A nonlinear harmonic multi-loop modelling method based on winding parameters reflecting magnetic saturation and spatial harmonic components, is developed to improve computational efficiency without sacrifice on prediction accuracy for electric machine drive simulation in Section 2.4.

All these schemes are employed to evaluate different aspects of the PMSM drive in this study. The proposed steady-state performance prediction method can be employed for accurate predictions of the electromagnetic parameters. These parameters will be further employed to evaluate the fundamental and sideband current components and hence associated ERFD components. Meanwhile, the proposed circuit-field co-simulation scheme can be employed to predict the phase-belt current harmonic components. Furthermore, the proposed nonlinear harmonic multi-loop model can be easily implemented to develop the control algorithm of the drive system. It can also be employed to efficiently carry out performance assessment of the drive system over the whole operational range.

Chapter 3

Sideband Voltage and Current Harmonics

As the advancements of microcontroller and power electronic devices keep on, power electronic converters, which can alter the voltage, current and frequency levels of electrical energy, have been the main driving force behind the development of various industries. Meanwhile, substantial modulation strategies have been developed to change the states of the electronic devices in such power electronic converters. Moreover, these power electronic converters are generally categorized into four families based on the electrical conversion types: AC/AC, AC/DC, DC/AC and DC/DC. Normally, each family has its own preferred modulation strategies in order to achieve optimal circuit operations. The VSIs, which change the electrical energy to AC form from DC source, are widely employed in electrical machine drive systems in order to boost the controllability and operational efficiency. The fundamental modulation concepts for such converter type include the variations of naturally and regularly sampled PWM, triangular and sawtooth carrier waveform, continuous and discontinuous switching. Moreover, SPWM and SVPWM techniques have become the two most popular modulation strategies for three-phase two-level VSIs to achieve excellent static and dynamic performances with rather simple implementation. However, such PWM techniques will inevitably generate additional sideband harmonics within both voltage and current during the switching process. The frequencies of these components are normally located nearby the carrier frequency and its multiples [129].

In a PMSM drive system, such sideband harmonics increase the iron core losses, copper resistive losses, PM eddy current losses and hence reduce the operational efficiency. Moreover, the switching frequency of the power devices is rigorously restricted due to the switching losses and $\mathrm{d}u/\mathrm{d}t$ problems in high-power applications such as railway traction drive and offshore wind power generation. The low switching frequency results in high amplitudes of sideband current harmonics and hence evident sideband torque pulsations in the machine [130]. Besides, Such sideband harmonics generate the corresponding air-gap magnetic field in PMSM so that the resultant sideband ERFD components can induce high-frequency electromagnetic

radial vibration and hence ear-piercing acoustic noise. Therefore, it is of particular importance to investigate the sideband voltage and current harmonics, the inherent concomitant of PWM schemes in PMSM drive. There are generally two types of approaches to study these sideband harmonics in PMSM drives: analytical and numerical methods. The numerical approaches normally can provide more accurate predictions at an expense of computational resource, while the analytical methods usually deliver insightful closed-form correlations which can be easily adopted for design and optimization purpose.

Despite numerous variants, only the most common symmetrical regular-sampled schemes are considered in this study. Without loss of generality, the analytical models of sideband voltage and current harmonics in three-phase PMSM powered by two-level VSI with symmetrical regular-sampled SVPWM technique have been developed and validated. The similar measure can be easily applied to obtain the analytical models for its SPWM counterpart, which are provided in Appendix C.

3.1 Principle of SVPWM Technique

The SVPWM technique can provide significant merits over its counterparts in terms of easy implementation, maximum transfer ratio and high performance [131, 93, 132]. The principle, which identifies SVPWM technique as simply an alternative for pulse width determination, is briefly presented in this section. As a matter of fact, the SVPWM technique can explicitly identify the pulse placement so that harmonic performance gains can be readily achieved. Apparently, this additional degree of freedom has become one of the main advantages of SVPWM technique.

In fact, there are only eight possible combinations with on and off states of upper power switches in a two-level three-phase VSI. Six of these eight states can be considered to form stationary nonzero space vectors (U_1-U_6) which divide the whole plane into six equal sectors in Figure 3.1(a), while the other two result in a short circuit on the output and form two zero space vectors (U_0 and U_7). It is noteworthy that each stationary nonzero vector has the same magnitude with respective fundamental angular position as shown in Figure 3.1(a). Therefore, any arbitrary required output voltage vector can be formed by these space vectors within one switching period by identifying the corresponding two adjacent stationary vectors. This is shown in Figure 3.1(b) for a target voltage vector in the first sector of the plane. Essentially, SVPWM technique matches the summation of two active space vector averages over half carrier period to the corresponding sampled target. Hence, SVPWM technique is an intrinsically regular-sampled process with an improved modulation index. Although the zero voltage vector can be made up of any combination of the zero space vectors U_0 and U_7, equal intervals for them are common practice to evenly distribute the switching power losses on upper and lower power switches. Thus time intervals can be determined for each vector by analytical calculation, which are listed in Table 3.1. It should be noted that t_1 and t_2 are the time intervals of clockwise leading and lagging vector in each sector respectively. This method can be easily implemented

in any digital signal processing system so that it is widely employed in modern VSI drive systems.

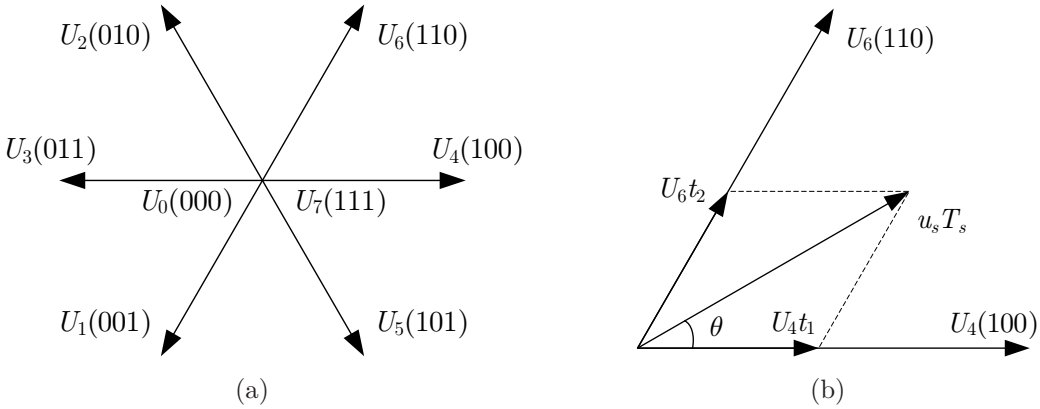

Figure 3.1: Principle of SVPWM: (a) basic switching vectors, (b) combination of adjacent vectors.

Table 3.1: Time intervals of basic vectors

Sector	U_4U_6	U_6U_2	U_2U_3	U_3U_1	U_1U_5	U_5U_4
t_2	X	Z	-Y	-X	-Z	Y
t_1	-Z	Y	X	Z	-Y	-X

In Table 3.1, X, Y, Z are associated parameters for duty calculation of basic vector in each switching cycle, and can be presented as

$$X = u_\beta, \quad Y = \frac{1}{2}\left(u_\beta + \sqrt{3}u_\alpha\right), \quad Z = \frac{1}{2}\left(u_\beta - \sqrt{3}u_\alpha\right) \tag{3.1}$$

while, u_α, u_β are per unit values of voltage components in stationary frame with the reference value of $U_{\max}$. They can be expressed as

$$u_\alpha = \frac{\sqrt{3}u_s\cos\theta}{U_{dc}}, \quad u_\beta = \frac{\sqrt{3}u_s\sin\theta}{U_{dc}} \tag{3.2}$$

3.2 Analytical Sideband Voltage Harmonic Modeling

There have been so far various analytical researches on the sideband voltage harmonics of electrical machine drive with SVPWM technique. The PWM switching pattern can be decomposed into series of symmetrical or mirror symmetrical waveforms, then the spectra of these patterns can be derived and synthesized to obtain

the resultant spectrum of the original waveform [133]. The double Fourier series method is also employed to develop the expressions in the form of Bessel functions for the voltage harmonic spectrum of single-phase converter [91], and the scheme is further extended to investigate the three-phase system with SVPWM technique in closed-form expressions [92]. Instead of frequency domain analysis, a novel graphical scheme, involving the harmonic flux trajectory in the space vector plane for each sampling interval, is presented to evaluate the harmonic distortion of PWM techniques [134]. The method is also developed for complex multilevel cascade inverter system by using the relation between reference voltage and the output phase voltage to the load neutral point [20], and further employed to optimize the PWM techniques in multiple level converters by reducing the harmonic distortion [21]. Similar to such harmonic flux trajectory method, the harmonic distortion factor expression is developed in single switching period based on the stator flux ripple [135].

Some characteristics of sideband harmonics can be derived by the digital model of voltage vector in the previous section by analyzing the switching state change in each SVPWM cycle. However, such model is usually employed for qualitative performance analysis only. Therefore, the universal modulation model is involved in order to obtain the exact analytical sideband harmonic expressions for SVPWM technique. Without loss of generality, the modulation model of the symmetrical sampled SVPWM technique is sketched by the interaction between saddle shaped modulation wave and triangle carrier wave as shown in Figure 3.2. The resultant modulated square waves of three phases are exactly the same as the output of digital model given in Table 3.1.

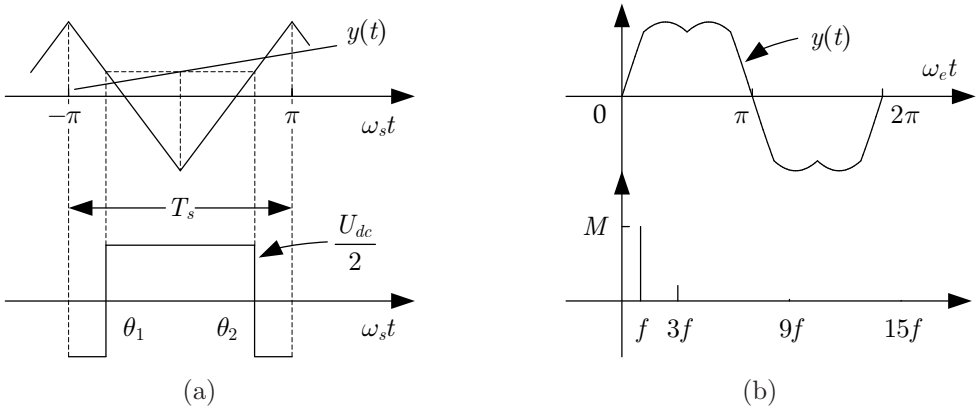

Figure 3.2: Modulation model of SVPWM: (a) symmetrical regular principle, (b) modulation waveform and spectrum.

The pulse width of the square wave is determined by the modulation function value at the middle point, which is employed to calculate the duty for each triangle by comparing with the carrier wave as depicted in Figure 3.2(a). It can be inspected from the figure that the state change moment of the pulse can be directly obtained as

$$\theta_1 = \frac{-\pi(1+y(t))}{2}, \quad \theta_2 = \frac{\pi(1+y(t))}{2} \tag{3.3}$$

Consequently, the phase output voltage over the whole carrier period can be expressed as

$$u_a = \begin{cases} \dfrac{-U_{dc}}{2}, & \omega_s t \leq \theta_1 \\ \dfrac{U_{dc}}{2}, & \theta_1 < \omega_s t < \theta_2 \\ \dfrac{-U_{dc}}{2}, & \omega_s t \geq \theta_2 \end{cases} \tag{3.4}$$

The pulse placement within each carrier period possesses a significant influence on both modulation index and the harmonic performance of the modulation implementation. The regularly sampled SVPWM technique can be considered equivalent to adding harmonics to the sinusoidal modulation wave. A saddle shaped modulation wave is expected from this technique, shown as Figure 3.2(b) in one electrical period. It can also be analytically expressed as

$$y(t) = \begin{cases} \sqrt{3}a\sin(\omega_e t), & 0 \leq \omega_e t \leq \dfrac{\pi}{6} \\ a\sin\left(\omega_e t + \dfrac{\pi}{6}\right), & \dfrac{\pi}{6} \leq \omega_e t \leq \dfrac{\pi}{2} \end{cases} \tag{3.5}$$

where $0 \leq a \leq 1$.

3.2.1 Sideband Voltage Harmonics in Stationary Frame

By applying Fourier series analysis based on electrical frequency ω_e, $y(t)$ can be rewritten as

$$y(t) = a\left(\frac{2}{\sqrt{3}}\sin(\omega_e t) + \sum_{k=0}^{\infty}\frac{6\times(-1)^{k+1}}{\pi(1-n^2)}\sin(n\omega_e t)\right) \tag{3.6}$$

where $n = 6k+3$, $k = 0, 1, 2, \cdots$. The coefficients of harmonics for $k \geq 1$ are generally very small and hence negligible in comparison with the fundamental component. Therefore, only the fundamental and third harmonics are considered in the study and $y(t)$ can be approximated as

$$y(t) \approx M\left(\sin(\omega_e t) + \xi\sin(3\omega_e t)\right) \tag{3.7}$$

where

$$M = \frac{2a}{\sqrt{3}}, \quad \xi = \frac{3\sqrt{3}}{8\pi} \tag{3.8}$$

The modulation index M can be analytically evaluated by Equation (2.10). However, the Fourier series analysis based on the electrical frequency ω_e of the modulation wave cannot be performed on the actual output voltage as the pulses are asymmetric within a fundamental period of the modulation wave. Consequently,

Fourier series analysis based on carrier frequency ω_s is carried out instead. Since u_a is an even function of ω_s in Figure 3.2(a), it can be expanded as

$$u_a = \frac{U_{dc}}{2}\left(\frac{a_0}{2} + \sum_{n=1}^{\infty} a_n \cos(n\omega_s t)\right) \tag{3.9}$$

where

$$\begin{cases} a_0 = 2M\left(\sin(\omega_e t) + \xi \sin(3\omega_e t)\right) \\ a_n = \dfrac{4}{n\pi}\sin\left(\dfrac{n\pi}{2} + \dfrac{nM\pi}{2}(\sin(\omega_e t) + \xi \sin(3\omega_e t))\right) \end{cases} \tag{3.10}$$

Due to their relatively high frequencies and associated large inductance in PMSMs, the impacts of the high-order sideband harmonics $n \geq 3$ are quite trivial and can be normally neglected. Without loss of generality, only the components with $n = 1$ and $n = 2$ are analytically investigated in this study. The high-order components can be derived accordingly with the same method. Series expansion can be applied to the items in Equation (3.10), as described in Appendix B.1. By neglecting the high-order terms, a_1 can be approximated as

$$a_1 \approx C_{10} + 2C_{12}\cos(2\omega_e t) + 2C_{14}\cos(4\omega_e t) \tag{3.11}$$

where

$$\begin{cases} C_{10} = \dfrac{4}{\pi} J_0\left(\dfrac{M\pi}{2}\right) J_0\left(\dfrac{M\pi\xi}{2}\right) \\ C_{12} = \dfrac{4}{\pi}\left(J_2\left(\dfrac{M\pi}{2}\right) J_0\left(\dfrac{M\pi\xi}{2}\right) - J_1\left(\dfrac{M\pi}{2}\right) J_1\left(\dfrac{M\pi\xi}{2}\right)\right) \\ C_{14} = \dfrac{4}{\pi} J_1\left(\dfrac{M\pi}{2}\right) J_1\left(\dfrac{M\pi\xi}{2}\right) \end{cases} \tag{3.12}$$

By substituting Equation (3.11) into Equation (3.9), the sideband harmonics in first carrier frequency domain can be expressed as

$$H_1 \approx \frac{U_{dc}}{2}\left(C_{10}\cos(\omega_s t) + C_{12}\cos((\omega_s \pm 2\omega_e)t) + C_{14}\cos((\omega_s \pm 4\omega_e)t)\right) \tag{3.13}$$

Similarly, a_2 can be approximated as

$$a_2 \approx 2C_{21}\sin(\omega_e t) + 2C_{23}\sin(3\omega_e t) + 2C_{25}\sin(5\omega_e t) + 2C_{27}\sin(7\omega_e t) \tag{3.14}$$

where

$$\begin{cases} C_{21} = -\dfrac{2}{\pi}\left(J_1(M\pi)J_0(M\pi\xi) + J_2(M\pi)J_1(M\pi\xi) - J_4(M\pi)J_1(M\pi\xi)\right) \\ C_{23} = -\dfrac{2}{\pi}\left(J_3(M\pi)J_0(M\pi\xi) + J_0(M\pi)J_1(M\pi\xi)\right) \\ C_{25} = -\dfrac{2}{\pi}J_2(M\pi)J_1(M\pi\xi) \\ C_{27} = -\dfrac{2}{\pi}J_4(M\pi)J_1(M\pi\xi) \end{cases} \tag{3.15}$$

As a resemblance, the sideband harmonics in the second carrier frequency domain can be represented as

$$\begin{aligned} H_2 \approx & \frac{U_{dc}}{2}(C_{21}\sin((\omega_e \pm 2\omega_s)t) + C_{23}\sin((3\omega_e \pm 2\omega_s)t) \\ & + C_{25}\sin((5\omega_e \pm 2\omega_s)t) + C_{27}\sin((7\omega_e \pm 2\omega_s)t)) \end{aligned} \tag{3.16}$$

The parameters expressed in Equation (3.12) and (3.15) can be considered as the per unit value of sideband harmonic voltage components with the base value of $U_{dc}/2$.

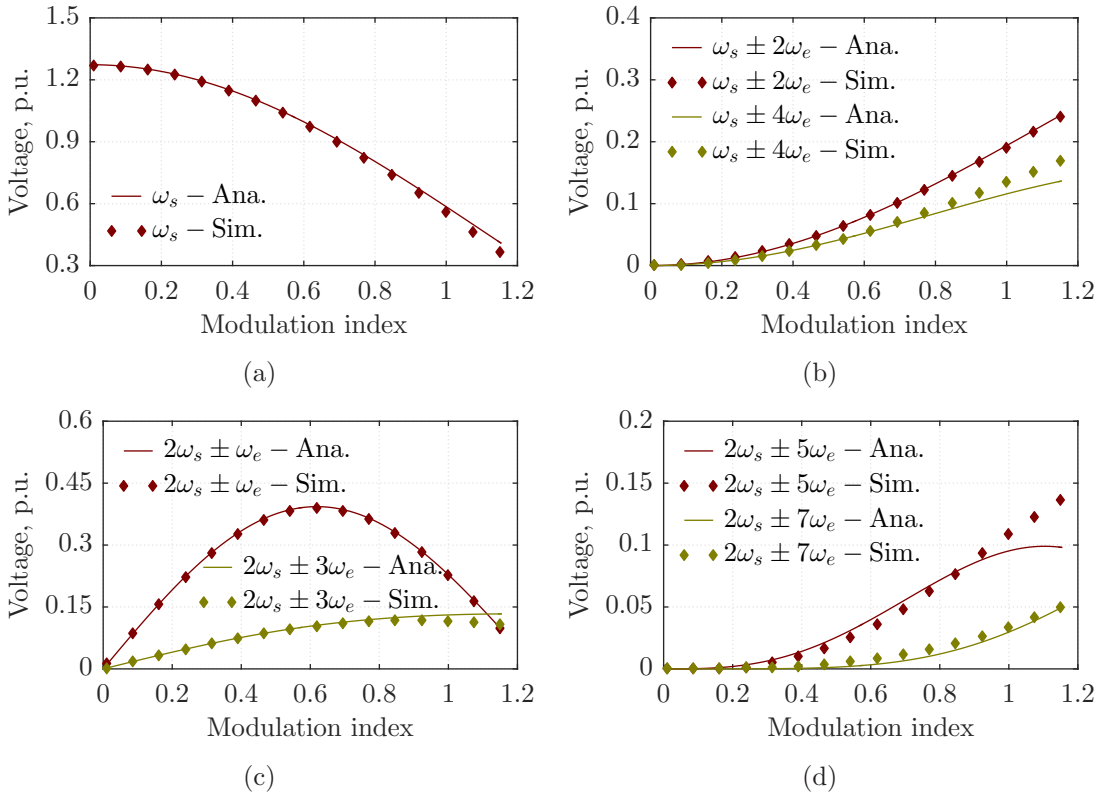

Figure 3.3: Validation of sideband voltage harmonics in stator stationary reference: (a) ω_s-order, (b) $(\omega_s \pm 2\omega_e)$ and $(\omega_s \pm 4\omega_e)$-order, (c) $(2\omega_s \pm \omega_e)$ and $(2\omega_s \pm 3\omega_e)$-order, (d) $(2\omega_s \pm 5\omega_e)$ and $(2\omega_s \pm 7\omega_e)$-order. (Ana. - Analytical model, Sim. - Simulation result)

Numerical circuit simulations on a two-level three-phase VSI system with respective carrier and modulation frequencies of 8kHz and 50Hz are carried out to validate the analytical model over the whole modulation index range. The voltage waveforms are derived and the corresponding sideband harmonics are compiled and compared with the analytical models in Figure 3.3. In first carrier frequency domain, the ω_s-order harmonic component declines as modulation index increases as shown in Figure 3.3(a) while Figure 3.3(b) reveals that the $(\omega_s \pm 2\omega_e)$- and $(\omega_s \pm 4\omega_e)$-order components gradually increase instead. Although the ω_s-order component is the dominant first sideband harmonic with the largest amplitude, the effect of such component can be eradicated with the three-phase configuration. On the other hand, Figure

3.3(c) and 3.3(d) show that the $(2\omega_s \pm 3\omega_e)$-, $(2\omega_s \pm 5\omega_e)$- and $(2\omega_s \pm 7\omega_e)$-order harmonics in second carrier frequency domain gradually ascend as modulation index rises. Whereas the $(2\omega_s \pm \omega_e)$-order harmonics first increase, reach their peak values when the modulation index is around 0.6, and then start to decrease again. It is noteworthy that three-phase configuration can also eliminate the impact of the $(2\omega_s \pm 3\omega_e)$-order components. Moreover, perfect agreements between analytical and simulation results have been achieved for the $(\omega_s \pm 2\omega_e)$- and $(2\omega_s \pm \omega_e)$-order components. For the other components, the analytical results coincide with the simulations under low modulation index but start to noticeably deviate as the modulation index exceeds about 0.6. Such discrepancy under high modulation index mainly originates from the approximation of analytical model. Overall, it is fair to state that the analytical model can deliver satisfactory sideband voltage harmonic predictions.

3.2.2 Sideband Voltage Harmonics in Synchronous Frame

The above subsection provides analytical derivation of the main phase voltage harmonics in the first and second carrier frequency domains in the stator stationary frame. Since the phase windings in three-phase PMSM are normally symmetric, the corresponding sideband harmonic voltage components of all three phases can be directly obtained. Moreover, these harmonics can be rearranged in the rotor synchronous frame by the Park transformation. Consequently, the corresponding *d*-*q* harmonics can be analytically obtained by applying the Park transformation on the harmonics in Equation (3.13) and (3.16), which is detailed in Appendix B.2. In first carrier frequency domain, it is revealed that only the $(\omega_s \pm 3\omega_e)$-order voltage harmonics exist in the rotor synchronous frame, and they can be represented as

$$\begin{cases} u_{(\omega_s \pm 2\omega_e)\_d} = -\dfrac{U_{dc}}{2} C_{12} \cos((\omega_s \pm 3\omega_e)t \mp \delta) \\ u_{(\omega_s \pm 4\omega_e)\_d} = -\dfrac{U_{dc}}{2} C_{14} \cos((\omega_s \pm 3\omega_e)t \pm \delta) \end{cases} \tag{3.17}$$

$$\begin{cases} u_{(\omega_s \pm 2\omega_e)\_q} = \pm\dfrac{U_{dc}}{2} C_{12} \sin((\omega_s \pm 3\omega_e)t \mp \delta) \\ u_{(\omega_s \pm 4\omega_e)\_q} = \mp\dfrac{U_{dc}}{2} C_{14} \sin((\omega_s \pm 3\omega_e)t \pm \delta) \end{cases} \tag{3.18}$$

By synthesizing the items with the same frequency, it can be derived as

$$\begin{cases} u_{d\_(\omega_s \pm 3\omega_e)} = U_{d\_13} \cos\left((\omega_s \pm 3\omega_e)t \pm \varphi_{d\_13}\right) \\ u_{q\_(\omega_s \pm 3\omega_e)} = \pm U_{q\_13} \sin\left((\omega_s \pm 3\omega_e)t \pm \varphi_{q\_13}\right) \end{cases} \tag{3.19}$$

where

$$\begin{cases} U_{d\_13} = \dfrac{U_{dc}}{2} \sqrt{C_{12}^2 + C_{14}^2 + 2C_{12}C_{14}\cos(2\delta)} \\ U_{q\_13} = \dfrac{U_{dc}}{2} \sqrt{C_{12}^2 + C_{14}^2 - 2C_{12}C_{14}\cos(2\delta)} \end{cases} \tag{3.20}$$

and φ_{d_13}, φ_{q_13} are determined by

$$\begin{cases} \varphi_{d\_13} = \pi + \arctan \dfrac{(C_{14} - C_{12}) \tan \delta}{(C_{14} + C_{12})} \\ \varphi_{q\_13} = \arctan \dfrac{(C_{14} + C_{12}) \tan \delta}{(C_{14} - C_{12})} \end{cases} \tag{3.21}$$

Similarly, the $(2\omega_s)$- and $(2\omega_s \pm 6\omega_e)$-order components in the second carrier frequency domain can be derived as

$$\begin{cases} u_{d\_(2\omega_s)} = -U_{dc} C_{21} \sin \delta \cos(2\omega_s t) \\ u_{q\_(2\omega_s)} = U_{dc} C_{21} \cos \delta \cos(2\omega_s t) \end{cases} \tag{3.22}$$

$$\begin{cases} u_{d\_(2\omega_s \pm 6\omega_e)} = U_{d\_26} \cos\left((2\omega_s \pm 6\omega_e)t \pm \varphi_{d\_26}\right) \\ u_{q\_(2\omega_s \pm 6\omega_e)} = \pm U_{q\_26} \sin\left((2\omega_s \pm 6\omega_e)t \pm \varphi_{q\_26}\right) \end{cases} \tag{3.23}$$

where

$$\begin{cases} U_{d\_26} = \dfrac{U_{dc}}{2} \sqrt{C_{25}^2 + C_{27}^2 + 2C_{25}C_{25} \cos(2\delta)} \\ U_{q\_26} = \dfrac{U_{dc}}{2} \sqrt{C_{25}^2 + C_{27}^2 - 2C_{25}C_{25} \cos(2\delta)} \end{cases} \tag{3.24}$$

and φ_{d_26}, φ_{q_26} are given by

$$\begin{cases} \varphi_{d\_26} = \pi + \arctan \dfrac{(C_{25} + C_{27}) \cot \delta}{(C_{25} - C_{27})}, \\ \varphi_{q\_26} = \arctan \dfrac{(C_{25} - C_{27}) \cot \delta}{(C_{25} + C_{27})}. \end{cases} \tag{3.25}$$

It can be inspected from Equation (3.19), (3.22) and (3.23) that the amplitudes of such first and second sideband voltage harmonics are mainly determined by the modulation index and torque angle. In order to validate the analytical model, comprehensive numerical circuit simulations on a two-level three-phase VSI system with respective carrier and modulation frequencies of 8kHz and 50Hz are carried out again. The voltage waveforms from the simulations with different modulation indices but constant torque of 30° are derived and the resultant amplitudes of the main first and second sideband harmonics are compared with the analytical models in Figure 3.4(a), 3.4(c) and 3.4(e). The same to their stator stationary counterparts, the amplitudes of $(\omega_s \pm 3\omega_e)$- and $(2\omega_s \pm 6\omega_e)$-order voltage harmonics in both d- and q-axis gradually ascend as the modulation index rises, while $(2\omega_s)$-order components first increase, reach their peak values when the modulation index is around 0.6, and then start to decrease again. Overall, good agreements between the analytical and simulation results have been reached except $(2\omega_s \pm 6\omega_e)$-order harmonics with high modulation index. On the other hand, the amplitudes of the main sideband harmonics in first and second carrier frequency domains from the simulations with different

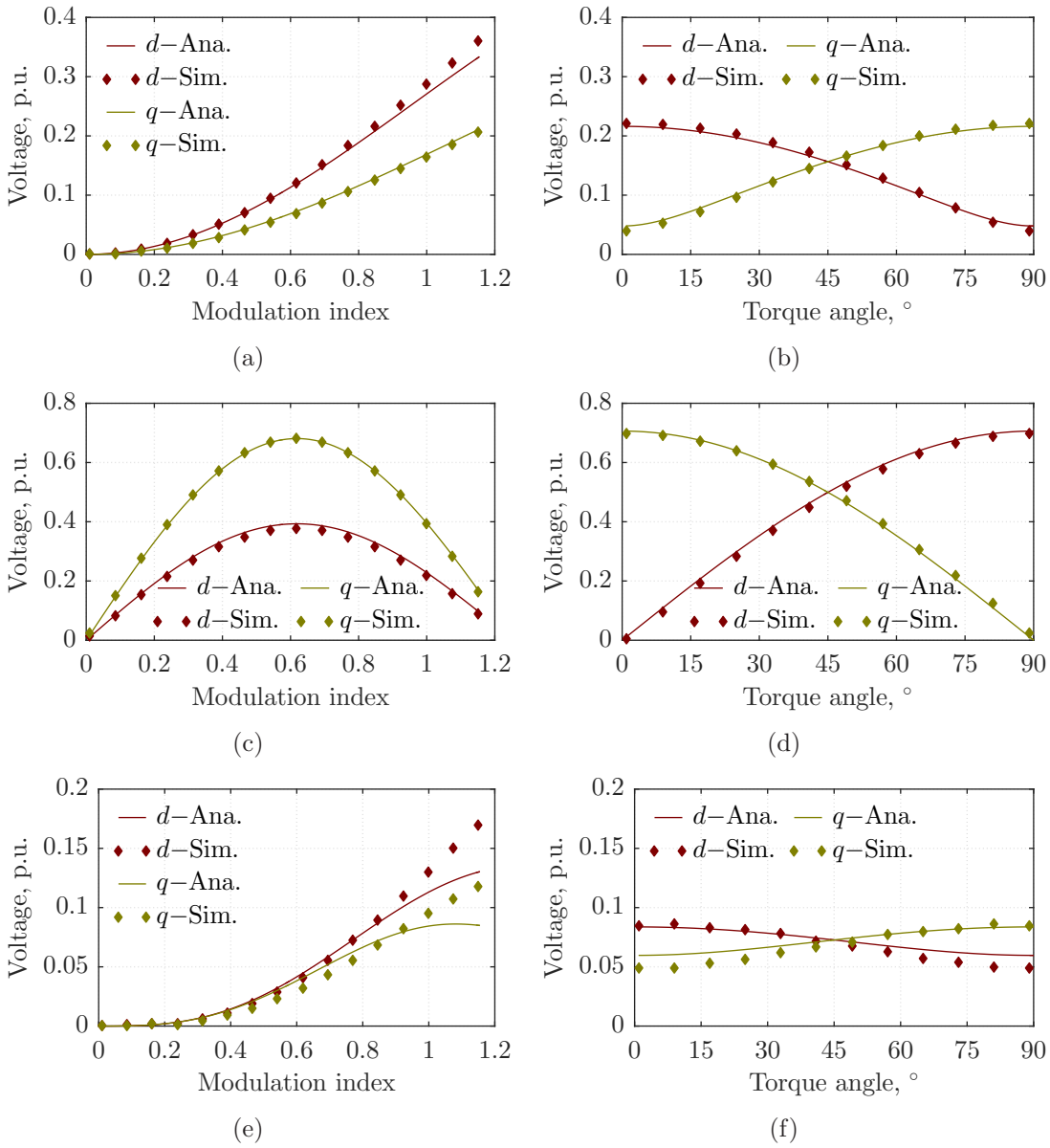

Figure 3.4: Validation of sideband voltage harmonics in the rotor synchronous frame: (a) $(\omega_s \pm 3\omega_e)$-order components for constant torque angle of 30°, (b) $(\omega_s \pm 3\omega_e)$-order components for constant modulation index of 0.8, (c) $(2\omega_s)$-order components for constant torque angle of 30°, (d) $(2\omega_s)$-order components for constant modulation index of 0.8, (e) $(2\omega_s \pm 6\omega_e)$-order components for constant torque angle of 30°, (f) $(2\omega_s \pm 6\omega_e)$-order components for constant modulation index of 0.8. (Ana. - Analytical model, Sim. - Simulation result)

torque angles but the same modulation index of 0.8 are obtained and presented together with the analytical results in Figure 3.4(b), 3.4(d) and 3.4(f). The figures have revealed that the d-axis $(\omega_s \pm 3\omega_e)$- and $(2\omega_s \pm 6\omega_e)$-order voltage harmonics gradually decline while the corresponding q-axis components progressively incline as the torque angle increases. Moreover the opposite is true for $(2\omega_s)$-order voltage harmonics, the q-axis component decreases but the d-axis component increases as

the torque angle mounts up. Some evident deviations between the analytical and simulation results can be observed for the d-axis $(2\omega_s \pm 6\omega_e)$-order voltage harmonics at large torque angle and the q-axis components at small torque angle. Nevertheless, great agreements have been achieved between the analytical and simulation results. The torque angle normally alters little in most of the PMSM drives, so that the modulation index becomes the most important factors for sideband harmonics.

3.3 Analytical Sideband Current Harmonic Modeling

In comparison with sideband voltage components, the analytical modeling of the sideband current harmonics with SVPWM technique is more complicated and burdensome. Therefore, the existing studies mainly concentrated on the derivation of the sideband current harmonic related coefficients, which can be regarded as a quality index to some extent. By studying the voltage pulse and resultant current harmonics in a single switching period, the approximate maximum current distortion and torque ripple in IM drive are analytically derived to evaluate different PWM techniques [93]. Similarly, the current waveform in one basic inverter cycle is investigated to obtain the analytical derivation of the ripple magnitudes of the d- and q-axis currents in surface-mounted PMSM [94]. Although the analytical derivation can be employed to quantify the deviations from the ideal models used in most control studies, it is limited to only the cases with low-switching frequency. Besides, various methods have been proposed to reduce and optimize the sideband current harmonics. The stator flux ripple based method is employed to design hybrid PWM techniques, which involve multiple sequences of active vector time division, so that the line current distortion can be effectively reduced [96]. Meanwhile, topologies with diode clamped and capacitor clamped [136], flying capacitor [137], cascaded two level converter [138] and hybrid cascaded inverter [95] are introduced in various multilevel inverters in order to cancel the corresponding current harmonics. Furthermore, several random pulse width PWM techniques based on random pulse position [139], random zero vector distribution [140] and random switching frequency [97] are all investigated to suppress the amplitudes of the sideband current harmonics.

As aforementioned, there have been hardly investigations on full direct analytical developments of sideband current harmonics in the PMSM drive system with SVPWM technique. However, the closed-form analytical expressions of sideband current harmonics can be used for prompt yet detailed harmonic characteristic analysis. Such analytical results can be further adapted to appraise the impacts of operational conditions, drive control strategies and electromagnetic parameters on the sideband current harmonics. Additionally, they can provide insightful guidelines to reduce the corresponding electromagnetic losses, torque pulsations and acoustic noises. Consequently, the sideband current harmonics in the PMSM drive system with SVPWM technique are analytically developed based on the corresponding voltage models in this section.

3.3.1 Sideband Current Harmonics in Synchronous Frame

The main d- and q-axis sideband current harmonics can be directly derived in analytical forms from the corresponding voltage harmonics based on a mathematical model of a PMSM. The analytical correlations between the ω_μ-order voltage and current harmonics in d- and q-axis can be easily developed from Equation (2.1). The resultant model can be expressed as

$$\begin{cases} u_{d\_\omega_\mu} = R_s i_{d\_\omega_\mu} + j\omega_\mu L_d i_{d\_\omega_\mu} - \omega_e L_q i_{q\_\omega_\mu} \\ u_{q\_\omega_\mu} = R_s i_{q\_\omega_\mu} + j\omega_\mu L_q i_{q\_\omega_\mu} + \omega_e L_d i_{d\_\omega_\mu} \end{cases} \tag{3.26}$$

As the sideband current harmonic frequency ω_μ are normally at least one order of magnitude higher than the electrical frequency ω_e, the sideband harmonic reactance will be much greater than the winding direct current resistance. Hence, the sideband voltage drops over the winding resistances, the first term in the right side of Equation (3.26), can be neglected without a considerable compromise on accuracy. Moreover, the corresponding EMF due to the rotational action, the last terms in the right side of Equation (3.26), are very trivial and negligible. Therefore, it is justifiable to assume that the sideband voltage harmonics are all consumed by the corresponding induction EMF. As a result, the ω_μ-order current harmonics of steady state can be approximated as

$$i_{d\_\omega_\mu} = \frac{u_{d\_\omega_\mu}}{j\omega_\mu L_d}, \quad i_{q\_\omega_\mu} = \frac{u_{q\_\omega_\mu}}{j\omega_\mu L_q} \tag{3.27}$$

By substituting the $(\omega_s \pm 3\omega_e)$-, $(2\omega_s)$- and $(2\omega_s \pm 6\omega_e)$-order voltage harmonic expressions from Equation (3.19), (3.22) and (3.23) into Equation (3.27), the corresponding current harmonics can be obtained as

$$\begin{cases} i_{d\_(\omega_s \pm 3\omega_e)} = \dfrac{U_{d\_13} \sin\left((\omega_s \pm 3\omega_e)t \pm \varphi_{d\_13}\right)}{(\omega_s \pm 3\omega_e)L_d} \\ i_{q\_(\omega_s \pm 3\omega_e)} = \dfrac{\mp U_{q\_13} \cos\left((\omega_s \pm 3\omega_e)t \pm \varphi_{q\_13}\right)}{(\omega_s \pm 3\omega_e)L_q} \end{cases} \tag{3.28}$$

$$\begin{cases} i_{d\_(2\omega_s)} = \dfrac{-U_{dc} C_{21} \sin\delta \sin(2\omega_s t)}{2\omega_s L_d} \\ i_{q\_(2\omega_s)} = \dfrac{U_{dc} C_{21} \cos\delta \sin(2\omega_s t)}{2\omega_s L_q} \end{cases} \tag{3.29}$$

$$\begin{cases} i_{d\_(2\omega_s \pm 6\omega_e)} = \dfrac{U_{d\_26} \sin\left((2\omega_s \pm 6\omega_e)t \pm \varphi_{d\_26}\right)}{(2\omega_s \pm 6\omega_e)L_d} \\ i_{q\_(2\omega_s \pm 6\omega_e)} = \dfrac{\mp U_{q\_26} \cos\left((2\omega_s \pm 6\omega_e)t \pm \varphi_{q\_26}\right)}{(2\omega_s \pm 6\omega_e)L_q} \end{cases} \tag{3.30}$$

3.3.2 Sideband Current Harmonics in Stationary Frame

The analytical expressions of the sideband current harmonics in the rotor synchronous frame can be converted into the expressions in the stator stationary frame

accordingly by applying the inverse Park transformation. The $(\omega_s \pm 3\omega_e)$-order current harmonics in the rotor synchronous frame can be transformed into $(\omega_s \pm 2\omega_e)$- and $(\omega_s \pm 4\omega_e)$-order harmonics in the stator stationary frame. The corresponding phase current harmonics can be obtained as

$$\begin{cases} i_{s\_(\omega_s \pm 2\omega_e)} = \pm I_{s\_12} \cos((\omega_s \pm 2\omega_e)t \mp \varphi_{s\_12}) \\ i_{s\_(\omega_s \pm 4\omega_e)} = \pm I_{s\_14} \cos((\omega_s \pm 4\omega_e)t \pm \varphi_{s\_14}) \end{cases} \tag{3.31}$$

The amplitudes and initial phases are determined by

$$\begin{cases} I_{s\_12} = \dfrac{U_{dc}\sqrt{\sigma_1^2 C_{12}^2 + \sigma_2^2 C_{14}^2 + 2\sigma_1\sigma_2 C_{12} C_{14}\cos(2\delta)}}{4(\omega_s \pm 3\omega_e)} \\ I_{s\_14} = \dfrac{U_{dc}\sqrt{\sigma_2^2 C_{12}^2 + \sigma_1^2 C_{14}^2 + 2\sigma_1\sigma_2 C_{12} C_{14}\cos(2\delta)}}{4(\omega_s \pm 3\omega_e)} \end{cases} \tag{3.32}$$

$$\begin{cases} \cos\varphi_{s\_12} = \dfrac{(\sigma_1 C_{12} - \sigma_2 C_{14})\sin\delta}{\sqrt{\sigma_1^2 C_{12}^2 + \sigma_2^2 C_{14}^2 + 2\sigma_1\sigma_2 C_{12} C_{14}\cos(2\delta)}} \\ \sin\varphi_{s\_12} = \dfrac{-(\sigma_1 C_{12} + \sigma_2 C_{14})\cos\delta}{\sqrt{\sigma_1^2 C_{12}^2 + \sigma_2^2 C_{14}^2 + 2\sigma_1\sigma_2 C_{12} C_{14}\cos(2\delta)}} \\ \cos\varphi_{s\_14} = \dfrac{(\sigma_2 C_{12} - \sigma_1 C_{14})\sin\delta}{\sqrt{\sigma_2^2 C_{12}^2 + \sigma_1^2 C_{14}^2 + 2\sigma_1\sigma_2 C_{12} C_{14}\cos(2\delta)}} \\ \sin\varphi_{s\_14} = \dfrac{(\sigma_2 C_{12} + \sigma_1 C_{14})\cos\delta}{\sqrt{\sigma_2^2 C_{12}^2 + \sigma_1^2 C_{14}^2 + 2\sigma_1\sigma_2 C_{12} C_{14}\cos(2\delta)}} \end{cases} \tag{3.33}$$

where σ_1 and σ_2 are expressed as

$$\sigma_1 = \frac{1}{L_d} + \frac{1}{L_q}, \quad \sigma_2 = \frac{1}{L_d} - \frac{1}{L_q} \tag{3.34}$$

By inspecting the analytical expressions in Equation (3.32), a relationship between the amplitudes of the $(\omega_s \pm 2\omega_e)$- and $(\omega_s \pm 4\omega_e)$-order current harmonics can be revealed as

$$I_{s\_12}^2 - I_{s\_14}^2 = \frac{U_{dc}^2(C_{12}^2 - C_{14}^2)}{4L_d L_q(\omega_s \pm 3\omega_e)^2} > 0 \tag{3.35}$$

It is apparent that the amplitudes of the $(\omega_s \pm 2\omega_e)$-order sideband phase current harmonics are always more significant than the $(\omega_s \pm 4\omega_e)$-order components in PMSM drives with SVPWM technique. Moreover, it can also be inspected from Equation (3.32) that the amplitudes of the main first sideband current harmonics are dependent on the operational condition of specific machine, such as modulation index and torque angle. In order to reveal the correlations between the sideband current harmonics in the first carrier frequency domain and operational conditions of the machine, the PMSM drive of prototype II with carrier wave frequency of 4kHz and DC power supply of 24V over the whole operational range has been investigated. The amplitudes of such components with different modulation indices and torque

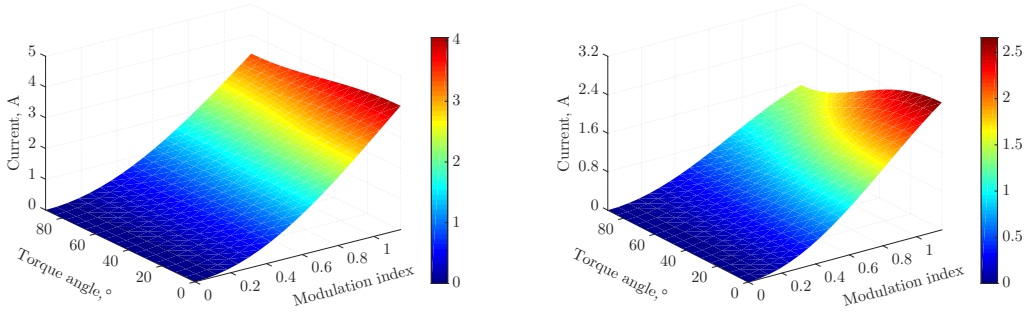

(a) (b)

Figure 3.5: First sideband harmonics of Prototype II with different conditions: (a) $(\omega_s \pm 2\omega_e)$-order, (b) $(\omega_s \pm 4\omega_e)$-order.

angles are analytically obtained and illustrated in Figure 3.5, which confirm the validity of Equation (3.35). The figure reveals that both the $(\omega_s \pm 2\omega_e)$- and $(\omega_s \pm 4\omega_e)$-order harmonics rise significantly as the modulation index increases. On the other hand, the q-axis inductance of prototype II is larger than its d-axis counterpart as the inset magnet configuration is employed in the rotor design. Hence, both the components gradually decrease as the torque angle mounts up. However, the decline of $(\omega_s \pm 4\omega_e)$-order is more notable than the $(\omega_s \pm 2\omega_e)$-order.

Analogously, the $(2\omega_s)$-order current harmonic component in the rotor synchronous frame can be converted into $(2\omega_s \pm \omega_e)$-order harmonics in the stator stationary frame, which are usually the predominant components in the second order carrier frequency domain. Meanwhile, the $(2\omega_s \pm 6\omega_e)$-order harmonics in the rotor synchronous frame can be converted into $(2\omega_s \pm 5\omega_e)$- and $(2\omega_s \pm 7\omega_e)$-order components in the stator stationary frame. Although they are normally much smaller than the $(2\omega_s \pm \omega_e)$-order harmonics, they can be quite close especially as the modulation index reaches up to the maximum value. The expressions of these harmonics can be accordingly derived as

$$i_{s\_(2\omega_s \pm \omega_e)} = \mp I_{s\_21} \cos((2\omega_s \pm \omega_e)t \pm \varphi_{s\_21}) \tag{3.36}$$

$$\begin{cases} i_{s\_(2\omega_s \pm 5\omega_e)} = \pm I_{s\_25} \cos((2\omega_s \pm 5\omega_e)t \mp \varphi_{s\_25}) \\ i_{s\_(2\omega_s \pm 7\omega_e)} = \pm I_{s\_27} \cos((2\omega_s \pm 7\omega_e)t \pm \varphi_{s\_27}) \end{cases} \tag{3.37}$$

Where the corresponding harmonic amplitudes and initial phases are respectively given by

$$I_{s\_21} = -\frac{U_{dc} C_{21}}{4\omega_s} \sqrt{\frac{\sin^2 \delta}{L_d^2} + \frac{\cos^2 \delta}{L_q^2}} \tag{3.38}$$

$$\cos \varphi_{s\_21} = \frac{L_d \cos \delta}{\sqrt{L_d^2 \cos^2 \delta + L_q^2 \sin^2 \delta}}, \quad \sin \varphi_{s\_21} = \frac{L_q \sin \delta}{\sqrt{L_d^2 \cos^2 \delta + L_q^2 \sin^2 \delta}} \tag{3.39}$$

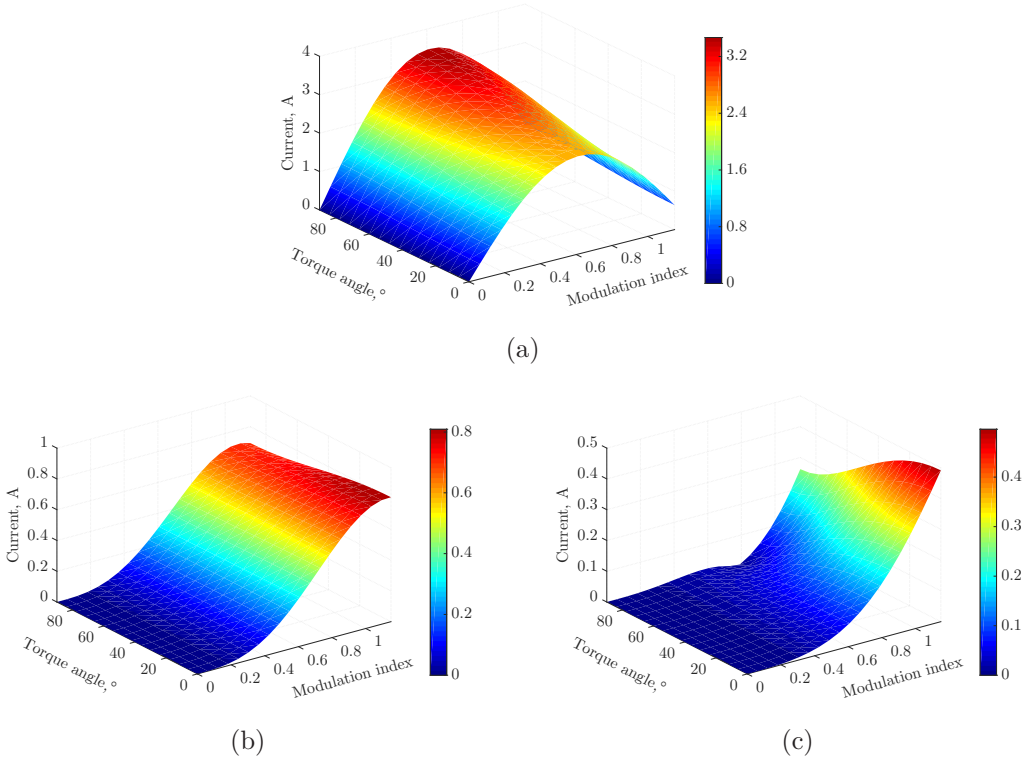

Figure 3.6: Second sideband harmonics of Prototype II with different conditions: (a) $(2\omega_s \pm \omega_e)$-order, (b) $(2\omega_s \pm 5\omega_e)$-order, (c) $(2\omega_s \pm 7\omega_e)$-order.

and

$$\begin{cases} I_{s\_25} = \dfrac{U_{dc}\sqrt{\sigma_1^2 C_{25}^2 + \sigma_2^2 C_{27}^2 + 2\sigma_1\sigma_2 C_{25} C_{27}\cos(2\delta)}}{4(2\omega_s \pm 6\omega_e)} \\ I_{s\_27} = \dfrac{U_{dc}\sqrt{\sigma_2^2 C_{25}^2 + \sigma_1^2 C_{27}^2 + 2\sigma_1\sigma_2 C_{25} C_{27}\cos(2\delta)}}{4(2\omega_s \pm 6\omega_e)} \end{cases} \tag{3.40}$$

$$\begin{cases} \cos\varphi_{s\_25} = \dfrac{(\sigma_1 C_{25} + \sigma_2 C_{27})\cos\delta}{\sqrt{\sigma_1^2 C_{25}^2 + \sigma_2^2 C_{27}^2 + 2\sigma_1\sigma_2 C_{25} C_{27}\cos(2\delta)}} \\ \sin\varphi_{s\_25} = \dfrac{(\sigma_1 C_{25} - \sigma_2 C_{27})\sin\delta}{\sqrt{\sigma_1^2 C_{25}^2 + \sigma_2^2 C_{27}^2 + 2\sigma_1\sigma_2 C_{25} C_{27}\cos(2\delta)}} \\ \cos\varphi_{s\_27} = \dfrac{(\sigma_2 C_{25} + \sigma_1 C_{27})\cos\delta}{\sqrt{\sigma_2^2 C_{25}^2 + \sigma_1^2 C_{27}^2 + 2\sigma_1\sigma_2 C_{25} C_{27}\cos(2\delta)}} \\ \sin\varphi_{s\_27} = \dfrac{-(\sigma_2 C_{25} - \sigma_1 C_{27})\sin\delta}{\sqrt{\sigma_2^2 C_{25}^2 + \sigma_1^2 C_{27}^2 + 2\sigma_1\sigma_2 C_{25} C_{27}\cos(2\delta)}} \end{cases} \tag{3.41}$$

Equation (3.38) and (3.40) indicate that the amplitudes of the main sideband current harmonics in the second carrier frequency domain are also mainly determined by modulation index and torque angle. The resultant amplitudes of the second sideband current harmonics of Prototype II with different modulation indices and torque angles are analytically evaluated and shown in Figure 3.6. Figure 3.6(a) shows that the $(2\omega_s \pm \omega_e)$-order harmonics first incline until they reach the maximum values, and

then descend as the modulation index increases. Meanwhile, they hike remarkably as the torque angle goes up, quite opposite to the $(\omega_s \pm 2\omega_e)$- and $(\omega_s \pm 4\omega_e)$-order harmonics. On the other hand, the $(2\omega_s \pm 5\omega_e)$- and $(2\omega_s \pm 7\omega_e)$-order current harmonics share very similar characteristics as the $(\omega_s \pm 2\omega_e)$- and $(\omega_s \pm 4\omega_e)$-order components. In fact, it can be seen from the figures that these two components are much smaller than their main counterparts for most cases. Therefore, they normally can be neglected and mere considerations of the $(\omega_s \pm 2\omega_e)$-, $(\omega_s \pm 4\omega_e)$- and $(2\omega_s \pm \omega_e)$-order harmonics mostly suffice for sideband current investigation of PMSM drive. It is worth mentioning that the synchronous inductances L_d and L_q are equal in PMSM with no saliency. Thus, it can be easily concluded from the equations above that the sideband current harmonics such as $(\omega_s \pm 2\omega_e)$-, $(\omega_s \pm 4\omega_e)$-, $(2\omega_s \pm \omega_e)$-, $(2\omega_s \pm 5\omega_e)$- and $(2\omega_s \pm 7\omega_e)$-order components are independent from the torque angle in such machine as surface-mounted PMSM.

Furthermore, experimental tests on the PMSM drive of prototype II are comprehensively conducted in order to validate the proposed analytical sideband current model. The prototype PMSM is powered by a conventional two-level three-phase VSI with SVPWM technique of 4kHz carrier frequency and $i_d = 0$ control strategy during the experiments. Generally, the modulation index and torque angle can be approximately represented by the rotational speed and load torque in PMSM drive respectively. Therefore, the current characteristics of the prototype with torque load and rotational speed ranged from 0N·m to 10N·m and 0rpm to 1800rpm are captured and investigated during the experiments. The armature reaction especially under heavily loaded conditions can result in severe magnetic saturation in the stator and rotor iron cores of the machine. However, magnetic saturation hardly occurs in the prototype II even with large load due to its inset magnet rotor structure. Hence, the electromagnetic parameters derived from no-load condition can be directly employed to carry out the analytical assessment on sideband current harmonics for all conditions without substantial compromise on accuracy. 2-D FEA method is implemented to evaluate the no-load electromagnetic parameters such as inductances and PM flux linkage of the prototype II.

The phase current waveform of the prototype PMSM under its rated condition of 5N·m and 1200rpm are captured during experimental test and its harmonic spectrum is compiled accordingly. The resultant waveform and spectra are minutely illustrated in Figure 3.7, which reveals that there are quite evident sideband harmonics in the phase current. As the machine has eight rotor poles and operates at 1200rpm, the corresponding electrical frequency is 80Hz. Figure 3.7(c) confirms that the $(\omega_s \pm 2\omega_e)$- and $(\omega_s \pm 4\omega_e)$-order current harmonics with respective frequencies of 3840Hz/4160Hz and 3680Hz/4320Hz are the main components in the first carrier frequency domain, while Figure 3.7(d) testifies that $(2\omega_s \pm \omega_e)$-order components with frequencies of 7920Hz/8080Hz are the key second sideband current harmonics. Moreover, Figure 3.7(d) also illustrates evident $(2\omega_s \pm 5\omega_e)$- and $(2\omega_s \pm 7\omega_e)$-order harmonics with frequencies of 7600Hz/8400Hz and 7440Hz/8560Hz in the second carrier frequency domain. However, they are of much less significance than their $(2\omega_s \pm \omega_e)$-order counterparts and hence negligible. Overall, the experimental results in Figure 3.7 have qualitatively validated the proposed analytical models of sideband

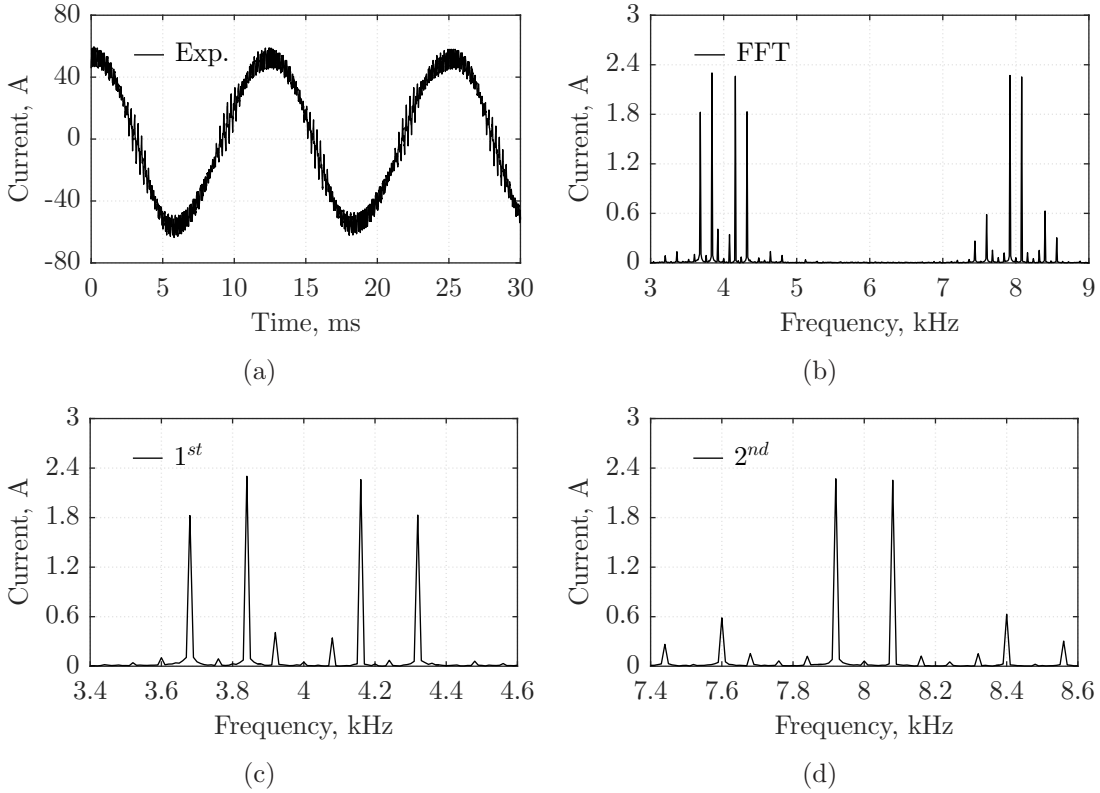

Figure 3.7: Experimental phase current waveform and its harmonic spectrum: (a) phase current waveform, (b) first and second sideband current harmonic spectrum, (c) first carrier frequency domain, (d) second carrier frequency domain. (Exp. - Experimental result)

current harmonic components.

Furthermore, the amplitude variations of the main sideband current harmonics in the first and second carrier frequency domains in the prototype PMSM drive are examined with different modulation indices and torque angles in order to validate the proposed analytical models quantitatively. By examining Equation (2.10) and Figure A.5(a), the modulation index of the proposed PMSM drive with SVPWM technique and a constant torque load is approximately proportional to its rotational speed as the voltage drop over the phase winding resistance can be neglected for most of the cases. Therefore, the PMSM drive is loaded with a constant light torque of 0.25N·m during the first stage of the experimental tests and different rotational speeds ranged from 0rpm to 1800rpm with step of 150rpm are implemented in order to achieve various modulation indices. Moreover, the d-axis flux linkage stays almost the same as the PM flux linkage with $i_d = 0$ control strategy while the q-axis component is nearly proportional to the stator current. Meanwhile, the stator current of the prototype PMSM drive is directly proportional to the torque load without consideration of magnetic saturation. As a result, the tangent value of the torque angle is somewhat proportional to the torque load, as shown in Figure A.5(b). Hence, the PMSM drive is operated under different load conditions ranged from 0N·m to 10N·m with step of 1N·m during the second stage of the experimental

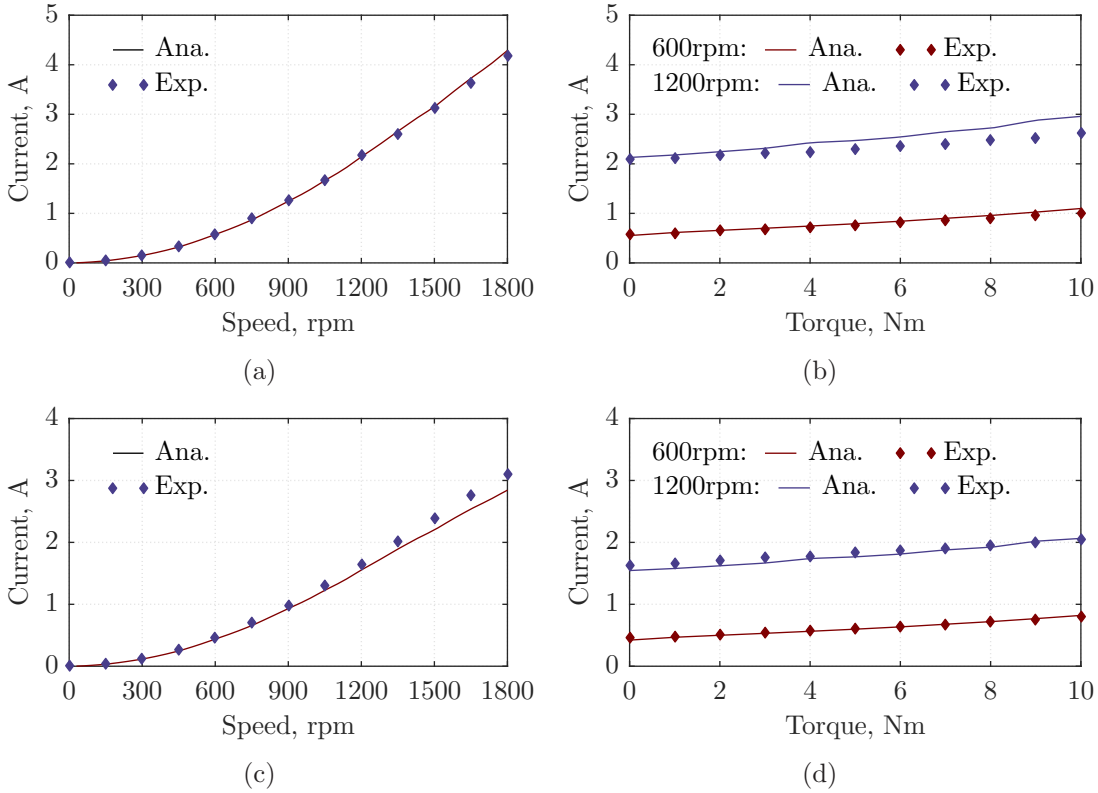

Figure 3.8: First sideband current harmonics validations: (a) $(\omega_s \pm 2\omega_e)$-order components under no-load and different speed conditions, (b) $(\omega_s \pm 2\omega_e)$-order components under speed of 600rpm and 1200rpm and different load conditions, (c) $(\omega_s \pm 4\omega_e)$-order components under no-load and different speed conditions, (d) $(\omega_s \pm 4\omega_e)$-order components under speed of 600rpm and 1200rpm and different load conditions. (Ana. - Analytical model, Exp. - Experimental result)

tests and constant rotational speed is maintained in order to achieve various torque angles. The rotational speeds of both 600rpm and 1200rpm are applied for these operational conditions. The experimental phase current waveforms have been captured for both stages of tests so that their spectra can be compiled accordingly. The resultant amplitudes of the main first and second sideband current harmonics, the $(\omega_s \pm 2\omega_e)$- and $(\omega_s \pm 4\omega_e)$-order components, as well as $(2\omega_s \pm \omega_e)$-, $(2\omega_s \pm 5\omega_e)$- and $(2\omega_s \pm 7\omega_e)$-order components, from both analytical evaluations and experimental results, are obtained and compared in Figure 3.8 and Figure 3.9 respectively. As the rotational speed and load torque are more or less equivalent to modulation index and torque angle, the profiles in Figure 3.8 and Figure 3.9 share nearly the same patterns as the corresponding results in Figure 3.4. Figure 3.8 shows that some noticeable discrepancies between the analytical and experimental results occur at high rotational speed for the $(\omega_s \pm 4\omega_e)$-order current harmonics while the experimental results for the $(\omega_s \pm 4\omega_e)$-order components deviate evidently from the analytical models at rotational speed of 1200rpm. On the other hand, it can be observed from 3.9 that the differences between analytical and experimental results for $(2\omega_s \pm 5\omega_e)$- and $(2\omega_s \pm 7\omega_e)$-order harmonics are getting quite significant as the modulation in-

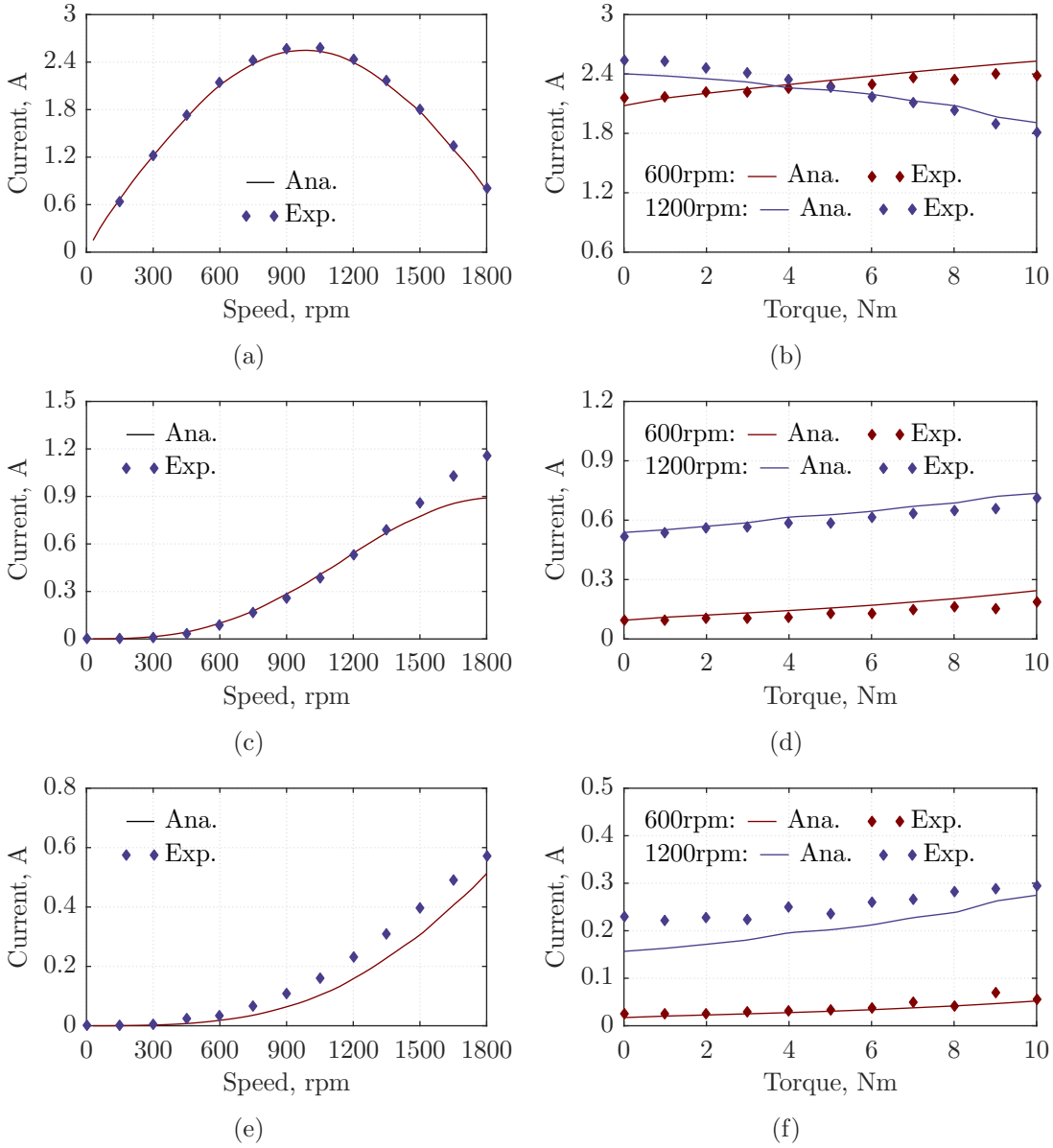

Figure 3.9: Second sideband current harmonics validations: (a) $(2\omega_s \pm \omega_e)$-order components under no-load and different speed conditions, (b) $(2\omega_s \pm \omega_e)$-order components under speed of 600rpm and 1200rpm and different load conditions, (c) $(2\omega_s \pm 5\omega_e)$-order components under no-load and different speed conditions, (d) $(2\omega_s \pm 5\omega_e)$-order components under speed of 600rpm and 1200rpm and different load conditions, (e) $(2\omega_s \pm 7\omega_e)$-order components under no-load and different speed conditions, (f) $(2\omega_s \pm 7\omega_e)$-order components under speed of 600rpm and 1200rpm and different load conditions. (Ana. - Analytical model, Exp. - Experimental result)

dex goes up. Besides, great agreements have been achieved between the analytical and experimental results for the other components. As aforementioned, the approximations made for the analytical model do sacrifice the accuracy to some extent. In practice, the inductances and PM flux linkage vary with the operational conditions but constant parameters are used for analytical evaluations. Moreover, the mechan-

ical transmission inevitably introduces variational friction loads and hence incurs measurement errors. By taking into account all these factors, it is fairly reasonable to conclude that the experimental measurements match well with the corresponding analytical predictions. On the whole, the validity of the analytical models have been quantitatively underpinned by the experimental results. Furthermore, both the analytical and experimental results in Figure 3.8(b), 3.8(d), 3.9(b), 3.9(d) and 3.9(f) reveal that the influences of the rotational speed on the sideband current harmonics are far greater than the load torque effects.

3.4 Comparison Between SPWM and SVPWM Techniques

Besides SVPWM, the SPWM technique is also commonly implemented in a PMSM drive system. It inevitably generates corresponding sideband harmonics in the drive system as well. The analytical models of such sideband harmonic components can be developed with close resemblance to the SVPWM scheme and the detailed derivation process and results are presented in Appendix C. The analytical expressions of the main first and second sideband current harmonics with SPWM technique are derived in the rotor synchronous frame as

$$\begin{cases} i_{d\_(\omega_s \pm 3\omega_e)} = \dfrac{-U_{dc} C'_{12} \sin(\omega_s t \pm 3\omega_e t \mp \delta)}{2(\omega_s \pm 3\omega_e) L_d} \\ i_{q\_(\omega_s \pm 3\omega_e)} = \dfrac{\mp U_{dc} C'_{12} \cos(\omega_s t \pm 3\omega_e t \mp \delta)}{2(\omega_s \pm 3\omega_e) L_q} \end{cases} \tag{3.42}$$

$$\begin{cases} i_{d\_(2\omega_s)} = -\dfrac{-U_{dc} C'_{21} \sin\delta \sin(2\omega_s t)}{2\omega_s L_d} \\ i_{q\_(2\omega_s)} = \dfrac{U_{dc} C'_{21} \cos\delta \sin(2\omega_s t)}{2\omega_s L_q} \end{cases} \tag{3.43}$$

C'_{12} and C'_{21} are defined in Equation (C.4).

By applying the inverse Park transformation, the resultant harmonics in the stator stationary frame can be derived. The $(\omega_s \pm 2\omega_e)$-, $(\omega_s \pm 4\omega_e)$- and $(2\omega_s \pm \omega_e)$-order harmonics are the main components for SPWM as well. The amplitudes of those components can be presented as

$$I_{s\_12} = \frac{U_{dc}\sigma_1 C'_{12}}{4(\omega_s \pm 3\omega_e)}, \quad I_{s\_14} = \frac{U_{dc}\sigma_2 C'_{12}}{4(\omega_s \pm 3\omega_e)} \tag{3.44}$$

And

$$I_{s\_21} = -\frac{U_{dc} C'_{21}}{4\omega_s} \sqrt{\frac{\sin^2\delta}{L_d^2} + \frac{\cos^2\delta}{L_q^2}} \tag{3.45}$$

With the same carrier frequency and operational condition, the frequencies of the main sideband current harmonics are identical for SPWM and SVPWM techniques.

Therefore, the corresponding amplitudes can be directly compared to investigate both techniques. Simple mathematical manipulations on the amplitude formulae in (3.32) and (3.44) of the $(\omega_s \pm 2\omega_e)$-order sideband current harmonics have been performed as

$$\begin{aligned}&\frac{U_{dc}\sqrt{\sigma_1^2 C_{12}^2 + \sigma_2^2 C_{14}^2 + 2\sigma_1\sigma_2 C_{12} C_{14}\cos(2\delta)}}{4(\omega_s \pm 3\omega_e)} \\ &\leq \frac{U_{dc}\left(\sigma_1 C_{12} + \sigma_2 C_{14}\right)}{4(\omega_s \pm 3\omega_e)} < \frac{U_{dc}\sigma_1\left(C_{12} + C_{14}\right)}{4(\omega_s \pm 3\omega_e)} < \frac{U_{dc}\sigma_1 C'_{12}}{4(\omega_s \pm 3\omega_e)}\end{aligned} \tag{3.46}$$

It clearly shows that SPWM technique will always result in larger amplitudes for those particular components than those of SVPWM scheme with the same modulation index. On the other hand, the relationships between SPWM and SVPWM techniques become much more complex for the $(\omega_s \pm 4\omega_e)$-order harmonics within the first carrier frequency domain. They are largely dependent on the electromagnetic parameters and load conditions. The saliency ratio of PMSM, $\rho = L_q/L_d$, is defined in order to simplify the analysis. For the $(\omega_s \pm 4\omega_e)$-order current harmonics with SVPWM technique, it can be obtained from Equation (3.32) that

$$\lim_{\rho\to 1} I_{s\_14} = \frac{U_{dc}\sigma_1 C_{14}}{4(\omega_s \pm 3\omega_e)}, \quad \lim_{\rho\to\infty} I_{s\_14} = \frac{U_{dc}\sigma_1\sqrt{C_{12}^2 + C_{14}^2 + 2C_{12}C_{14}\cos 2\delta}}{4(\omega_s \pm 3\omega_e)} \tag{3.47}$$

Whilst, it can be derived from (3.44) with SPWM technique that

$$\lim_{\rho\to 1} I_{s\_14} = 0, \quad \lim_{\rho\infty} I_{s\_14} = \frac{U_{dc}\sigma_1 C'_{12}}{4(\omega_s \pm 3\omega_e)} \tag{3.48}$$

It is obvious that the $(\omega_s \pm 4\omega_e)$-order sideband current harmonics in PMSM drive with SPWM technique stem from the difference between the d- and q-axis inductances (saliency). Therefore, they almost do not exist in the machine with small saliency such as surface-mounted PMSMs but have nearly the same amplitudes as the $(\omega_s \pm 2\omega_e)$-order harmonics in the machine with large saliency. Consequently, SVPWM technique will normally produce more significant $(\omega_s \pm 4\omega_e)$-order harmonics in PMSM with small saliency ratio than SPWM. On the contrary, SPWM technique will usually result in greater $(\omega_s \pm 4\omega_e)$-order harmonics in PMSM with a large saliency ratio than SVPWM scheme. Moreover, it is noteworthy that the severe magnetic saturation in machine with a large saliency ratio can significantly narrow the difference between the d- and q-axis inductances and hence will cause larger $(\omega_s \pm 4\omega_e)$-order current harmonics with SVPWM technique. Although the initial phases of the $(2\omega_s \pm \omega_e)$-order current harmonics for SPWM technique are exactly the same as those for SVPWM, $-C'_{21}$ in Equation (3.45) is always slightly smaller than $-C_{21}$ in Equation (3.38) with the same modulation index M. Consequently, the SVPWM technique engenders larger amplitudes of the $(2\omega_s \pm \omega_e)$-order current harmonics within the second carrier frequency domain than the SPWM.

Furthermore, the associated acoustic noise originating from PMSM is normally proportional to the square of the corresponding current harmonic amplitude. Therefore, it is of particular interest to compare the root mean square values of the sideband current harmonics in the first and second carrier frequency domains. As the

$(2\omega_s \pm \omega_e)$-order current harmonics are the main components, it is obvious that harmonics of SPWM technique will be slightly smaller in the second carrier frequency domain than SVPWM components. Meanwhile, the $(\omega_s \pm 2\omega_e)$ and $(\omega_s \pm 4\omega_e)$-order current harmonics are the main components in the first carrier frequency domain, the corresponding root mean square value can be approximately derived as

$$\begin{cases} I_{\text{rms\_SV}_1} = \dfrac{U_{dc}\sqrt{(\sigma_1^2+\sigma_2^2)(C_{12}^2+C_{14}^2)+4\sigma_1\sigma_2 C_{12}C_{14}\cos 2\delta}}{4(\omega_s \pm 3\omega_e)} \\ I_{\text{rms\_SP}_1} = \dfrac{U_{dc}C'_{12}\sqrt{\sigma_1^2+\sigma_2^2}}{4(\omega_s \pm 3\omega_e)} \end{cases} \tag{3.49}$$

It can be obtained that

$$\begin{aligned} I_{\text{rms\_SV}_1} &\leq \frac{U_{dc}\sqrt{(\sigma_1^2+\sigma_2^2)(C_{12}^2+C_{14}^2)+4\sigma_1\sigma_2 C_{12}C_{14}}}{4(\omega_s \pm 3\omega_e)} \\ &\leq \frac{U_{dc}\sqrt{(\sigma_1^2+\sigma_2^2)(C_{12}^2+C_{14}^2+2C_{12}C_{14})}}{4(\omega_s \pm 3\omega_e)} < I_{\text{rms\_SP}_1} \end{aligned} \tag{3.50}$$

It clearly reveals that SPWM technique would always introduce larger harmonics in the first carrier frequency domain than SVPWM. Additionally, the power loss are also highly relevant to the root mean square values of different order sideband current harmonics.

The comprehensive experimental tests on the prototype I drive system with SPWM and SVPWM techniques under no-load condition at different speeds are carried out to validate the proposed analytical derivations. The actual experimental setup of the proposed testing systems is depicted in Figure A.2, and the prototype machine is driven with i_d=0 control strategy and carrier frequency of 4kHz. In order to experimentally validate the analytical models quantitatively, the amplitude variations of the main sideband current harmonics with different modulation indices are examined for the proposed prototype. The experimental tests of the prototype with different speeds from 60rpm to 720rpm under no-load condition are conducted to achieve various modulation indices. Both SPWM and SVPWM techniques are compared in the experimental drive system to validate the inequality relationship revealed in this subsection.

The resultant amplitudes of the main first and second sideband current harmonics, including $(\omega_s \pm 2\omega_e)$-, $(\omega_s \pm 4\omega_e)$- and $2(\omega_s \pm \omega_e)$-order components, together with the root mean square values of the current harmonics in the first carrier frequency domain, are compiled from the experimental results and compared with the analytical models in Figure.3.10. The figures demonstrate very close agreements between the analytical and experimental results for all the harmonics, and validate that the proposed analytical models can deliver reasonably accurate predictions with minimum computational requirement. Moreover, Figure 3.10(a) clearly shows the amplitudes of the $(\omega_s \pm 2\omega_e)$-order harmonics from SPWM technique are more significant than the components from SVPWM scheme while Figure 3.10(c) reveals that SVPWM technique produces slightly larger $(2\omega_s \pm \omega_e)$-order harmonics than SPWM components especially with high rotational speed. On the other hand, the saliency of

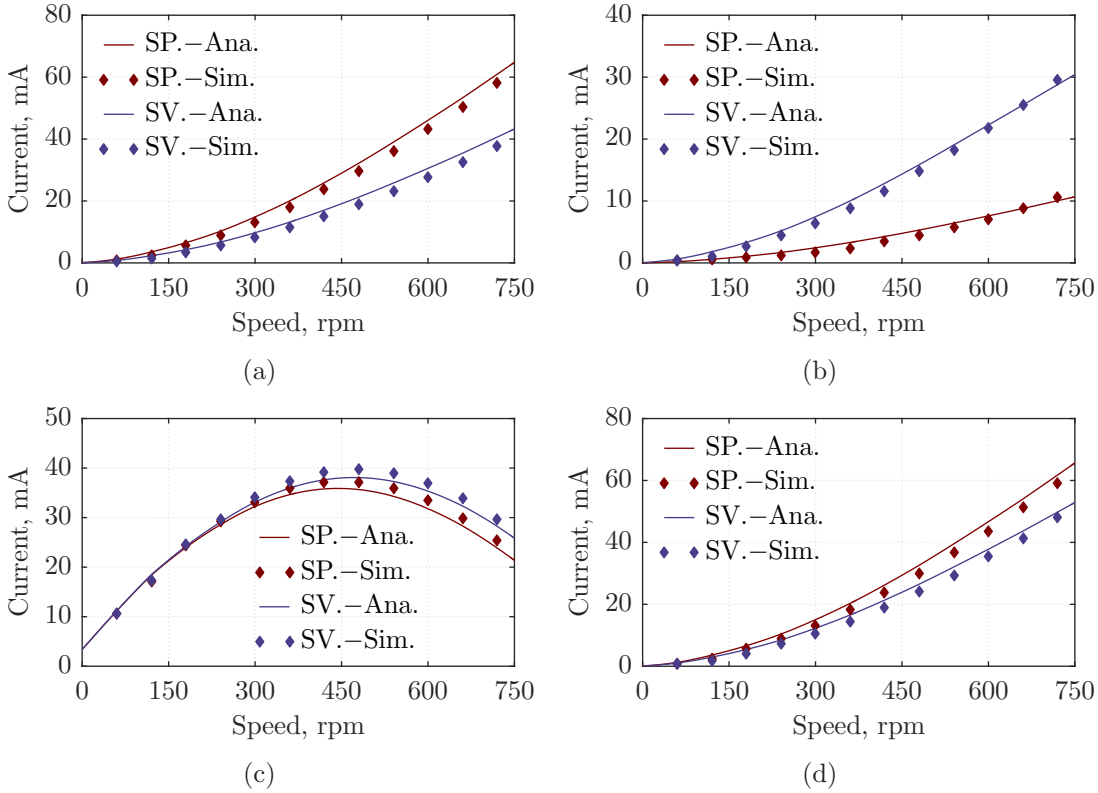

Figure 3.10: Sideband harmonics in no-load conditions with SPWM and SVPWM techniques: (a) $(\omega_s \pm 2\omega_e)$-order, (b) $(\omega_s \pm 4\omega_e)$-order, (c) $(2\omega_s \pm \omega_e)$-order, (d) the RMS values of first sideband current harmonics. (Ana. - Analytical model, Exp. - Experimental result, SP. - SPWM, SV. - SVPWM)

the prototype PMSM is somehow quite small despite the interior PM configuration. As a result, the $(\omega_s \pm 4\omega_e)$-order current harmonics from SVPWM technique are much more remarkable than the components from SPWM scheme, as illustrated in Figure 3.10(b). Finally, Figure 3.10(d) demonstrates that the SPWM technique delivers more severe overall first sideband current harmonics in the prototype than SVPWM. Overall, all the main sideband current harmonic component relationships between SPWM and SVPWM techniques discussed in this subsection have been firmly validated by the experimental results.

3.5 Improved Analytical Sideband Current Harmonic Modeling

The analytical models of the sideband current harmonics are developed based on the assumption of invariant inductances and completely decoupled d- and q-axis model. However, this hypothesis establishes on no magnetic saturation in the corresponding PMSMs so that the proposed analytical models are merely valid for PMSMs with surface-mounted and inset PM configurations. Nowadays, the interior PM

configuration has often been regarded as the preferred option for PMSM in order to increase both flux concentration and rotor saliency. As a result, both the PM induction torque and reluctance torque can be accordingly boosted and then harnessed to further improve the overall torque performance [141]. The proposed analytical models may still be applicable in such type of PMSM under light load conditions. However, the inherent features of such structure and the nonlinearity of ferromagnetic material inevitably bring about severe magnetic saturation and cross-coupling effects in the machine under large load conditions. These unavoidable effects will impose the nonlinear dependency of machine inductances on the armature current and rotor position. Moreover, the mutual inductance between d- and q-axis will hence appear, and all the synchronous inductances are no longer constants and depend on the magnetic state of the machine [142, 143]. Consequently, the direct implementation of the proposed analytical models can potentially introduce large errors to the corresponding predictions in interior PMSM drives with load conditions. Hence, analytical models of sideband current harmonics by incorporating the nonlinear factors are of particular importance for interior PMSMs with load conditions. This section aims to improve the existing analytical models for accurate sideband current harmonic predictions in PMSM drive systems with considerations of magnetic saturation and cross-coupling effects.

3.5.1 Sideband Current Harmonics in Synchronous Frame

The analytical models of the main first and second sideband voltage harmonics from Equation (3.19), (3.22) and (3.23) are independent from the electromagnetic parameters of PMSMs and hence can still be directly used for current evaluations. By taking into consideration the magnetic saturation and cross-coupling effects, the sideband voltage and current correlation in the rotor synchronous frame from Equation (3.26) can be updated and approximated as

$$\begin{cases} u_{d\_\omega_\mu} \approx j\omega_\mu (L_d i_{d\_\omega_\mu} + M_{dq} i_{q\_\omega_\mu}) \\ u_{q\_\omega_\mu} \approx j\omega_\mu (L_q i_{q\_\omega_\mu} + M_{dq} i_{d\_\omega_\mu}) \end{cases} \tag{3.51}$$

The d- and q-axis inductances and mutual inductance between d- and q-axis are all incremental components and normally current dependent, and they can be derived as

$$\begin{cases} L_d = \dfrac{\partial \psi_d (i_d, i_q)}{\partial i_d}, L_q = \dfrac{\partial \psi_q (i_d, i_q)}{\partial i_q} \\ M_{dq} = \dfrac{\partial \psi_d (i_d, i_q)}{\partial i_q} = \dfrac{\partial \psi_q (i_d, i_q)}{\partial i_d} \end{cases} \tag{3.52}$$

Generally, nonlinear FEA sweeping can be carried out with different d- and q-axis currents, and rotor positions in order to derive the corresponding d- and q-axis flux linkages. As a result, two resultant 4-D flux linkage tables can be translated into three 4-D incremental inductance tables by implementing numerical current-partial differential operations. Since the proposed analytical models generally predict the

sideband current harmonics of the machine under steady state conditions, three 3-D inductance tables suffice for the prediction. They can be obtained by taking average over the rotor positions. Normally, the mutual inductance can also be defined as

$$M_{dq} = \sigma_M \sqrt{L_d L_q} \tag{3.53}$$

By rearranging Equation (3.51), the model of sideband current harmonics can be improved as

$$i_{d\_\omega_\mu} = \frac{L_q u_{d\_\omega_\mu} - M_{dq} u_{q\_\omega_\mu}}{j\omega_\mu \left(L_d L_q - M_{dq}^2\right)}, \quad i_{q\_\omega_\mu} = \frac{L_d u_{q\_\omega_\mu} - M_{dq} u_{d\_\omega_\mu}}{j\omega_\mu \left(L_d L_q - M_{dq}^2\right)} \tag{3.54}$$

By substituting the voltage harmonic expressions from Equation (3.19), (3.22) and (3.23) into Equation (3.54), the corresponding main sideband current harmonics in first and second carrier frequency domains can be obtained as

$$\begin{cases} i_{d\_(\omega_s \pm 3\omega_e)} = \dfrac{U_{d\_13} \sin\left((\omega_s \pm 3\omega_e)t \pm \varphi_{d\_13}\right)}{(\omega_s \pm 3\omega_e)\left(1 - \sigma_M^2\right) L_d} \\ i_{q\_(\omega_s \pm 3\omega_e)} = \dfrac{\mp U_{q\_13} \cos\left((\omega_s \pm 3\omega_e)t \pm \varphi_{q\_13}\right)}{(\omega_s \pm 3\omega_e)\left(1 - \sigma_M^2\right) L_q} \end{cases} \tag{3.55}$$

$$\begin{cases} i_{d\_(2\omega_s)} = \dfrac{-U_{dc} C_{21} \left(L_q \sin\delta + M_{dq} \cos\delta\right) \sin(2\omega_s t)}{2\omega_s \left(1 - \sigma_M^2\right) L_d L_q} \\ i_{q\_(2\omega_s)} = \dfrac{U_{dc} C_{21} \left(L_d \cos\delta + M_{dq} \sin\delta\right) \sin(2\omega_s t)}{2\omega_s \left(1 - \sigma_M^2\right) L_d L_q} \end{cases} \tag{3.56}$$

$$\begin{cases} i_{d\_(2\omega_s \pm 6\omega_e)} = \dfrac{U_{d\_26} \sin\left((2\omega_s \pm 6\omega_e)t \pm \varphi_{d\_26}\right)}{(2\omega_s \pm 6\omega_e)\left(1 - \sigma_M^2\right) L_d} \\ i_{q\_(2\omega_s \pm 6\omega_e)} = \dfrac{\mp U_{q\_26} \cos\left((2\omega_s \pm 6\omega_e)t \pm \varphi_{q\_26}\right)}{(2\omega_s \pm 6\omega_e)\left(1 - \sigma_M^2\right) L_q} \end{cases} \tag{3.57}$$

As a result of the cross-coupling effect, the coefficients such as U_{d_13}, U_{q_13}, U_{d_26}, U_{q_26}, φ_{d_13}, φ_{q_13}, φ_{d_26} and φ_{q_26} here, are much more complex than the coefficients in Equation (3.20), (3.21), (3.24) and (3.25). The corresponding parameters can be updated as

$$\begin{cases} U_{d\_13} = \dfrac{U_{dc}}{2} \sqrt{C_{12}^2 + C_{14}^2 + 2C_{12}C_{14}\cos(2\delta) + C_{md\_13}} \\ U_{q\_13} = \dfrac{U_{dc}}{2} \sqrt{C_{12}^2 + C_{14}^2 - 2C_{12}C_{14}\cos(2\delta) + C_{mq\_13}} \end{cases} \tag{3.58}$$

$$\begin{cases} U_{d\_26} = \dfrac{U_{dc}}{2} \sqrt{C_{25}^2 + C_{27}^2 + 2C_{25}C_{27}\cos(2\delta) + C_{md\_26}} \\ U_{q\_26} = \dfrac{U_{dc}}{2} \sqrt{C_{25}^2 + C_{27}^2 - 2C_{25}C_{27}\cos(2\delta) + C_{mq\_26}} \end{cases} \tag{3.59}$$

$$\begin{cases} \cos\varphi_{d\_13} = \dfrac{(C_{12}+C_{14})\,(M_{dq}\sin\delta - L_q\cos\delta)}{\sqrt{L_q^2\,(C_{12}^2+C_{14}^2+2C_{12}C_{14}\cos(2\delta)+C_{md\_13})}} \\ \sin\varphi_{d\_13} = \dfrac{(C_{12}-C_{14})\,(M_{dq}\cos\delta + L_q\sin\delta)}{\sqrt{L_q^2\,(C_{12}^2+C_{14}^2+2C_{12}C_{14}\cos(2\delta)+C_{md\_13})}} \\ \cos\varphi_{q\_13} = \dfrac{(C_{12}-C_{14})\,(M_{dq}\sin\delta + L_d\cos\delta)}{\sqrt{L_d^2\,(C_{12}^2+C_{14}^2-2C_{12}C_{14}\cos(2\delta)+C_{mq\_13})}} \\ \sin\varphi_{q\_13} = \dfrac{(C_{12}+C_{14})\,(M_{dq}\cos\delta - L_d\sin\delta)}{\sqrt{L_d^2\,(C_{12}^2+C_{14}^2-2C_{12}C_{14}\cos(2\delta)+C_{mq\_13})}} \end{cases} \tag{3.60}$$

$$\begin{cases} \cos\varphi_{d\_26} = \dfrac{(C_{25}-C_{27})\,(L_q\sin\delta + M_{dq}\cos\delta)}{\sqrt{L_q^2\,(C_{25}^2+C_{27}^2+2C_{25}C_{27}\cos(2\delta)+C_{md\_26})}} \\ \sin\varphi_{d\_26} = \dfrac{(C_{25}+C_{27})\,(L_q\cos\delta - M_{dq}\sin\delta)}{\sqrt{L_q^2\,(C_{25}^2+C_{27}^2+2C_{25}C_{27}\cos(2\delta)+C_{md\_26})}} \\ \cos\varphi_{q\_26} = \dfrac{(C_{27}+C_{25})\,(M_{dq}\cos\delta - L_d\sin\delta)}{\sqrt{L_d^2\,(C_{25}^2+C_{27}^2-2C_{25}C_{27}\cos(2\delta)+C_{mq\_26})}} \\ \sin\varphi_{q\_26} = \dfrac{(C_{27}-C_{25})\,(M_{dq}\sin\delta + L_d\cos\delta)}{\sqrt{L_d^2\,(C_{25}^2+C_{27}^2-2C_{25}C_{27}\cos(2\delta)+C_{mq\_26})}} \end{cases} \tag{3.61}$$

in which

$$\begin{cases} C_{md\_13} = \dfrac{M_{dq}^2\,(C_{12}^2+C_{14}^2-2C_{12}C_{14}\cos(2\delta)) - 4C_{12}C_{14}M_{dq}L_q\sin(2\delta)}{L_q^2} \\ C_{mq\_13} = \dfrac{M_{dq}^2\,(C_{12}^2+C_{14}^2+2C_{12}C_{14}\cos(2\delta)) - 4C_{12}C_{14}M_{dq}L_d\sin(2\delta)}{L_d^2} \end{cases} \tag{3.62}$$

$$\begin{cases} C_{md\_26} = \dfrac{M_{dq}^2\,(C_{25}^2+C_{27}^2-2C_{25}C_{27}\cos(2\delta)) - 4C_{25}C_{27}M_{dq}L_q\sin(2\delta)}{L_q^2} \\ C_{mq\_26} = \dfrac{M_{dq}^2\,(C_{25}^2+C_{27}^2+2C_{25}C_{27}\cos(2\delta)) - 4C_{25}C_{27}M_{dq}L_d\sin(2\delta)}{L_d^2} \end{cases} \tag{3.63}$$

3.5.2 Sideband Current Harmonics in Stationary Frame

Likewise, the same order sideband current harmonics in the stator stationary frame can be derived by applying the inverse Park transformation. The respective amplitudes of those harmonics can be accordingly obtained as

$$\begin{cases} I_{s\_12} = \dfrac{U_{dc}\sqrt{\sigma_1^2C_{12}^2+\sigma_2^2C_{14}^2+2\sigma_1\sigma_2C_{12}C_{14}\cos(2\delta)+R_{12}}}{4(\omega_s\pm3\omega_e)\,(1-\sigma_M^2)} \\ I_{s\_14} = \dfrac{U_{dc}\sqrt{\sigma_2^2C_{12}^2+\sigma_1^2C_{14}^2+2\sigma_1\sigma_2C_{12}C_{14}\cos(2\delta)+R_{14}}}{4(\omega_s\pm3\omega_e)\,(1-\sigma_M^2)} \end{cases} \tag{3.64}$$

$$I_{s\_21} = -\frac{U_{dc}C_{21}}{4\omega_s\left(1-\sigma_M^2\right)}\sqrt{\frac{\sin^2\delta}{L_d^2}+\frac{\cos^2\delta}{L_q^2}+R_{21}} \tag{3.65}$$

$$\begin{cases} I_{s\_25} = \dfrac{U_{dc}\sqrt{\sigma_1^2C_{25}^2+\sigma_2^2C_{27}^2+2\sigma_1\sigma_2C_{25}C_{27}\cos(2\delta)+R_{25}}}{4(2\omega_s\pm 6\omega_e)\left(1-\sigma_M^2\right)} \\ I_{s\_27} = \dfrac{U_{dc}\sqrt{\sigma_2^2C_{25}^2+\sigma_1^2C_{27}^2+2\sigma_1\sigma_2C_{25}C_{27}\cos(2\delta)+R_{27}}}{4(2\omega_s\pm 6\omega_e)\left(1-\sigma_M^2\right)} \end{cases} \tag{3.66}$$

The coefficients, R_{12}, R_{14}, R_{21}, R_{25} and R_{27}, can be expressed as

$$\begin{cases} R_{12} = \dfrac{4\sigma_M^2C_{14}^2}{L_dL_q} - \dfrac{4\sigma_1M_{dq}C_{12}C_{14}}{L_dL_q}\sin(2\delta) \\ R_{14} = \dfrac{4\sigma_M^2C_{12}^2}{L_dL_q} - \dfrac{4\sigma_1M_{dq}C_{12}C_{14}}{L_dL_q}\sin(2\delta) \\ R_{21} = \dfrac{\sigma_M^2}{L_dL_q} + \left(\dfrac{1}{L_d}+\dfrac{1}{L_q}\right)\dfrac{M_{dq}}{L_dL_q}\sin(2\delta) \\ R_{25} = \dfrac{4\sigma_M^2C_{27}^2}{L_dL_q} - \dfrac{4\sigma_1M_{dq}C_{25}C_{27}}{L_dL_q}\sin(2\delta) \\ R_{27} = \dfrac{4\sigma_M^2C_{25}^2}{L_dL_q} - \dfrac{4\sigma_1M_{dq}C_{25}C_{27}}{L_dL_q}\sin(2\delta) \end{cases} \tag{3.67}$$

Moreover, the phases of those harmonics can also be derived accordingly with rather complex form. Normally, the phases of those sideband current harmonics are much less essential than their amplitudes. Without loss of generality, the complex analytical formulae of those phases are not provided.

3.5.3 Improvement Validation

Prototype I with interior PM rotor is employed in order to validate the accuracy improvements on the main sideband current harmonic predictions as it experiences rather severe magnetic saturation under load conditions. The nonlinear 2-D FEA models of prototype I are employed to obtain the corresponding incremental inductance parameters for the improved models in order to account for the magnetic saturation and cross-coupling effects under different operational conditions. Although the incremental inductance parameters are dependent on not only stator currents but also rotor positions, the variations for different rotor positions of prototype I are relatively small in practice. Without loss of generality, the flux linkage values are calculated with d-axis current ranged from -10A to 0A and q-axis current ranged from 0A to 16A at a fixed rotor position in order to minimize the computational effort significantly. This specific rotor position aligns the d-axis with one stator phase winding. Moreover, 50 steps are taken for both d- and q-axis currents so that the computational errors from the numerical partial differential operations can be minimized. The numerical partial differential operations based on Equation (3.52)

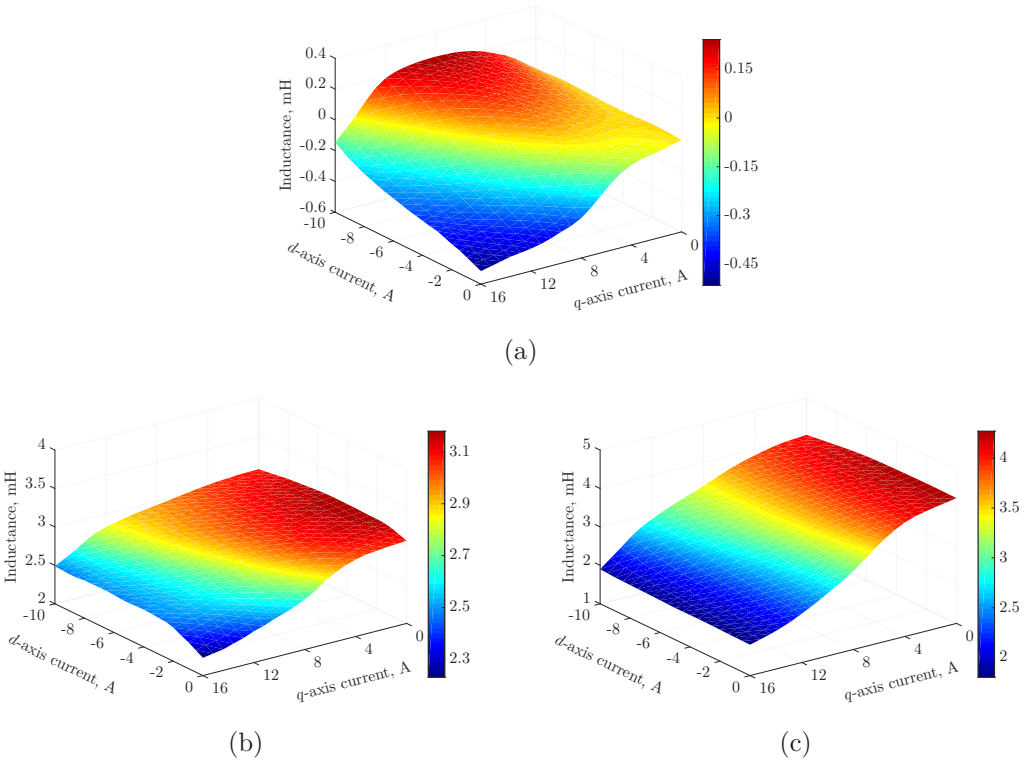

Figure 3.11: Incremental inductance values with different current excitations: (a) M_{dq}, (b) L_d, (c) L_q.

are applied to obtain three 3-D tables of the incremental inductances for prototype I. Those incremental inductance values under different d- and q-axis current excitations are plotted in Figure 3.11. Although the d- and q-axis flux vectors are orthogonal, the flux linkage cross-coupling and hence mutual inductance between d- and q-axis exists due to the core saturation, as shown in Figure 3.11(a). The figure reveals that the mutual component can reach up to the same order of magnitude with self-inductances especial with deeply saturated conditions. Moreover, it can be found from Figure 3.11(b) and 3.11(c) that the d- and q-axis inductances are highly dependent on the currents. The inductances, especially the q-axis component, decline remarkably as the q-axis current increases. On the other hand, they gradually increase along with the demagnetizing current as saturation level relieves accordingly. It implies that control strategy will have significant impact on the corresponding inductances as different current combinations can be involved for the same output torque.

With the corresponding d- and q-axis currents in torque-current characteristics curves from MTPA and $i_d = 0$ control strategies in Figure 2.4, the resultant torque-inductance curves can be compiled from Figure 3.11 and illustrated in Figure 3.12(a) and 3.12(b) respectively. It can be easily observed from Figure 3.12 that d- and q-axis incremental inductances declines as the output torque rises under both control schemes due to the aggravating magnetic saturation in prototype I. Since the demagnetizing currents generated by the MTPA control can prevent the prototype from magnetic saturation to some extent, the corresponding inductances for $i_d = 0$ control

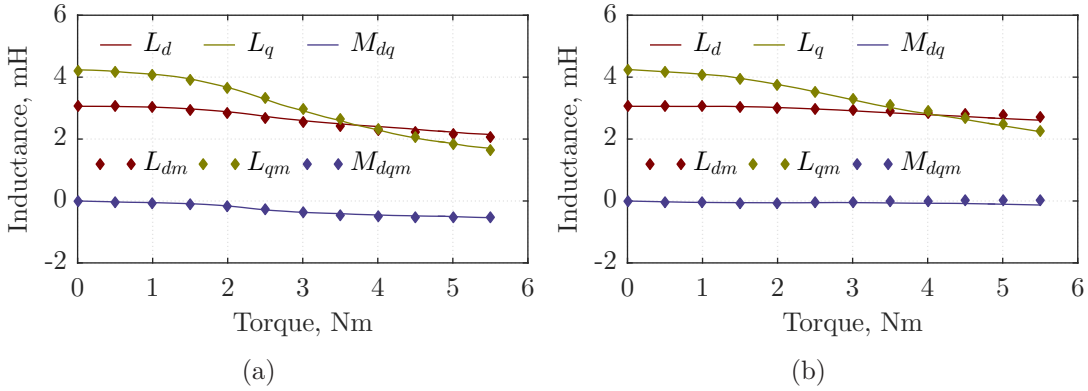

Figure 3.12: The incremental inductance parameters: (a) $i_d = 0$ vector control, (b) MTPA vector control. (L_d - d-axis inductance in phase A axis, L_{dm} - mean value of d-axis inductance, L_q - q-axis inductance in phase A axis, L_{qm} - mean value of q-axis inductance, M_{dq} - Mutual inductance in phase A axis, M_{dqm} - mean value of mutual inductance)

scheme decrease much faster than those for MTPA control. With the same reason, the cross-couple effect, which can be represented by the mutual inductance between d- and q-axis, barely occur under MTPA operations, but can reach quite noticeable level under $i_d = 0$ operations. Generally, $i_d = 0$ operations will result in smaller inductance parameters, which implies that more severe sideband current harmonics can be expected. Moreover, Figure 3.12 indicates that the d- and q-axis incremental inductances keeps nearly constant and the mutual inductance between d- and q-axis hardly exists for both control strategies with small load conditions. Hence, the analytical linear models is sufficient enough to deliver accurate predictions for those circumstances.

Furthermore, the inductances vary with the rotor position even with the same current vector by virtue of the permeance harmonic components contributing to the overall inductance. In order to validate the single-position method of inductance evaluation, Figure 3.12 also depicts the mean value of different positions, which shows some small differences between exist. However, the corresponding relative errors are well below 5% and very trivial in the prototype, so that they can be neglected. Normally, the proposed single-position method can deliver confident inductance predictions with minimum computational effort.

The improved analytical models change back into the exactly same forms as the linear models from Section 3.3 when the mutual inductance between d- and q-axis becomes zero. The variations of d- and q-axis incremental inductances and cross-coupling effects between d- and q-axis can be normally neglected in most PMSMs with light load conditions. Therefore, the experimental validations in Section 3.3 can also be employed to assert the accuracy of the improved analytical models for such cases. However, the neglect of magnetic saturation and cross coupling effects in the analytical linear models from Section 3.3 will be translated into large prediction errors in prototype I with large load conditions while the proposed improved models

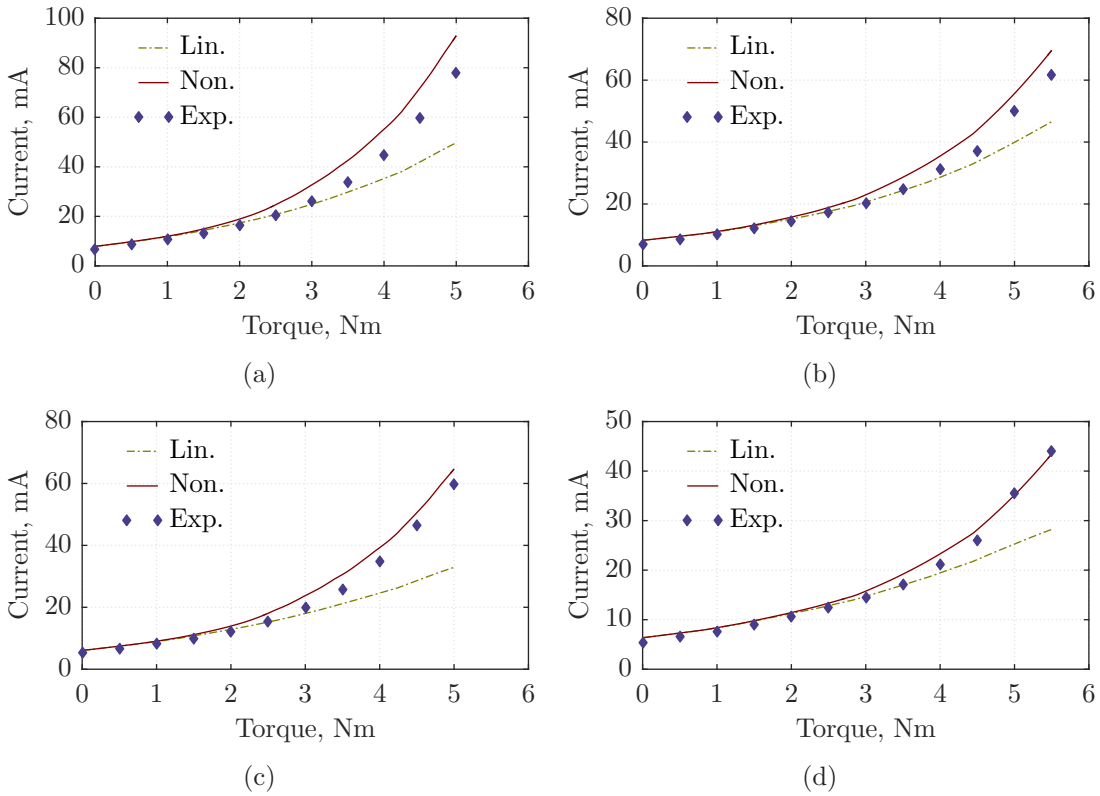

Figure 3.13: First sideband current harmonics validations: (a) $(\omega_s \pm 2\omega_e)$ components with $i_d = 0$ control, (b) $(\omega_s \pm 2\omega_e)$ components with MTPA control, (c) $(\omega_s \pm 4\omega_e)$ components with $i_d = 0$ control, (d) $(\omega_s \pm 4\omega_e)$ components with MTPA control. (Lin. - Linear analytical model, Non. - Nonlinear analytical model, Exp. - Experimental result)

can effectively compensate such discrepancies. Therefore, the experimental tests on PMSM drive of prototype I under torque load ranged from 0N·m to 5N·m with step of 0.5N·m at a constant rotational speed of 300rpm are carried out to quantitatively validate the actual improvement from the proposed models. Both MTPA and $i_d = 0$ control strategies are implemented during the experimental tests. The corresponding current waveforms are captured so that the amplitudes of the main first and second sideband current harmonics can be compiled and compared with the results from the linear and improved nonlinear analytical models in Figure 3.13 and 3.14 respectively.

The main sideband current harmonics in the first and second carrier frequency domains of prototype I with MTPA control scheme are heavily influenced by the torque load due to the aggravating magnetic saturation. Consequently, large deviations between the results from the linear analytical models proposed in Section 3.3 and experimental tests are expected and revealed in Figure 3.13(b), 3.13(d), 3.14(b), 3.14(d) and 3.14(f), especially under large load conditions. The incremental inductance parameters in the linear analytical models are independent from the load condition and hence constant. As a result, they are normally greater than the actual inductances so that the linear analytical models substantially underestimate

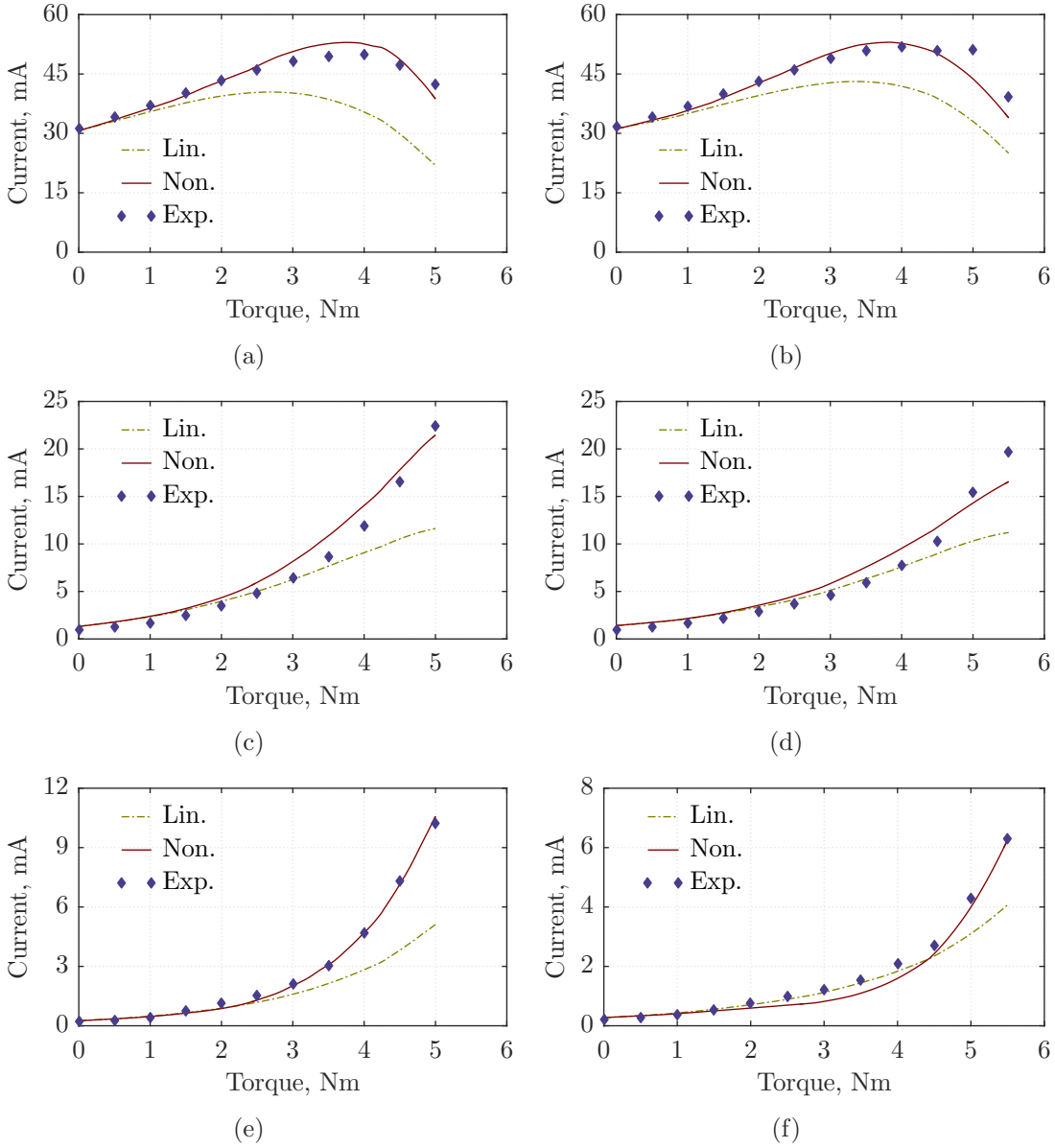

Figure 3.14: Second sideband current harmonics validation: (a) $(2\omega_s \pm \omega_e)$ components with $i_d = 0$ control, (b) $(2\omega_s \pm \omega_e)$ components with MTPA control, (c) $(2\omega_s \pm 5\omega_e)$ components with $i_d = 0$ control, (d) $(2\omega_s \pm 5\omega_e)$ components with MTPA control, (e) $(2\omega_s \pm 7\omega_e)$ components with $i_d = 0$ control, (f) $(2\omega_s \pm 7\omega_e)$ components with MTPA control. (Lin. - Linear analytical model, Non. - Nonlinear analytical model, Exp. - Experimental result)

the sideband current harmonics. On the other hand, the figures reveal that the discrepancies between the results from the proposed nonlinear models and experimental tests have been effectively narrowed for all the main first and second order sideband current harmonics. The remaining small differences are primarily caused by the errors on the incremental inductance parameter evaluations as well as the experimental measurement errors. Generally, B-H characteristics of the lamination material in FEA models cover only up to 2.0T, and empirical formula based on curve

fitting is employed to approximate the region beyond that value. The magnetic flux density of pole shoes of the prototype interior PMSM under heavy load conditions can well exceed that value, thus potential estimation errors can be expected. In addition, the influences of the end windings and end flux leakages are not considered in the 2-D FEA models employed for incremental inductance predictions. On the other hand, the mechanical transmission brings practically unmeasurable friction torque, which cannot be accurately factored in the experimental results. By taking into account all those factors and allowing for errors due to instrumentation, the agreements between the improved analytical and experimental results are considered satisfactory. On the whole, the prediction accuracy has been significantly ameliorated by the proposed improved models over their linear counterparts.

Furthermore, more distinct errors between the results from linear analytical models and experimental tests occurs in prototype I under heavy load conditions with $i_d = 0$ control strategy, for all five sideband current harmonics as demonstrated in Figure 3.13(a), 3.13(c), 3.14(a), 3.14(c) and 3.14(e). This is due to the more severe decline on the incremental inductances and extra influences from the cross-coupling effects from prototype I with $i_d = 0$ control scheme. Consequently, the $(\omega_s \pm 2\omega_e)$-, $(\omega_s \pm 4\omega_e)$-, $(2\omega_s \pm 5\omega_e)$- and $(2\omega_s \pm 7\omega_e)$-order sideband current harmonics are much larger than the MTPA control counterparts under the same load conditions, as expected. However, the amplitudes of the $(2\omega_s \pm \omega_e)$-orders are somewhat in very similar level for both control algorithms. As the sharp current incline under heavy load conditions can result in a large winding voltage drop, the associated modulation index will be significantly increased. On the other side, the $(2\omega_s \pm \omega_e)$-order harmonics will start to decrease as the modulation index reaches up to around 0.6. When the modulation index exceeds that particular value under heavy load conditions, the $(2\omega_s \pm \omega_e)$-order harmonics will decline rapidly and the impacts of the magnetic saturation and cross-coupling effects will gradually diminish in this particular case. Meanwhile, it can be observed from Figure 3.12 that the incremental inductance parameters of prototype I with both control algorithms are quite close under the conditions of light output torque. Moreover, the slightly smaller inductance values with $i_d = 0$ control scheme, together with mildly larger power angles with MTPA control strategy, jointly make the $(2\omega_s \pm \omega_e)$-order sideband components from both control methods have very close amplitudes. The resultant errors between the results from the improved model and experimental tests are somewhat satisfactory, particularly the trend of all major sideband current harmonics under extreme conditions have been accurately reflected.

3.6 Summary

This chapter focused on the analytical investigation of main sideband harmonics in PMSM drive with SVPWM technique in first and second frequency domains. The unequal self and mutual phase inductances bring about complex coupling effect and make the direct derivation of phase sideband current harmonics unattainable. However, such coupling effect can be eliminated by converting the stator stationary frame into rotor synchronous frame through a Park transformation. Thus the

analytical models of sideband current harmonics in the rotor synchronous frame can be derived. In succession, the resultant analytical models can be accordingly turned into the stator stationary frame by the inverse Park transformation. Besides the first and second sideband components, this procedure is also applicable to derive higher order components. Moreover, it can also be employed investigate the sideband harmonics for other electrical machine drive systems with different PWM schemes. Comparison and discussion of the main sideband current harmonics in a PMSM drive between SVPWM and SPWM techniques are carried out based on the corresponding analytical models and experimental validations. It is revealed that the SVPWM technique produces lower overall first sideband current harmonics but higher second sideband components than the SPWM scheme.

Furthermore, the analytical models are extended and improved to take into account the impacts of magnetic saturation and cross-coupling effect on the prediction of sideband current harmonics. Essentially, both the original linear and improved nonlinear models can deliver accurate predictions for PMSM drive with negligible magnetic saturation. However, the improved nonlinear analytical models can significantly improve the prediction accuracy for PMSM drive with severe magnetic saturation, and the linear method will result in a large underestimation and hence fail to provide credible predictions.

The corresponding experimental platforms are employed to validate the proposed models:

- Prototype II, an surface-inset PMSM, together with $i_d = 0$ vector control and SVPWM technique is employed to carry out the experiments for the linear analytical sideband current model validation;
- Prototype I, an interior PMSM, driven by $i_d = 0$ control strategy with both SPWM and SVPWM technique is employed to validate the analytical comparison and discussion.
- Prototype I, driven by $i_d = 0$ and MTPA control schemes with SVPWM technique, is also involved for the experimental validations of the improved nonlinear sideband current models;

The new contributions in this area include:

- New analytical models of sideband current harmonics introduced by SVPWM technique are proposed in closed-form for PMSM drive system in Section 3.3;
- With consideration of magnetic saturation and cross-coupling effect on the sideband current, the analytical models are extended to predict the sideband harmonics of interior PMSM drive under large load conditions in Section 3.5;
- Both the linear and nonlinear analytical sideband current models are presented for PMSM drive system with SPWM scheme in Chapter C.

Besides delivering accurate predictions, the proposed analytical sideband current models provide insightful relationship on the factors of the sideband current harmonics, such as carrier frequency, modulation index, torque angle, inductances and cross-coupling coefficient. Meanwhile, it can offer intuitive information to promptly assess the effectiveness of different techniques on associated loss, torque pulsation and electromagnetic acoustic noise reduction. Moreover, it can be employed to further study the corresponding sideband magnetic flux density, sideband ERFD and relevant acoustic noise of stator system.

Chapter 4

Air-Gap Magnetic Field Components in PMSM

As aforementioned, the ERFD components are one of the main sources of vibration and acoustic noise in radial-flux PMSMs. According to Maxwell stress tensor theory, such ERFD components are induced by the interactions of various magnetic field components in the air gap. The air-gap magnetic field flux density components in the machine are mainly introduced by the interactions between different MMF sources and permeance components [56]. It is of particular importance to study the characteristics of magnetic fields including the fundamental, interharmonic and phase-belt components. Nowadays, FEA tools are widely employed to carry out the magnetic field analysis for PMSMs with high accuracy. Although such a method can deliver confident numerical predictions of magnetic field, it is unable to directly give much information of the underlying magnetic mechanism. Therefore, it is essential to study the main important magnetic field components analytically so that the correlations between the machine parameters and magnetic field components hence associated ERFD components can be effectively revealed. Moreover, such an analytical model can also offer an insightful revelation of the relationship between the fundamental and interharmonic components. As a consequence, this chapter mainly concentrates on the analytical investigations of the air-gap magnetic field components in PMSMs with particular emphasis on the interior PM configuration. A new and comprehensive model to analytically predict the PM magnetic field components in interior PMSMs is developed based on the existing research. In addition, a novel permeance model is analytically elaborated to intuitively manifest the complex magnetic field phenomenon inside such machines. Finally, the analytical models of the armature-reaction interharmonic components and the sideband harmonics are further derived based on the new permeance model. The proposed analytical models are comprehensively validated by corresponding FEA results throughout the chapter.

4.1 The Universal Magnetic Model in PMSM

Based on the MMF source, the air-gap magnetic field flux density can be divided into two main categories: PM induced and armature-reaction components. With the different armature current components, usually the latter one can be further subdivided into fundamental, phase-belt harmonic and sideband harmonic components. They are introduced by the fundamental phase current, phase-belt current harmonic and sideband phase current components respectively. All the armature-reaction MMF components will interact with the air-gap permeance to produce corresponding air-gap magnetic field flux density components with different spatial and temporal orders.

4.1.1 PM Air-Gap Magnetic Field

Normally, The rotational direction of the fundamental, the p^{th} spatial order magnetic field component is defined as positive. As a result, the MMF components provided by PMs in the machine can be expressed as

$$f_r(\theta_m, t) = \sum_{\kappa_1} F_{r\_\upsilon_1} \cos(\kappa_1 p\theta_m - \kappa_1 p\omega_r t) \tag{4.1}$$

where,

$$\upsilon_1 = \kappa_1 p, \quad \kappa_1 = 2k+1, \quad k = 0, 1, 2, \cdots \tag{4.2}$$

It can be directly noticed that the spatial and temporal orders are identical for each PM MMF component. As the spatial and temporal orders are the key parameters for air-gap magnetic field components and their associated ERFD components. They are normally employed to categorize the items for investigation. It can also be inspected from Equation (4.1) that the temporal order number is based on mechanical frequency. It is quite common to express the temporal order related to electrical frequency. Therefore, Equation (4.1) can be rewritten as

$$f_r(\theta_m, t) = \sum_{\kappa_1} F_{r\_\upsilon_1} \cos(\kappa_1 p\theta_m - \kappa_1 \omega_e t) \tag{4.3}$$

By taking into account the slot opening and rotor saliency effects, the air-gap permeance distribution in the machine can be presented as

$$\lambda(\theta_m, t) = \Lambda_0 \cdot \bar{\lambda}_r(\theta_m, t) \cdot \bar{\lambda}_s(\theta_m, t) \tag{4.4}$$

where

$$\begin{cases} \bar{\lambda}_r(\theta_m, t) = 1 + \sum_{n_1=1}^{\infty} \bar{\Lambda}_{2n_1} \cos\left(2n_1 p\theta_m - 2n_1\omega_e t\right) \\ \bar{\lambda}_s(\theta_m, t) = 1 + \sum_{n_2=1}^{\infty} \bar{\Lambda}_{n_2 Z} \cos\left(n_2 Z\theta_m\right) \end{cases} \tag{4.5}$$

where Λ_0 is the mean value of air-gap permeance, while $\bar{\Lambda}_{2n_1}$ and $\bar{\Lambda}_{n_2Z}$ are the relative permeance components introduced by the rotor saliency and slot opening respectively. The PM air-gap magnetic field can be expressed as

$$b_r(\theta_m, t) = f_r(\theta_m, t) \cdot \lambda(\theta_m, t) \tag{4.6}$$

By substituting Equation (4.3) and (4.4) into Equation (4.6), all the PM air-gap magnetic field components can be obtained with corresponding spatial and temporal orders, which are listed in Table 4.1. Normally, the fundamental component expressed as $\kappa_1 = 1$ of item 1 in Table 4.1 is the main component as it is the primary contributor of electromagnetic torque in the machine, while other low orders of items 1, 2 and 3 are the main air-gap magnetic field harmonic components. The fourth item, together with the high orders of items 1, 2 and 3, are usually very small, and hence can be neglected.

Table 4.1: PM Air-Gap Magnetic Field Components

No.	Order	Frequency	Amplitude
1	$\kappa_1 p$	$\kappa_1\omega_e$	$F_{r\_v_1}\Lambda_0$
2	$\kappa_1 p \pm n_2 Z$	$\kappa_1\omega_e$	$F_{r\_v_1}\Lambda_0\bar{\Lambda}_{n_2Z}/2$
3	$(2n_1 \pm \kappa_1)p$	$(2n_1 \pm \kappa_1)\omega_e$	$F_{r\_v_1}\Lambda_0\bar{\Lambda}_{2n_1}/2$
4	$(2n_1 \pm \kappa_1)p \pm n_2 Z$	$(2n_1 \pm \kappa_1)\omega_e$	$F_{r\_v_1}\Lambda_0\bar{\Lambda}_{2n_1}\bar{\Lambda}_{n_2Z}/4$

It can be noticed that the sign $'\pm'$ is involved in the items from Table 4.1. It will be employed frequently together with sign $'\mp'$ in current, magnetic field components and ERFD components later. Generally, they are with one-to-one correspondence. For instance, the spatial order of $(2n_1+\kappa_1)p$ in the third item has only $(2n_1+\kappa_1)\omega_e$ temporal order, while $(2n_1-\kappa_1)p$ spatial order corresponds to $(2n_1-\kappa_1)\omega_e$ temporal order. However, the $'\pm'$ at front of n_2Z in Table 4.1 are independent. That means both spatial components are with the same temporal order. In second item, the spatial order of $\kappa_1\omega_e$ components can be either $(\kappa_1 p + n_2 Z)$ or $(\kappa_1 p - n_2 Z)$. This rule will be adopted in Table 4.2 to Table 4.4 as well.

4.1.2 Fundamental Armature-Reaction Air-Gap Magnetic Field

Generally, the fundamental phase current in three-phase PMSMs can be written as

$$\begin{cases} i_a(t) = I_s \cos\left(\omega_e t + \varphi_s\right) \\ i_b(t) = I_s \cos\left(\omega_e t - \dfrac{2\pi}{3} + \varphi_s\right) \\ i_c(t) = I_s \cos\left(\omega_e t - \dfrac{4\pi}{3} + \varphi_s\right) \end{cases} \tag{4.7}$$

The initial phase of current is mainly determined by the electromagnetic torque and control strategy. It can be normally expressed in the form of d- and q-axis currents as

$$\varphi_s = \frac{\pi}{2} - \arctan\frac{i_d}{i_q} \tag{4.8}$$

Consequently, the MMF components of the fundamental armature-reaction current can be presented as

$$f_s(\theta_m, t) = \sum_{\kappa_2} F_{s\_\upsilon_2} \cos(\kappa_2 p\theta_m - \omega_e t - \varphi_s) \tag{4.9}$$

where,

$$F_{s\_\upsilon_2} = \frac{3NK_{w\upsilon_2}}{\upsilon_2 \pi} I_s, \quad \upsilon_2 = |\kappa_2|\, p \tag{4.10}$$

κ_2 is the spatial order and highly dependent on the winding arrangement. For the integral-slot configuration, it can be expressed as

$$\kappa_2 = \begin{cases} 3k+1, & \text{for single layer winding} \\ 6k+1, & \text{for double layer winding} \end{cases} \tag{4.11}$$

where $k = 0, \pm1, \pm2, \cdots$. While for the FSCW configuration, κ_2 can be written as

$$\kappa_2 = \begin{cases} \dfrac{3k+1}{p_0}, & Z_0 \text{ is odd} \\ \dfrac{6k+1}{p_0}, & Z_0 \text{ is even} \end{cases} \tag{4.12}$$

where

$$p_0 = \frac{p}{t_0}, \quad Z_0 = \frac{Z}{t_0}, \quad t_0 = \gcd(Z, p) \tag{4.13}$$

It is noteworthy that the FSCW PMSMs with both odd and even Z_0 can be arranged with double-layer windings while only the machines with even Z_0 can facilitate single-layer windings. It can be inspected from Equation (4.11) and (4.12) that the spatial order κ_2 can be negative. That implies opposite rotational directions of the MMF components. The fundamental component $\kappa_2 = 1$ in Equation (4.12) can be negative as well. For such cases, all the signs of the corresponding spatial order items need to be reversed due to the assumption of positive fundamental rotational direction.

In integra-slot and fractional-slot machines with the distributed winding configuration, the fundamental MMF is normally the predominant component. While there can be abundant MMF interharmonics apart from the fundamental component in the FSCW PMSMs. The slot harmonic components can have significant amplitudes based on Equation (4.10) due to the large winding coefficient with the same value as fundamental component, typically the $(p-Z)^{th}$ spatial order harmonic in FSCW PMSMs. Additionally, there can be significant low order MMF components associated with a small value υ_2 such as t_0^{th} or $-t_0^{th}$ order harmonic in single-layer winding machines.

It should be noted that the frequencies of all fundamental armature-reaction MMF harmonic components are ω_e, different from the PM magnetic fields. It is determined by the current frequency and independent from the spatial orders. Furthermore, $F_{s\_\upsilon_2}$ can be negative as the corresponding winding coefficient can be negative.

Table 4.2: Fundamental Armature-Reaction Magnetic Field Components

No.	Order	Frequency	Amplitude
1	$\kappa_2 p$	ω_e	$F_{s\_\upsilon_2}\Lambda_0$
2	$\kappa_2 p \pm n_2 Z$	ω_e	$F_{s\_\upsilon_2}\Lambda_0\bar{\Lambda}_{n_2 Z}/2$
3	$(2n_1 \pm \kappa_2)p$	$(2n_1 \pm 1)\omega_e$	$F_{s\_\upsilon_2}\Lambda_0\bar{\Lambda}_{2n_1}/2$
4	$(2n_1 \pm \kappa_2)p \pm n_2 Z$	$(2n_1 \pm 1)\omega_e$	$F_{s\_\upsilon_2}\Lambda_0\bar{\Lambda}_{2n_1}\bar{\Lambda}_{n_2 Z}/4$

Similar to PM air-gap magnetic field, the fundamental armature-reaction air-gap magnetic flux density components can be derived by

$$b_s(\theta_m, t) = f_s(\theta_m, t) \cdot \lambda(\theta_m, t) \tag{4.14}$$

All the resultant fundamental armature-reaction air-gap magnetic field components are listed in Table 4.2. The fundamental armature-reaction air-gap magnetic field can be much more complex than the PM induced magnetic field in FSCW PMSMs due to the abundance of interharmonics.

4.1.3 Phase-Belt Armature-Reaction Air-Gap Magnetic Field

There are inevitable phase-belt harmonic components in the phase current even with an ideal three-phase sinusoidal voltage source due to the existence of high order components in the back EMF of PMSMs. Additionally, the torque pulsations, which are introduced by the interactions between the back EMF and current harmonic components, together with cogging torque, can produce speed fluctuation in PMSM drive. As a result from the speed control, the phase-belt current harmonic components can also be introduced by the controller. In general, the ν^{th} order phase-belt current harmonic component can be expressed as

$$\begin{cases} i_{a\nu}(t) = I_{s\nu}\cos\left(\nu\omega_e t + \varphi_\nu\right) \\ i_{b\nu}(t) = I_{s\nu}\cos\left(\nu\omega_e t - \dfrac{2\nu\pi}{3} + \varphi_\nu\right) \\ i_{c\nu}(t) = I_{s\nu}\cos\left(\nu\omega_e t - \dfrac{4\nu\pi}{3} + \varphi_\nu\right) \end{cases} \tag{4.15}$$

where,

$$\nu = \pm 6k + 1, \quad k = 1, 2, \cdots \tag{4.16}$$

The resultant MMF components and corresponding air-gap magnetic field components can be presented as

$$\begin{cases} f_\nu(\theta_m, t) = \sum_{\kappa_3} F_{\upsilon_3 \nu} \cos(\kappa_3 p \theta_m - \nu \omega_e t - \varphi_\nu) \\ b_\nu(\theta_m, t) = \sum_{\nu} f_\nu(\theta_m, t) \cdot \lambda(\theta_m, t) \end{cases} \tag{4.17}$$

where,

$$F_{\upsilon_3 \nu} = \frac{3NK_{w\upsilon_3}}{\pi \upsilon_3} I_{s\nu}, \quad \upsilon_3 = |\kappa_3| \, p \tag{4.18}$$

while κ_3 is with the same definition of κ_2. Similarly, the phase-belt armature-reaction air-gap magnetic field components are derived and presented in Table 4.3.

Table 4.3: Phase-Belt Armature-Reaction Air-Gap Magnetic Field Components

No.	Order	Frequency	Amplitude
1	$\kappa_3 p$	$\nu\omega_e$	$F_{\upsilon_3 \nu}\Lambda_0$
2	$\kappa_3 p \pm n_2 Z$	$\nu\omega_e$	$F_{\upsilon_3 \nu}\Lambda_0\bar{\Lambda}_{n_2 Z}/2$
3	$(2n_1 \pm \kappa_3)p$	$(2n_1 \pm \nu)\omega_e$	$F_{\upsilon_3 \nu}\Lambda_0\bar{\Lambda}_{2n_1}/2$
4	$(2n_1 \pm \kappa_3)p \pm n_2 Z$	$(2n_1 \pm \nu)\omega_e$	$F_{\upsilon_3 \nu}\Lambda_0\bar{\Lambda}_{2n_1}\bar{\Lambda}_{n_2 Z}/4$

4.1.4 Sideband Armature-Reaction Air-Gap Magnetic Field

The modern PMSM drive is normally powered by VSI with various PWM techniques to achieve great performances. As described in Chapter 3, the PWM schemes will inevitably produce sideband armature current harmonic components in the drive. Such sideband current harmonic components will also produce corresponding sideband armature-reaction air-gap magnetic field components. The frequencies of the sideband current harmonic components can be expressed as $(m_1\omega_s \pm m_2\omega_e)$. Thereinto, m_2 and m_1 are highly dependent, and the relationship between can be expressed as

$$m_2 = \begin{cases} 6k+2, & m_1 \text{ is odd} \\ 6k+1, & m_1 \text{ is even} \end{cases} \tag{4.19}$$

where $k = 0, \pm1, \pm2, \cdots$. Furthermore, the initial phases of $(m_1\omega_s + m_2\omega_e)$ and $(m_1\omega_s - m_2\omega_e)$-order sideband current harmonic components are always opposite. Consequently, the sideband armature-reaction current harmonic components can be written as

$$\begin{cases} i_{a\mu}(t) = I_{s\mu} \cos\left((m_1\omega_s \pm m_2\omega_e)t \pm \varphi_\mu\right) \\ i_{b\mu}(t) = I_{s\mu} \cos\left((m_1\omega_s \pm m_2\omega_e)t \mp \dfrac{2m_2\pi}{3} \pm \varphi_\mu\right) \\ i_{c\mu}(t) = I_{s\mu} \cos\left((m_1\omega_s \pm m_2\omega_e)t \mp \dfrac{4m_2\pi}{3} \pm \varphi_\mu\right) \end{cases} \tag{4.20}$$

The resultant corresponding MMF components can be derived as

$$f_\mu(\theta_m,t)=\begin{cases}\sum\limits_{\kappa_4} F_{\upsilon_4\_\mu}\cos(\kappa_4 p\theta_m \pm (m_1\omega_s \pm m_2\omega_e)t+\varphi_\mu), & m_1 \text{ is odd}\\ \sum\limits_{\kappa_4} F_{\upsilon_4\_\mu}\cos(\kappa_4 p\theta_m \mp (m_1\omega_s \pm m_2\omega_e)t-\varphi_\mu), & m_1 \text{ is even}\end{cases} \tag{4.21}$$

where κ_4 is of the same definition to κ_2. $F_{\upsilon_4\_\mu}$ is given by

$$F_{\upsilon_4\_\mu}=\frac{3NK_{w\upsilon_4}}{\pi\upsilon_4}I_{s\mu},\quad \upsilon_4=|\kappa_4|\,p \tag{4.22}$$

As a result, the expression of sideband armature-reaction air-gap magnetic field components can be obtained as

Table 4.4: Sideband Armature-Reaction Air-Gap Magnetic Field Components

No.	Order	Frequency	Amplitude
1	$\kappa_4 p$	ω_μ	$F_{\upsilon_4\_\mu}\Lambda_0$
2	$\kappa_4 p \pm n_2 Z$	ω_μ	$F_{\upsilon_4\_\mu}\Lambda_0\bar{\Lambda}_{n_2Z}/2$
3	$(2n_1 \pm \kappa_4)p$	$2n_1\omega_e \pm \omega_\mu$	$F_{\upsilon_4\_\mu}\Lambda_0\bar{\Lambda}_{2n_1}/2$
4	$(2n_1 \pm \kappa_4)p \pm n_2 Z$	$2n_1\omega_e \pm \omega_\mu$	$F_{\upsilon_4\_\mu}\Lambda_0\bar{\Lambda}_{2n_1}\bar{\Lambda}_{n_2Z}/4$

$$b_\mu(\theta_m,t)=\sum_\mu f_\mu(\theta_m,t)\cdot\lambda(\theta_m,t) \tag{4.23}$$

All the sideband armature-reaction air-gap magnetic field components are derived and given in Table 4.4. ω_μ is defined by

$$\omega_\mu=\begin{cases}\mp m_1\omega_s - m_2\omega_e, & m_1 \text{ is odd}\\ \pm m_1\omega_s + m_2\omega_e, & m_1 \text{ is even}\end{cases} \tag{4.24}$$

There can be some other armature-reaction current harmonic components when some special control techniques such as the harmonic current injection in sensorless control are implemented in PMSM drives. Without loss of generality, the corresponding MMF and air-gap magnetic field harmonic components can be analyzed in the same way. Moreover, the air-gap magnetic field components induced by the stator slot permeance Λ_{n_2Z} in Table 4.1 to Table 4.4 will not be further discussed as the slot effects on the ERFD components are included in the stator tooth modulation model in Chapter 5. Consequently, the investigation on air-gap magnetic field will mainly concentrated on the first and third items in those tables.

4.2 PM Air-Gap Magnetic Field Characteristics

The open-circuit magnetic field flux density distribution in the air gap is one of the most important characteristics in PMSMs. The fundamental PM air-gap magnetic

field component largely determines the overall performance of the machine. In addition, the cogging torque and phase back EMF harmonic components, which are the preliminary indicators of torque ripple in the machine, can be directly calculated from the PM air-gap magnetic field. Hence, it is always favorable to evaluate the PM air-gap magnetic field flux density distribution promptly and accurately throughout optimization, design and analysis stage of PMSMs. The recent advance of cost-effective computer systems with high-fidelity motor design and analysis tools has prompted the FEA as the main method for PM air-gap magnetic field predictions. Although the FEA method can provide very accurate evaluations, it normally fails to deliver insightful revelation of the influences of the machine geometric parameters on the PM air-gap magnetic field characteristics. On the other side, the analytical method can be employed to evaluate the open-circuit air-gap flux density distribution in PMSM rapidly and reveal the intuitive correlations. The closed-form analytical solution of the open-circuit air-gap flux density distribution can be easily obtained by directly solving Laplacian-Poissonian equations for surface-mounted [144] and surface-inset [145] PMSMs due to their rather simple rotor magnetic structures. In fact, there has been an abundance of analytical investigations on PM air-gap magnetic field characteristics in such machines. However, the interior PM configuration will exhibit significant leakage magnetic flux and magnetic saturation in the rotor flux bridges. Such features result in practical issues for closed-form analytical methods to accurately predict the open-circuit air-gap flux density distribution in interior PMSMs. The analytical models for PM flux linkage and stator inductances are proposed to evaluate the electromagnetic performance of interior PMSMs [146, 147], but the methods only consider the fundamental components of the air-gap magnetic field. While a saturating lumped-parameter magnetic equivalent circuit model is developed to determine the parameters and hence performance of such machines by taking into account the magnetic flux leakage and iron saturation [148]. However, these analytical methods cannot give exact analytical solution for PM air-gap magnetic field characteristics in the machine. Therefore, a closed-form analytical prediction of the PM air-gap flux density distribution has been attempted in interior PMSM with particular rotor geometry by employing space harmonic analysis and conformal transformation technique [149]. However, the leakage flux in the rotor flux bridges has not been specifically detailed. Furthermore, simple yet efficient methods based on lumped-parameter magnetic equivalent circuit models are proposed to analytically derive the open-circuit air-gap magnetic field distribution in the machine with one-layer [150] and multi-layer [151] configurations. The methods neglect the flux density variations over the rotor magnetic flux leakage path and therefore introduce additional errors in the predictions. Such a method is further developed to cope with inconstant air-gap length and saturation level variation in salient-pole interior PM synchronous generator [152].

4.2.1 Analytical Model of PM Air-Gap Magnetic Field

Due to the existence of PMs and saliency in the rotor, PMSMs with interior PM configuration can harness both PM reaction torque and reluctance torque to enhance

the overall performance. Hence, interior PMSM prevails and picks up momentum in various critical industrial applications. Although a nonlinear electromagnetic FEA method can accurately obtain the open-circuit air-gap flux density distribution in such machine with arbitrary rotor configuration, it is somewhat too time-consuming for parametric optimization in most cases. A surrogate model based on magnetostatic FEA method is proposed to significantly reduce the computational time [153, 154] and applied to optimize the machine performance [99, 155]. However, accurate and versatile analytical methods are still in high demand for interior PMSMs. An improved analytical method is developed in this subsection to accurately predict the PM air-gap magnetic field in interior PMSMs. A new flux iteration scheme using section integration to identify the flux density variation over the rotor magnetic flux leakage path is implemented to improve the accuracy of the PM air-gap magnetic field predictions. Moreover, rotor magnetic flux leakage coefficients are also derived by iterations. Without loss of generality, only the rotor structure with single-layer PM configuration is employed here to demonstrate the analytical method, and the analytical model can be easily extended to cover machines with different rotor configurations such as multi-layer PM structure.

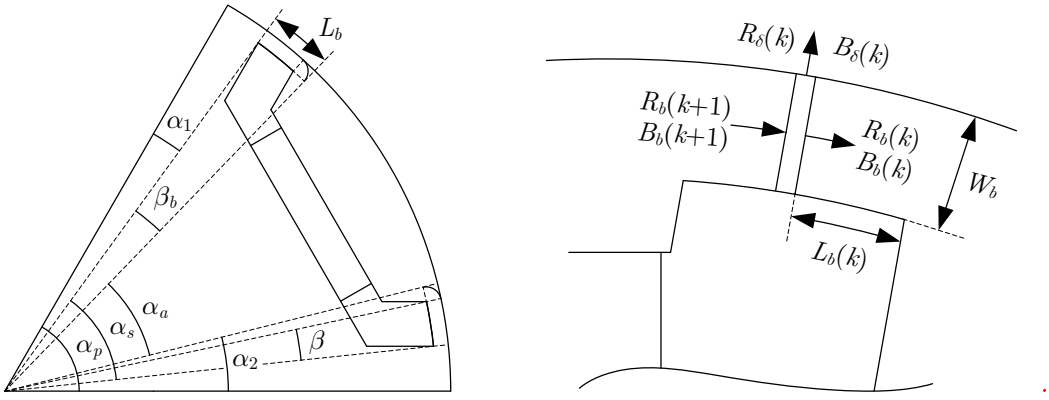

Figure 4.1: Rotor model of PM flux density: (a) rotor structure, (b) rotor bridge.

Figure 4.1(a) demonstrates the single rotor pole structure with single-layer embedded PM configuration, while Figure 4.1(b) illustrates the enlarged view of the saturated rotor bridge region in the rotor. The fringing effects from the core saturation near the inner side of bridge are taken into account by the equivalent length L_b or angle β_b. The corresponding compensations can be expressed as

$$L_b \approx R_0\beta + W_b, \quad \beta_b \approx \beta + \frac{W_b}{R_0} \tag{4.25}$$

The radii of air gap and rotor flux leakage bridge are approximately the same as R_0. As shown in Figure 4.1(b), the rotor flux leakage bridge is divided into n equal sections with the length of $\Delta L_b = L_b/n$ in order to simplify the analytical model. Therefore, the reluctance relationship between the adjacent sections can be derived as

$$R_b(k+1) = R_b(k) \parallel R_\delta(k) + \Delta R_b(k) \approx R_b(k) + \Delta R_b(k) \tag{4.26}$$

where

$$R_\delta(k) = \frac{\delta_{ef}}{\mu_0 L_{ef} \Delta L_b}, \quad \Delta R_b(k) = \frac{\Delta L_b}{\mu_b(k) W_b L_{ef}} \tag{4.27}$$

The reluctance through the air gap and PM slot within each unit are normally much larger than that over the bridge section, so it is practically reasonable to neglect $R_\delta(k)$ in Equation (4.26).

By assuming the permeability maintains a constant value of μ_b over the bridge, the k^{th} section reluctance $R_b(k)$ and overall rotor flux leakage bridge reluctance R_b can be simplified as

$$R_b(k) = \frac{k\Delta L_b}{\mu_b W_b L_{ef}}, \quad R_b = R_b(n) = \frac{L_b}{\mu_b W_b L_{ef}} \tag{4.28}$$

Based on the Kirchhoff's rule on magnetic flux, the flux density in the k^{th} section can be expressed as

$$B_b(k+1) = B_b(k) + \frac{\Delta L_b}{W_b} B_\delta(k) \tag{4.29}$$

Meanwhile, the flux density over the flux leakage bridge and air gap are constrained by Ohm's law of magnetic circuit. Consequently, it can be obtained that

$$R_b(k) B_b(k) W_b = R_\delta(k) B_\delta(k) \Delta L_b \tag{4.30}$$

By substituting the air-gap reluctance Equation (4.27) into Equation (4.30), it can be obtained that

$$B_\delta(k) = \frac{\mu_0 W_b L_{ef} R_b(k)}{\delta_{ef}} B_b(k) \tag{4.31}$$

The iteration expression of flux density sequence over rotor flux leakage bridge can be derived based on Equation (4.28), (4.29) and (4.31) as

$$B_b(k+1) = \left(1 + \frac{\mu_0 L_b^2}{\mu_b W_b \delta_{ef}} \frac{k}{n^2}\right) B_b(k) \tag{4.32}$$

As a result, the flux density models of rotor flux leakage bridge section k and its associated air gap section can be approximately obtained as

$$B_b(k) \approx \left(1 + \frac{\mu_0 L_b^2}{2\mu_b W_b \delta_{ef}} \frac{k^2}{n^2}\right) B_{b_0}, \quad B_\delta(k) \approx \frac{\mu_0 L_b}{\mu_b \delta_{ef}} \left(\frac{k}{n} + \frac{\mu_0 L_b^2}{2\mu_b W_b \delta_{ef}} \frac{k^3}{n^3}\right) B_{b_0} \tag{4.33}$$

Consequently, the corresponding air-gap flux density distribution over a half pole pitch can be derived as

$$B_\delta(\theta_m) = \begin{cases} 0, & 0 \le \theta_m \le \alpha_1 \\ K_{b_1}(\theta_m - \alpha_1)\left(1 + K_{b_2}(\theta_m - \alpha_1)^2\right) B_{b_0}, & \alpha_1 \le \theta_m \le \alpha_2 \\ K_{b_1}\beta_b\left(1 + K_{b_2}\beta_b^2\right) B_{b_0}, & \alpha_2 \le \theta_m \le 0.5\alpha_p \end{cases} \tag{4.34}$$

where

$$K_{b_1} = \frac{\mu_0 R_0}{\mu_b \delta_{ef}}, \quad K_{b_2} = \frac{\mu_0 R_0^2}{2\mu_b W_b \delta_{ef}} \tag{4.35}$$

It is apparent from Figure 4.1(a) that the difference between α_1 and α_2 in Equation (4.34) is determined by β and fringing parameters. Additionally, the pole arc coefficient τ_s and rotor flux leakage bridge factor τ_b are more commonly used to replace α_s and β in machine designs. They are defined as

$$\tau_s = \frac{\alpha_s}{\alpha_p}, \quad \tau_b = \frac{\beta}{\alpha_p} \tag{4.36}$$

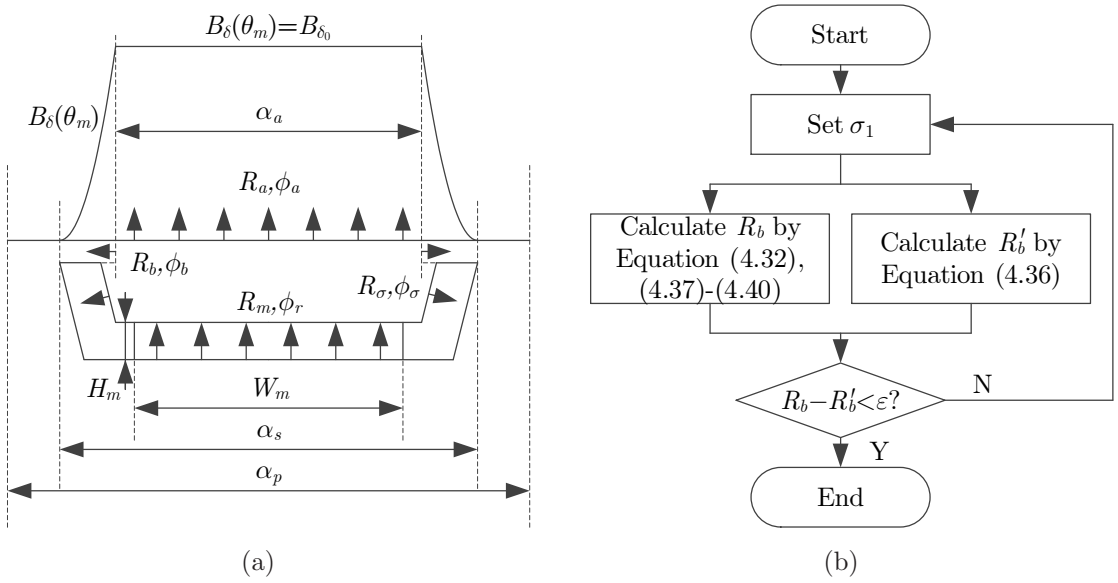

Figure 4.2: Air-gap flux density calculation procedure: (a) magnetic field model, (b) flux leakage coefficient calculation.

As a result, the PM air-gap flux density distribution over one rotor pole is illustrated in Figure 4.2(a) with cubic curves over rotor flux leakage bridges and constant value over α_a. However, there are still two unknown parameters μ_b and B_{b_0} in the proposed model. In order to derive the flux density, a flux leakage coefficient is defined as

$$\sigma_1 = 1 + \frac{2\phi_b}{\phi_a} = 1 + \frac{2R_a}{R_b} \tag{4.37}$$

It represents the level of flux leakage over the bridges. The corresponding air-gap reluctance can be expressed as

$$R_a = \frac{\delta_{ef}}{\mu_0 \alpha_a R_0 L_{ef}} \tag{4.38}$$

Besides the flux leakages over the rotor bridges, there are normally other flux leakage paths in most interior PMSMs such as ϕ_σ shown in Figure 4.2(a). All these items can be estimated by the linear flux leakage permeance according to the rotor structure. Based on the leakage model, the flat top flux density can be derived from PM magnetic circuit and expressed as

$$B_{\delta_0} = \frac{\phi_r}{\sigma_1 \sigma_2 \alpha_a R_0} \frac{R_m}{R_m + R_a} \tag{4.39}$$

where

$$R_m = \frac{H_m}{\mu_0 W_m L_{ef}} \tag{4.40}$$

and σ_2 represents the flux leakage coefficient introduced by ϕ_σ. Sometimes, there can be other leakage paths in the machine rotor such as reinforcement rib in each pole. Such flux leakage can also be included in σ_2 similar to ϕ_σ. By substituting Equation (4.39) into Equation (4.33) and (4.34), it can be obtained that

$$B_{b_0} = \frac{B_{\delta_0}}{K_{b_1}\beta_b(1 + K_{b_2}\beta_b^2)}, \quad B_b(n) = \frac{B_{\delta_0}}{K_{b_1}\beta_b} \tag{4.41}$$

Therefore, the flux density distribution in the air gap can be calculated with a new procedure based on Equation (4.33), (4.37), (4.39) and (4.41), as depicted in Figure 4.2(b). First, an initial value of σ_1 is set for the $R_b(n)$ evaluation based on Equation (4.37). At the same time, the B_{b_0} can be derived from Equation (4.39) and (4.41). It can be substituted into Equation (4.33) to obtain the corresponding flux density over the rotor flux leakage bridge and hence the bridge reluctance $R'_b(n)$. The absolute difference between the two bridge reluctance values, $\mid R_b(n) - R'_b(n) \mid$, is employed for the convergence judgement of the iteration procedure.

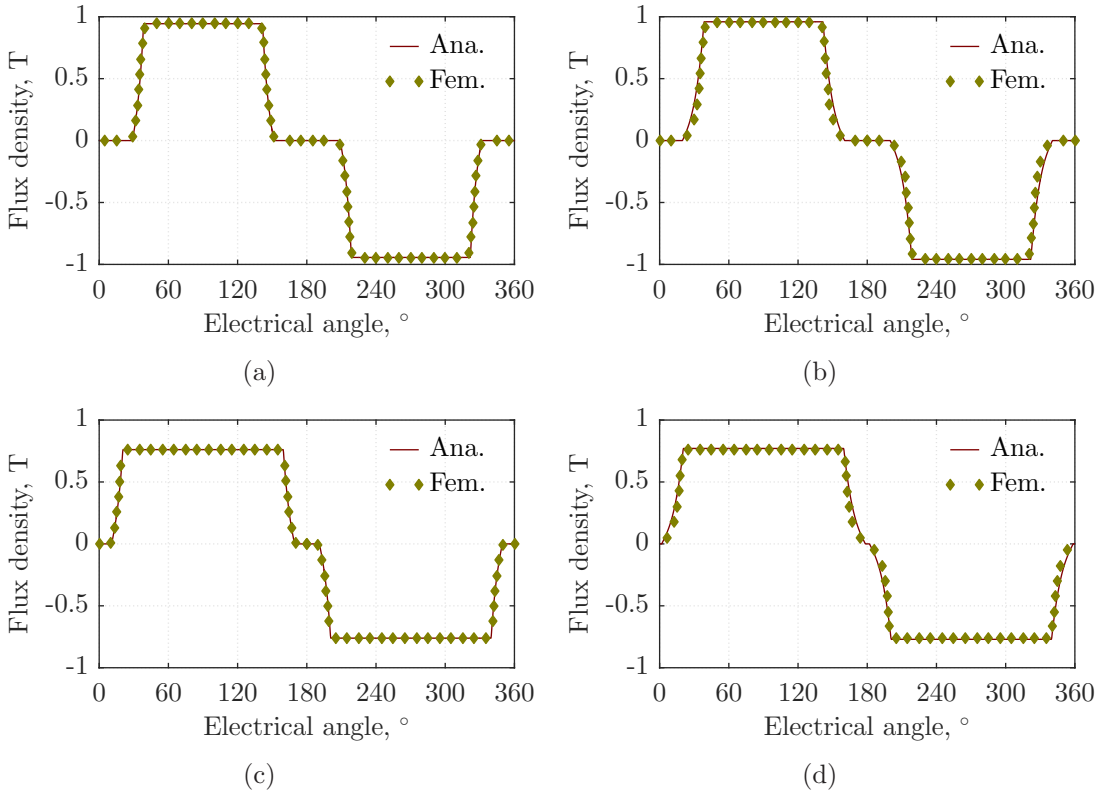

Figure 4.3: Air gap flux density model validation: (a) $\tau_s = 0.68, \tau_b = 0.04$, (b) $\tau_s = 0.78, \tau_b = 0.09$, (c) $\tau_s = 0.88, \tau_b = 0.04$, (d) $\tau_s = 0.98, \tau_b = 0.09$.

FEA models of interior PMSMs with different bridge parameters are employed to validate the proposed PM air-gap flux density distribution estimation method. The

pole pairs number of the machine is 3. The stator inner radius is 52mm with an air-gap height of 0.575mm. The overall width and height of the PM are 38mm and 2.8mm respectively with the V-shape structure. The PM air-gap flux density distributions in interior PMSMs with different combinations of τ_s and τ_b are derived from the analytical and FEA results. The respective analytical and FEA results are demonstrated and compared in Figure 4.3. It can be easily noticed that the results from the proposed analytical model agree very well with the corresponding FEA simulations for the machines with different pole arc coefficients and rotor flux leakage bridge lengths. However, some noticeable errors still occur especially with extremely large rotor flux leakage bridge length. Such errors are mainly caused by the simple assumption of linear permeance in the rotor flux leakage bridges.

4.2.2 PM Air-Gap Magnetic Field Spectrum Analysis

The spectrum of the PM air-gap flux density distribution can be obtained based on the model proposed in Equation (4.34) by Fourier series expansion. The amplitude of the fundamental component can be presented as

$$\begin{aligned} B_1 =& \frac{4B_{\delta_0}}{\pi}\cos(p\alpha_2) + \frac{4K_{b_2}B_{\delta_0}}{\pi\left(1+K_{b_2}p^2\beta_b^2\right)}\left(3p\beta_b\sin(p\alpha_2) - p^2\beta_b^2\cos(p\alpha_2)\right) \\ &+ \frac{4K_{b_2}B_{\delta_0}}{\pi p\beta_b\left(1+K_{b_2}p^2\beta_b^2\right)}\left(6\sin(p\alpha_1) - 6\sin(p\alpha_2) + 6p\beta_b\cos(p\alpha_2)\right) \\ &+ \frac{4B_{\delta_0}}{\pi p\beta_b\left(1+K_{b_2}p^2\beta_b^2\right)}\left(\sin(p\alpha_2) - \sin(p\alpha_1) - p\beta_b\cos(p\alpha_2)\right) \end{aligned} \tag{4.42}$$

where α_1, α_2 are depicted in Figure 4.1(a), and can be expressed as

$$\alpha_1 = \frac{\alpha_p - \alpha_s}{2}, \quad \alpha_2 = \frac{\alpha_p - \alpha_a}{2} \tag{4.43}$$

Since $(p\beta)$ is usually very small, Equation (4.40) can be further approximated as

$$B_1 = \frac{4B_{\delta_0}}{\pi}\cos(p\alpha_2) + \frac{p\beta_b\left(2+K_{b_2}p^2\beta_b^2\right)B_{\delta_0}}{\pi\left(1+K_{b_2}p^2\beta_b^2\right)}\sin(p\alpha_2) \tag{4.44}$$

Furthermore, it can be obtained for multi-pole machine that

$$K_{b_2}p^2\beta_b^2 = \frac{\mu_0}{\delta_{ef}B_{\delta_0}}\frac{L_bB_{bm}}{\mu_b}\frac{L_b}{2W_b}\frac{B_{\delta_0}}{B_{bm}}p^2 = \frac{L_b}{2W_b}\frac{B_{\delta_0}}{B_{bm}}p^2 \gg 1 \tag{4.45}$$

where B_{bm} is the equivalent mean value of flux density in the rotor flux leakage bridge. As a result, Equation (4.44) can be further simplified as

$$B_1 = \frac{4B_{\delta_0}}{\pi}\cos(p\alpha_2) + \frac{p\beta_bB_{\delta_0}}{\pi}\sin(p\alpha_2) \tag{4.46}$$

The analytical results of the fundamental PM air-gap magnetic field components in the machine with different pole arc coefficient τ_s and rotor flux leakage bridge factor

τ_b are evaluated based on the proposed model, and compared with the corresponding FEA simulations in Figure 4.4(a). It can be directly observed that excellent agreements between the analytical and FEA results have been achieved with short rotor flux leakage bridge over the wide range of τ_s. However, considerable deviations between the analytical and FEA results appear with a long rotor flux leakage bridge. As aforementioned, such errors arise from the neglect of the material nonlinearity in the rotor flux leakage bridge and several simplifications made above. Generally, it is reasonable to conclude that the proposed analytical model can offer fast and accurate prediction of fundamental PM air-gap flux density component in interior PMSMs. Moreover, the rotor flux leakage bridge factor has been inherently integrated into the model.

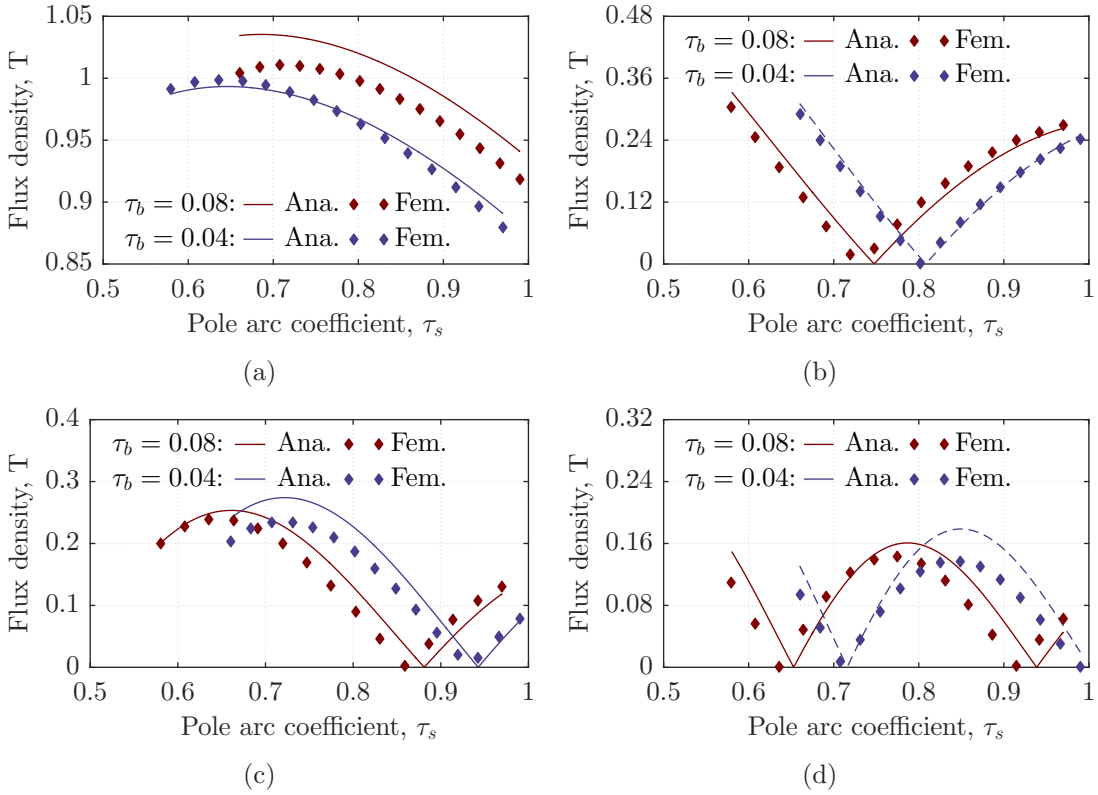

Figure 4.4: Flux density model validation: (a) the fundamental component, (b) the third order component, (c) the fifth order component, (d) the seventh order component. (Ana. - Analytical model, Fem. - Finite element model)

Similarly, the amplitude of the k^{th} PM air-gap flux density harmonic component can be approximately presented as

$$B_k = \frac{2\left(6+(6K_{b_2}-k^2)p^2\beta_b^2\right)B_{\delta_0}}{3k\pi\left(1+K_{b_2}p^2\beta_b^2\right)}\cos(kp\alpha_2) + \frac{p\beta_b\left(2+K_{b_2}p^2\beta_b^2\right)B_{\delta_0}}{\pi\left(1+K_{b_2}p^2\beta_b^2\right)}\sin(kp\alpha_2) \tag{4.47}$$

It can be further simplified as

$$B_k \approx \frac{4B_{\delta_0}}{k\pi}\cos(kp\alpha_2) + \frac{p\beta_b B_{\delta_0}}{\pi}\sin(kp\alpha_2) \tag{4.48}$$

The corresponding analytical and FEA results of the third, fifth and seventh PM air-gap magnetic field harmonic components are also evaluated and compared in Figure 4.4(b), 4.4(c) and 4.4(d) respectively. Satisfactory agreements have been achieved between the analytical and FEA results. Hence, the proposed analytical models can provide reasonable predictions on the characteristics of all the main PM air-gap magnetic field harmonic components. Although the third back EMF harmonic induced by the third PM air-gap flux density harmonic component can be eradicated by the star connection of the three-phase windings, such magnetic field component will still interact with other flux density harmonic components to produce ERFD components in the machine. Besides the corresponding back EMF harmonic components and hence torque pulsations, the fifth and seventh PM air-gap magnetic field harmonic components can result in associated ERFD components. It can be inspected from Figure 4.4 that the corresponding PM air-gap magnetic field components can be effectively minimized by optimal selection of pole arc coefficient and rotor flux leakage bridge factor. With similar spatial order and frequency, the ERFD components from the interactions between fundamental PM air-gap magnetic field component and sideband components are normally much more significant. Consequently, all these high order PM air-gap magnetic field harmonic components can be ignored in high-frequency sideband ERFD analysis. On the other hand, it is essential to consider them for low-frequency ERFD and vibration investigations due to the evident deviations of spatial and temporal orders induced by these harmonic components.

It is noteworthy that the proposed analytical models are restricted for low-order PM air-gap magnetic field harmonic components due to the cutting error of Fourier series expansion. Nonetheless, they are sufficient enough for accurate predictions on the main PM air-gap magnetic field components such as the fundamental, third, fifth and seventh components. Moreover, the proposed method only predicts the PM air-gap flux density distribution with slotless configuration. The actual PM air-gap magnetic field ought to include the slot harmonic components by introducing permeance from stator slot openings. However, the slot harmonic components are no longer required to be considered in the ERV investigation according to stator tooth modulation effect model.

4.3 The Analytical Model of Permeance

The aforementioned universal model of armature-reaction air-gap magnetic field involves both armature-reaction MMF and air-gap permeance distributions. Normally, the armature-reaction MMF harmonic components can be directly derived from the winding arrangement and FFT analysis. On the other hand, the air-gap permeance distribution is determined by the machine structure mainly the stator slot and rotor pole numbers, slot opening shape and width, and magnet slot shape and size. Furthermore, it will be also affected by the local magnetic saturations in the machine. For the sake of simplicity, the influences of the magnetic saturations are usually neglected in analytical investigations. Most attention has been devoted

in the existing research to the air-gap permeance components contributed by the stator slot opening effect. The slot-opening air-gap permeance distribution can be directly evaluated by simple 1-D magnetic circuit [156] and complex 2-D conformal transformation [144, 157] methods. A more sophisticated subdomain model has been also developed to accurately predict the stator slot opening effect. However, the method can only applied to one particularly uncommon slot opening shape and more importantly the solution is no longer closed-form and hence unable to provide insightful information. As it is not needed in stator tooth modulation model, this chapter does not dwell on the air-gap permeance components contributed by the stator slot opening effect. Hence, this section mainly focuses on the air-gap permeance components introduced by the rotor configuration. As the PM permeability is very close to the permeability of air, the rotor saliency of surface-mounted PMSMs is negligible and hence the corresponding air-gap permeance can be considered as a constant and independent of position.

4.3.1 Air-Gap Permeance of Surface-Inset PMSM

In the surface-inset PMSM, the rotor iron core surface is slotted to accommodate the PMs, and the length of the equivalent air gap is no longer constant. As a result, rotor saliency and hence the associated air-gap permeance components are introduced in such type machine. The rotor outer periphery of a typical surface-inset PMSM for one pole pair is depicted in Figure 4.5(a), which shows evenly distributed open slots on the rotor iron core surface. By neglecting the magnetic fringing effect, the corresponding air-gap permeance distribution for fundamental armature-reaction magnetic field component can be easily derived and demonstrated in Figure 4.5(b).

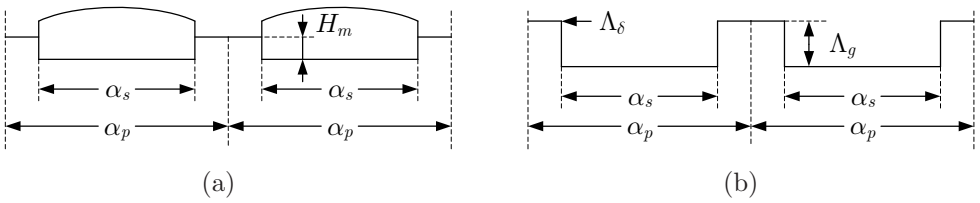

Figure 4.5: Surface-inset PMSM rotor and permeance: (a) Surface-inset rotor, (b) permeance.

In the figure, Λ_g represents the permeance drop over the rotor slot regions while Λ_δ is the permeance induced by the air gap. They can be directly derived from simple magnetic circuit method as

$$\Lambda_\delta = \frac{\mu_0}{\delta_{ef}}, \quad \Lambda_g = \frac{H_m}{\delta_{ef} + H_m}\Lambda_\delta \tag{4.49}$$

where δ_{ef} is the equivalent air-gap length considering the Carter factor. The average air-gap permeance can be directly obtained from the figure as

$$\Lambda_0 = \Lambda_\delta - \tau_s \Lambda_g \tag{4.50}$$

Generally, this is the main factor for the armature-reaction air-gap magnetic field components. While, the air-gap permeance harmonic components Λ_{2n_1} in Equation (4.5) for surface-inset PMSMs can be easily derived as,

$$\Lambda_{2n_1} = \frac{2}{n_1\pi}\Lambda_g \sin(n_1(1-\tau_s)\pi) \tag{4.51}$$

Normally, Λ_2 ($n_1 = 1$) is the main air-gap permeance harmonic component in the air-gap magnetic field analysis and it can be approximated as

$$\Lambda_2 \approx 2(1-\tau_s)\Lambda_g \tag{4.52}$$

Besides additional air-gap magnetic field harmonic components, this second-order air-gap permeance harmonic component will interact with the fundamental armature-reaction MMF component to produce a significant fundamental air-gap magnetic field component. Consequently, it is essential to take it into account in the fundamental armature-reaction magnetic field evaluation. In fact, a small portion of the magnetic flux will travel through the slot sides to form shorter magnetic path. It is expected that such magnetic fringing effects near the slot side regions will introduce some errors in the proposed air-gap permeance model.

The FSCW configuration can result in one corresponding rotor rib under most of the stator teeth so that most of the flux inside a particular tooth can directly form a close path through the rib. Therefore, the air-gap permeance distribution in Figure 4.5(b) can still be employed to approximate the main interharmonic armature-reaction magnetic field components.

4.3.2 Air-Gap Permeance of Interior PMSM

The air-gap permeance distribution in interior PMSM becomes much more complex due to its rather sophisticated magnetic flux paths in the rotor. The investigations of air-gap permeance distribution in interior PMSM are quite limited due to various rotor configurations. Hence, the existing research becomes quite specific and not versatile. Without loss of generality, only the air-gap permeance model for interior PMSM with single-layer PM rotor configuration is developed in details here. However, such a method can be easily further extended to cover spoke and multi-layer interior PMSMs.

For the sake of simplicity for analysis, it is assumed that

- The influence of rotor flux leakage bridges can be neglected and hence a square distribution of permeance can be characterized as the magnetic flux go through the PM slots;
- The flux leakage through the air gap under flux leakage bridges can also be ignored;
- The core saturation affected by the armature reaction is neglected;

- All the fluxes entering rotor are normal to the rotor surface;
- Without loss of generality, only the unit machine with rotor pole pairs of p_0 and stator slot number of Z_0 is considered in the model.

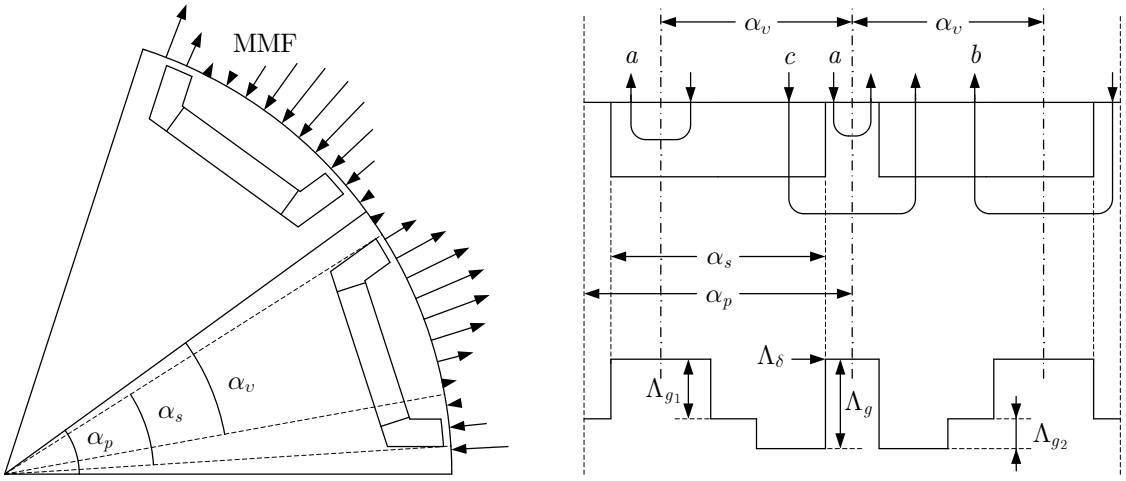

Figure 4.6: Demonstration of magnetic path and associated permeance: (a) rotor structure of interior PMSM, (b) magnetic path and its permeance.

The rotor structure of a typical interior PMSM with single-layer PM rotor configuration is depicted as Figure 4.6(a), while the magnetic flux paths under υ^{th} armature-reaction MMF harmonic component are demonstrated in Figure 4.6(b). It can be inspected from the figure that the embedded PM slots in the rotor will have rather complex and significant impacts on the air-gap permeance components. The iron pole shoes above the PM slots will enable more flexible magnetic flux paths in the rotor and cause more complex scenarios. The armature-reaction MMF harmonics with pole arc width of $\alpha_\upsilon \ll \alpha_s$ can form magnetic flux short circuit over the iron pole shoe areas, while the harmonics with pole arc width of $\alpha_\upsilon \gg \alpha_s$ apparently experience more reluctance due to the PM slots. As a consequence, the air-gap permeance distribution for all the armature-reaction MMF harmonic components is no longer the same. It varies with the spatial order of the armature-reaction MMF harmonic components. Furthermore, the relative position difference between armature-reaction MMF vector and rotational d-axis can also have huge impact on the air-gap permeance distribution shape. With the assumption, the permeance of the fundamental q-axis armature-reaction MMF component can be approximately derived as Λ_δ as the magnetic flux short circuit over the iron pole shoe, while the corresponding permeance of the fundamental d-axis armature-reaction MMF component can be approximated as the model presented in Figure 4.5(b). Therefore, Equation (4.50) and (4.51) can be directly employed to calculate the permeance components for fundamental d-axis armature-reaction MMF component in interior PMSMs.

For the υ^{th} armature-reaction magnetic field component in Figure 4.6(b), the flux paths can be generally categorized into three types:

- The flux path only encounters the air gap, annotated as path a in the figure. The flux is short-circuit in the rotor by the iron pole shoe or rotor rib. The corresponding permeance is the same as the first item in Equation (4.49);
- The flux path passes the air gap and one PM slot, labeled as path b in the figure. The permeance drop by passing one PM slot is defined as Λ_{g1};
- The flux path experiences the air gap and two PM slots, shown as path c in the figure. The permeance drop by passing two PM slots is defined as $(\Lambda_{g1} + \Lambda_{g2})$.

Based on these three basic flux path types, the air-gap permeance distribution for the υ^{th} armature-reaction MMF harmonic component can be derived from the rotor structure shown in Figure 4.6(b). Such permeance distribution is completely different from the fundamental component. It can be directly observed from the figure that Λ_δ for interior PMSMs is exactly the same as the surface-inset PMSM in Equation (4.49). However, Λ_g cannot be directly adopted from Equation (4.49) due to the rotor flux leakage bridges and more complex PM slot structure. Based on Figure 4.2(a), the reluctance introduced by the rotor structure for armature-reaction magnetic field can be expressed as

$$R_g = \frac{R_b}{2} \parallel \frac{R_\sigma}{2} \parallel R_m \tag{4.53}$$

where R_b can be derived by the iteration procedure proposed in Figure 4.2(b), and R_m and R_σ are the reluctance components introduced by the PM slot structure. Consequently, the associated permeance drops by the first and second PM slot can be expressed as

$$\Lambda_{g_1} = \frac{R_g}{2R_a + R_g}\Lambda_\delta, \quad \Lambda_{g_2} = \frac{R_a R_g}{(R_a + R_g)(2R_a + R_g)}\Lambda_\delta \tag{4.54}$$

where R_a can be directly derived from Equation (4.38).

Similar to the surface-inset PMSMs, the average permeance is the main factor for the interharmonic armature-reaction air-gap magnetic field components. However, the average permeance is also highly dependent on the spatial order and initial phase of the armature-reaction MMF harmonic components. The corresponding order of $\upsilon_0 = \upsilon/t_0$ in single unit, instead of υ^{th} harmonic component, is used in this study. Nonetheless, the associated permeance is exactly of the same amplitude. The analytical model will be discussed in two different scenarios including $\alpha_\upsilon \geq \alpha_s$ and $\alpha_\upsilon < \alpha_s$.

The Average Permeance Model under $\alpha_\upsilon \geq \alpha_s$

The permeance model of $\alpha_\upsilon \geq \alpha_s$ demonstrated in Figure 4.7 can be divided into four parts for each α_υ range. The overall permeance can be derived by the superposition of these four parts as

$$\Lambda_\upsilon = \Lambda_A + \Lambda_B + \Lambda_C + \Lambda_D \tag{4.55}$$

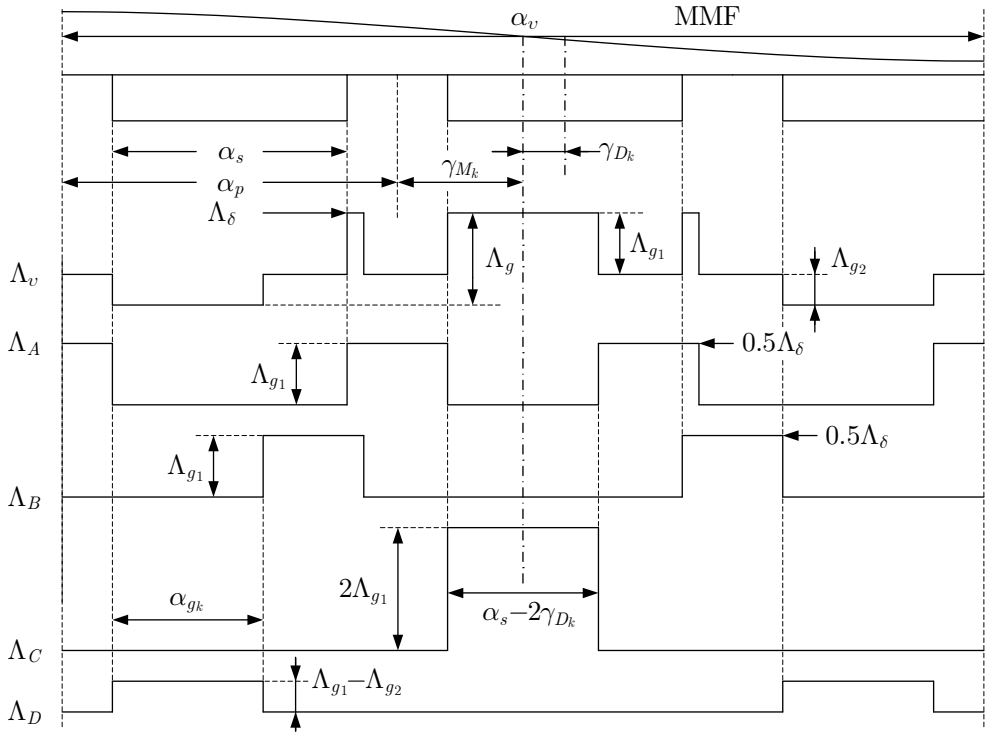

Figure 4.7: The υ-order permeance model with $\alpha_\upsilon \geq \alpha_s$.

The component Λ_A represents the permeance associated with the rotor part left to the inter-pole centre line. The permeance of the flux path without PM slots is $0.5\Lambda_\delta$, while it will be dropped by Λ_{g1} with PM slot. This left part of Λ_A can be directly mirrored by inter-pole centre line to form the whole α_υ range. On the other hand, the component Λ_B denotes the permeance related to the rotor part right to the inter-pole centre line. The average permeance of these two components can be readily derived based on the rotor parameters as

$$\Lambda_A + \Lambda_B = \Lambda_\delta - 2\tau_s\Lambda_{g_1} \tag{4.56}$$

The component Λ_C compensates the effect of short-circuit flux path in the iron pole shoe above PM slot when the inter-pole centre line of υ^{th} MMF harmonic component encounters the iron pole shoe. It is mistaken as the permeance of flux path with one PM slot in both Λ_A and Λ_B. During the superposition of Λ_A and Λ_B, a permeance reduction of $2\Lambda_{g1}$ is assumed for the contribution of this part. However, the flux enters the iron pole shoe and forms a close loop without passing through PM slot. Therefore, the corresponding permeance is increased in practice and hence a compensation is required to include this particular phenomenon. In a single unit of the machine, it can be further derived that

$$\upsilon_0 = \upsilon_1 t_1, \quad p_0 = p_1 t_1, \quad t_1 = \gcd(\upsilon_0, p_0) \tag{4.57}$$

For υ^{th} MMF harmonic component, the angle between a particular inter-pole centre

line and the d-axis, γ_{D_k}, becomes a variable. It can be determined by

$$\gamma_{D_k} = k\Delta\gamma_D + \gamma_{D_0}, \quad -\frac{\pi}{2p_0} \leq \gamma_{D_k} < \frac{\pi}{2p_0} \tag{4.58}$$

where k is an integer and γ_{D_0} is confined by

$$0 \leq \gamma_{D_0} < \Delta\gamma_D \tag{4.59}$$

and $\Delta\gamma_D$ can be expressed as

$$\Delta\gamma_D = \frac{\pi}{\upsilon_1 p_0} \tag{4.60}$$

It can be found that the number of γ_{D_k} will be υ_1 in single unit of the machine and they are all different. It is defined $\gamma_{D_k} > 0$ when the corresponding inter-pole centre line is on the left side of d-axis and vice versa. It can be observed from Figure 4.7 that the angle range of the permeance increase due to the iron pole shoe short-circuit effect becomes $(\alpha_s - 2\gamma_{D_k})$ with $\gamma_{D_k} > 0$ but $(\alpha_s + 2\gamma_{D_k})$ with $\gamma_{D_k} < 0$. As the permeance is associated with α_s, it is essential to turn α_s to a function of $\Delta\gamma_D$ as

$$\alpha_s = N_D\Delta\gamma_D + \alpha_{rm}, \quad 0 \leq \alpha_{rm} < \Delta\gamma_D \tag{4.61}$$

This means there will be either N_D or $N_D + 1$ different short-circuit regions and summation of these respective permeance is required. It is noteworthy that the short-circuit region with the same angular range will repeat t_1 times in single unit of the machine. When N_D is an odd number, the resultant permeance can be derived as

$$\Lambda_C = \begin{cases} \dfrac{t_1}{\pi}(2N_D\alpha_s - (N_D^2 - 1)\Delta\gamma_D - 4\gamma_{D_0})\Lambda_{g_1}, & 0 \leq \gamma_{D_0} \leq \dfrac{\Delta\gamma_D - \alpha_{rm}}{2} \\ \dfrac{t_1}{\pi}(2(N_D + 1)\alpha_s - (N_D + 1)^2\Delta\gamma_D)\Lambda_{g_1}, & \dfrac{\Delta\gamma_D - \alpha_{rm}}{2} < \gamma_{D_0} \leq \dfrac{\Delta\gamma_D}{2} \end{cases} \tag{4.62}$$

When N_D is an even number, it can be expressed as

$$\Lambda_C = \begin{cases} \dfrac{t_1}{\pi}(2(N_D + 1)\alpha_s - N_D(N_D + 2)\Delta\gamma_D - 4\gamma_{D_0})\Lambda_{g_1}, & 0 \leq \gamma_{D_0} \leq \dfrac{\alpha_{rm}}{2} \\ \dfrac{t_1}{\pi}(2N_D\alpha_s - N_D^2\Delta\gamma_D)\Lambda_{g_1}, & \dfrac{\alpha_{rm}}{2} < \gamma_{D_0} \leq \dfrac{\Delta\gamma_D}{2} \end{cases} \tag{4.63}$$

The above analytical development only applies to the conditions of $\gamma_{D_0} \leq \Delta\gamma_D/2$. However, the average permeance under the condition of $\gamma_{D_0} > \Delta\gamma_D/2$ can be derived by replacing γ_{D_0} with $(\Delta\gamma_D - \gamma_{D_0})$ in the formulae.

Based on the analytical derivations above, Λ_C is a variable and correlated to γ_{D_0} which is determined by the machine torque angle and spatial order of the MMF harmonic component. For the fundamental MMF component with $\upsilon_0 = p_0$, it can be directly obtained that $\upsilon_1 = 1$ and hence $\gamma_{D_0} = \alpha_p > \alpha_s$. Therefore, it can be derived from Equation (4.61) that $N_r = 0$ and $\alpha_{rm} = \alpha_s$. The corresponding Λ_C can be evaluated by Equation (4.63) with different γ_{D_0} associated. When the fundamental MMF component aligns with the d-axis, it can be gained that

$$\gamma_{D_0} = \frac{\alpha_p}{2} > \frac{\alpha_{rm}}{2} = \frac{\alpha_s}{2} \tag{4.64}$$

and hence

$$\Lambda_C = 0 \tag{4.65}$$

When the fundamental MMF component aligns with the q-axis, it can be derived that $\gamma_{D_0} = 0$ and therefore

$$\Lambda_C = 2\tau_s \Lambda_{g_1} \tag{4.66}$$

In FSCW PMSMs with the single-layer winding configuration, the sub-harmonic component $\upsilon_0 = 1$ becomes one of the main harmonic components. Similar to the case of fundamental component, it can be derived that $\upsilon_1 = 1$ and hence $N_r = 0$ and $\alpha_{rm} = \alpha_s$. The corresponding permeance can be calculated by Equation (4.63). As $t_1 = 1$, it can be derived that

$$0 \leq \Lambda_C \leq \frac{2}{p_0}\tau_s \Lambda_{g_1} \tag{4.67}$$

Normally, Λ_C for this particular harmonic component is much smaller than the corresponding Λ_A and Λ_B and hence negligible.

For other spatial order MMF harmonic components, $\Delta\gamma_D$ in Equation (4.60) is normally quite insignificant so that N_D in Equation (4.61) becomes relatively large. As a result, Equation (4.61) can be further approximated as

$$\alpha_s \approx N_D \Delta\gamma_D \tag{4.68}$$

By submitting Equation (4.68) to Equation (4.62) and (4.63), it can be derived that

$$\Lambda_C \approx \begin{cases} \dfrac{t_1}{\pi}(N_D\alpha_s + \Delta\gamma_D - 4\gamma_{D_0})\Lambda_{g_1}, & 0 \leq \gamma_{D_0} \leq \dfrac{\Delta\gamma_D - \alpha_{rm}}{2} \\ \dfrac{t_1}{\pi}(N_D\alpha_s - \Delta\gamma_D)\Lambda_{g_1}, & \dfrac{\Delta\gamma_D - \alpha_{rm}}{2} < \gamma_{D_0} \leq \dfrac{\Delta\gamma_D}{2} \end{cases} \tag{4.69}$$

and

$$\Lambda_C \approx \begin{cases} \dfrac{t_1}{\pi}(N_D\alpha_s - 4\gamma_{D_0})\Lambda_{g_1}, & 0 \leq \gamma_{D_0} \leq \dfrac{\alpha_{rm}}{2} \\ \dfrac{t_1}{\pi}N_D\alpha_s\Lambda_{g_1}, & \dfrac{\alpha_{rm}}{2} < \gamma_{D_0} \leq \dfrac{\Delta\gamma_D}{2} \end{cases} \tag{4.70}$$

It is quite obvious that the components associated with N_D are the dominant terms in the equations above. Therefore, the equation can be further simplified into

$$\Lambda_C = \frac{t_1}{\pi}N_D\alpha_s\Lambda_{g_1} = \frac{\upsilon}{p}\tau_s^2\Lambda_{g_1} \tag{4.71}$$

The component Λ_D takes into account the flux path experiencing two PM slots. As discussed earlier, the permeance will be reduced by $(\Lambda_{g_1} + \Lambda_{g_2})$ by passing two PM slots. It is over-reduced by $(\Lambda_{g_1} - \Lambda_{g_2})$ with the permeance of flux path with one PM slot in both Λ_A and Λ_B. Therefore, component Λ_D is constructed to cover this discrepancy. Similarly, the minimum angle between a particular inter-pole centre lines of the υ^{th} MMF harmonic component and rotor, γ_{M_k}, can be defined as

$$\gamma_{M_k} = k\Delta\gamma_M + \gamma_{M_0}, \quad -\frac{\pi}{2p_0} \leq \gamma_{M_k} < \frac{\pi}{2p_0} \tag{4.72}$$

where

$$\Delta\gamma_M = \Delta\gamma_D = \frac{\pi}{\upsilon_1 p_0} \tag{4.73}$$

There can be more than one PM slot over the range of $\alpha_\upsilon/2$ with $\alpha_\upsilon \geq \alpha_p$. For interharmonic components, the angular range of the flux path passing two PM slots can be very different. They can be mainly divided into three circumstances:

- This angular range in the PM slot which does not intersect with the inter-pole centre line of the υ^{th} MMF harmonic component is $(2\alpha_s - \alpha_p)$ as $(\alpha_p - \alpha_s)/2 \leq \gamma_{M_k} \leq \alpha_s/2$. The corresponding permeance can be derived as

$$\Lambda_{D_1} = (2\tau_s - 1)(\Lambda_{g_1} - \Lambda_{g_2}) \tag{4.74}$$

- This angular range is further increased by $(\alpha_p - \alpha_s - 2\gamma_{M_k})$ with $0 \leq \gamma_{M_k} \leq (\alpha_p - \alpha_s)/2$ or $(2\gamma_{M_k} - \alpha_s)$ with $\alpha_s/2 \leq \gamma_{M_k} \leq \alpha_p/2$. Similar to component Λ_C, γ_{M_0} can be neglected for interharmonic component so that $(\alpha_p - \alpha_s)/2 \approx N_M \Delta\gamma_M$. As a result, such range will form four repetitive series of $2\Delta\gamma_M$, $4\Delta\gamma_M$, ..., $2N_M\Delta\gamma_M$ over single unit of the machine. The corresponding permeance can be obtained as

$$\Lambda_{D_2} = \frac{\upsilon}{p}(1 - \tau_s)^2(\Lambda_{g_1} - \Lambda_{g_2}) \tag{4.75}$$

- When the MMF harmonic inter-pole centre line intersects with one of the rotor iron pole shoe, the angular range of resultant short-circuit flux path ought to be removed. The corresponding permeance can be derived from Equation (4.71) as

$$\Lambda_{D_3} = \frac{\upsilon}{p}\tau_s^2(\Lambda_{g_1} - \Lambda_{g_2}) \tag{4.76}$$

Based on the analysis above, for interharmonic components with $\alpha_\upsilon > \alpha_p$, the overall permeance can be rewritten as

$$\Lambda_\upsilon = \Lambda_\delta - 2\tau_s\Lambda_{g_1} + \frac{\upsilon}{p}\tau_s^2\Lambda_{g_1} + (2\tau_s - 1)(1 - \frac{\upsilon}{p})(\Lambda_{g_1} - \Lambda_{g_2}) \tag{4.77}$$

$N_M = 0$ can be obtained for fundamental MMF component with $\upsilon_0 = p_0$ or sub-harmonic component with $\upsilon_0 = 1$. Similar to the derivation of corresponding Λ_C, Λ_D can be evaluated with γ_{M_0} ranged from 0 to α_p. For the fundamental component with $\gamma_{M_0} = 0$, it can be derived that

$$\Lambda_D \approx \tau_s(\Lambda_{g_1} - \Lambda_{g_2}) \tag{4.78}$$

With $\gamma_{M_0} = \alpha_p/2$, this component will become zero. For the sub-harmonic component with $\upsilon_0 = 1$, both $\gamma_{M_0} = 0$ and $\gamma_{M_0} = \alpha_p/2$ approximately deliver the same result as Equation (4.78).

Therefore, the q-axis component of the resultant permeance for the fundamental component can be obtained as

$$\Lambda_{\upsilon=p} = \Lambda_\delta \tag{4.79}$$

Whilst the d-axis component can be derived as

$$\Lambda_{\upsilon=p} = \Lambda_\delta - \tau_s(\Lambda_{g_1} + \Lambda_{g_2}) \tag{4.80}$$

On the other hand, the resultant average permeance for the sub-harmonic component of $\upsilon_0 = 1$ can be evaluated as

$$\Lambda_{\upsilon=t_0} = \Lambda_\delta - \tau_s(\Lambda_{g_1} + \Lambda_{g_2}) \tag{4.81}$$

It can be easily observed from Equation (4.80) and (4.81) that the average permeance of the $\upsilon_0 = 1$ harmonic component approximates to the d-axis permeance of the fundamental component. Consequently, t_0^{th} spatial order magnetic field component from the armature reaction is normally smaller than the fundamental counterpart in interior PMSMs.

Moreover, there are flux paths passing two PM slots with $\alpha_\upsilon < \alpha_p$ when $\gamma_{M_k} < (\alpha_\upsilon + \alpha_s - \alpha_p)/2$. The corresponding angular range is $(\alpha_\upsilon + \alpha_s - \alpha_p - 2\gamma_{M_k})$. With approximation of $(\alpha_\upsilon + \alpha_s - \alpha_p)/2 \approx N_M \Delta\gamma_M$, it can be derived as

$$\Lambda_D = \frac{\upsilon}{p}(\frac{p}{\upsilon} - 1 + \tau_s)^2(\Lambda_{g_1} - \Lambda_{g_2}) \tag{4.82}$$

Therefore, the corresponding overall permeance for interharmonic components with $\alpha_s \leq \alpha_\upsilon < \alpha_p$ can be gained as

$$\Lambda_\upsilon = \Lambda_\delta - 2\tau_s\Lambda_{g_1} + \frac{\upsilon}{p}\tau_s^2\Lambda_{g_1} + \frac{\upsilon}{p}(\frac{p}{\upsilon} - 1 + \tau_s)^2(\Lambda_{g_1} - \Lambda_{g_2}) \tag{4.83}$$

The Average Permeance Model under $\alpha_\upsilon < \alpha_s$

The permeance model of $\alpha_\upsilon < \alpha_s$ demonstrated in Figure 4.8 can be also decomposed into four parts for each α_υ range. The overall permeance can be derived by the superposition of these four parts as

$$\Lambda_\upsilon = \Lambda_A - \Lambda_B - \Lambda_C + \Lambda_D \tag{4.84}$$

The component Λ_A represents permeance without PM slots and hence can be easily derived as

$$\Lambda_A = \Lambda_\delta \tag{4.85}$$

$\alpha_\upsilon < \alpha_s$ makes one pole of the α_υ^{th} MMF harmonic component is not able to fully cover one whole PM slot. When one pole of the α_υ^{th} MMF harmonic component is fully covered by one particular PM slot, the corresponding MMF over this pole only passes air gap and is directly short-circuited in the rotor iron pole shoe over the PM slot. The PM slot will impose impact to reduce the corresponding permeance only when one pole of the α_υ^{th} MMF harmonic component intersects with the left or right edge of the PM slot. The component Λ_B represents the permeance drop of the

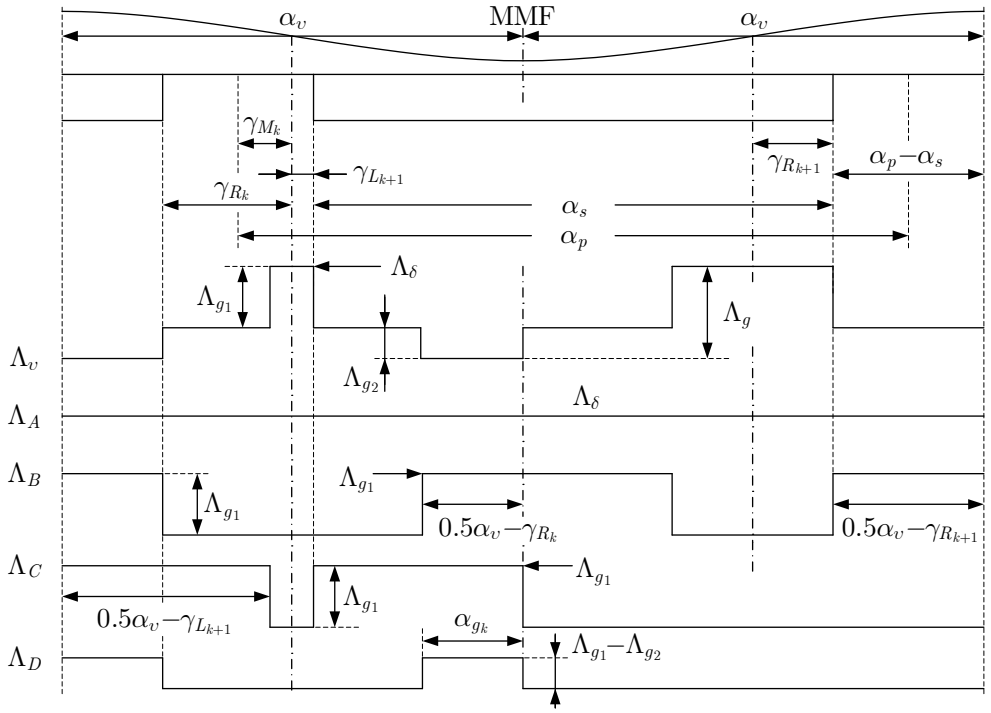

Figure 4.8: The υ-order permeance model with $\alpha_\upsilon < \alpha_s$.

overlap between the pole of the α_υ^{th} MMF harmonic component and left side of the PM slot while the component Λ_C covers the right side part. With the left and right edges as the respective references, the relative positions of the inter-pole centre lines can be written as

$$\begin{cases} \gamma_{L_k} = k\Delta\gamma_L + \gamma_{L_0}, & -\dfrac{\pi}{2\upsilon_0} \le \gamma_{L_k} < \dfrac{\pi}{2\upsilon_0} \\ \gamma_{R_k} = k\Delta\gamma_R + \gamma_{R_0}, & -\dfrac{\pi}{2\upsilon_0} \le \gamma_{R_k} < \dfrac{\pi}{2\upsilon_0} \end{cases} \tag{4.86}$$

where $0 \le \gamma_{L_0} < \Delta\gamma_L$ and $0 \le \gamma_{R_0} < \Delta\gamma_R$. $\Delta\gamma_L$ and $\Delta\gamma_R$ is given by

$$\Delta\gamma_L = \Delta\gamma_R = \frac{\pi}{p_1\upsilon_0} = \Delta\gamma \tag{4.87}$$

The angular ranges for Λ_B and Λ_C over one pole of the α_υ^{th} MMF harmonic component are $(\alpha_\upsilon - 2\gamma_{R_k})$ and $(\alpha_\upsilon - 2\gamma_{L_k})$ respectively. There are p_1 pairs of such angular ranges over single unit of the machine. When p_1 is an odd number, the resultant permeance can be evaluated as

$$\Lambda_B + \Lambda_C = \frac{p}{\upsilon}\Lambda_{g_1} + \frac{t_1}{\pi}(\Delta\gamma - 2\gamma_{L_0} - 2\gamma_{R_0})\Lambda_{g_1} \tag{4.88}$$

When p_1 is an even number, it can be expressed as

$$\Lambda_B + \Lambda_C = \frac{p}{\upsilon}\Lambda_{g_1} \tag{4.89}$$

The component associated with $\Delta\gamma$, γ_{L_0} and γ_{R_0} in Equation (4.88) is quite trivial and hence can be neglected. As a result, Equation (4.89) can be employed for approximation of $(\Lambda_B + \Lambda_C)$ for both cases.

The component Λ_D compensates the permeance drop of the flux path experiencing two PM slots. With $\alpha_\upsilon < (\alpha_p - \alpha_s)$, there is no flux path that encounters two PM slots and hence $\Lambda_D = 0$. On the other hand, it can be evaluated by Equation (4.82) with $\alpha_\upsilon \geq (\alpha_p - \alpha_s)$.

In conclusion, the resultant average permeance with $(\alpha_p - \alpha_s) \leq \alpha_\upsilon < \alpha_s$ can be derived as

$$\Lambda_\upsilon = \Lambda_\delta - \frac{p}{\upsilon}\Lambda_{g_1} + \frac{\upsilon}{p}(\frac{p}{\upsilon} - 1 + \tau_s)^2(\Lambda_{g_1} - \Lambda_{g_2}) \tag{4.90}$$

and it can be rewritten for $\alpha_\upsilon < (\alpha_p - \alpha_s)$ as

$$\Lambda_\upsilon = \Lambda_\delta - \frac{p}{\upsilon}\Lambda_{g_1} \tag{4.91}$$

4.4 Main Low-Frequency Magnetic Fields and Inductance Analysis

Based on the key permeance derivations in the previous section, the main low-frequency magnetic field components induced by the PM and fundamental armature current component can be analytically approximated. Without loss of generality, it is assumed that:

- The superposition principle of air-gap magnetic field is valid;
- Only the components with fundamental electrical frequency are included in the derivations.
- Only the key permeance components Λ_0 and Λ_2 are considered in the investigation;

For υ^{th} permeance in interior PMSM, Λ_0 is Λ_υ. The air-gap magnetic field flux density components from the fundamental armature-reaction current component in Equation (4.14) can be derived as

$$b_{\upsilon_2}(\theta_m) = F_{s\_\upsilon_2}\Lambda_0\cos(\kappa_2 p\theta_m - \omega_e t - \varphi_s) + \frac{1}{2}F_{s\_\upsilon_2}\Lambda_2\cos((\kappa_2 - 2)p\theta_m + \omega_e t - \varphi_s) \tag{4.92}$$

It can be easily inspected from the above equation that the fundamental MMF component ($\kappa_2 = 1$) can interact with Λ_2 permeance component to produce the fundamental magnetic field. However, for any other circumstances $\kappa_2 \neq 1$, the resultant $(\kappa_2 - 2)$ order magnetic field, expressed by the second term in the equation, will not be the same spatial order with any κ_2 component expressed in the first term. Therefore, the investigation of fundamental component will be conducted accounting for the Λ_2 permeance component. For any other components $\kappa_2 \neq 1$, study of magnetic field will be carried out based on the average permeance.

4.4.1 Fundamental Magnetic Fields of PM and Armature Reaction

The fundamental armature-reaction magnetic field components in rotor synchronous frame can be derived as

$$\begin{cases} b_d(\theta_m) = F_{s\_d}\Lambda_0 \cos(p\theta_m) - F_{s\_d}\Lambda_2 \cos(p\theta_m)\cos(2p\theta_m) \\ b_q(\theta_m) = F_{s\_q}\Lambda_0 \sin(p\theta_m) - F_{s\_q}\Lambda_2 \sin(p\theta_m)\cos(2p\theta_m) \end{cases} \tag{4.93}$$

By neglecting the third spatial order harmonic components, they can be further approximated as

$$B_d = F_{s\_d}\Lambda_d, \quad B_q = F_{s\_q}\Lambda_q \tag{4.94}$$

The negligible rotor saliency in surface-mounted PMSMs will result in identical d- and q-axis permeance for the respective fundamental armature-reaction MMF harmonic components as

$$\Lambda_d = \Lambda_q = \Lambda_\delta \tag{4.95}$$

Whilst, the surface-inset and interior PM configurations introduce rotor saliency in the machine and hence result in deviation between the corresponding d- and q-axis permeance values. They can be directly obtained based on the analysis in the previous section. The fundamental d- and q-axis permeance values of surface-inset PMSMs can be expressed as

$$\Lambda_d = \Lambda_\delta - \Lambda_g, \quad \Lambda_q = \Lambda_\delta + (1 - 2\tau_s)\Lambda_g \tag{4.96}$$

In interior PMSMs, they can be evaluated as

$$\Lambda_d = \Lambda_\delta - \Lambda_g, \quad \Lambda_q = \Lambda_\delta \tag{4.97}$$

The d- and q-axis components of the fundamental armature-reaction magnetic field harmonic component, B_d and B_q, can be directly obtained for different PMSM types based on Equation (4.95), (4.96) and (4.97) respectively. Consequently, the amplitude of the fundamental armature-reaction magnetic field harmonic component can be evaluated as

$$B_p = \sqrt{B_d^2 + B_q^2} \tag{4.98}$$

On the other hand, the fundamental armature-reaction magnetic field harmonic component can also be calculated based on the corresponding flux linkage model as

$$\psi_{ad} = L_{ad} i_d, \quad \psi_{aq} = L_{aq} i_q \tag{4.99}$$

where the inductances are contributed by respective fundamental (p^{th}) spatial permeance Λ_d and Λ_q. As the d-axis is defined as the position reference for the air-gap magnetic field, the d- and q-axis expressions of the fundamental armature-reaction magnetic field harmonic component can be derived accordingly as

$$b_{ad}(\theta_m) = \frac{\psi_{ad}\cos(p\theta_m)}{\alpha\tau_p N K_{wp} L_{ef}}, \quad b_{aq}(\theta_m) = \frac{\psi_{aq}\sin(p\theta_m)}{\alpha\tau_p N K_{wp} L_{ef}} \tag{4.100}$$

where α can be approximated as $2/\pi$. With the superposition principle, the fundamental armature-reaction magnetic field harmonic component can be synthesized in rotor synchronous reference frame as

$$b_p(\theta, t) = B_p \cos(p\theta - \varphi_p) \tag{4.101}$$

where

$$B_p = \frac{\sqrt{L_{ad}^2 i_d^2 + L_{aq}^2 i_q^2}}{\alpha \tau_p N K_{wp} L_{ef}}, \quad \varphi_p = \frac{\pi}{2} - \arctan \frac{L_{ad} i_d}{L_{aq} i_q} \tag{4.102}$$

It can also be presented in the stator stationary reference frame as

$$b_p(\theta, t) = B_p \cos(p\theta - \omega_e t - \varphi_p) \tag{4.103}$$

The d- and q-axis fundamental flux linkage components from both PM and armature reaction can be derived based on the superposition principle as

$$\psi_{md} = L_{ad} i_d + \psi_f, \quad \psi_{mq} = L_{aq} i_q \tag{4.104}$$

Similarly, the corresponding fundamental air-gap magnetic field harmonic component can be written in the stator stationary reference frame as

$$b_0(\theta_m, t) = B_0 \cos(p\theta_m - \omega_e t - \varphi_0) \tag{4.105}$$

where

$$B_0 = \frac{\sqrt{\psi_{md}^2 + \psi_{mq}^2}}{\alpha \tau_p N K_{wp} L_{ef}}, \quad \varphi_0 = \arctan \frac{\psi_{mq}}{\psi_{md}} \tag{4.106}$$

By neglecting the winding resistance voltage drop, φ_0 can be approximated as δ based on the definition of φ_0. It is noteworthy that the severe magnetic saturations in the PMSM under heavy load operations can make the simple superposition principle of magnetic field invalid. This will ultimately reflect on the strong interaction effect between the magnetic fields from the PMs and armature reaction. Therefore, the parameters, such as L_{ad}, L_{aq} and ψ_f, become current dependent. The FEA method with frozen permeability technique can be employed to predict such parameters accurately so that the superposition principle is somewhat still applicable.

In most integral-slot PMSMs, the fundamental (p^{th}) spatial order is the dominant component in armature-reaction air-gap magnetic field. Whilst, there is an abundance of interharmonic components in FSCW PMSMs, especially the slot MMF harmonic components. The associated magnetic field harmonic components become rather assignable. The corresponding amplitudes can be very close to, and sometimes even larger than the fundamental (p^{th}) component. Consequently, it is essential to include them in the investigation of armature-reaction magnetic field in FSCW PMSMs.

4.4.2 Interharmonic Magnetic Fields of Armature Reaction

In surface-mounted PMSMs, the fundamental armature-reaction magnetic field component can be directly obtained from (4.92) that

$$B_p = F_{s\_p}\Lambda_p, \quad \Lambda_p = \Lambda_d = \Lambda_q = \Lambda_\delta \tag{4.107}$$

While the υ^{th} order harmonic can be derived as

$$b_\upsilon(\theta_m, t) = B_\upsilon \cos(\upsilon\theta_m - \omega_e t - \varphi_s), \quad B_\upsilon = F_{s\_\upsilon}\Lambda_\upsilon \tag{4.108}$$

Surface-mounted PMSM has the feature of $\Lambda_\upsilon = \Lambda_p$. It is noteworthy that υ is negative when rotational direction of the harmonic component is opposite to the fundamental magnetic field. It is different from the definition in Equation (4.10). Therefore, the amplitude of the corresponding interharmonic component can be proposed as

$$B_\upsilon = K_\upsilon B_p, \quad K_\upsilon = \frac{pK_{w\upsilon}}{\mid \upsilon \mid K_{wp}} \tag{4.109}$$

Where K_υ is the flux density coefficient representing the ratio between the interharmonic and fundamental components. By substituting B_p presented in Equation (4.102) into Equation (4.109), the interharmonic component can be evaluated. The flux density coefficient is exactly the winding coefficient in surface mounted machine.

Similarly, a virtual fundamental permeance and associated inductance can be introduced to evaluate the interharmonic components in surface-inset and interior PMSMs. The new virtual fundamental permeance is defined as

$$\Lambda_p = \frac{\Lambda_d + \Lambda_q}{2} \tag{4.110}$$

By substituting Equation (4.96) into Equation (4.110), it can be obtained for surface-inset PMSMs as

$$\Lambda_p = \Lambda_0 = \Lambda_\delta - \tau_s\Lambda_g \tag{4.111}$$

While it can be obtained from Equation (4.97) and (4.110) for interior PMSMs as

$$\Lambda_p = \Lambda_0 = \Lambda_\delta - \frac{\Lambda_g}{2} \tag{4.112}$$

The associated inductance component can be expressed as

$$L_p = \frac{L_{ad} + L_{aq}}{2} \tag{4.113}$$

Consequently, the corresponding magnetic field component can be derived as

$$b_a(\theta, t) = B_a \cos(p\theta - \omega_e t - \varphi_s), \quad B_a = \frac{L_p i_s}{\alpha\tau_p N K_{wp} L_{ef}} \tag{4.114}$$

Equation (4.92) shows the interaction between υ^{th} spatial MMF component and Λ_2 cannot introduce the υ^{th} spatial magnetic field component. Equation (4.108) is

also applicable for surface-inset and interior PMSMs. The permeance Λ_υ is equal to Λ_0 in surface-inset PMSMs. Therefore, the flux density coefficient in Equation (4.109) is still valid for surface-inset PMSMs. The amplitude of the corresponding interharmonic component can be evaluated by

$$B_\upsilon = K_\upsilon B_a \tag{4.115}$$

In interior PMSMs, the permeance Λ_υ needs to be updated by the model proposed in section 4.3.2. The corresponding flux density coefficient can be expressed as

$$K_\upsilon = \frac{pK_{w\upsilon}\Lambda_\upsilon}{\mid \upsilon \mid K_{wp}\Lambda_p} \tag{4.116}$$

Based on the proposed permeance models, the flux density coefficients and the inductances can be evaluated. Therefore, the main interharmonic armature-reaction magnetic field components can be predicted based on the equations developed.

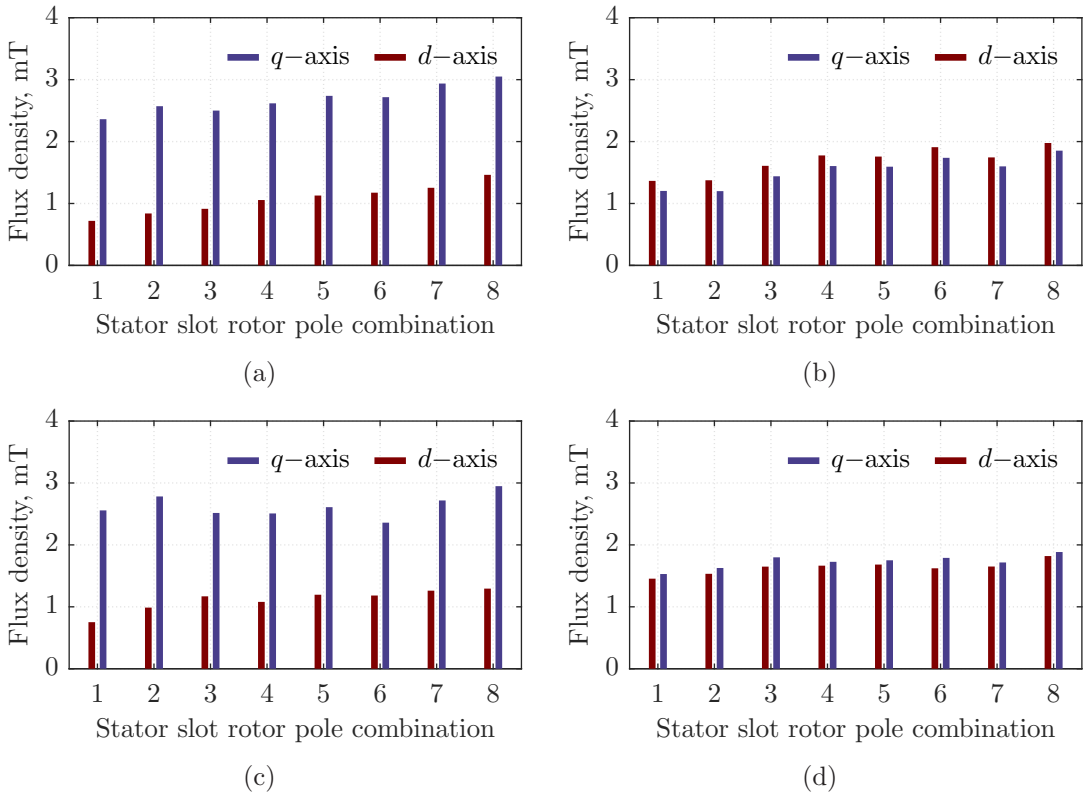

Figure 4.9: Rotor saliency influence on magnetic field: (a) fundamental components in inset PMSMs, (b) $(p - Z)^{th}$ order harmonics in inset PMSMs, (c) fundamental components in interior PMSMs, (d) $(p - Z)^{th}$ order harmonics in interior PMSMs. (1 - 8-pole 9-slot, 2 - 10-pole 12-slot, 3 - 14-pole 15-slot, 4 - 20-pole 21-slot, 5 - 22-pole 24-slot, 6 - 26-pole 27-slot, 7 - 26-pole 30-slot, 8 - 38-pole 42-slot)

As discussed in Subsection 4.3.2 and revealed in Equation (4.92), The influences of the rotor saliency on interharmonic armature-reaction magnetic field components, which are sometimes quite significant in FSCW PMSMs, can be ignored. However,

the rotor saliency imposes a significant impact on the fundamental armature-reaction magnetic field component due to the resultant large deviation between the corresponding d- and q-axis permeance components. As it is practically impossible to directly measure interharmonic armature-reaction magnetic field components, 2-D FEA results of PMSMs with different stator slot and rotor pole combinations are employed to verify the validity of the proposed models. The simulation models are demonstrated in Table D.1 and D.2. Figure 4.9 illustrates the main armature-reaction magnetic field components of both surface-inset and interior PMSMs from 2-D FEA results. The d- and q-axis components of the fundamental armature-reaction magnetic field component of surface-inset and interior PMSMs are shown in Figure 4.9(a) and 4.9(c) respectively. While the results of the main interharmonic $(p-Z)^{th}$ armature-reaction magnetic field component are given in 4.9(b) and 4.9(d). It can be seen from the figure that significant deviations between d- and q-axis fundamental armature-reaction magnetic field components exist due to the rotor saliency characteristic. Based on Equation (4.115), the $(p-Z)^{th}$ armature-reaction magnetic field component is normally quite close to the fundamental counterpart in FSCW PMSMs, revealed in Figure 4.9. Figure 4.9(b) and 4.9(d) have also demonstrated that the differences of the associated d- and q-axis components are very small in FSCW PMSMs with different stator slot and rotor pole configurations. Therefore, it is validated that the influence of the rotor saliency is quite trivial on these main interharmonic armature-reaction magnetic field components. As a result, it is very reasonable to assume these components independent from position in FSCW interior PMSMs.

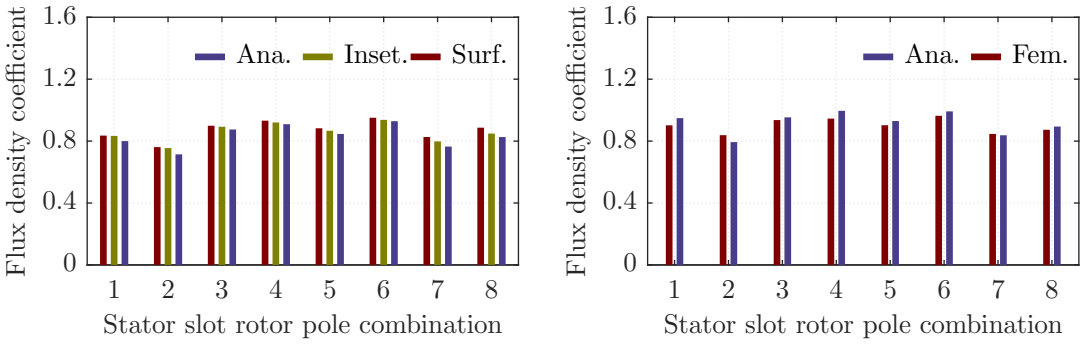

Figure 4.10: Validation of K_{p-Z} by FEM: (a) K_{p-Z} in surface PMSMs, (b) K_{p-Z} in interior PMSMs. (Surf. - Simulation results of surface-mounted motor, Inset. - Simulation results of surface-inset motor, FEM. - Simulation, Ana. - Analytical model)

As K_v represents the ratio between the average value of the corresponding interharmonic and fundamental armature-reaction magnetic field components, it is derived from the 2-D FEA results to underpin the validity of the analytical model. Figure 4.10(a) depicts the comparison of flux density coefficients for the $(p-Z)^{th}$ armature-reaction magnetic field component between the analytical and FEM results of surface-mounted and surface-inset PMSMs with different stator slot and rotor

pole combinations and double-layer concentrated-winding arrangement. Furthermore, the comparisons for interior FSCW PMSMs are also given in Figure 4.10(b). Generally, close agreements have been achieved between the analytical and FEA results so that the validity and accuracy of the analytical model have been underpinned. It is noteworthy that K_{p-Z} can be further approximated as $p/(Z-p)$ for quick assessment for the cases of $2p < Z$.

4.4.3 Teeth Flux Leakage Influence

Besides the $(p-Z)^{th}$ component, the $(t_0/-t_0)^{th}$ armature-reaction magnetic field component can be of particular importance in FSCW PMSMs, especially with the single-layer winding configuration. However, the low spatial order armature-reaction magnetic field components, such as $(t_0/-t_0)^{th}$ component, will experience noticeable flux leakage in the stator teeth between each pair MMF poles, as shown in Figure 4.11(a). It can be expected that the larger Z_0 the more flux leakage occurs due to the bigger reluctance in the rotor yoke. Such flux leakage will lead to significantly reduced armature-reaction magnetic field components. Therefore, it cannot be neglected in the proposed analytical model for the low spatial order sub-harmonic components.

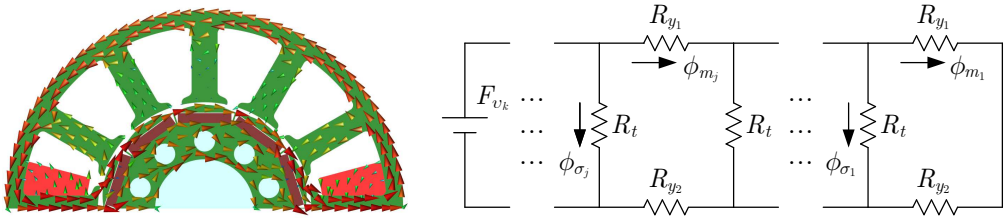

(a) (b)

Figure 4.11: Magnetic path of low order magnetic field: (a) demonstration of flux leakage between one teeth pair, (b) magnetic circuit of low order MMF.

In order to evaluate the influence of such flux leakage, a simple equivalent magnetic circuit method is employed. Figure 4.11(b) demonstrates the magnetic circuit network of low spatial order $(t_0/-t_0)^{th}$ armature-reaction magnetic field component. R_{y_1}, R_{y_2} in the figure are the respective reluctance of stator and rotor yoke under each slot, while R_t represents the overall reluctance of the air gap, PM and stator tooth under each tooth. Normally, the reluctance of both stator and rotor yoke can be ignored for fundamental and other high spatial order components due to their relatively small value. However, there will be severe flux leakage on the teeth for low spatial order components as a result of a long yoke path and hence large yoke reluctance. It is assumed there are n teeth over each quarter of v^{th} order MMF component. In practice, n is normally a mixed number rather than integer. however, the round of n into integer makes very little difference in the magnetic flux path so that integer n is employed here for simplification. The v^{th} MMF component in k^{th}

tooth can be expressed as

$$F_{v_k} = F_{s\_v} \sin \frac{k\pi}{2n} \tag{4.117}$$

Normally, $R_t \gg R_{y_0}(R_{y_0} = R_{y_1} + R_{y_2})$ can be expected in PMSMs. Therefore, for arbitrary j^{th} magnetic flux path, the flux in the tooth can be approximated as

$$\phi_{\sigma_j} \approx \frac{jR_{y_0}}{R_t}\phi_{m_j} \tag{4.118}$$

Hence, the flux leakage coefficient for v^{th} MMF component in the k^{th} tooth can be evaluated by

$$K_{\sigma_k} = 1 + \frac{R_{y_0}}{R_t}\frac{k(k-1)}{2} \tag{4.119}$$

As a result, the whole flux leakage coefficient for all teeth can be approximated by

$$K_\sigma = \frac{\sum_{k=1}^{n} \sin \frac{k\pi}{2n}}{\sum_{k=1}^{n} K_{\sigma_k} \sin \frac{k\pi}{2n}} \tag{4.120}$$

Accordingly, the flux density coefficient can be derived as

$$K_v = \frac{pK_{wv}\Lambda_v}{\mid v \mid K_{wp}K_\sigma\Lambda_p} \tag{4.121}$$

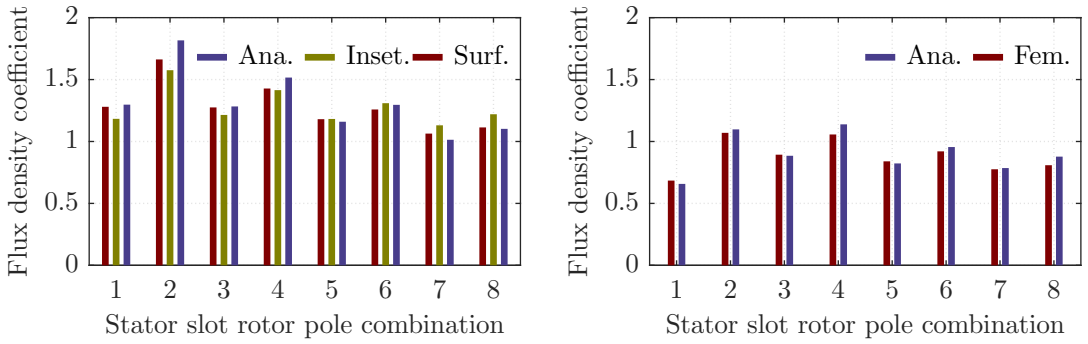

Figure 4.12: Validation of $K_{t_0/-t_0}$ by FEM: (a) $K_{t_0/-t_0}$ in surface PMSMs, (b) $K_{t_0/-t_0}$ in interior PMSMs. (1 - 10-pole 12-slot, 2 - 14-pole 12-slot, 3 - 22-pole 24-slot, 4 - 26-pole 24-slot, 5 - 34-pole 36-slot, 6 - 38-pole 36-slot, 7 - 46-pole 48-slot, 8 - 50-pole 48-slot)

The flux density coefficients of the $(t_0/-t_0)^{th}$ armature-reaction magnetic field component are evaluated by both analytical and 2-D FEA models for the FSCW PMSMs with different stator slot rotor pole combinations and single-layer winding configuration. The key parameters of 2-D FEA models are depicted in Table D.3

and D.4. The comparison of analytical and FEA results are carried out and depicted in Figure 4.12 for surface-mounted, surface-inset and interior PMSMs. Whether K_{t_0} or K_{-t_0} in the machine is determined by the value of fundamental pole pair number p. The FEA results for all the configurations have further validated the accuracy of the flux density coefficient model. It can be seen from figure that the $(t_0/-t_0)^{th}$ flux density coefficients in interior PMSMs are generally smaller than surface PMSMs. It can be explained by the smaller permeance in interior PMSMs as revealed in Equation (4.121).

4.4.4 Analytical Model of d- and q-axis Inductance Components

The fundamental d- and q-axis inductances are required in the analytical magnetic field models. Moreover, the overall inductances are also essential for the sideband current harmonic component evaluation. Although they can be derived from FEA method proposed in Section 3.5.1, the corresponding analytical models are introduced here to reveal the relationship between the permeance and inductance. They are both involved in the interharmonic armature-reaction magnetic field component and hence the further ERFD models. By incorporating the interior PM flux path and teeth leakage effect, the corresponding analytical inductance model can be improved.

The inductance components can be derived accordingly from the associated permeance components. The fundamental inductance components can be rewritten as

$$L_{ad} = 3\alpha L_{ef} R_0 (\frac{NK_{wp}}{p})^2 \Lambda_d, \quad L_{aq} = 3\alpha L_{ef} R_0 (\frac{NK_{wp}}{p})^2 \Lambda_q \tag{4.122}$$

By substituting the permeance values proposed in Equation (4.95), (4.96) and (4.97), the d- and q-axis inductance components for surface-mounted, surface-inset and interior PMSMs can be derived respectively. Furthermore, the associated interharmonic inductance components can be obtained accordingly as

$$L_\upsilon = 3\alpha L_{ef} R_0 K_\sigma (\frac{NK_{w\upsilon}}{\upsilon})^2 \Lambda_\upsilon \tag{4.123}$$

The teeth leakage coefficient K_σ only applies for low spatial order sub-harmonic components with $\upsilon \ll p$. As discussed in previous section, the influences of rotor saliency on main interharmonic components are very trivial. Therefore it can be considered that the corresponding d- and q-axis components are identical. As a result, the overall armature-reaction inductance can be expressed as

$$L_d = L_{ad} + \sum_{\upsilon \neq p} L_\upsilon + L_\sigma, \quad L_q = L_{aq} + \sum_{\upsilon \neq p} L_\upsilon + L_\sigma \tag{4.124}$$

where, L_σ is the total leakage inductance contributed by the end-winding, slot and tooth-tip leakage. They can be derived by analytical model [158, 159]. The interharmonic components L_υ normally can be ignored in integral-slot machine due to their insignificance.

Table 4.5: The *d*- and *q*-axis inductance validation in interior PMSM

Prototype	Items	Analytical	Frozen	Derivation	Experiment
I	L_d	3.134mH	3.445	3.019mH	3.048mH
	L_q	4.443mH	4.359mH	4.211mH	4.164mH
III	L_d	7.493mH	9.675mH	6.289mH	6.264mH
	L_q	30.436mH	29.509mH	21.256mH	18.865mH

In order to validate the proposed model, the inductance components of Prototype I and III, which are interior PMSMs with integral-slot and FSCW configurations, are measured under no-load condition. The corresponding results are listed in Table 4.5 with the analytical and FEA results. Two methods including frozen permeability and derivation techniques, are employed to evaluate the inductance in the FEA models. The *d*- and *q*-axis inductances are derived by the transformation from three phase inductances in the frozen permeability method, while they are obtained from the corresponding flux linkages in derivation method. The armature reaction will have an impact on the permeance of the magnetic circuit, hence it will lead to the shift of the PM working point. The change of PM flux linkage can further introduce extra mutual inductance component. Therefore, there can be significant deviation in the *d*- and *q*-axis results from these two methods. L_q, normally associated with small equivalent air-gap length, is more prone to large impact from armature reaction. It is noteworthy that the incremental inductance of the machine is evaluated in derivation method. On the other hand, the experimental results are obtained by the current with a sinusoidal voltage source, also an incremental component. Therefore, the results from the derivation results are much closer to the experimental results.

The analytical model, which neglects core saturation variation, delivers closer results to the frozen permeability method when the machine is under no-load condition. It can be observed from Table 4.5 that the analytical results agree very well with the FEA results from frozen permeability method. On the other hand, the FEA results from derivation method are in close agreement with the experimental results. Noticeable deviations are introduced by the neglect of the armature reaction influence on the lamination saturation in Prototype III. Overall, satisfactory agreements are achieved between the analytical, FEA and experimental results. The rotor surface of Prototype I is profiled to reduce the PM magnetic field harmonic components, and the air-gap length is ranged from minimum of 0.5mm to maximum of 1.0mm. An equivalent average value of 0.67mm is obtained and it is further increased by Carter factor for the inductance calculation.

4.5 Main Sideband Magnetic Field Components

As a resemblance to the low-frequency armature-reaction, the air-gap magnetic field components from the sideband current harmonic components are analytically de-

rived based on the sideband current models for both SVPWM and SPWM techniques in this section. For the sake of simplicity, the impacts of magnetic saturation and cross-coupling effect on the sideband current harmonic components are neglected.

4.5.1 Sideband Fundamental Magnetic Fields of SVPWM Technique

Similarly, the fundamental air-gap magnetic field components caused by the μ^{th} sideband current component can be expressed as,

$$b_{d\_\omega_\mu}(\theta_m,t)=\frac{L_{ad}i_{d\_\omega_\mu}\cos(p\theta_m)}{\alpha\tau_p NK_{wp}L_{ef}},\quad b_{q\_\omega_\mu}(\theta_m,t)=\frac{L_{aq}i_{q\_\omega_\mu}\sin(p\theta_m)}{\alpha\tau_p NK_{wp}L_{ef}} \tag{4.125}$$

By substituting the $(\omega_s\pm 3\omega_e)$ sideband current harmonic components in Equation (3.28) into Equation (4.125), the corresponding sideband magnetic field components can be derived based on the superposition principle. The resultant components can be analytically presented as

$$\begin{aligned} b_{p\_\omega_s\pm 3\omega_e}(\theta_m,t)=&\mp(\sigma_3C_{12}+\sigma_4C_{14})B_{\mu 1}\sin(p\theta_m\pm(\omega_s\pm 3\omega_e)t)\cos\delta)\\ &\pm(\sigma_3C_{12}-\sigma_4C_{14})B_{\mu 1}\cos(p\theta_m\pm(\omega_s\pm 3\omega_e)t)\sin\delta)\\ &\pm(\sigma_3C_{14}+\sigma_4C_{12})B_{\mu 1}\sin(p\theta_m\mp(\omega_s\pm 3\omega_e)t)\cos\delta)\\ &\mp(\sigma_3C_{14}-\sigma_4C_{12})B_{\mu 1}\cos(p\theta_m\mp(\omega_s\pm 3\omega_e)t)\sin\delta) \end{aligned} \tag{4.126}$$

where

$$\begin{aligned} &\sigma_3=L_{ad}/L_d+L_{aq}/L_q,\quad \sigma_4=L_{ad}/L_d-L_{aq}/L_q\\ &B_{\mu 1}=\frac{U_{dc}}{4\alpha\tau_p NK_{wp}L_{ef}(\omega_s\pm 3\omega_e)} \end{aligned} \tag{4.127}$$

As the $(\omega_s\pm 3\omega_e)$ sideband current harmonics are the main components in the first carrier domain in the rotor synchronous reference frame, the resultant air-gap magnetic field harmonic components with frequency of $(\omega_s\pm 3\omega_e)$ are expected as the main first sideband fundamental components. However, it can be inspected from the equation that there are items with opposite rotational directions despite the same spatial order and frequency. As a result, the p^{th} spatial air-gap magnetic field harmonic components in the stator stationary reference frame will have frequencies of $(\omega_s\pm 2\omega_e)$ and $(\omega_s\pm 4\omega_e)$. These components can be directly transformed from the rotor synchronous reference frame and presented as

$$\begin{cases} b_{p\_\omega_s\pm 2\omega_e}(\theta_m,t)=\mp\sigma_3B_{\mu 1}C_{12}\sin(p\theta_m\pm(\omega_s\pm 2\omega_e)t-\delta)\\ \qquad\qquad\qquad\mp\sigma_4B_{\mu 1}C_{14}\sin(p\theta_m\pm(\omega_s\pm 2\omega_e)t+\delta)\\ b_{p\_\omega_s\pm 4\omega_e}(\theta_m,t)=\pm\sigma_4B_{\mu 1}C_{12}\sin(p\theta_m\mp(\omega_s\pm 4\omega_e)t+\delta)\\ \qquad\qquad\qquad\pm\sigma_3B_{\mu 1}C_{14}\sin(p\theta_m\mp(\omega_s\pm 4\omega_e)t-\delta) \end{cases} \tag{4.128}$$

It can be noticed that the coupling effect between the sideband armature-reaction MMF harmonic components with different frequencies has been taken into account

by the terms with σ_4 for both $(\omega_s \pm 2\omega_e)$ and $(\omega_s \pm 4\omega_e)$ magnetic field harmonic components. With the same approach, the main second sideband fundamental magnetic field components can be derived as

$$\begin{aligned} b_{p\_2\omega_s \pm \omega_e}(\theta_m, t) = &\mp \frac{L_{ad}}{L_d} B_{\mu 2} C_{21} \sin\delta \sin(p\theta_m \pm (2\omega_s \mp \omega_e)t) \\ &\mp \frac{L_{aq}}{L_q} B_{\mu 2} C_{21} \cos\delta \cos(p\theta_m \pm (2\omega_s \mp \omega_e)t) \end{aligned} \tag{4.129}$$

where

$$B_{\mu 2} = \frac{U_{dc}}{4\alpha\tau_p N K_{wp} L_{ef} \omega_s} \tag{4.130}$$

By synthesizing the components with the same spatial and temporal orders proposed in Equation (4.128) and (4.129), the main sideband fundamental magnetic field components in first and second carrier domains can be rearranged as

$$\begin{cases} b_{p\_\omega_s \pm 2\omega_e}(\theta_m, t) = \pm K_{12} B_{\mu 1} \cos(p\theta_m \pm (\omega_s \pm 2\omega_e)t - \varphi_{p\_12}) \\ b_{p\_\omega_s \pm 4\omega_e}(\theta_m, t) = \pm K_{14} B_{\mu 1} \cos(p\theta_m \mp (\omega_s \pm 4\omega_e)t - \varphi_{p\_14}) \\ b_{p\_2\omega_s \pm \omega_e}(\theta_m, t) = \mp K_{21} B_{\mu 2} \cos(p\theta_m \mp (2\omega_s \pm \omega_e)t - \varphi_{p\_21}) \end{cases} \tag{4.131}$$

where

$$\begin{cases} K_{12} = \sqrt{\sigma_3^2 C_{12}^2 + \sigma_4^2 C_{14}^2 + 2\sigma_3\sigma_4 C_{12} C_{14} \cos(2\delta)} \\ K_{14} = \sqrt{\sigma_3^2 C_{14}^2 + \sigma_4^2 C_{12}^2 + 2\sigma_3\sigma_4 C_{12} C_{14} \cos(2\delta)} \\ K_{21} = -\dfrac{C_{21}}{L_d L_q} \sqrt{(L_{ad} L_q \sin\delta)^2 + (L_d L_{aq} \cos\delta)^2} \end{cases} \tag{4.132}$$

$$\begin{cases} \cos\varphi_{p\_12} = \dfrac{(\sigma_3 C_{12} - \sigma_4 C_{14}) \sin\delta}{K_{12}}, \quad \sin\varphi_{p\_12} = \dfrac{-(\sigma_3 C_{12} + \sigma_4 C_{14}) \cos\delta}{K_{12}} \\ \cos\varphi_{p\_14} = \dfrac{(-\sigma_3 C_{14} + \sigma_4 C_{12}) \sin\delta}{K_{14}}, \quad \sin\varphi_{p\_14} = \dfrac{(\sigma_3 C_{14} + \sigma_4 C_{12}) \cos\delta}{K_{14}} \\ \varphi_{p\_21} = \arctan \dfrac{L_q L_{ad} \sin\delta}{L_d L_{aq} \cos\delta} \end{cases} \tag{4.133}$$

Normally, the fundamental armature-reaction inductance components L_{ad} and L_{aq} are very close to L_d and L_q in integral-slot machine. As a result, σ_4 turns into nearly zero and the associated items in the equations can be neglected. Therefore, K_{12} and K_{14} can be further simplified in those machines as

$$K_{12} \approx \sigma_3 C_{12}, \quad K_{14} \approx \sigma_3 C_{14} \tag{4.134}$$

4.5.2 Sideband Interharmonic Magnetic Fields of SVPWM Technique

As the spatial interharmonic components of the armature-reaction air-gap magnetic field can be quite significant in PMSMs with FSCW configuration, it is essential to include them in the sideband magnetic field investigation. The derivations of

υ^{th} spatial components of air-gap magnetic field generated by the corresponding sideband current harmonics can follow exactly the same approach as the fundamental current. The fundamental components induced by average air-gap permeance in first sideband magnetic field can be derived from Equation (4.113) and (4.128) as

$$\begin{cases} b_{12}(\theta_m,t) = \mp\sigma_3' B_{\mu 1} C_{12}\sin(p\theta_m \pm (\omega_s \pm 2\omega_e)t - \delta) \\ \qquad\qquad \mp\sigma_4' B_{\mu 1} C_{14}\sin(p\theta_m \pm (\omega_s \pm 2\omega_e)t + \delta) \\ b_{14}(\theta_m,t) = \pm\sigma_4' B_{\mu 1} C_{12}\sin(p\theta_m \mp (\omega_s \pm 4\omega_e)t + \delta) \\ \qquad\qquad \pm\sigma_3' B_{\mu 1} C_{14}\sin(p\theta_m \mp (\omega_s \pm 4\omega_e)t - \delta) \end{cases} \tag{4.135}$$

where

$$\sigma_3' = L_p/L_d + L_p/L_q, \quad \sigma_4' = L_p/L_d - L_p/L_q \tag{4.136}$$

On the other hand, the corresponding sideband components in second carrier domain can be obtained from Equation (4.129) with the same method as

$$\begin{aligned} b_{21}(\theta_m,t) = &\mp\frac{L_p}{L_d} B_{\mu 2} C_{21}\sin\delta\sin(p\theta_m \pm (2\omega_s \mp \omega_e)t) \\ &\mp\frac{L_p}{L_q} B_{\mu 2} C_{21}\cos\delta\cos(p\theta_m \pm (2\omega_s \mp \omega_e)t) \end{aligned} \tag{4.137}$$

The respective items in the right hand of Equation (4.135) and (4.137) can be synthesized and the equations can be rearranged as

$$\begin{cases} b_{12}(\theta_m,t) = \pm K_{12}' B_{\mu 1}\cos(p\theta_m \pm (\omega_s \pm 2\omega_e)t - \varphi_{a\_12}) \\ b_{14}(\theta_m,t) = \pm K_{14}' B_{\mu 1}\cos(p\theta_m \mp (\omega_s \pm 4\omega_e)t - \varphi_{a\_14}) \\ b_{21}(\theta_m,t) = \mp K_{21}' B_{\mu 2}\cos(p\theta_m \mp (2\omega_s \pm \omega_e)t - \varphi_{a\_21}) \end{cases} \tag{4.138}$$

where the amplitudes are given by

$$\begin{cases} K_{12}' = \sqrt{\sigma_3'^2 C_{12}^2 + \sigma_4'^2 C_{14}^2 + 2\sigma_3'\sigma_4' C_{12} C_{14}\cos(2\delta)} \\ K_{14}' = \sqrt{\sigma_3'^2 C_{14}^2 + \sigma_4'^2 C_{12}^2 + 2\sigma_3'\sigma_4' C_{12} C_{14}\cos(2\delta)} \\ K_{21}' = -\dfrac{C_{21} L_p}{L_d L_q}\sqrt{(L_q\sin\delta)^2 + (L_d\cos\delta)^2} \end{cases} \tag{4.139}$$

and the initial phases are determined by

$$\begin{cases} \cos\varphi_{a\_12} = \dfrac{(\sigma_3' C_{12} - \sigma_4' C_{14})\sin\delta}{K_{12}'}, \quad \sin\varphi_{a\_12} = \dfrac{-(\sigma_3' C_{12} + \sigma_4' C_{14})\cos\delta}{K_{12}'} \\ \cos\varphi_{a\_14} = \dfrac{(-\sigma_3' C_{14} + \sigma_4' C_{12})\sin\delta}{K_{14}'}, \quad \sin\varphi_{a\_14} = \dfrac{(\sigma_3' C_{14} + \sigma_4' C_{12})\cos\delta}{K_{14}'} \\ \varphi_{a\_21} = \arctan\dfrac{L_q\sin\delta}{L_d\cos\delta} \end{cases} \tag{4.140}$$

Consequently, the corresponding υ^{th} spatial components of the first and second sideband air-gap magnetic field in the stator stationary reference frame can be directly derived as

$$\begin{cases} b_{\upsilon\_\omega_s \pm 2\omega_e}(\theta_m,t) = \pm K_\upsilon K_{12}' B_{\mu 1}\cos(\upsilon\theta_m \pm (\omega_s \pm 2\omega_e)t - \varphi_{a\_12}) \\ b_{\upsilon\_\omega_s \pm 4\omega_e}(\theta_m,t) = \pm K_\upsilon K_{14}' B_{\mu 1}\cos(\upsilon\theta_m \mp (\omega_s \pm 4\omega_e)t - \varphi_{a\_14}) \\ b_{\upsilon\_2\omega_s \pm \omega_e}(\theta_m,t) = \mp K_\upsilon K_{21}' B_{\mu 2}\cos(\upsilon\theta_m \mp (2\omega_s \pm \omega_e)t - \varphi_{a\_21}) \end{cases} \tag{4.141}$$

4.5.3 Sideband Magnetic Field of SPWM Technique

With the same procedure, the main first and second sideband fundamental air-gap magnetic field components can be derived by substituting the sideband current harmonic components from SPWM technique in Equation (3.42) and (3.43) into Equation (4.125). The Equation (4.131) can still be employed for the fundamental sideband magnetic field components from SPWM technique with different values of parameters K_{12}, K_{14}, K_{21}, φ_{p_12}, φ_{p_14} and φ_{p_21}. These parameters for SPWM technique can be derived as

$$K_{12} = \sigma_3 C'_{12}, \quad K_{14} = \sigma_4 C'_{12}, \quad K_{21} = -\frac{C'_{21}}{L_d L_q}\sqrt{(L_{ad} L_q \sin\delta)^2 + (L_d L_{aq} \cos\delta)^2} \tag{4.142}$$

and

$$\begin{cases} \cos\varphi_{p\_12} = \sin\delta, \quad \sin\varphi_{p\_12} = -\cos\delta \\ \cos\varphi_{p\_14} = \sin\delta, \quad \sin\varphi_{p\_14} = \cos\delta \\ \varphi_{p\_21} = \arctan\dfrac{L_q L_{ad} \sin\delta}{L_d L_{aq} \cos\delta} \end{cases} \tag{4.143}$$

The same method can be applied to obtain the main first and second sideband interharmonic air-gap magnetic field components from SPWM technique. Consequently, Equation (4.141) can be also employed to express these components with different parameter values. The corresponding parameters for SPWM technique can be evaluated by

$$K'_{12} = \sigma'_3 C'_{12}, \quad K'_{14} = \sigma'_4 C'_{12}, \quad K'_{21} = -\frac{C'_{21} L_p}{L_d L_q}\sqrt{(L_q \sin\delta)^2 + (L_d \cos\delta)^2} \tag{4.144}$$

and the initial phases are determined by

$$\begin{cases} \varphi_{a\_12} = \varphi_{p\_12}, \quad \varphi_{a\_14} = \varphi_{p\_14} \\ \varphi_{a\_21} = \arctan\dfrac{L_q \sin\delta}{L_d \cos\delta} \end{cases} \tag{4.145}$$

4.6 Summary

The analytical models of the key air-gap magnetic field components, including the PM and armature-reaction components, are the main focus of this chapter. A new analytical method to predict PM air-gap magnetic field of interior PMSM is developed by taking into account the flux density variation over the rotor magnetic flux leakage path, and the associated magnetic field characteristics are further discussed. Meanwhile, the key air-gap permeance components for armature-reaction MMF harmonic components are analytically investigated in surface-inset and interior PMSMs with consideration of the complex magnetic flux paths and magnetic flux leakage in the rotor. Thereafter, the fundamental and interharmonic air-gap magnetic fields in the machine can be analytically evaluated and the correlations

between them are insightfully revealed. Furthermore, the analytical models of the main sideband air-gap magnetic field components are derived accordingly based on the proposed analytical sideband current harmonic models in Chapter 3. As the measurement of air-gap magnetic field components in PMSMs is practically very difficult and almost impossible, the FEA results instead are employed to validate the corresponding analytical models.

The new contributions in this chapter include:

- A new analytical model of PM air-gap flux density distribution in interior PMSM is proposed by taking into account the flux density variation over the rotor magnetic flux leakage path in Section 4.2;
- New analytical models of permeance components for armature-reaction MMF harmonic components are developed with consideration of the complex magnetic flux paths and magnetic flux leakage of surface and interior PMSMs in Section 4.3;
- The main air-gap magnetic field harmonic components induced by the fundamental and sideband current harmonic components are analytically derived in Section 4.4 and 4.5 respectively.

The proposed analytical models of PM air-gap magnetic field can be directly employed not only for the feature analysis, but also machine design. Based on the discussion, it can be found the fundamental air-gap magnetic field is normally the dominant component in the machine. Whilst the other magnetic fields including the interharmonic and phase-belt components are generally relatively small for most cases. On the other hand, the frequency of sideband ERFD component is more or less up to the sideband air-gap magnetic field component while the corresponding amplitude is mainly determined by the associated low-frequency air-gap magnetic field component. Therefore, all the low-frequency air-gap magnetic field components except the fundamental component can be effectively neglected for high-frequency sideband ERFD and ERV investigations. However, they are quite essential for low-frequency ERFD and ERV analysis as the deviation between the corresponding spatial and temporal order can result in significant ERV in the stator and rotor. Meanwhile, the correlations between the respective fundamental and interharmonic armature-reaction air-gap magnetic field components are analytically revealed. Such insightful revelation can be directly employed to identify the key interharmonic armature-reaction magnetic field components effectively. Moreover, the main influence factors on the sideband air-gap magnetic field harmonic components have been effectively unveiled by the analytical models. These analytical models can be further employed to promptly assess the associated sideband ERFD components.

Chapter 5

ERFD and Stator Tooth Effect

Acoustic noise and vibration, which are the main parasitic effects in PMSM drives, have been drawing particular attention throughout their design and operation stages. Extensive research has been dedicated to the origin, analysis and mitigation of these undesirable phenomena in various PMSM types over the decades. Generally, the sources of acoustic noise and vibration in PMSMs can be categorized into three types: aerodynamic, mechanical and electromagnetic [160]. Thereinto, electromagnetic source is the primary component and hence the most important in low- to medium-power rated PMSMs [76], and its associated noise and vibration are nearly always prevailing in low-speed condition [160]. Such source is attributed to the electromagnetic forces acting upon physical parts of the machine, which can be further split into circumferential and radial components in the common radial-flux machine. They are normally associated with the forced electromagnetic torsional and radial vibrations respectively. Additionally, the electromagnetic torque is the manifestation of the circumferential vibration. Consequently, cogging torque, torque ripple and ERFD are the main electromagnetic sources of acoustic noise and vibration in PMSMs. Numerous design techniques such as rotor magnet profiling [161, 162, 163], magnet segmentation [164, 165, 166], magnet pole pairing [167, 168, 169], special combinations of the stator slot and rotor pole number [170, 171], and rotor skewing [172, 173], have been proposed to minimize the cogging torque and torque ripple in PMSMs. Although the attenuated torque pulsations generally ensure the smooth operation, they cannot guarantee the removal of acoustic noise and vibration from PMSMs. The magnetic field in the air gap of PMSMs normally consists of numerous components with different spatial and temporal orders. These components can interact with each other to introduce ERFD components, which can be translated into deformations of the stator core. The resultant deformations are mainly determined by the associated mode shapes of the stator core, and the lower the mode number is, the higher the deformation amplitude will be. Such deformations manifest as vibration and lead to undesirable acoustic noise in PMSMs. Consequently, the low spatial order ERFDs can be the primary cause of acoustic noise and vibration of PMSMs.

The investigations on characteristics of ERFD and vibration in PMSMs have been

well covered over the decades. There are generally two distinct types of approaches to analyze ERFD characteristics: analytical and numerical. Analytical methods are usually impractical for PMSMs with a complex structure. Hence, they are only suitable for relatively simple geometries, and may result in inaccuracies due to the oversimplifications involved. However, these approaches provide closed-form solutions that can directly facilitate design optimization. As a result, various closed-form analytical models have been proposed to evaluate the air-gap magnetic field flux density components and resultant ERFD in surface-mounted PMSMs [174, 52, 73, 72], but rarely for rather complex PMSMs such as interior PMSMs. On the other hand, the numerical approaches, which are commonly actualized by nonlinear 2-D and 3-D FEA methods, offer accurate predictions in PMSMs with arbitrary geometries. Consequently, these are widely implemented to investigate ERFD characteristics of both surface-mounted [175, 176, 177, 178] and interior [179, 180, 80, 88] PMSMs, by taking into account the magnetic saturation. However, such FEA methods are normally computationally demanding, and hence become extremely time-consuming especially for optimization requiring large repetitive computations. Moreover, it can sometimes be very difficult to decouple the ERFD components from the FEA results. Thus, it is advisable to consider analytical and numerical measures as complementary so that both insight and accuracy can be achieved [78, 181].

Once the magnet configuration in the rotor is fixed, the constituent of magnetic field in the air gap of PMSMs is mainly affected by the stator slot rotor pole combination and winding patterns. The stator slot and rotor pole number combination determine the lowest spatial order of the ERFD components while the winding configuration influences their amplitudes. The impacts of these two factors on the ERFD and its associated vibration are comprehensively investigated for PMSMs with fractional-slot and concentrated-winding configuration [182, 183, 87]. Besides inner-rotor PMSMs, ERFD components have been also derived and investigated in rotor synchronous reference frame for outer-rotor machines [184, 185, 89]. Similarly, various analytical [174, 76, 186, 78] and numerical [179, 180, 83, 80, 187] approaches have been proposed and widely employed to predict the vibration characteristics associated with ERFD in PMSMs. These ERFD components act on the stator tooth surface and the resultant force components are transmitted through the teeth to the stator yoke to cause deformations. Consequently, the influence of the stator tooth structure can be considered as an equivalent mechanical modulation on the ERFD components. However, most of the existing research, such as the aforementioned, has utilized stator slot permeance harmonic components to formulate the complex stator tooth effect on the ERFD characteristics in PMSMs. Such simplification can make the analysis and prediction invalid in many cases. Instead, the resultant ERFDs acting on each individual stator tooth are employed to predict the corresponding vibration characteristics in PMSMs [85, 188, 189, 86]. Nevertheless, such forces on the stator teeth are contributed by ERFD components with different spatial and temporal orders, and the tooth effects on these components vary depending on their spatial orders. Apparently, the methods from the aforementioned studies are quite circumscribed and impossible to carry out comprehensive analysis. Most importantly, these methods cannot provide the intrinsic relationship between

the stator tooth configuration such as number and geometric shape, and ERFD characteristics. Consequently, it is of particular importance to develop a general method, which can precisely describe the stator tooth effect on the overall ERFD characteristics.

In this chapter, the effect of tooth modulation on the ERFD characteristics will be numerically and experimentally demonstrated, then compared with the results from the conventional approach. The air-gap permeance harmonic components introduced by the stator slot opening, employed in the conventional ERFD calculation, are not required in the new tooth effect model. Instead, the slot open factor will be automatically included in the procedure of ERFD transmission through stator tooth. Meanwhile, new methods of electromagnetic radial vibration analysis are developed to accurately reflect the tooth modulation effect. Furthermore, analytical models are also developed to promptly and accurately evaluate the stator tooth effect on ERFD characteristics, whose validity is underpinned by the experimental results. The analytical derivations can reveal the critical ERFD components introduced by the modulation effect, and also take into account the impact of the geometric parameters of the stator tooth. The proposed analytical models, together with the new procedure of electromagnetic radial vibration analysis, can be easily applied to all types of PMSMs.

5.1 ERFD and Associated Vibration

ERFD can be the key contributor of vibration and acoustic noise in certain PMSM drive systems. The resultant air-gap ERFD components act on the stator periphery and excite electromagnetic radial vibration and acoustic noise from the stator system. In this section, the main ERFD components in the air gap of PMSMs are first revealed and briefly discussed. Afterwards, the conventional analytical formulae, which are commonly employed to predict the associated electromagnetic radial vibration and acoustic noise based on the ERFD, are also presented and appraised.

5.1.1 Air-Gap ERFD Components

All the magnetic flux density components in the air gap of PMSM interact with each other to produce various ERFD components. The Maxwell stress tensor method can be employed to directly evaluate the ERFD distribution based on the radial and circumferential components of the air-gap magnetic flux density. The circumferential magnetic flux density components are usually much smaller than their radial counterparts. Moreover, the circumferential and radial magnetic flux density components have the exactly same spatial and temporal orders so that the neglect of circumferential components only affects the amplitudes of the ERFD components. Consequently, the ERFD is commonly estimated by only considering the radial components with a very small compromise on the accuracy of amplitudes. As a result,

the ERFD in the air gap of PMSM can be approximated as

$$p_r(\theta,t) \simeq -\frac{(b_r(\theta,t)+b_s(\theta,t)+b_\nu(\theta,t)+b_\mu(\theta,t))^2}{2\mu_0} \tag{5.1}$$

The radial magnetic flux density components involved in Equation (5.1) are provided in detail from Section 4.1. The rich magnetic field constituents ultimately yield an abundance of ERFD components. By expanding the above equation, all the ERFD components in PMSMs can be derived and are listed in Table 5.1. Generally, All these ERFD components can be divided into three main categories:

- The primary components induced by the PM and fundamental current armature reaction magnetic field components, including b_r^2, b_s^2 and $b_r b_s$. These are one of the main source of vibration in the machine, and normally are required to be analyzed for most of the PMSMs;
- The phase-belt components associated with the phase-belt current armature reaction magnetic field components, including $b_\nu b_r$, $b_\nu b_s$, $b_\mu b_\nu$ and b_ν^2. Normally, the phase-belt and sideband current components in PMSM drive are relatively insignificant so that $b_\mu b_\nu$ and b_ν^2 can be neglected for phase-belt ERFD analysis.
- The sideband components associated with the sideband current armature reaction magnetic field components, including $b_\mu b_r$, $b_\mu b_s$, $b_\mu b_\nu$ and b_μ^2. On the same principle, considering only $b_\mu b_r$ and $b_\mu b_s$ will suffice for most sideband ERFD investigations.

Table 5.1: ERFD on stator

-	b_r	b_s	b_ν	b_μ
b_r	$-b_r^2/(2\mu_0)$	$-b_r b_s/(2\mu_0)$	$-b_r b_\nu/(2\mu_0)$	$-b_r b_\mu/(2\mu_0)$
b_s	$-b_s b_r/(2\mu_0)$	$-b_s^2/(2\mu_0)$	$-b_s b_\nu/(2\mu_0)$	$-b_s b_\mu/(2\mu_0)$
b_ν	$-b_\nu b_r/(2\mu_0)$	$-b_\nu b_s/(2\mu_0)$	$-b_\nu^2/(2\mu_0)$	$-b_\nu b_\mu/(2\mu_0)$
b_μ	$-b_\mu b_r/(2\mu_0)$	$-b_\mu b_s/(2\mu_0)$	$-b_\mu b_\nu/(2\mu_0)$	$-b_\mu^2/(2\mu_0)$

The components in the above table concisely demonstrate the different magnetic field sources behind ERFD. However, they are too general to reveal the insightful relations between the ERFD components and key machine drive parameters. Nonetheless, the amplitude, spatial order, frequency and phase angle of each individual component can be directly obtained by substituting the analytical formulae of the corresponding magnetic field components into ERFD items in Table 5.1.

5.1.2 The Vibration and Acoustic Noise of the Stator

Generally, each ERFD component given in Table 5.1 arises primarily from the product of either two of the same or two different magnetic field components. Hence,

trigonometric operations are carried out based on the model of magnetic field components to achieve a general analytical form of the ERFD component, which can be expressed as

$$p_{m\_\omega_k}(\theta_m, t) = P_{m\_\omega_k} \cos(m\theta_m - \omega_k t - \varphi_{m\_\omega_k}) \tag{5.2}$$

where $P_{m\_\omega_k}$, ω_k, m and $\varphi_{m\_\omega_k}$ are the amplitude, angular frequency, spatial order and phase angle of the ERFD component. The electromagnetic vibration and acoustic noise can be accordingly assessed from the ERFD components. The amplitude of vibration displacement can be derived by

$$A_m = \frac{F_{m\_\omega_k}}{M_s \sqrt{(\omega_m^2 - \omega_k^2)^2 + 4\zeta^2 \omega_m^2 \omega_k^2}} \tag{5.3}$$

Normally, mechanical structural FEA models can be employed to predict the eignenvalue ω_m so that the accuracy can be somewhat improved. Moreover, ζ is the corresponding modal damping ratio, and an empirical expression for the small sized electrical machines is suggested in [190] as

$$\zeta = \frac{1}{2\pi}(2.76 \times 10^{-5} f_m + 0.062) \tag{5.4}$$

and $F_{m\_\omega_k}$ is the amplitude of the electromagnetic radial force, which can be expressed as

$$F_{m\_\omega_k} = 2\pi R_0 L_{ef} P_{m\_\omega_k} \tag{5.5}$$

where R_0 is the inner radius of the stator. This formula can also be rewritten in the terms of stator yoke radius instead as

$$F_{m\_\omega_k} = 2\pi R_y L_{ef} P'_{m\_\omega_k} \tag{5.6}$$

$P'_{m\_\omega_k}$ is the equivalent ERFD component acting on the yoke, as depicted in Figure 5.1(a). Based on the geometry, it is normally obtained by

$$P'_{m\_\omega_k} = \frac{R_0}{R_y} P_{m\_\omega_k} \tag{5.7}$$

Consequently, the radiated sound pressure from the outer surface of the machine stator can be evaluated by

$$I_m = \rho c \omega_k A_m \tag{5.8}$$

and the sound pressure level of the acoustic noise are given by

$$L = 20 \lg I_m - 20 \lg I_0 \tag{5.9}$$

where I_0 is the standard reference sound pressure of 2×10^{-5} Pa.

Equation (5.3) and (5.6) imply that all the ERFD components induced by various air-gap magnetic field components act on the stator yoke in the analysis equivalently. Since the whole stator of the machine has been considered as an ideal cylindrical shell, all the air-gap ERFD components are directly transmitted to stator yoke with an amplitude drop but no change of spatial mode and frequency. This assumption

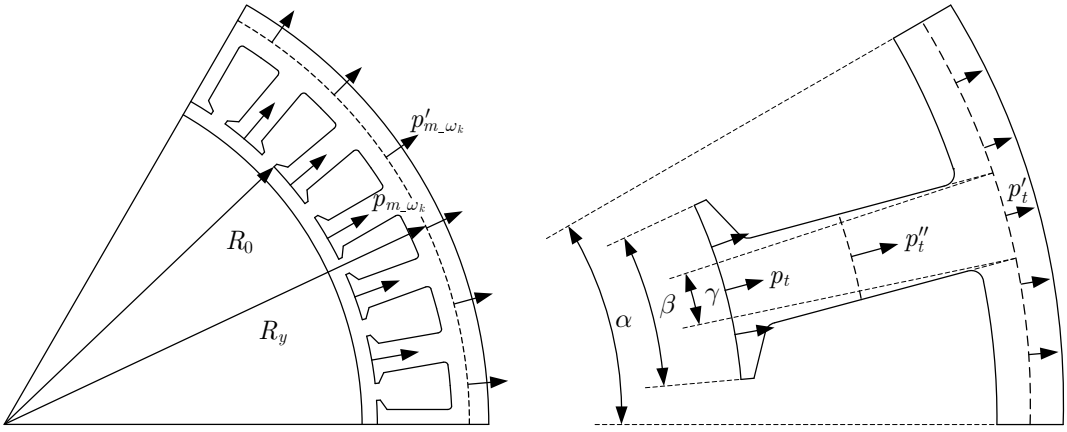

Figure 5.1: Radial force acting on stator yoke: (a)existing model, (b) tooth effect model.

has been widely made for stator vibration analysis of electric machines, and the corresponding ERFD components are directly derived from either analytical formulae or FEA simulation. However, the existence of slots and teeth in the stator do not only affect the stator mechanical characteristics but also alter the electromagnetic force behavior. The aforementioned method takes into account the mechanical aspect but neglects the electromagnetic aspect. As shown in Figure 5.1(b), the ERFD components act on the stator tooth shoes over an arc angle of β, and overall ERFDs are transmitted through the teeth to produce pressure and vibration on the stator yoke. Clearly, the ERFD components over the slot opening region cannot be effectively transmitted to the yoke. In practice, there will be no effective ERFDs in the slot opening region. On the other hand, the traditional method above accounts for the slot opening effect by introducing slot harmonic components into the air-gap magnetic field. Even then, the inclusion of ERFDs over the slot opening regions may bring considerable errors in vibration predictions.

5.2 Tooth Effect of ERFD

It is traditionally considered that the existence of the stator teeth only introduces slot-opening flux permeance in the air gap and hence affect the magnetic field by producing slot harmonics. Generally, the ERFD components involved in the vibration analysis, are directly derived from the air-gap magnetic fields in PMSMs so that the tooth effect phenomenon is directly integrated into the ERFD calculation. However, consideration of stator slot harmonics alone cannot properly explain the ERFD transmission procedure inside the stator. The stator teeth will introduce mechanical modulation on the ERFD through its transmission and complicate the problem. As a consequence, traditional methods can bring considerable errors and hence a new approach should be developed. A surface-mounted PMSM with nearly closed-slot, prototype III, is employed in order to demonstrate the stator tooth

modulation effect.

The stator tooth effect cannot be directly detected from experiments on the machine. Instead, only the mechanical vibration components of the stator shell can be measured for an indirect validation. As there is no existing theory that can explain the stator tooth modulation effect, it is essential that the experimental system can deliver measurements that contain only the vibration components from the stator tooth modulation factor. Therefore, the experimental system is constructed accordingly to meet the stringent requirements of the indirect validation. Additionally, 3-D FEA results are employed to assist the analysis and deliver more detailed explanations for the stator tooth modulation effect.

The width of slot opening in prototype III is so small that its effect on the air-gap magnetic field can be neglected. Thus, the ERFD components induced by the slot opening can be ignored as well. Moreover, the effective air-gap length is very large due to the thick ferrite magnets so that the armature reaction magnetic field under light load condition is negligible. The experimental tests are carried out under a no-load condition in order to minimize the impact of the winding current. As a result, the air-gap magnetic field is almost exclusively produced by PMs in prototype III. By neglecting the slot harmonic components, it can be found that the main air-gap PM magnetic field components, the first and third items in Table 4.1, have exactly the same temporal and spatial orders. Consequently, all the major ERFD components offer the same temporal and spatial orders. In prototype III consisting of three magnet pole pairs, the resultant spatial orders of the main ERFD components are $2p = 6$, $4p = 12$, $6p = 18$, and so on. The respective angular frequencies of those components are $2\omega_e$, $4\omega_e$, $6\omega_e$, and so forth. Hence, each frequency component from the experimental vibration spectra only relates to one specific spatial order ERFD component. Based on the traditional method, the dominant component with the lowest spatial order of $2p = 6$ and frequency of $2\omega_e$ is expected from the experimental results of prototype III, while all other high spatial order components are relatively insignificant and hence negligible.

It can be observed from Figure 5.1(b) that the high spatial order ERFD components will be mechanically modulated by the stator tooth number to produce additional components with spatial orders of $(m \pm kZ)(k = 0, 1, 2, \dots)$ but the same frequency. In other words, the high spatial order ERFD components from the air gap can actually introduce corresponding low spatial order ERFD components on the stator yoke through stator tooth structure. For instance, the ERFD components with spatial orders of $4p = 12$, $8p = 24$ and $10p = 30$, can engender components with a spatial order of 3 and frequencies of $4\omega_e$, $8\omega_e$ and $10\omega_e$ respectively by the modulation of $Z = 9$ stator teeth in prototype III. The main ERFD component with spatial order of $2p = 6$ can also be modulated into ERFD on the stator yoke with spatial order of 3, which becomes the dominant excitation source for vibration with frequency of $2\omega_e$. Moreover, air-gap ERFD components with spatial orders of $6p = 18$ and $12p = 36$ can result in zeroth spatial order components on the stator yoke with frequencies of $6\omega_e$ and $12\omega_e$. The analysis of the stator tooth modulation effect implies that the experimental results will reveal quite significant vibrations at frequencies of $4\omega_e$,

$6\omega_e$, $8\omega_e$, and so on, besides $2\omega_e$. If that is the case, it can be considered that the tooth modulation effect has been validated indirectly. Near unity magnet pole-arc coefficient and closed-slot configuration are implemented in prototype III to produce abundant air-gap PM magnetic field components with notable amplitudes including the third, fifth and seventh orders. Therefore, evident resultant ERFD components with different spatial orders can be realized for the indirect validation.

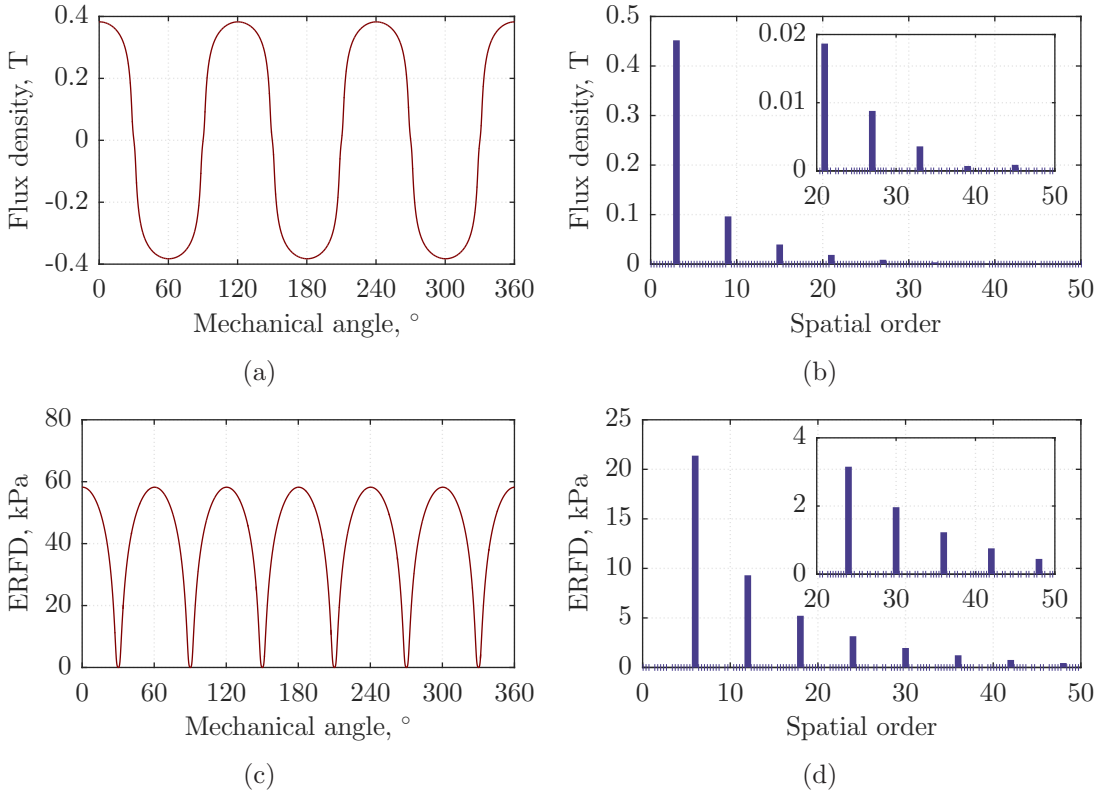

Figure 5.2: ERFD in prototype III with no-load condition: (a) air-gap PM magnetic field, (b) air-gap PM magnetic field spectrum, (c) ERFD distribution, (d) ERFD spectrum.

5.2.1 Magnetic Field Analysis Without Slot Effect

The main slotless air-gap magnetic field distribution produced by the PMs in prototype III in the no-load condition can be obtained using a 2-D FEA model without stator slots, which is depicted in Figure 5.2(a). The actual slot harmonics in prototype III will be investigated separately. It can be observed from the figure that the overall air-gap PM magnetic field flux density, whose peak value is approximately 0.4T, is rather small due to the low energy ferrite magnets. However, it effectively avoids severe magnetic saturation in the narrow tooth shoes so that the cogging torque and slot opening effect can be minimized. Moreover, there are numerous air-gap PM magnetic field harmonic components with evident amplitudes from spectrum analysis in Figure 5.2(b), as expected in prototype III. As discussed

previously, the spatial orders of all these harmonic components are the same as their temporal orders. The corresponding air-gap ERFD distribution can be directly obtained from the dot-product of the air-gap magnetic field in Figure 5.2(a), which is illustrated in Figure 5.2(c). The corresponding spectrum can be directly compiled and is given in Figure 5.2(d). The air-gap PM magnetic field harmonic components will interact with each other to produce numerous ERFD components with different spatial and temporal orders. Similarly, each specific ERFD component has the same spatial and temporal orders. The main ERFD components in Figure 5.2(d) will be applied as load pressure excitations in a 3-D mechanical FEA model, together with their corresponding spatial and temporal orders.

It can be seen from the figure that the ERFD component with the lowest spatial order of $2p = 6$ is of the largest amplitude. This component mainly arises from the fundamental ($p = 3$) air-gap PM magnetic field. As the spatial order increases, the corresponding structural eigenvalue frequency of the stator will significantly increase. Together with their relatively small amplitudes, the high spatial order harmonic components in Figure 5.2(d) can be neglected in the traditional analysis method. However, the ERFD component with spatial order of $4p = 12$ is 44%, very close to half the amplitude of the $2p = 6$ component, while even the amplitude of $8p = 24$ order component can reach up to 15%. Furthermore, the frequencies of those two components are double and quadruple of the main component, and hence the corresponding acceleration components on the stator yoke can be quite significant due to the stator tooth modulation effect. The ERFD components with spatial order higher than 40 will not be taken into account in further analysis due to their small amplitudes. It is noteworthy that there is a significant zeroth spatial order ERFD component, which is not included in Figure 5.2(d). However, the corresponding frequency of this component is zero, and hence it will only cause a static stator shell deformation but no vibration.

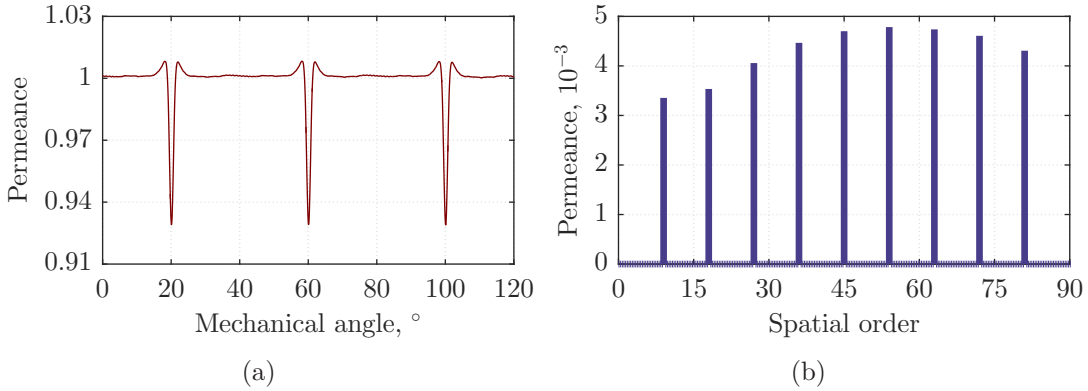

Figure 5.3: Relative slot permeance and its spectrum: (a) relative slot permeance, (b) relative permeance spectrum.

5.2.2 The PM Slot Harmonic Components

The interaction of the stator relative slot permeance and air-gap PM or armature reaction magnetic field will result in slot harmonic components. Different from the primary air-gap PM magnetic field components, the spatial and temporal orders of specific slot harmonic components are normally different. However, slot harmonic components with different spatial orders can have the same temporal orders, such as the second and forth items in Table 4.1. The relative slot permeance of the machine can be derived based on the division between air-gap magnetic field distribution curves of realistic and slotless FEA models. However, there are several zero crossing points for both curves, and a specific numerical algorithm is dedicated to eliminate computational errors near such points. The resultant relative permeance waveform of prototype III is obtained and depicted together with its spectrum in Figure 5.3. It can be found that all the relative slot permeance harmonic components are small, with the largest amplitude of 0.0048, as a result of the nearly closed-slot configuration. Based on the relative slot permeance and main air-gap PM magnetic field components, the PM slot harmonic components can be directly evaluated as shown in Figure 5.4(a). It can be observed that there are many more components than the slotless magnetic field. The amplitudes of those slot harmonic components are only half the product of the corresponding relative slot permeance and PM magnetic field harmonic components. Therefore, the largest slot harmonic component has an amplitude of less than 0.25% of fundamental PM amplitude. This result suggests that all PM slot harmonic components can be neglected in prototype III. The stator slot permeance will also affect the air-gap armature reaction magnetic field and will be discussed later.

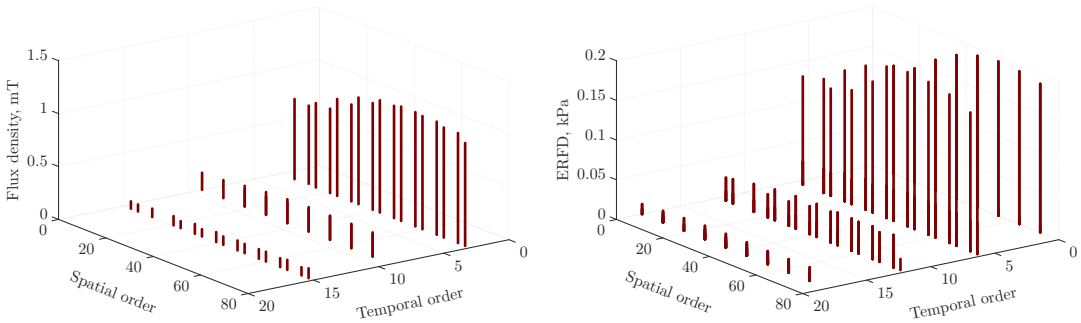

(a) (b)

Figure 5.4: PM slot harmonic and associated ERFD components: (a) PM slot magnetic field harmonics, (b) ERFD components associated with PM slot harmonics.

Besides interactions between themselves, the PM slot harmonic components can also interact with the main air-gap PM magnetic field components to generate associated ERFD. Using trigonometric operations between two arbitrary field components, the primary resultant ERFD components with associated spatial and temporal orders are evaluated and plotted in Figure 5.4(b). Here, all the ERFD components introduced by the interactions of two PM slot harmonic components are omitted due to

their insignificant amplitudes. Generally, even the largest ERFD component associated with the PM slot harmonic is still two orders of magnitude smaller than the primary component with the same temporal order shown in Figure 5.2(d). Consequently, it is reasonable to exclude all the ERFD components associated with PM slot harmonics in further vibration analysis of prototype III.

Furthermore, the PM slot harmonic components will introduce cogging torque in the machine, which is one of the primary sources of torsional vibration in PMSMs. Moreover, the radial and circumferential components of the vibration from the measurement may interfere with each other due to imperfect installation of the accelerometer. The vibration frequencies of the potential interferences are strongly correlated with the respective spatial orders of cogging torque. The corresponding spatial orders of cogging torque are the common multiple of the rotor pole and stator slot numbers and can be obtained as $18k(k = 1, 2, \dots)$ for prototype III. Thus, they are in accordance with the ERFD components with frequencies of $6\omega_e$, $12\omega_e$, $18\omega_e$, and so on. Nevertheless, the cogging torque in prototype III is trivial owing to the small slot opening and large air-gap length. On the whole, the influences of the slots on vibration characteristics in prototype III are effectively minimized due to its small slot opening. Consequently, neglecting the slot effect during vibration analysis of prototype III will not result in a substantial loss of accuracy for the prediction.

5.2.3 The Armature Reaction Under No-load Condition

The experimental tests on prototype III are carried out under no-load conditions in order to mitigate the armature currents in the stator phase windings. Therefore, the air-gap armature reaction magnetic field in the machine can be minimized. Moreover, a sensorless vector control with $i_d = 0$ scheme is implemented on prototype III to perform two different speed operations so that any background noise can be identified and remove from the measurement results. The experimental phase current waveforms under operational speeds of 2000rpm and 3000rpm are captured and illustrated in Figure 5.5(a) and 5.5(c) respectively. The respective spectra are compiled and depicted in Figure 5.5(b) and 5.5(d) respectively. The fundamental electric frequency can be easily derived as 100Hz and 150Hz. Figure 5.2(b) reveals notable fifth and seventh air-gap PM magnetic field harmonic components. Together with the rather high winding factors, the corresponding harmonic components of the phase back EMF in prototype III are quite significant. As a result, significant current harmonic components will be generated in the VSI powered windings, as shown in Figure 5.5. The fifth harmonics are much larger than the seventh harmonics due to the higher PM magnetic field amplitude but lower impedance. It can be determined from the figures that the fundamental current components are 97mA and 108mA at speeds of 2000rpm and 3000rpm due to the electromagnetic losses, mechanical ventilation and friction losses. The amplitudes of the fifth harmonic components are about 54mA and 60mA, while the seventh harmonics are around 8mA and 11mA. Overall, the current harmonic components are effectively reduced during the experimental tests and all the current harmonic components have simi-

lar low amplitudes. Hence, their corresponding air-gap armature reaction magnetic field components will be on a similar level.

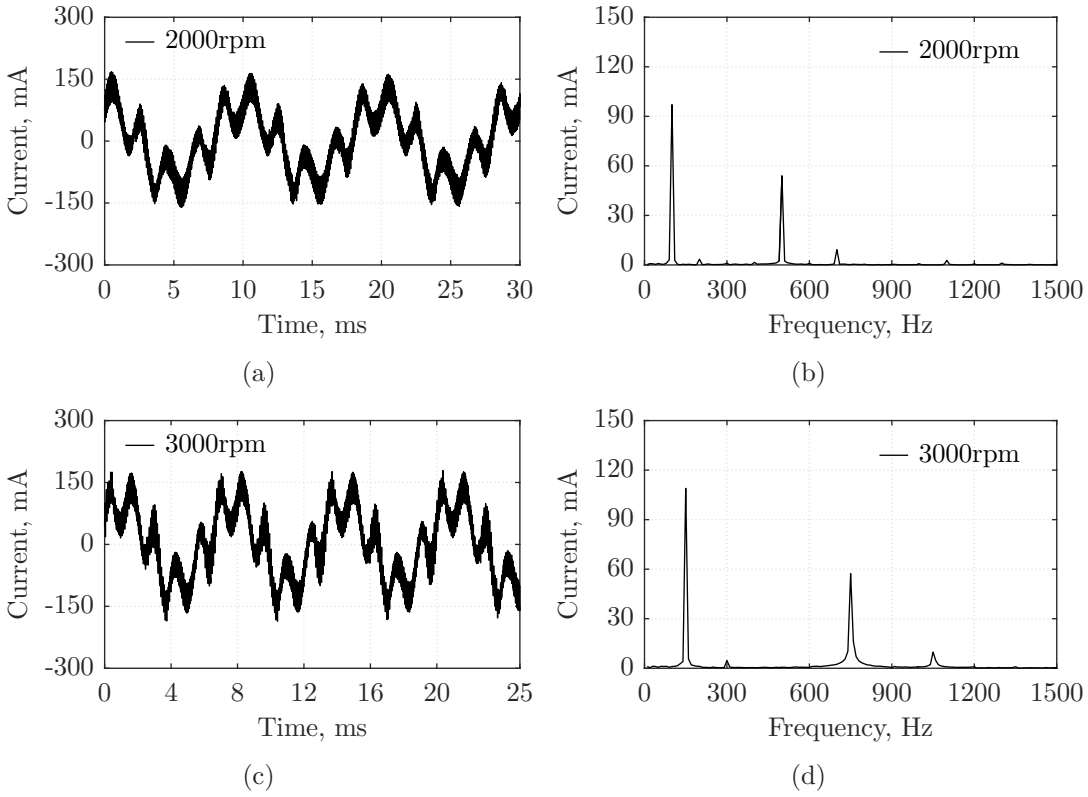

Figure 5.5: Experimental phase current waveforms and their spectra: (a) current waveform at 2000rpm, (b) spectrum of Current at 2000rpm, (c) current waveform at 3000rpm, (d) spectrum of Current at 3000rpm.

Without loss of generality, a fundamental current of 108mA is employed as the armature excitation for the FEA model to evaluate the air-gap armature reaction magnetic field. The corresponding magnetic field distributions are derived from the FEA results and the resultant radial and tangential components are shown in Figure 5.6(a) and 5.6(c) respectively. The tangential components are close to their radial counterparts as a result of the small slot opening. All the frequencies of these components are the same as the frequency of the excitation current component. Here, it is the fundamental electric frequency. The spectrum analysis are performed on both the radial and tangential components and the respective spectra are given in Figure 5.6(b) and 5.6(d). The FSCW configuration brings about rich slot harmonic components in the armature MMF and hence the associated magnetic field. However, it can be seen directly from the figure that the amplitudes of such magnetic field harmonic components are very close to those of the PM slot harmonics in Figure 5.4. Consequently, all these armature reaction magnetic fields in prototype III with no-load conditions can also be neglected for the further ERFD and vibration analysis thanks to their trivial amplitudes.

Besides the fundamental current component, there are also fifth and seventh current

harmonic components in Figure 5.5. The air-gap armature reaction magnetic field components from these current harmonic components can be evaluated by exactly the same procedure. Much smaller amplitudes of the magnetic field components are expected and hence all those components can also be excluded in further analysis. Furthermore, the armature reaction slot harmonic components will be even smaller than the main armature reaction magnetic field components so that they can be completely disregarded for this case.

In addition, the back EMF and armature current harmonic components can incur torque pulsations in prototype III. It can be seen in Figure 5.5 that the fifth harmonic is the main current phase belt harmonic component. The interaction between the fifth current harmonic and fundamental back EMF components will contribute to the main torque ripple component with frequency of $6\omega_e$. On the other hand, the fifth and seventh back EMF harmonic components will also interact with the fundamental current to produce torque pulsations with the same frequency. Similar to cogging torque, the interference between the radial and circumferential vibration measurements can occur at frequency of $6\omega_e$.

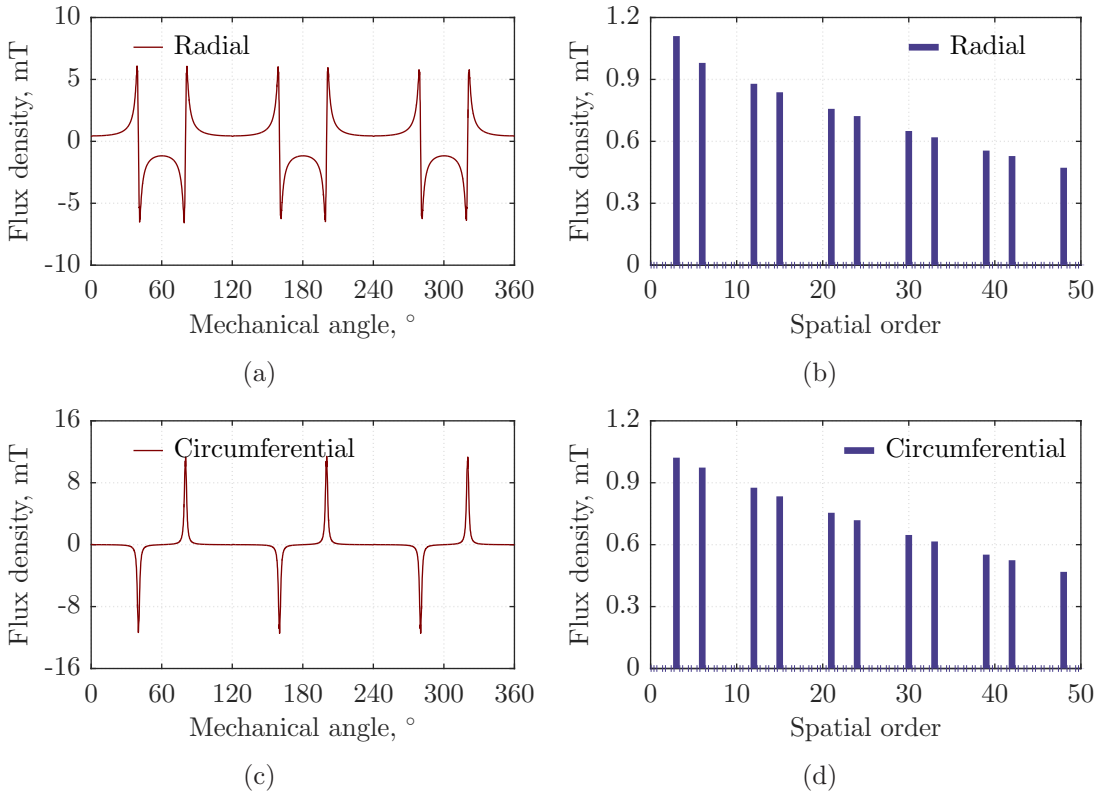

Figure 5.6: Air-gap magnetic field induced by armature reaction: (a) the radial component, (b) the radial component spectrum, (c) the circumferential components, (d) the circumferential component spectrum.

As discussed above, it can be concluded that consideration of only the ERFD components induced by the main air-gap PM magnetic field suffices in prototype III with no-load conditions. Due to their negligible amplitudes, the components asso-

ciated with stator slot and armature reaction harmonic components can be ignored during analysis. Consequently, only the ERFD components in Figure 5.2(d) can potentially result in significant vibration on the stator and hence all these components will be further employed for the mechanical vibration analysis of prototype III under no-load conditions.

5.2.4 Tooth Modulation Effect Validation

Both mechanical FEA simulations and experimental tests on the prototype III with no-load conditions are performed to underpin the validity of the stator tooth modulation effect on ERFD. The mechanical FEA results can describe such effects visually while the experimental results will validate it indirectly.

FEA Validation

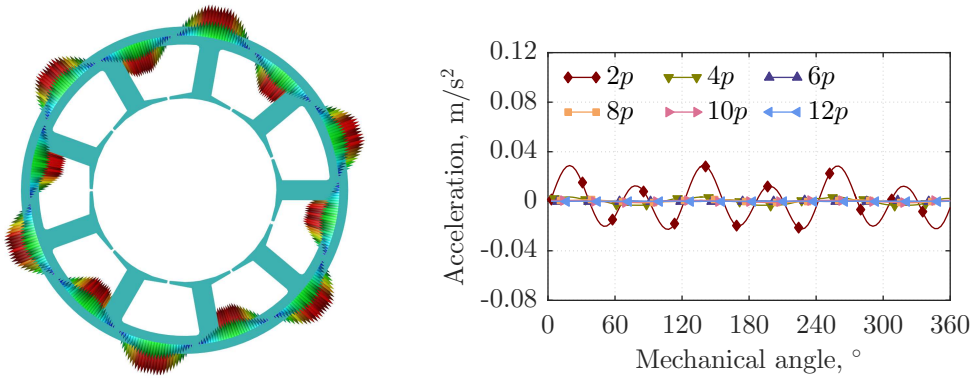

(a) (b)

Figure 5.7: Yoke loading ERFD model: (a) yoke loading model, (b) acceleration prediction.

In the traditional method based on Equation (5.3) and (5.6), it can be considered that the equivalent ERFD components derived are directly acting on the stator yoke. In order to examine the resultant vibration characteristics, the mechanical FEA simulation model with equivalent ERFD components acting on the stator yoke is constructed as shown in Figure 5.7(a). By applying all the equivalent ERFD components derived in Figure 5.2(d), the corresponding vibration responses are obtained from the FEA results and shown in Figure 5.7(b). It is worth noting that the equivalent ERFD component $P'_{m\_\omega_k}$ acting on the yoke can be directly evaluated by Equation (5.7). As expected, only the ERFD component with spatial order of $2p = 6$ delivers dominant vibration while all the other components result in very small and hence negligible responses. Furthermore, the sixth order shape deformation of the stator shell which originates from the ERFD with spatial order of $2p = 6$ is the largest component. In fact, the ERFD components act on the tooth shoe surfaces instead of stator yoke. Therefore, the mechanical FEA simulation model with

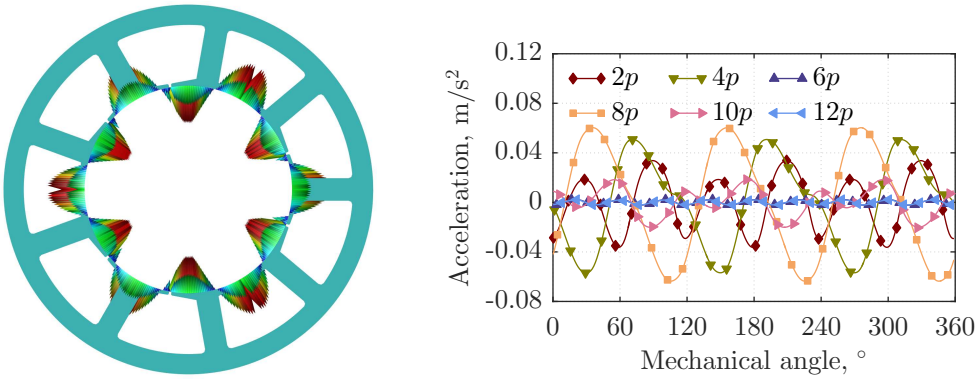

(a) (b)

Figure 5.8: Teeth loading ERFD model: (a) teeth loading model, (b) acceleration prediction.

ERFD components acting on the stator tooth surfaces is established and illustrated in Figure 5.8(a) for direct comparison. By applying all the ERFD components in Figure 5.2(d), the acceleration from each ERFD component is predicted by the corresponding FEA model and all these vibration responses are revealed and compared in Figure 5.8(b). It can be seen from the figure that all the ERFD components with spatial order of $4p = 12$ and $8p = 24$ can incur more significant accelerations than the component with spatial order of $2p = 6$. The ERFD component with spatial order of $10p = 30$ will also produce quite a significant vibration response on the stator system. Based on the stator tooth modulation effect, the third order shape deformation of the stator shell, which is modulated from the ERFDs with spatial order of $2p = 6$, $4p = 12$, $8p = 24$ and $10p = 30$, is the primary component.

The typical stator shell deformation modes from the teeth loading ERFD components of $4p = 12$ and $6p = 18$ are derived from the mechanical FEA results and revealed in Figure 5.9. As a result of the modulation effect of the teeth on the ERFD transmission in the stator, significant deformation of the third order mode is incident on the stator shell by the ERFD component with spatial order of $4p = 12$ as depicted in Figure 5.9(a). Moreover, zeroth order shape deformation should be introduced on the stator shell by the ERFD component with spatial order of $6p = 18$. However, the tooth shoe arc width is nearly double the wavelength of the 18^{th} spatial order component due to its nearly closed-slot configuration. As a result, the overall ERFD acting on each tooth surface contributed by the ERFD component with spatial order of $6p = 18$ is close to zero so that the corresponding deformation is quite small. Therefore, the resultant vibration responses from the ERFD components with spatial orders of $6p = 18$ and $12p = 36$ are much smaller than other components. As such ERFD is sinusoidally distributed on each tooth shoe surface, and the resultant local radial forces on the left sides of all the stator tooth shoes are always opposite to the right components with almost the same amplitudes. As a consequence, ERFD characteristics on the stator teeth excite the modal shape with the stator teeth leaning in the same direction, as shown in Figure 5.9(b). With the frequency of $6\omega_e$, it can lead to circumferential vibration on the stator shell. Similar

circumferential vibrations can be induced by other ERFD components such as the $12p = 36$-order component.

Experimental Validation

Based on the comprehensive comparisons between the FEA results of two different methods, significant deviations have been demonstrated with the same ERFD components. The traditional method suggests that only the vibration induced by the ERFD component with spatial order of $2p = 6$ and frequency of $2\omega_e$ is expected in prototype III with no-load conditions. On the other hand, frequencies of $2\omega_e$, $4\omega_e$ and $8\omega_e$ should be observed in the stator radial vibration spectrum, which are introduced by the ERFD components with spatial orders of $2p = 6$, $4p = 12$ and $8p = 24$ through the stator tooth modulation effect. Hence, further experimental tests are carried out to validate the stator tooth modulation effect indirectly.

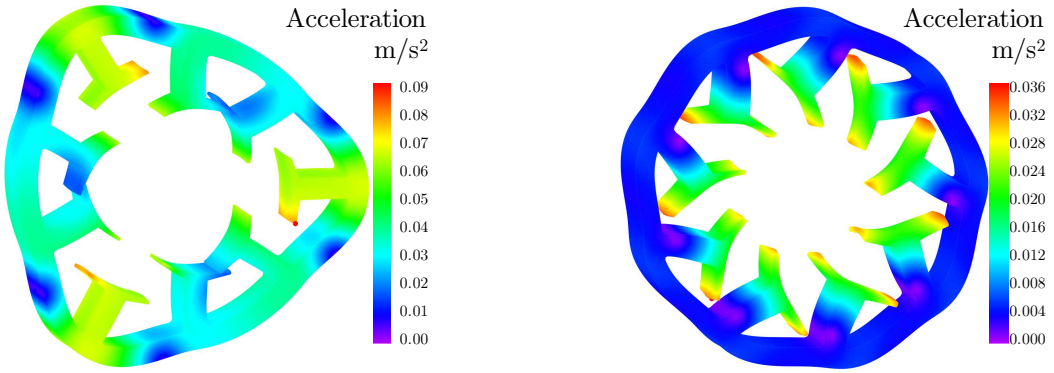

(a) (b)

Figure 5.9: Modal shape of teeth loading ERFD model: (a) $4p = 12$, (b) $6p = 18$.

The stator radial vibration of prototype III with no-load condition are measured accordingly under different speeds of 2000rpm and 3000rpm in order to validate the stator tooth modulation effect. Normally, the vibration measurement under one specific operational speed is sufficient for most cases as its spectra are similar in theory for different speeds. However, the ERFD components in prototype III are relatively small, so are the resultant stator radial vibrations. Moreover, there are some inevitable errors from the test platform installation and instrumental interference. Consequently, the stator vibration measurements from the prototype with two different speed conditions can improve the credibility of the results, and effectively reduce the potential error and confidently validate the tooth modulation effect. The FEA results from both teeth and yoke loading ERFD model are further employed to obtain the corresponding amplitudes of the stator radial vibration induced by different ERFD components. The experimental results, together with FEA results, are illustrated and compared in Figure 5.10. It can be inspected from the figure that significant vibrations occur at frequencies of $2\omega_e$, $4\omega_e$, $8\omega_e$ and $10\omega_e$ in the experimental results for both operational speeds, while the vibrations at frequencies of $6\omega_e$ and $12\omega_e$ are much smaller. It is apparent from the figure that the teeth

loading ERFD model can offer more reasonable and realistic vibration predictions of the prototype. Whilst, the yoke loading ERFD model based on traditional method significantly underestimates all the vibration components except the component induced by the $2p = 6$-order ERFD. Moreover, cogging torque and torque ripple in the prototype III with no-load conditions are insignificant and hence their influences on the stator radial vibrations with frequencies of $6\omega_e$ and $12\omega_e$ can be neglected. Overall, it can be concluded that the tooth modulation effect is effectively validated by the FEA and experimental results.

As a consequence, the existing traditional method can introduce unacceptable errors to the tooth effect on the stator radial vibration characteristics by just integrating the stator slot permeance and its associated slot harmonic components. A new approach, which can effectively represent the stator tooth modulation effect, is highly desirable to deliver accurate predictions of stator radial vibration in PMSMs. The teeth loading ERFD FEA model presented in this section inherently incorporates the stator tooth modulation effect in the simulations and hence can give very realistic predictions.

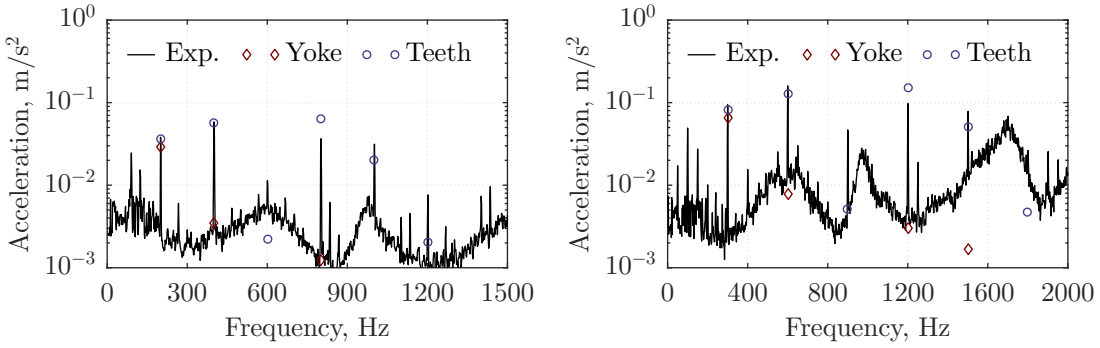

Figure 5.10: Experimental validation of the stator tooth modulation effect: (a) vibration at 2000rpm, (b) vibration at 3000rpm.

5.3 Analytical Model of Tooth Modulation Effect

As aforementioned, the stator tooth modulation effect instead of slot harmonic components is considered during stator radial vibration analysis. The tooth modulation effect has been numerically investigated and validated by mechanical FEA models. However, the numerical models cannot offer intuitive knowledge of the stator tooth modulation effect so that an effective and yet simple analytical model can benefit the stator radial vibration significantly. In this section, an analytical model of the tooth modulation effect is developed by exactly following the analysis employed in the previous section. The analytical model can be employed to not only promptly investigate the stator radial vibration characteristics but also perform effective optimization.

5.3.1 Symmetrical Stator Tooth Modulation Effect

Based on the universal ERFD model expressed in Equation (5.2), the overall radial force acting on the whole tooth contributed by a certain ERFD component with spatial order of m and frequency of ω_k can be obtained by integration over the tooth shoe arc width and presented as

$$f_t(\theta_m, t) = \frac{2R_0 L_{ef} P_{m\_\omega_k}}{m} \sin\frac{m\beta}{2} \cos\left(m\theta_0 - \omega_k t - \varphi_{m\_\omega_k}\right) \tag{5.10}$$

θ_0 is defined as position angle at center of the tooth. It can be noticed that $m > 0$ is assumed in Equation (5.10). With $m = 0$, it can be rewritten as

$$f_t(\theta_m, t) = R_0 L_{ef} \beta P_{0\_\omega_k} \cos\left(\omega_k t + \varphi_{m\_\omega_k}\right) \tag{5.11}$$

As demonstrated in Figure 5.1(b), it is assumed that the ERFD acting on the stator tooth shoe is evenly distributed and hence transmitted in radial direction only. Consequently, the corresponding equivalent ERFD component can be approximated as

$$P_t'' = \frac{2R_0 P_{m\_\omega_k}}{mR_y\gamma} \sin\frac{m\beta}{2} \cos\left(m\theta_0 - \omega_k t - \varphi_{m\_\omega_k}\right) \tag{5.12}$$

while the zeroth order component can be written as

$$P_t'' = \frac{\beta R_0 P_{0\_\omega_k}}{R_y\gamma} \cos\left(\omega_k t + \varphi_{0\_\omega_k}\right) \tag{5.13}$$

Hence the resultant ERFD component acting on the stator yoke becomes a square wave over the whole shell circle. By applying the Fourier series expansion of the load on the tooth, the amplitudes of the n^{th} harmonic components can be obtained and expressed as

$$\begin{cases} a_{n_1} = \dfrac{2R_0 P_{m\_\omega_k}}{nm\pi\gamma R_y} \sin\dfrac{n\gamma}{2} \sin\dfrac{m\beta}{2} \cos((m \pm n)\theta_0 - \omega_k t - \varphi_{m\_\omega_k}) \\ b_{n_1} = \pm\dfrac{2R_0 P_{m\omega_k}}{nm\pi\gamma R_y} \sin\dfrac{n\gamma}{2} \sin\dfrac{m\beta}{2} \sin((m \pm n)\theta_0 - \omega_k t - \varphi_{m\_\omega_k}) \end{cases} \tag{5.14}$$

Similarly, the corresponding amplitudes of the n^{th} ERFD harmonic components on the stator yoke from the $(i+1)^{th}$ tooth, where $0 < i < Z - 1$, can be derived as

$$\begin{cases} a_{n_{i+1}} = \dfrac{2R_0 P_{m\_\omega_k}}{nm\pi\gamma R_y} \sin\dfrac{n\gamma}{2} \sin\dfrac{m\beta}{2} \cos((m \pm n)(\theta_0 + i\alpha) - \omega_k t - \varphi_{m\_\omega_k}) \\ b_{n_{i+1}} = \pm\dfrac{2R_0 P_{m\_\omega_k}}{nm\pi\gamma R_y} \sin\dfrac{n\gamma}{2} \sin\dfrac{m\beta}{2} \sin((m \pm n)(\theta_0 + i\alpha) - \omega_k t - \varphi_{m\_\omega_k}) \end{cases} \tag{5.15}$$

It can be derived for $m = 0$ as

$$\begin{cases} a_{n_{i+1}} = \dfrac{\beta R_0 P_{0\_\omega_k}}{n\pi\gamma R_y} \sin\dfrac{n\gamma}{2} \cos(\pm n(\theta_0 + i\alpha) - \omega_k t - \varphi_{0\_\omega_k}) \\ b_{n_{i+1}} = \pm\dfrac{\beta R_0 P_{0\_\omega_k}}{n\pi\gamma R_y} \sin\dfrac{n\gamma}{2} \sin(\pm n(\theta_0 + i\alpha) - \omega_k t - \varphi_{0\_\omega_k}) \end{cases} \tag{5.16}$$

By superposition of the components from all the stator teeth, the n^{th} ERFD harmonic component introduced by $P_{m\_\omega_k}$ can be proposed as

$$p'_{n\_\omega_k}(\theta_m, t) = \sum_{i=1}^{Z} \left(a_{n_i} \cos(n\theta_m) + b_{n_i} \sin(n\theta_m)\right) \tag{5.17}$$

By substituting Equation (5.15) into Equation (5.17), the corresponding harmonic component can be derived. It can be noticed that $p'_{n\_\omega_k}$ will be zero as $m \pm n \neq kZ$, where k is integer. With $m \pm n = kZ$, $p'_{n\_\omega_k}$ can be represented as

$$p'_{n\_\omega_k}(\theta_m, t) = K_{m\_n} P'_{m\_\omega_k} \cos(n\theta_m \pm \omega_k t \mp kZ\theta_0 \pm \varphi_{m\_\omega_k}) \tag{5.18}$$

where K_{m_n} is defined as tooth effect coefficient and is determined by

$$K_{m\_n} = \frac{2Z}{nm\pi\gamma} \sin\frac{n\gamma}{2} \sin\frac{m\beta}{2} \tag{5.19}$$

It can be inspected from Equation (5.18)that the rotational direction of the modulated ERFD is opposite to the original component with $m + n = kZ$, while it keeps the same rotational direction with $m - n = kZ$.

Moreover, $p'_{0\_\omega_k}$ component will be introduced with $m = kZ$, $k = 1, 2, \ldots$, and it can be still written in the same form as Equation (5.18). The corresponding tooth effect coefficient can be obtained as

$$K_{kZ\_0} = \frac{1}{k\pi} \sin\frac{kZ\beta}{2} \tag{5.20}$$

In particular, the ERFD harmonic component with spatial order of 0 can be expanded analogously and presented as

$$K_{0\_0} = \frac{Z\beta}{2\pi}, \quad K_{0\_kZ} = \frac{2\beta}{k\pi\gamma} \sin\frac{kZ\gamma}{2}. \tag{5.21}$$

By substituting Equation (5.18) into Equation (5.6), the corresponding stator radial vibration can be analytically obtained. The low spatial order ERFD harmonic components on the stator yoke from stator tooth modulation effect are prone to significant vibration. Consequently, considerations of the harmonic components with spatial order of $n \leq Z/2$ in (5.19) are sufficient for most cases. Meanwhile, the modulated harmonic component with spatial order of n, where $Z/2 < n \leq Z$, possesses spatial order component of $(n - Z)$ and is more likely to cause stator vibration. Furthermore, the angle of γ, which is dependant on the stator tooth width, is normally smaller than π/Z. As a result, $\sin(n\gamma/2) \approx n\gamma/2$ can be approximated, and the tooth effect coefficient in (5.19) can be approximated as

$$K_{m\_n_0} = \frac{Z}{m\pi} \sin\frac{m\beta}{2} \tag{5.22}$$

where, n_0 represents the component with spatial order less than or equal to $Z/2$.

Normally, the slot opening coefficient is more frequently employed for the machine design so that Equation (5.22) can be rewritten as

$$K_{m\_n_0} = \frac{Z}{m\pi} \sin \frac{mK_t\pi}{Z} \tag{5.23}$$

where

$$K_t = 1 - \frac{W_{b_0}}{W_t} \tag{5.24}$$

It can be inspected from Equation (5.23) that the slot opening coefficient is the only parameter that will influence the tooth modulation effect. Therefore, the radial vibration of the stator shell can be effectively reduced by optimizing the slot opening coefficient. As the ERFD acting on each tooth shoe surface from a certain ERFD component is evenly exerted in the proposed analytical model, Equation (5.18) can be named accordingly as symmetrical modulation model of stator tooth effect.

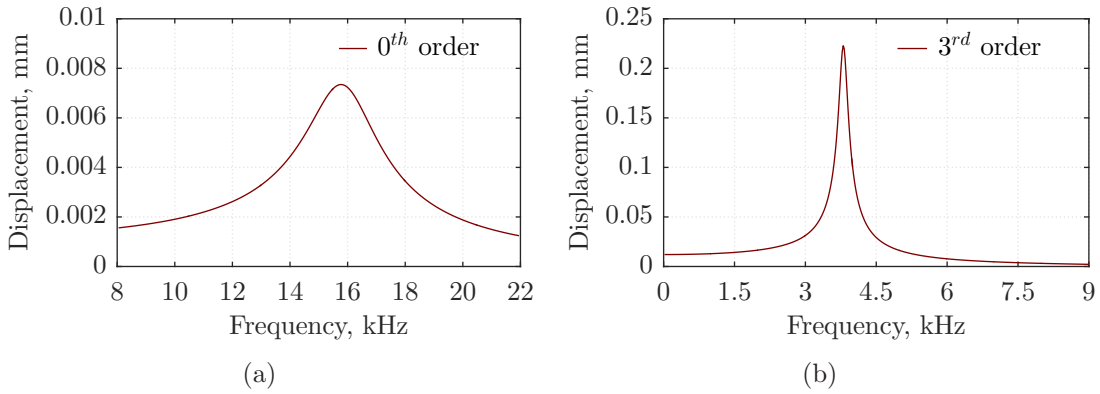

Figure 5.11: Natural resonance frequency analysis of different modes: (a) 0-order, (b) 3-order.

5.3.2 Stator Natural Frequency Analysis

Based on the symmetrical modulation model of stator tooth effect in Equation (5.18), the modulated equivalent ERFD component can be directly applied on the stator yoke. Consequently, the stator radial vibration can be analytically predicted. Additionally, the structural eigenvalue ω_m of stator system with mode m is still required for the analytical vibration evaluation. Nowadays, mechanical structural FEA method is a common practice for accurate eigenvalue extraction. Due to the rather complex stator structure, more than one resonance can exist for some specific stator modes. Hence, the frequency sweeping method, which is widely adopted in the practical measurement, is implemented in FEA frequency response models to identify the natural frequency of stator for each mode. As a result of the stator tooth modulation effect, the deformation shapes of the stator shell from ERFD components with certain spatial orders can be quite close and hence very difficult to distinguish. However, the frequency sweeping method can reveal the corresponding eigenvalue of the stator intuitively by the displacement-frequency response profile. The unit

ERFD component with specific spatial order is applied on the stator teeth, and the stator yoke deformation under different frequencies can be easily evaluated by mechanical FEA models. The damping ratios employed in FEA models are directly derived from Equation (5.4).

As aforementioned, all the main ERFDs in Figure 5.2(d) will introduce the components with spatial orders of 0 and 3 due to the stator tooth modulation effect. Those zeroth and third spatial order harmonic components are the main cause of stator radial vibration in prototype III under no-load condition. Therefore, the 3-D mechanical FEA simulations are carried out to obtain the natural frequencies of the stator with zeroth and third spatial order modes. Figure 5.11 demonstrates the respective stator displacement-frequency response curves of prototype III with unit zeroth and third spatial order ERFD components. It can be directly obtained from the figure that the natural frequencies of the stator with zeroth and third spatial order modes are 15870Hz and 3807Hz respectively. The corresponding mode shapes

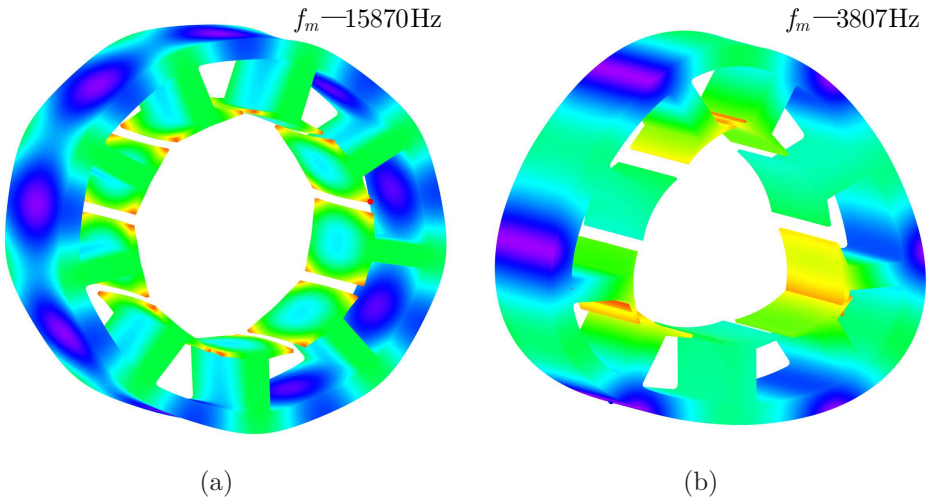

Figure 5.12: Modal shapes of zeroth and third order: (a) zeroth mode, (b) third mode.

of the stator from such ERFD components are derived from FEA results and depicted as Figure 5.12. As a result of the stator tooth modulation effect, the n^{th} and $(n-Z)^{th}$ spatial order modes are always concomitant. Figure 5.12(b) demonstrates distinctive third order mode characteristics of the stator. Meanwhile, noticeable sixth order mode characteristics of the stator yoke coexist due to the nine stator teeth. It can be observed from Figure 5.12(a) that the coexistence of the zeroth and ninth order mode characteristics of the stator is quite apparent. Although zeroth order mode is the lowest spatial order, the corresponding eigenvalue is much larger than its third order counterpart. It implies that zeroth spatial order ERFD will not necessarily induce more significant vibration than other components even with the same amplitude and frequency.

5.3.3 Experimental Validation and Discussion

With the natural frequencies of the stator from mechanical FEA evaluations, the radial vibration of the stator system can be directly derived based on Equation (5.3) and (5.18). The experimental results obtained in Subsection 5.2.4 are employed in order to validate the proposed analytical model of stator tooth modulation effect. The analytical and FEA results of prototype III with no-load condition under different speeds of 2000rpm and 3000rpm are evaluated and compared with the corresponding experimental results in Figure 5.13.

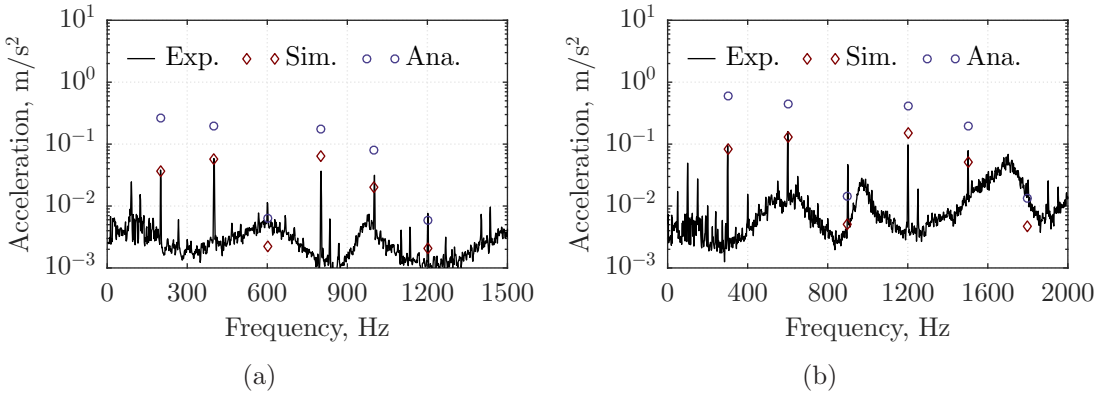

Figure 5.13: Experimental validation of analytical model: (a) vibration at 2000rpm, (b) vibration at 3000rpm.

It can be seen from the figure that the analytical model can well reveal the stator radial vibration characteristics of prototype III. Relatively severe radial vibrations occur at frequencies of $2\omega_e$, $4\omega_e$, $8\omega_e$ and $10\omega_e$, while they hardly exist at frequencies of $6\omega_e$ and $12\omega_e$. As the corresponding ERFD components with spatial orders of $2p = 6$, $4p = 12$, $8p = 24$ and $10p = 30$ can be modulated into third spatial order with the unchanged frequencies, evident radial vibrations will be induced accordingly on the stator yoke. On the other hand, the large stator natural frequency of zeroth mode result in trivial vibrations from ERFD components of $6p = 18$ and $12p = 36$ orders.

There are notable deviations between analytical and experimental results. The proposed analytical model tends to overestimate the corresponding vibration amplitudes, especially the component induced by the ERFD with spatial order of $2p = 6$. The underlying assumption of the proposed analytical model neglect the impacts of the actual complex ERFD distributions on the stator tooth shoe surfaces on stator vibration. The uneven ERFD distributions on the stator tooth shoe surfaces will affect the mechanical response of the stator significantly and hence result in evident prediction errors in the proposed analytical model.

The proposed analytical model of stator tooth modulation effect assumes the equal distribution of ERFD component on each individual tooth shoe surface by its mean value, p_t''', as depicted in Figure 5.14(a). However, such ERFD component is applied

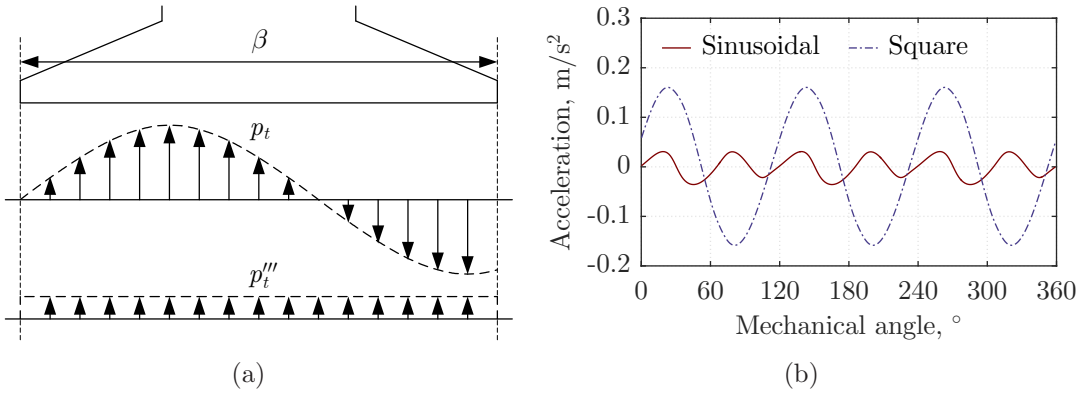

Figure 5.14: Influence of teeth loading ERFD mode: (a) schematic of ERFD component, (b) vibration response.

on the stator tooth shoe surface as a sinusoidal function of the position in practice, p_t, as illustrated in Figure 5.14(a) as well. The mechanical FEA models with the two different teeth loading ERFD modes are constructed. The corresponding stator radial vibration responses from the ERFD component with spatial order of $2p = 6$ are evaluated and compared in Figure 5.14(b). It can be observed from the figure that the two methods deliver completely different results. The square wave load model employed in the proposed analytical analysis will not only overestimate the vibration amplitude but also predict the wrong dominant vibration mode for this particular ERFD component. Figure 5.14(b) clearly shows that the predominant vibration mode of the stator induced by the ERFD with spatial order of $2p = 6$ is the sixth spatial order component from the practical sinusoidal model. Though the simplified square wave model artificially exaggerates the stator tooth modulation effect of the $2p = 6$ spatial order component in this case, it still can effectively uncover the tooth modulation effect. The prediction errors mainly arise from the lack of the ERFD distribution characteristics in the model, which will complicate the stator deformation feature. In practice, there are evident manifestation of sixth spatial order component. This is mainly caused by the interaction between the radial vibration of the stator yoke and circumferential vibration of the stator teeth.

The deformation shapes of the stator from the two different FEA models are derived and illustrated in Figure 5.15 for direct comparison. It can be directly seen from Figure 5.15(a) that the simplified square wave model delivers stator deformation shape with very distinctive third spatial order mode characteristics. Besides such third spatial order mode from the resultant average ERFD component, the practical sinusoidal model will exert radial force components with different amplitudes and directions on the left and right sides of each stator tooth shoe. Since the stator tooth shoes lack rigid mechanical constraints in the machine, majority of such peculiar ERFD will be expended locally to cause circumferential vibration of the teeth instead of being transmitted to stator yoke, as shown in Figure 5.15(b). Such circumferential vibration has a third spatial order characteristic. Therefore, the twists on the adjacent stator teeth pair are always in opposite direction. The combinational effect of the stator yoke radial vibration and teeth circumferential vibration

will result in a $2p = 6$ spatial order alike mode. Figure 5.15 also manifests that the simplified square wave model will significantly overestimate the radial vibration amplitude of the stator yoke but underestimate the circumferential vibration of the stator tooth shoes. Consequently, the proposed analytical model of stator tooth modulation effect requires improvement and extension to take into account this particular phenomenon.

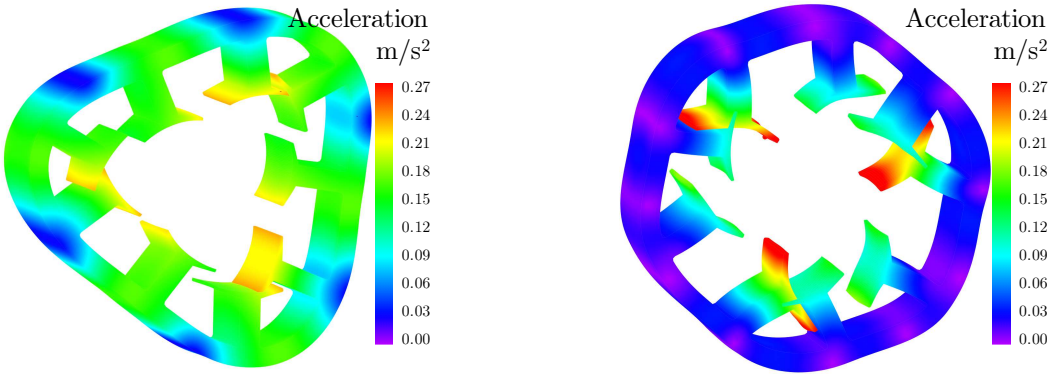

(a) (b)

Figure 5.15: Structural shape under different teeth loading ERFD modes: (a) average ERFD, (b) sinusoidal ERFD.

5.4 The Improved Tooth Modulation Effect Model

As revealed in the previous section, the uneven ERFD distribution on the stator tooth shoe surface will have quite vital effects on the radial vibration of the stator system. Significant prediction errors are introduced by the proposed analytical model of stator tooth modulation effect based on the assumption of even ERFD distribution. Consequently, an improved analytical model is developed with consideration of the unequal ERFDs on both sides of the stator tooth shoes. As the local phenomenon is partially included in the extended model, the prediction accuracy can be effectively improved.

5.4.1 Asymmetrical Stator Tooth Modulation Effect

It can be inspected from Figure 5.14(a) that the ERFD component over one stator tooth shoe surface can be surprisingly different. Therefore, the resultant ERFDs on the two sides of each stator tooth shoe are of different amplitudes and sometimes even opposite directions. Such ERFD characteristics tend to twist the stator teeth and hence result in a very peculiar mechanical behavior of stator system. In practice, the eventual ERFD acting on the stator yoke parts becomes unequal as well. As a result, the corresponding stator vibration modal shape induced by this particular ERFD component may alter. In order to take into account all these effects, it

is assumed that two ERFD parts, instead of single overall radial force, are acting on the left and right sides of each stator tooth respectively. Moreover, the left and right parts have the same acting range of $\gamma/2$ so that the overall acting range of γ keeps invariable, as shown in Figure 5.16(a). For the sake of simplicity, it is further assumed that the ERFD component is evenly distributed over each part. Moreover, the center positions of the left and right parts are $(\theta_0 \pm \beta/4)$, and hence the corresponding equivalent acting positions on the yoke are also considered as $(\theta_0 \pm \beta/4)$, as demonstrated in Figure 5.16(b). As the uneven distribution of ERFD component is factored, the improved model is also defined as asymmetrical modulation model of stator tooth effect.

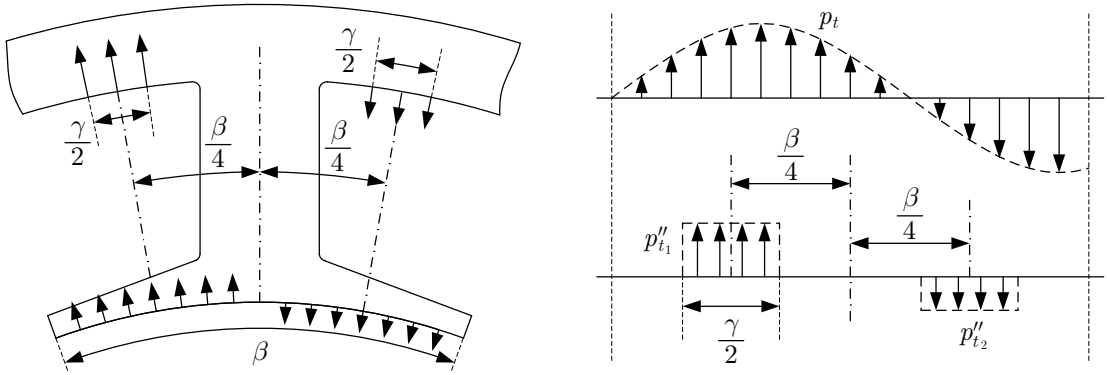

Figure 5.16: Improved tooth modulation effect model schematic: (a) equivalent asymmetrical ERFD, (b) shift ERFD model.

The corresponding analytical model can be derived by the same procedure as the symmetrical model. Similar to P''_t, both P''_{t_1} and P''_{t_2} can be obtained accordingly. As the zeroth spatial order ERFD component guarantees even distribution over the stator tooth shoe surfaces, the symmetrical and asymmetrical models will have exactly the same formulae. Furthermore, the equivalent ERFD amplitudes acting on the yoke can be respectively derived for non-zeroth spatial order components as

$$\begin{cases} P''_{t_1} = \dfrac{4R_0 P_{m\_\omega_k}}{mR_y\gamma} \sin\dfrac{m\beta}{4} \cos\left(m(\theta_0 - \dfrac{\beta}{4}) - \omega_k t\right) \\ P''_{t_2} = \dfrac{4R_0 P_{m\_\omega_k}}{mR_y\gamma} \sin\dfrac{m\beta}{4} \cos\left(m(\theta_0 + \dfrac{\beta}{4}) - \omega_k t\right) \end{cases} \tag{5.25}$$

By applying the Fourier series expansion on both components, the n^{th} order $(n \neq 0)$ component can be derived by synthesizing the items with the same order as

$$\begin{cases} a_{n_1} = \dfrac{8R_0 P_{m\_\omega_k}}{nm\pi\gamma R_y} \sin\dfrac{n\gamma}{4} \sin\dfrac{m\beta}{4} \cos\dfrac{(m \pm n)\beta}{4} \cos((m \pm n)\theta_0 - \omega_k t - \varphi_{m\_\omega_k}) \\ b_{n_1} = \pm\dfrac{8R_0 P_{m_{\omega_k}}}{nm\pi\gamma R_y} \sin\dfrac{n\gamma}{4} \sin\dfrac{m\beta}{4} \cos\dfrac{(m \pm n)\beta}{4} \sin((m \pm n)\theta_0 - \omega_k t - \varphi_{m\_\omega_k}) \end{cases} \tag{5.26}$$

By comparison with Equation (5.14), the above expressions of the improved model are with exactly the same format except the different coefficients. Similarly, the n^{th}

ERFD harmonic component introduced by $P_{m\_\omega_k}$ does not exist unless $m \pm n = kZ$ is true. With $m \pm n = kZ$, the corresponding $p'_{n\_\omega_k}$ can be expressed in exactly the same formula as Equation (5.18) with an improved tooth effect coefficient

$$K_{m\_n} = \frac{8Z}{nm\pi\gamma} \sin\frac{n\gamma}{4} \sin\frac{m\beta}{4} \cos\frac{kZ\beta}{4} \tag{5.27}$$

It can be inferred that the ERFD component over one stator tooth shoe surface can be divided into more parts in order to improve the accuracy. The more parts it divides into, the more accurate the analytical model will become. Without loss of generality, $2N_s$ ERFD parts can be assumed over each stator tooth shoe surface. Similarly, the overall tooth modulation effect coefficient can be derived as

$$K_{m\_n} = \frac{8ZN_s}{nm\pi\gamma} \sin\frac{n\gamma}{4N_s} \sin\frac{m\beta}{4N_s} \sum_{i=1}^{N_s} \cos kZ(i - \frac{1}{2})\frac{\beta}{2N_s} \tag{5.28}$$

When $N_s \to \infty$, the model can be further simplified as

$$K_{m\_n} = \frac{1}{k\pi} \sin\frac{kZ\beta}{2} = \frac{1}{k\pi} \sin kK_t\pi \tag{5.29}$$

It should be noted that the tooth modulation effect coefficient becomes K_t when $m = n$. It can be also inspected from Equation (5.29) the slot opening coefficient becomes the only parameter that will affect the stator tooth modulation effect. By substituting the tooth effect coefficient proposed in Equation (5.29) into Equation (5.18), the improved modulated ERFD component can be derived analytically. Together with Equation (5.3), the stator radial vibration can be further evaluated. As the uneven characteristics of the ERFD distribution on the teeth are partially included in the improved model, more accurate predictions of stator radial vibration can be offered.

5.4.2 Experimental Validation

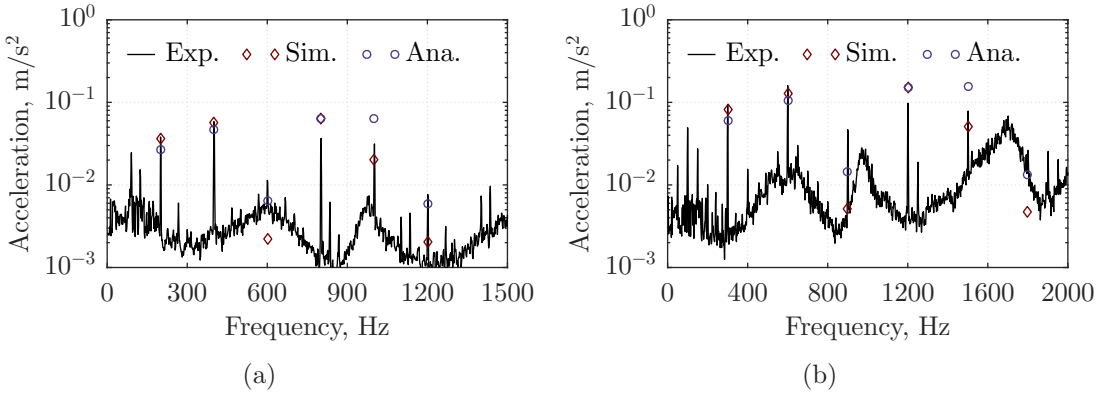

Figure 5.17: Experimental validation of the improved analytical model: (a) vibration at 2000rpm, (b) vibration at 3000rpm.

By substituting the improved asymmetrical modulation model, together with the corresponding natural frequency of the stator from mechanical FEA results, into Equation (5.3), the radial vibration of stator system can be analytically derived. The FEA and experimental results obtained in Subsection 5.2.4 are further employed to validate the improvement of the proposed asymmetrical modulation model for the stator tooth effect. The analytical result of prototype III with no-load condition under different speeds of 2000rpm and 3000rpm are predicted and compared with the corresponding FEA and experimental results in Figure 5.17. It can be seen from the figure that the improved analytical model still maintains the capability of accurate revelation on stator radial vibration frequency characteristics. Generally, the analytical results are in good agreements with the corresponding FEA and experimental results. The improved analytical model offers reasonably accurate predictions of all stator radial vibration components. It slightly underestimates the $2\omega_e$ and $4\omega_e$ components and mildly overestimates the $8\omega_e$ and $10\omega_e$ components. By comparison with Figure 5.13, it is apparent that the accuracy of the stator radial vibration prediction has been significantly improved. However, the mechanical behaviour in the stator system is rather complex. It is practically impossible to analytically characterize such sophisticated phenomenon completely. The improved asymmetrical modulation model of the stator tooth effect can promptly deliver reasonably accurate predictions of stator radial vibration by incorporating a simplified uneven characteristics of ERFD distribution.

5.4.3 Influence of Slot Parameters

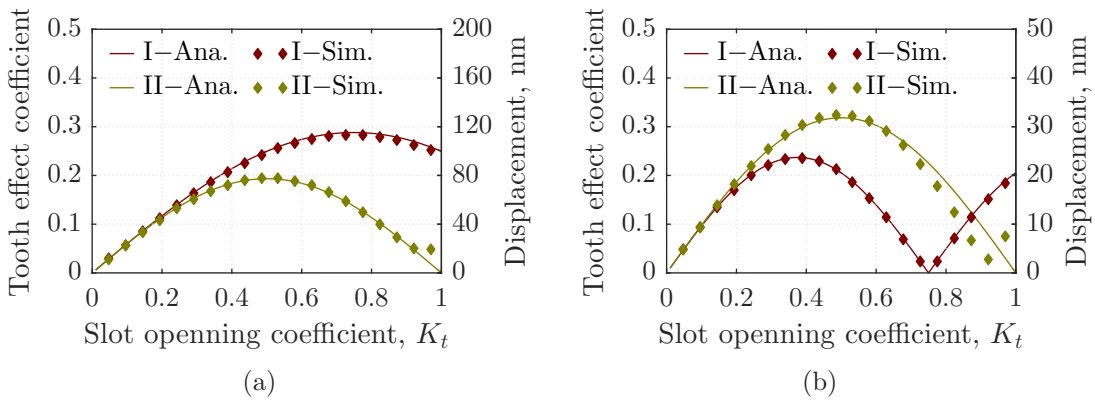

Figure 5.18: Influence of slot opening coefficient on the stator tooth effect: (a) $2p = 6$, (b) $4p = 12$. (I - Symmetrical model, II - Asymmetrical model, Ana. - Analytical result, Sim. - FEA result)

The tooth effect coefficient in Equation (5.29) suggests that the equivalent ERFD components transmitted to the stator yoke are highly dependant on the slot opening coefficient. As a result, the impact of the slot opening coefficient is synchronized with the stator slot and rotor pole number combination. Figure 5.18 reveals the influences of slot opening coefficient on the tooth effect coefficient of the modulated third spatial order ERFDs from the original components with spatial orders of $2p = 6$ and

$4p = 12$ respectively. It is noteworthy that the investigated machine has nine stator slots and six rotor magnet poles, the same as prototype III. Moreover, the FEA results of vibration displacement are derived from the simplified square wave and practical sinusoidal models. The amplitudes of $2p = 6$ and $4p = 12$-order ERFDs are 21.4kPa and 9.3kPa respectively. The results from both symmetrical and asymmetrical modulation model are evaluated and compared with the FEA simulations in Figure 5.18. It can be observed from the figure that the symmetrical modulation model will significantly overestimate the tooth effect coefficients and hence the corresponding modulated vibration especially with near unity slot opening coefficient. Moreover, excellent agreements between the analytical results from the symmetrical modulation model and FEA simulations from the simplified square wave model have been achieved. Meanwhile, the analytical results from the asymmetrical modulation model agree very well with the FEA simulations from the practical sinusoidal model when the slot opening coefficient is extremely small, but the incline of slot opening coefficient can gradually aggravate the deviation. The discrepancy becomes quite significant with near unity slot opening coefficient. Although the stator radial vibration highly depends on the stator mechanical structure, a mere change of the slot opening coefficient will have minimum impact on the stator vibration characteristics. Hence, it is reasonable to assume the radial vibration components are in line with the corresponding ERFD components, and the proposed improved analytical model can be employed to promptly evaluate the effect of slot opening coefficient.

Normally, there ought to be one or more slot opening coefficients which can minimize the modulated ERFD component of specific spatial order induced by certain original component. However, such optimal slot opening coefficients are heavily influenced by the stator slot and rotor pole number combination. In general, a practical machine has slot opening coefficient $K_t > 0.5$ so that direct use of the symmetrical modulation model can incur significant prediction errors as shown in Figure 5.18. Moreover, the results in the figure confirm that the uneven characteristics of the ERFD distribution are the main cause of the prediction errors from the symmetrical modulation model. The improved asymmetrical modulation model can effectively mitigate such errors for most cases. However, special attention should be paid to the cases with near unity slot opening coefficient as even the asymmetrical modulation model can induce large errors. Besides the main modulated order, there are still some other modulated ERFD components with high spatial orders or even circumferential items. Those components can introduce associated radial vibration components in the stator. However, those components can normally be neglected as the amplitudes of the associated radial vibration components are quite trivial. It can be easily found that the air-gap magnetic field components normally vary with stator slot opening coefficient. Hence, the amplitudes of the air-gap ERFD components are somewhat dependant on the slot opening coefficient as well. Without loss of generality, the amplitudes of the air-gap ERFD components keep unchanged during this impact investigation of slot opening coefficient.

It can be deduced from Equation (5.29) that the actual tooth width has almost negligible effect on the transmission of the main ERFD components. 3-D mechanical FEA models of prototype III with stator tooth widths of 5mm and 8mm are

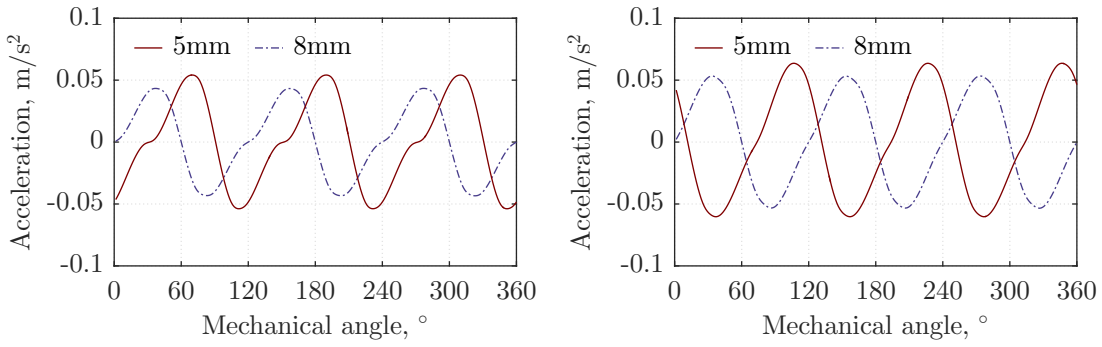

Figure 5.19: Influence of tooth width on the stator tooth effect: (a) $2p = 6$-order ERFD, (b) $4p = 12$-order ERFD.

constructed and analyzed in order to validate such conclusion. The radial vibration components induced by different ERFD components are evaluated with such two different stator tooth widths. The corresponding FEA results of the stator radial vibration components from the ERFD components with spatial order of $2p = 6$ and $4p = 12$ are derived and illustrated in Figure 5.19 for direct comparison. It can be observed from the figure that the corresponding vibration components have very close amplitudes and nearly the same profiles for both tooth widths. The stator with tooth width of 8mm has around 19% weight increase over the 5mm model. It can be considered that the abate of vibration amplitudes in the stator with width of 8mm mainly owes to the weight increase. Hence, it can be concluded that the validity of the proposed improved analytical model has been underpinned once again. The impact of the tooth width on stator tooth modulation effect is normally trivial and hence can be ignored.

5.5 Stator Radial Vibration Analysis

Both analytical and numerical methods are widely implemented to investigate the stator radial vibration in radial-flux PMSMs. The cylindrical shell model is commonly employed in traditional analytical method for stator modal and vibration predictions. The influence of the stator slots on the ERFD components is revealed by the corresponding slot harmonic components in air-gap magnetic field. Consequently, the actual ERFD transmission mechanism in the stator teeth, namely stator tooth modulation effect, are ignored in such method. It can potentially result in significant prediction errors. On the other hand, both air-gap magnetic field and mechanical response can be accurately evaluated by numerical methods such as FEA simulations. The ERFD components in these methods are usually derived by direct FFT analysis of the air-gap magnetic field results from FEA simulation. Normally, the stator tooth modulation effect is preliminarily embedded in some numerical methods by coupling scheme, in which the ERFD distribution obtained from electromagnetic FEA results is directly transferred into the corresponding mechanical

model.

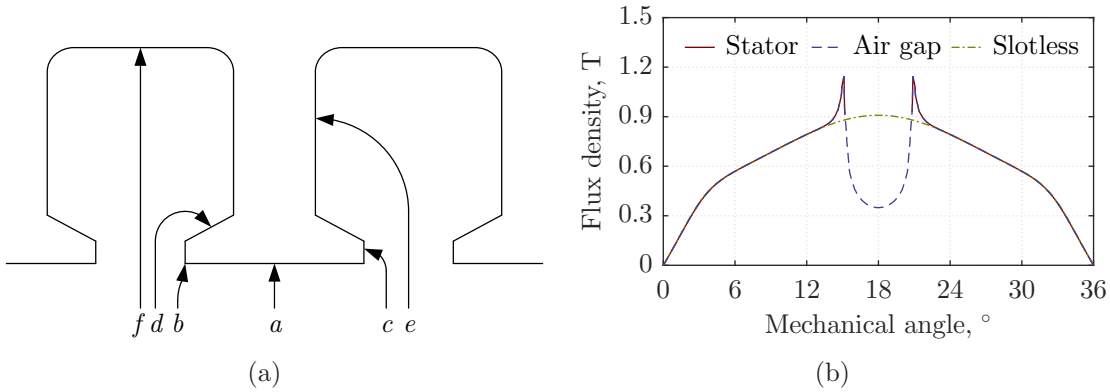

Figure 5.20: Magnetic path and air-gap magnetic field: (a) magnetic path, (b) magnetic field model for ERFD analysis.

Commonly, the ERFD components acting on the stator can be derived from FEA analysis over the air gap. Both the radial and circumferential magnetic field components are required to achieve accurate prediction. As the whole electromagnetic radial force is independent with the integration trajectory, this method can be applied for accurate prediction of the resultant electromagnetic radial force on the stator. However, it is deficient to predict the actual ERFD distribution over the inner periphery of the stator. The air-gap magnetic field will be drastically suppressed over the stator opening regions with typical flux path c, d, e and f as shown in Figure 5.20(a). Normally, the components of d and f are trivial and negligible, while the magnetic field components of c and e will mainly contribute the circumferential ERFD components instead. The ERFD components over the slot opening regions can be neglected. Therefore, only the consideration of magnetic field over the stator teeth shoe surface as depicted by solid line in Figure 5.20(b) will suffice, while the slot opening part demonstrated by dashed line can be ignored. On the other hand, the soft magnetic stator core material makes the circumferential magnetic field components over the stator tooth surface vanish, and hence only the radial components remain as depicted by a in Figure 5.20(a). Additionally, the magnetic field gets distorted in the tooth edges due to the magnetic fringing effect. Such distortion will introduce considerable spikes to the radial component, accompanied with evident circumferential component as shown by magnetic path b.

Comprehensive transient FEA simulations can deliver the radial and circumferential magnetic flux density distributions in the air gap of the machine at each individual time step so that the corresponding ERFD distributions over the stator tooth shoe surfaces can be derived based on Maxwell stress tensor method. Thereafter, 2-D FFT method can be employed to reveal the amplitudes and phases of all the existing ERFD components based on their spatial and temporal orders. However, such method is too computationally demanding and thus time-consuming, especially for the harmonic current models. On the other hand, the resultant decomposition of the ERFD components from such method is unable to directly identify their corresponding sources.

By contrary, the overall ERFD distribution over the stator tooth shoe regions keeps unaffected and maintains the same as the magnetic field from slotless counterpart except the two edges, as demonstrated in Figure 5.20(b). However, the influence of the magnetic fringing effect on two side edges of the stator tooth shoe surface is generally quite mild and hence neglected for the sake of simplicity. Therefore, Equation (5.1) can be directly employed to accurately predict the ERFD components over stator tooth shoe area based on the magnetic field derived from slotless model.

5.5.1 Multi-Physics Analysis Procedure

Since the slot opening regions are excluded for the ERFD calculation on the stator tooth, only the ERFD components from the equivalent slotless machine are required for the accurate evaluations. Without the slot harmonic permeance components, the air-gap flux density harmonic components from PM and armature reaction magnetic fields can be easily decoupled without transient FEA simulations. Hence, the ERFD components can be completely decomposed by spatial and temporal orders without large effort.

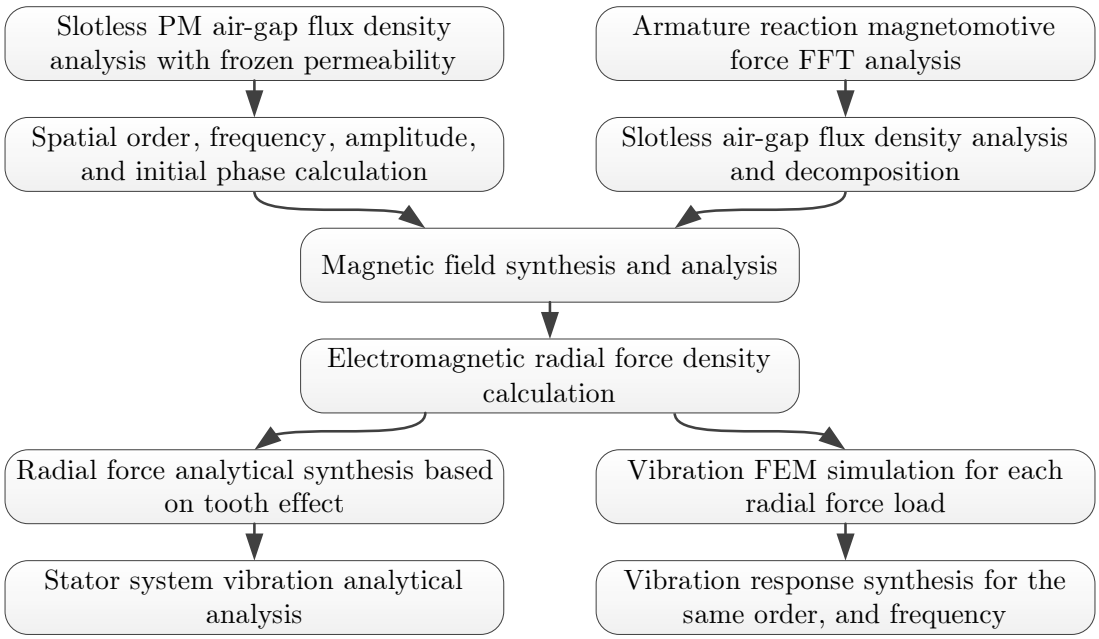

Figure 5.21: The PMSM stator vibration analysis flow chart.

With the assistance of several analytical models, this method can be easily implemented to deliver accurate predictions. The corresponding computational efficiency can be significantly ameliorated. Based on the stator tooth modulation effect on ERFD components, a new multi-physics analysis approach on stator radial vibration is proposed here and the flow chart of the actual procedure is depicted in Figure 5.21. As the slot harmonic components of the magnetic field is not involved in the proposed method, the air-gap flux density harmonic components from PM and armature reaction magnetic fields are derived from the corresponding slotless FEA

models with different techniques, and hence the spatial order, amplitude and initial phase of each component can be obtained accordingly by Fourier series expansion. With assistance from the analytical model of air-gap magnetic field, the corresponding frequency and rotational direction can also be derived. The PM and armature reaction magnetic flux density harmonic components with the same spatial and temporal orders can be vectorially synthesized. As a consequence, the associated ERFD components can be calculated by simplified Maxwell stress tensor method in Equation (5.1). Moreover, the rotational direction of both magnetic field and ERFD components can be embedded into either spatial order or temporal order component. Wherein, positive value means the same rotational direction as the fundamental component while negative value represents the opposite.

Thereafter, either analytical or numerical methods can be employed to evaluate the radial vibration of the stator system based on the resultant ERFD components. Low spatial order ERFD components, which are the main source of the stator radial vibration, can be modulated from certain high order ERFDs based on the stator tooth modulation effect in section 5.4. The corresponding stator radial vibration components can be analytically evaluated by Equation (5.3). However, mechanical FEA simulations are still recommended in order to obtain reasonably accurate eigenvalues of different stator modes for the analytical method. On the other hand, each ERFD component is directly applied on the stator tooth shoe surfaces in mechanical FEA models individually in order to gain corresponding stator radial vibration response. As aforementioned, high spatial order ERFD components may introduce radial vibration of the stator with low spatial order modes. Consequently, it is essential to superpose all vibration responses with the same spatial and temporal orders.

Electromagnetic and mechanical FEA tools are employed in the proposed approach to perform the respective magnetic field and structural analysis, and they are linked unilaterally by the ERFD data based on the analytical model. Consequently, the proposed analysis procedure is a multi-physics weak-coupling method for stator radial vibration analysis. The interior PM rotor configuration, which is normally accompanied with a small air gap length, will result in a severe armature reaction in Prototype I. Furthermore, abundant interharmonic components will be introduced in the air-gap magnetic field from armature reaction due to its FSCW configuration. By taking into account all these factors, prototype I becomes an ideal candidate of stator radial vibration analysis based on the proposed multi-physics method. Meanwhile, specific experimental tests on Prototype I are constructed and performed to verify the validity of the proposed method. The experimental tests of prototype I with no-load conditions under MTPA scheme and flux weakening operation are carried out. With a DC link voltage of 21V, the prototype I with 8A stator current and flux weakening operation can reach maximum speed of 1200rpm . Meanwhile, the DC link voltage is increased to 60V under no-load condition to achieve the same speed as well. Consequently, the stator radial vibration of the machine under different operations can be fairly compared.

5.5.2 ERFD Analysis

The ERFD components used in the proposed method are derived from the air-gap magnetic field components excluding the slot harmonic components. Generally, there are two approaches which can effectively achieve such derivations of the resultant ERFD components. Equivalent slotless FEA model can be constructed to evaluate the main PM and armature reaction air-gap magnetic field components and hence the ERFD components. Instead, the actual FEA model can be employed to evaluate the PM and armature reaction air-gap magnetic field components including the slot harmonics at first. With the assistance of analytical models, the slot harmonic components can be artfully removed.

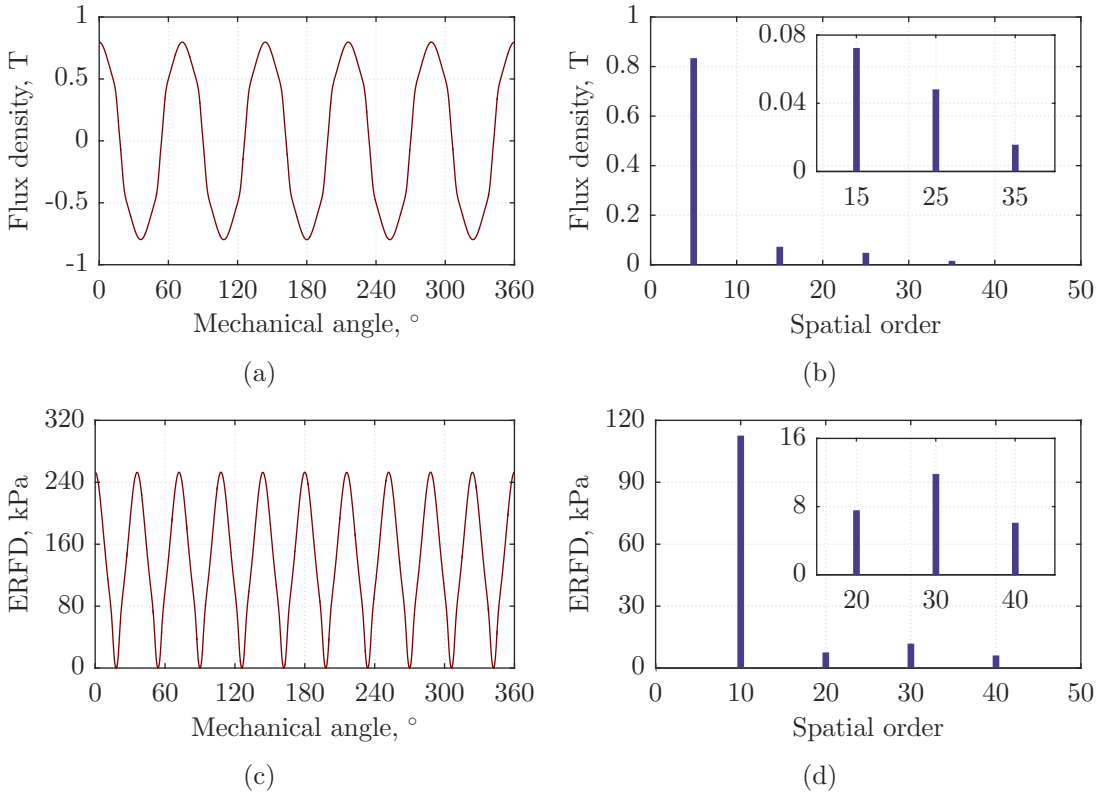

Figure 5.22: ERFD in no-load condition: (a) magnetic flux density, (b) magnetic flux density spectrum, (c) ERFD, (d) ERFD spectrum.

Slotless Model Based Harmonic Components

By changing the slot region material from air to soft magnetic lamination in the FEA model, slotless equivalence of prototype I is realized for corresponding ERFD evaluation. Under no-load condition with PMs as the only magnetic field source, the air-gap PM flux density distribution is derived and depicted in Figure 5.22. In order to take into considerations the effect of the stator and rotor core saturation, frozen permeability technique is implemented here for the magnetic field analysis. It can be seen from Figure 5.22(b) that the high order components of the PM air-gap

magnetic field are insignificant. It confirms that the eccentric rotor pole surface technique, as illustrated in Figure A.1(a), can effectively minimize the air-gap PM flux density distribution distortion. Consequently, the ERFD with spatial order of $2p = 10$ is the dominant component with a commanding amplitude while the rest ERFDs are one order of magnitude smaller. Moreover, the ERFD components with spatial order above 50 are all very trivial and hence neglected for further analysis. It is noteworthy that the temporal orders of these components are exactly the same as their spatial orders. Besides the $2p = 10$-order component, the zeroth spatial order ERFD is also quite significant. However, it can only impose a static load on the stator system with zero frequency, and hence is unable to induce stator radial vibration.

In the meantime, the no-load condition with flux weakening operation is implemented in prototype I to achieve a high level armature phase current and hence an evident armature reaction magnetic field. Therefore, the influence of the armature reaction on the stator radial vibration can be effectively demonstrated and investigated. By comparison with on load condition, it can eliminate the mechanical transmission and load and hence completely avoid the associated potential interference in the experimental tests. Some interharmonic components in the air-gap armature reaction magnetic field of the prototype I with FSCW configuration, can possess the same level of amplitude as the fundamental component. With demagnetization current of about 8A, the prototype I can reach speed of 1200rpm under no-load condition. The corresponding armature current waveform is captured and depicted in Figure 5.23(a), while its spectrum is also compiled and shown in Figure 5.23(b). It can be observed from the figure that the armature phase current is essentially sinusoidal with negligible phase-belt harmonic distortion. Consequently, it is practically justifiable to only consider the fundamental current harmonic component for armature reaction analysis. It is worth mentioning that the carrier frequency of the SVPWM technique involved in the experimental tests is 8kHz to improve the overall performance of the drive system, as the sideband harmonic components are outside the scope of interest in this section.

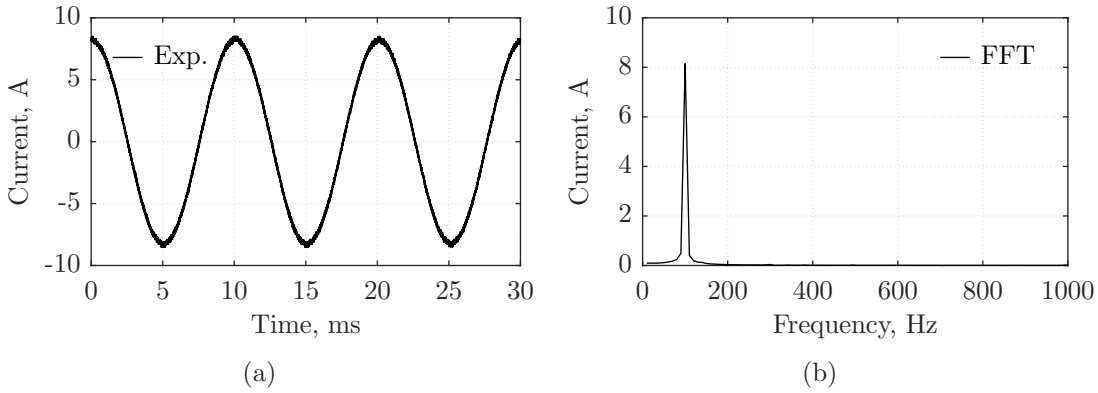

(a) (b)

Figure 5.23: Experimental current under flux weakening condition at 1200rpm: (a) current waveform, (b) current spectrum.

The MMF distribution by the winding arrangement at the given armature current can be directly evaluated and plotted in Figure 5.24(a), while the corresponding spectrum is compiled and shown as Figure 5.24(b). Each MMF harmonic component with its associated initial phase is set as the virtual excitation source in the air gap band of the slotless FEA model to obtain corresponding magnetic field components. Hence, only the first and third items in Table 4.2 will be introduced in the air gap as the corresponding slot harmonic components are absent. The frequency of each magnetic flux density harmonic component, expressed as $(2n_1 \pm 1)\omega_e$, is in one-to-one correlation with the spatial order number of $(2n_1 \pm \kappa_2)p$ for the $(\kappa_2 p)^{th}$ MMF. As a consequence, the frequency can be easily identified by simple FFT investigation of the corresponding air-gap flux density distribution.

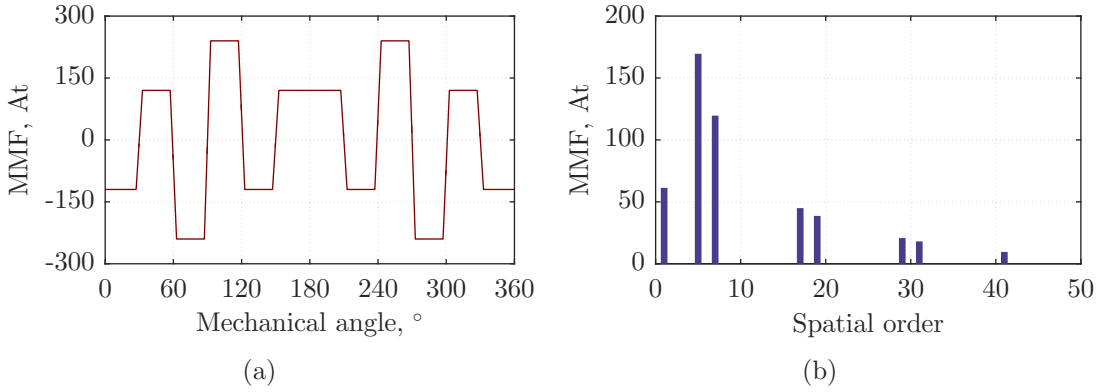

Figure 5.24: Armature reaction MMF of prototype I with flux weakening condition: (a) MMF distribution, (b)MMF Spectrum.

Moreover, the rotational direction information of those air-gap magnetic field components is embedded in the corresponding temporal order number at this stage. As a consequence, the spatial order numbers of the resultant ERFD components are always positive. The negative temporal order number represents opposite rotational direction as the fundamental component. As there are several air-gap magnetic field components with the same spatial and temporal orders, vector synthesis based on their amplitudes and phases is required to obtain the overall composition. Comprehensive predictions of the main air-gap magnetic field components from the armature reaction in prototype I with flux weakening operation are achieved and the corresponding amplitudes are plotted against spatial and temporal orders in Figure 5.25(a). Moreover, the PM magnetic field components in prototype I with flux weakening operation can be obtained in the FEA model with frozen permeability technique, similar procedure as the no-load condition. Thereafter, the vectorial synthesization of the PM and armature reaction air-gap magnetic field components with the same spatial and temporal orders are carried out. The ERFD components with different spatial and temporal orders can be decoupled accordingly, the corresponding amplitudes can be easily derived from the analytical model in Equation (5.1) and illustrated in Figure 5.25(b). By comparison with Figure 5.22(d), it can be inspected that more ERFD components appear in prototype I with flux weakening operation due to the abundant interharmonic components from the armature-reaction mag-

netic field. Although their amplitudes are all lower than the component with spatial order of $2p = 10$ under no-load condition, more severe stator radial vibration tends to happen. Consequently, comprehensive stator radial vibration analysis based on each ERFD component should be carefully carried out.

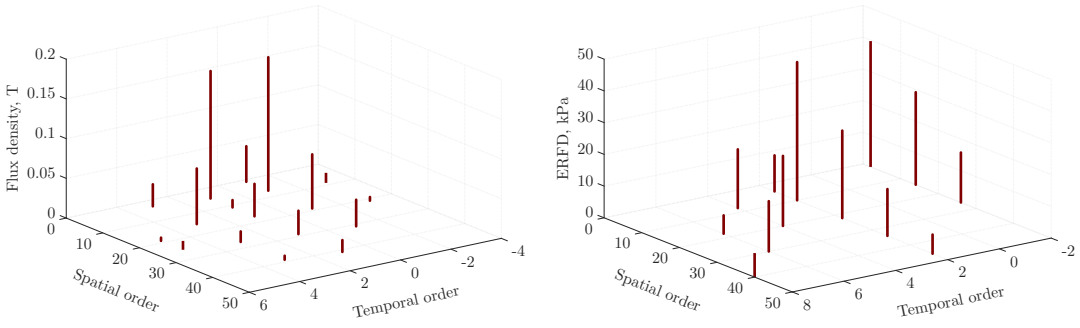

(a) (b)

Figure 5.25: ERFD analysis of prototype I under flux weakening condition: (a) air-gap magnetic field components from armature reaction, (b) ERFD amplitudes.

Slot Harmonic Component Decouple

The slotless FEA models employed above can potentially introduce errors in magnetic field predictions due to the simple assumption of the soft magnetic material for slot regions. Consequently, an alternative method based on FEA models with the practical machine with actual stator slots is proposed to predict the slotless air-gap magnetic flux density components. With the guidance of analytical derivation and mathematical manipulation, the corresponding slot harmonic components can be decoupled and hence effectively eliminated.

Based on the PM air-gap magnetic field components in Table 4.1, the slotless components including the first and third items from the table can be rewritten as

$$b_{r_1}(\theta_m, t) = \sum_{\kappa=1}^{\infty} B_\kappa \sin(\kappa p \theta_m - \kappa \omega_e t) \tag{5.30}$$

The spatial order parameter κ can be either κ_1 or $(2n_1 \pm \kappa_1)$ from Table 4.1. Meanwhile, the slot associated harmonic components including the second and forth items can be accordingly expressed as

$$b_{r_2}(\theta_m, t) = \sum_{\kappa=1}^{\infty} \sum_{n=1}^{\infty} B_\kappa \bar{\Lambda}_{nZ} \sin(\kappa p \theta_m - \kappa \omega_e t) \cos(nZ\theta_m) \tag{5.31}$$

The corresponding amplitudes of the harmonic components in Equation (5.30) and (5.31) can be directly obtained from Table 4.1. It can be noticed that the position θ_m in the sinusoidal part of the equations corresponds to the rotor position, while θ_m in the cosinusoidal part is related to the angle between stator slot and rotor

q-axis. Moreover, it is assumed in the above equations that the center of one certain stator slot opening fully aligns with rotor q-axis at the initial state (zero time). As a consequence, the slotless air-gap magnetic field components, b_{r_1}, are only dependant on the rotor position. Besides the rotor position, the stator slot placement position also imposes a substantial impact on the slot harmonic components b_{r_2}.

Now, it is assumed to rotate the stator by an angle of $\Delta\theta_m$ at the initial time of zero, and hence the $(\kappa p \pm nZ)$ order harmonic components in the right side of Equation (5.31) can be represented as

$$b_{\kappa p \pm nZ}(\theta_m, t) = B_\kappa \bar{\Lambda}_{nZ} \sin(\kappa p \theta_m - \kappa \omega_e t) \cos\left(nZ(\theta_m + \Delta\theta_m)\right) \tag{5.32}$$

Furthermore, it is assumed that one tooth pitch can be divided into m parts with equal angle of $\Delta\theta_m$. Consequently, $\Delta\theta_m$ can be easily determined by

$$\Delta\theta_m = \frac{2\pi}{mZ} \tag{5.33}$$

As a resemblance, the corresponding air-gap flux density components can be derived by rotating stator with an angle of $i\Delta\theta_m, i = 1, 2, \ldots, m$ in Equation (5.32). With $n \neq km, k = 1, 2, \cdots$, it can be obtained that

$$\sum_{i=1}^{m} B_\kappa \bar{\Lambda}_{nZ} \sin(\kappa p \theta_m - \kappa \omega_e t) \cos\left(nZ(\theta_m + i\Delta\theta_m)\right) = 0 \tag{5.34}$$

Consequently, all the slot harmonics except the components induced by the stator slot permeance with the spatial orders of multiple mZ can be completely cancelled. As m is large enough, the slot harmonic components caused by $(kmZ)^{th}$ spatial order slot permeance become relatively insignificant and hence can be practically neglected. Consequently, it can be reasonably assumed that the slot harmonic components are eliminated by this method with sufficiently large m. The corresponding magnetic flux density harmonic components can be expressed as

$$b_{r_1}(\theta_m, t) = \frac{1}{m} \sum_{i=1}^{m} b_r(\theta_m, t, i\Delta\theta_m) \tag{5.35}$$

Based on Equation (5.35), the resultant slotless air-gap magnetic field components can be calculated by the superposition of practical magnetic fields from different initial stator positions, which can be derived by magnetostatic FEA models. It is noteworthy that the additional influence of the stator slot opening on the slotless magnetic field components, commonly with compensation of Carter coefficient has to be considered in this method. Meanwhile, the frozen permeability scheme is also implemented to take into account the magnetic saturation caused by armature reaction.

Afterwards, the relative slot opening permeance can be obtained by

$$\bar{\lambda}_s(\theta_m, t) = \frac{b_r(\theta_m, t)}{b_{r_1}(\theta_m, t)} \tag{5.36}$$

As a consequence, the slotless armature reaction magnetic field components can be derived by

$$b_{s_1}(\theta_m, t) = \frac{b_s(\theta_m, t)}{\bar{\lambda}_s(\theta_m, t)} \tag{5.37}$$

where b_s is the air-gap magnetic field from armature reaction by FEA models with actual stator slots.

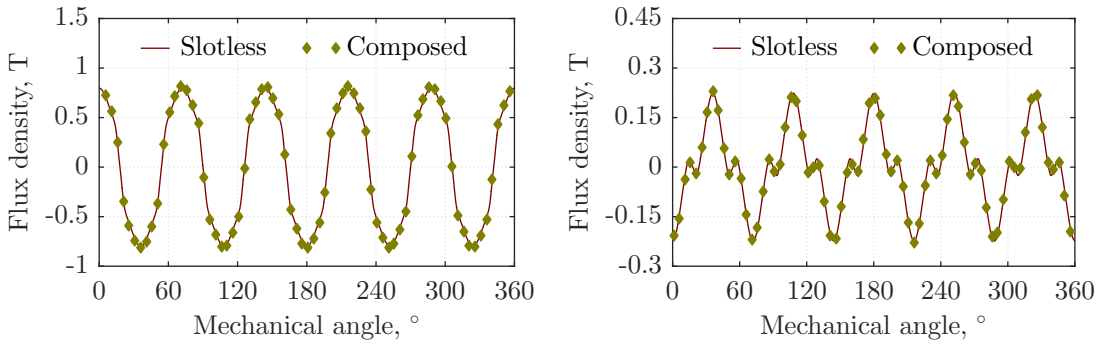

Figure 5.26: Flux density comparison between slot-less and composed model: (a) PM magnetic flux density, (b) the fundamental armature-reaction magnetic flux density.

At this point, both the slotless PM and armature reaction air-gap magnetic field components can be effectively decoupled from the FEA results of the machine with actual stator slots. The method is implemented for prototype I with flux weakening operation, and the corresponding air-gap magnetic harmonic components are decoupled successfully. The PM and armature-reaction magnetic field components with the fundamental spatial order of $p = 5$ are derived and compared with their counterparts from the slotless FEA models in Figure 5.26. Excellent agreements between the results have been demonstrated in the figure. The elimination of stator slot in the FEA model will have very mild impact on the main air-gap magnetic field components from PM and armature reaction. As a consequence, the slotless FEA model is sufficient for the air-gap magnetic field and hence ERFD calculation for most cases as it can deliver reasonably accurate predictions on the harmonic characteristics in PMSMs.

5.5.3 Stator Radial Vibration Analysis and Validation

Figure 5.22(d) shows that the ERFD with spatial order of $2p = 10$ is the only dominant component in prototype I under no-load condition while the rest components are all very small and hence can be neglected for stator radial vibration analysis. For the sake of comparison, the ERFD component with spatial order of $4p = 20$ is also employed for further vibration investigation. Based on the stator tooth modulation effect, stator radial vibration component with spatial order of $(2p - Z) = 2$

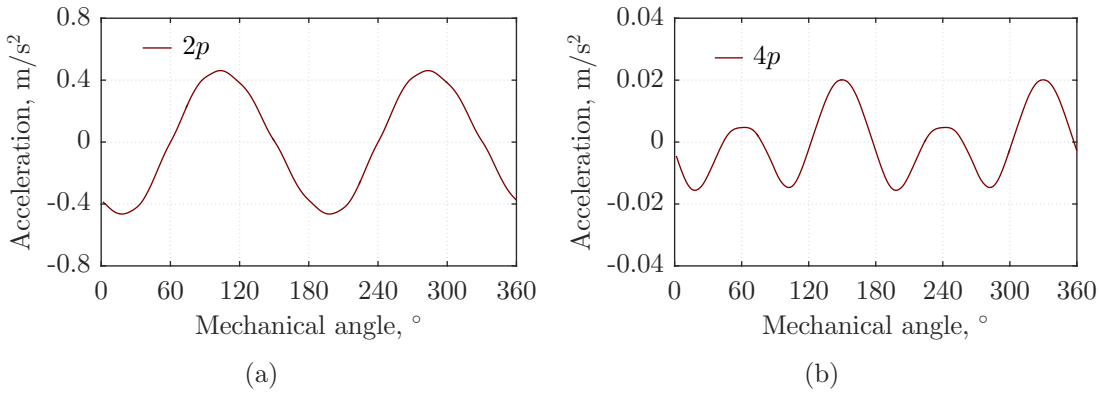

Figure 5.27: Vibration simulation in no-load condition: (a) $2\omega_e$ frequency with $(2p)^{th}$ order, (b) $4\omega_e$ frequency with $(4p)^{th}$ order.

will be produced by the ERFD component with spatial order of $2p = 10$, while the vibration component with spatial order of $(4p - 2Z) = 4$ is modulated by the ERFD component with spatial order of $4p = 20$. The corresponding stator radial vibration components can be evaluated by either the proposed analytical method or numerical FEA simulations. The ERFD components of these two spatial orders are directly applied to respective 3-D mechanical FEA models to predict the corresponding stator radial vibration responses. The resultant stator radial vibration components are obtained from the 3-D mechanical FEA results and demonstrated in Figure 5.27. As expected, the stator radial vibration responses with spatial order modes of 2 and 4 can be induced by the corresponding ERFD components respectively. It can be inspected from the figure that the resultant stator radial vibration from ERFD with spatial order of $2p = 10$ are much stronger than the components from spatial order of $4p = 20$. The frequencies of those two vibration components are 200Hz ($2\omega_e$) and 400Hz ($4\omega_e$) respectively for prototype I at rotational speed of 1200rpm. Moreover, stator radial vibration response from the ERFD component with spatial order of $4p = 20$ contains an evident component of 2-order. That implies the mechanical response system is not linear and the nonlinear mechanical coupling effect can occur during the stator tooth modulation. As a consequence, further spatial harmonic decouple and synthesis sometimes are essentially required for more accurate predictions.

The stator radial vibration characteristics of prototype I with flux weakening operation become much more complex as a larger number of associated ERFD components has been built up. It can be observed from Figure 5.25(b) the ERFD components with spatial orders of 2, 14 and 26, have quite evident amplitudes and the same frequency of $-2\omega_e$. Based on the stator tooth modulation effect, stator radial vibration response with spatial order mode of 2 and frequency of $-2\omega_e$ are introduced by the 14^{th} and 26^{th} spatial order ERFDs. On the other hand, there are also remarkable ERFDs with spatial orders of 10, 22 and 34, and frequency of $2\omega_e$. These components will also be modulated to induce stator radial vibration with spatial order mode of 2 and frequency of $-2\omega_e$. Therefore, all these components are derived and illustrated in Figure 5.28(a), and all these stator radial vibration responses are with

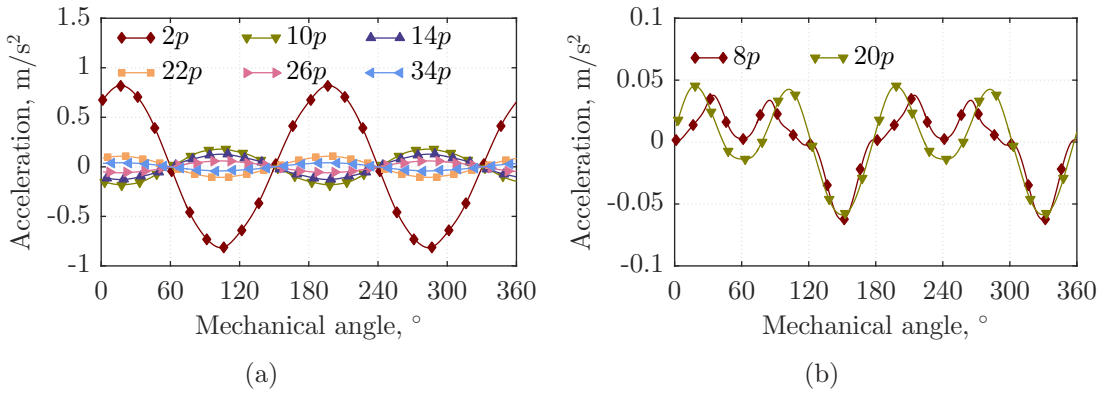

Figure 5.28: Vibration simulation in flux weakening condition: (a) $2\omega_e$ frequency with different order components, (b) $4\omega_e$ frequency with different order components.

the same spatial order mode and frequency. They should be superposed together to obtain the resultant overall vibration. As the tooth effect coefficient generally decreases as the spatial order number of the original ERFD component rises, the resultant stator radial vibration responses from the ERFD components with high spatial order are normally quite small in prototype I and hence can be practically ignored. Analogously, the 8^{th} and 20^{th} spatial order ERFDs with frequency of $4\omega_e$

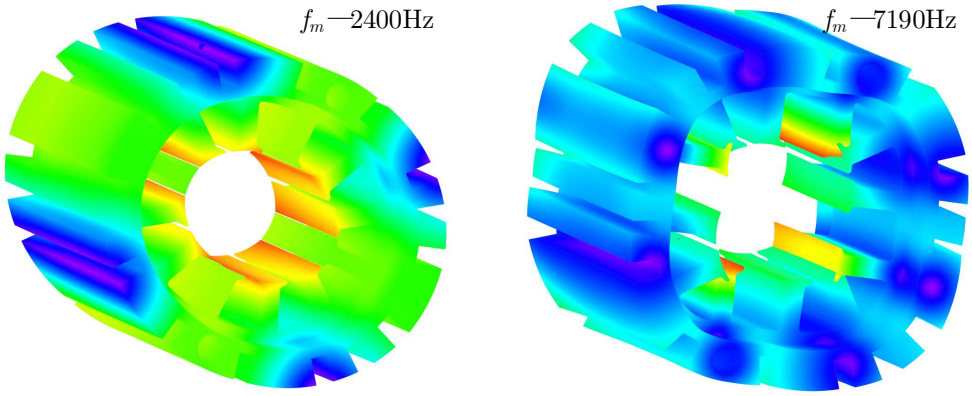

Figure 5.29: Stator system natural frequency analysis of different modes: (a) 2^{nd} order, (b) 4^{th} order.

will be modulated into the stator radial vibration components of a spatial order mode of 4. The stator radial vibration responses are evaluated by 3-D mechanical FEA models and the results are given in Figure 5.28(b). The higher spatial order mode, together with the smaller ERFD amplitudes, result in stator radial vibration responses with one order of magnitude lower than the $2\omega_e$ component.

Moreover, the analytical model with the stator tooth modulation effect is also employed to perform stator radial vibration analysis. From the analysis above, the two low spatial order modes of 2 and 4 are the main cause of stator radial vibration for prototype I. Hence, 3-D mechanical FEA method is employed to accurately obtain

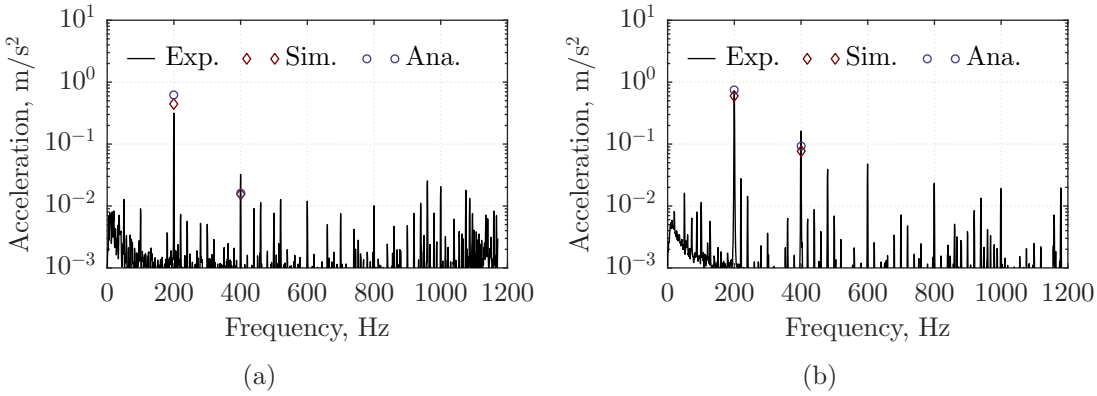

Figure 5.30: Experimental validation of vibration: (a) no-load condition, (b) flux weakening condition. (Exp. - Experimental result, Sim. - Simulation result, Ana. - Analytical model)

the corresponding eigenvalues. The resultant natural frequencies of stator spatial order modes of 2 and 4 are derived as 2400Hz and 7190Hz as shown in Figure 5.29, which can be directly used for analytical vibration predictions. Instead of superposing the resultant stator radial vibration responses with same spatial and temporal order in the numerical FEA method, all the original and modulated ERFD components with the same spatial and temporal order are first synthesized based on stator tooth modulation effect model of Equation (5.18). First, the ERFD component with spatial order of 2 and frequency of $-2\omega_e$ induced by the associated ERFD components with spatial orders of 2, 14, 26, 10, 22 and 34 is analytically calculated, and followed by the vectorial synthesis. Then, the corresponding stator radial vibration is evaluated by Equation (5.3). Moreover, the same procedure is applied to the ERFD component with spatial order of 4 and frequency of $-4\omega_e$ and the relevant stator radial vibration. The analytical results of such two stator radial vibration components for prototype I with no-load condition and flux weakening operation are obtained at the rotational speed of 1200rpm and compared with the FEA counterparts in Figure 5.30. Furthermore, corresponding experimental tests are carried out and the stator radial vibration are measured for validations. The spectra of the stator radial vibration for both conditions are compiled and also depicted in Figure 5.30. The figure shows the stator radial vibration with spatial order mode of 2 and frequency of $-2\omega_e$ are the dominant components for prototype I with both operational conditions. Generally, the analytical and FEA models provide very close predictions. Both the analytical and FEA models tend to slightly overestimate the stator radial vibration component with frequency of $-2\omega_e$ in prototype I under no-load condition. The analytical model also accurately estimates this component under flux weakening condition while the FEA model delivers a slight underestimate. It can be also inspected from the figures that they all slightly underestimate the stator radial vibration components with frequency of $-4\omega_e$ in prototype I under both conditions. It is noteworthy that both analytical and FEA models ignore the impact of the stator armature winding on the stator radial vibration characteristics. By considering the approximations of the ERFD transmission procedure and rather complex stator structure, it is reasonable to conclude that the experimental results

are in very good agreements with the corresponding analytical and FEA predictions. Overall, the validity of the multi-physics analysis method on stator radial vibration characteristics proposed has been underpinned by the experimental results.

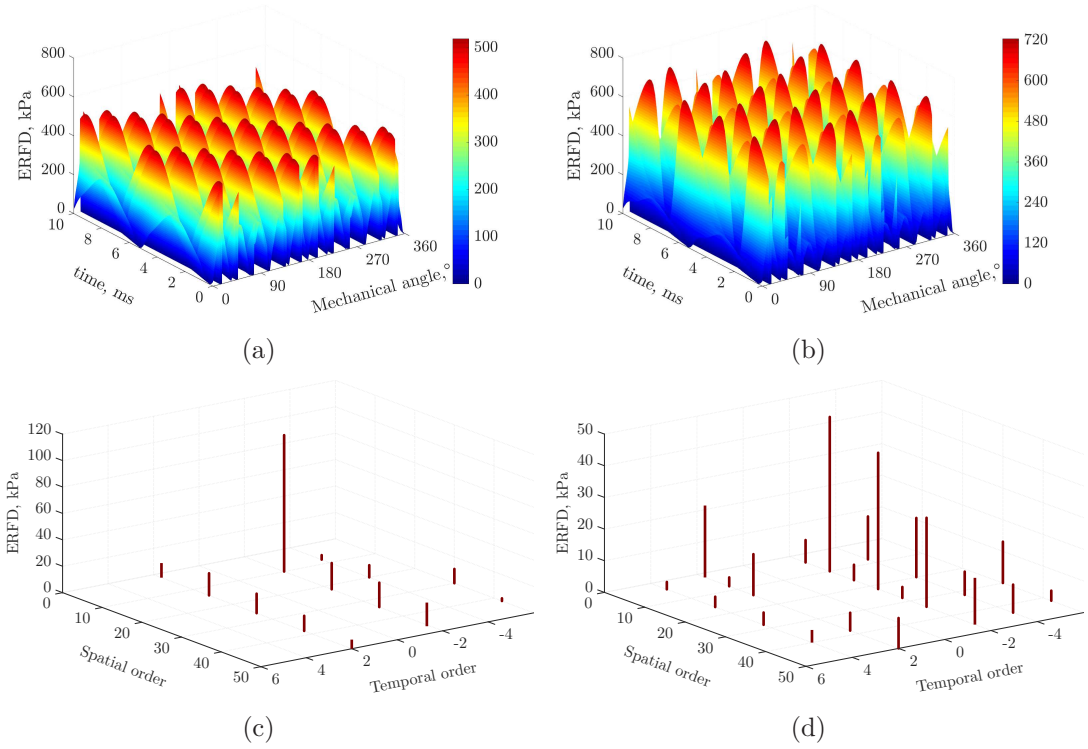

Figure 5.31: ERFD analysis based on the time-stepping method: (a) ERFD on the stator teeth shoe under no-load condition, (b) ERFD on the stator teeth shoe under flux weakening condition, (c) ERFD components under no-load condition, (d) ERFD components under flux weakening condition.

5.5.4 ERFD Analysis Based on Time-Stepping Method

According to Equation (5.29), only the ERFD distribution over the stator tooth shoe surface areas can be radially mapped to the stator yoke with the same angular range of β. Hence, direct FFT analysis on the ERFD distribution over the stator tooth shoe surface suffices the ERV analysis. The modulation effect is automatically included in such analysis. Normally, the ERFD distributions of various time steps over a single fundamental electrical period can be directly derived by corresponding transient FEA simulations. Then, 2-D FFT can be applied to such results to reveal the spatial and temporal orders. Such a method takes into consideration the magnetic fringing effects near the tooth edges. Figure 5.31(a) and 5.31(b) demonstrate such ERFD distribution results of Prototype I at different time steps for no-load and flux weakening conditions respectively. It can be observed that the ERFD distribution over the slot opening areas is considered as zero. The resultant amplitudes, spatial and temporal orders of ERFD components are shown in Figure 5.31(c) and

5.31(d).

As the stator vibration modes of Prototype I associated with high spatial order ERFD components have rather high frequencies, only the low spatial orders are of interest for vibration and acoustic noise investigations. The corresponding stator vibration can be evaluated by Equation (5.3). The comparisons between the proposed time-stepping method and experimental results are also carried out and demonstrated in Figure 5.32. A close agreement has been achieved for the $2\omega_e$-order vibrations of both conditions. However, an underestimation of $4\omega_e$-order vibrations are still delivered by the proposed method. Although the proposed time-stepping method can offer a direct yet simple approach for the ERFD prediction, it hardly provides insightful information for design and optimization. More importantly, it may result in intensive computational burden when harmonic current components are involved in the analysis.

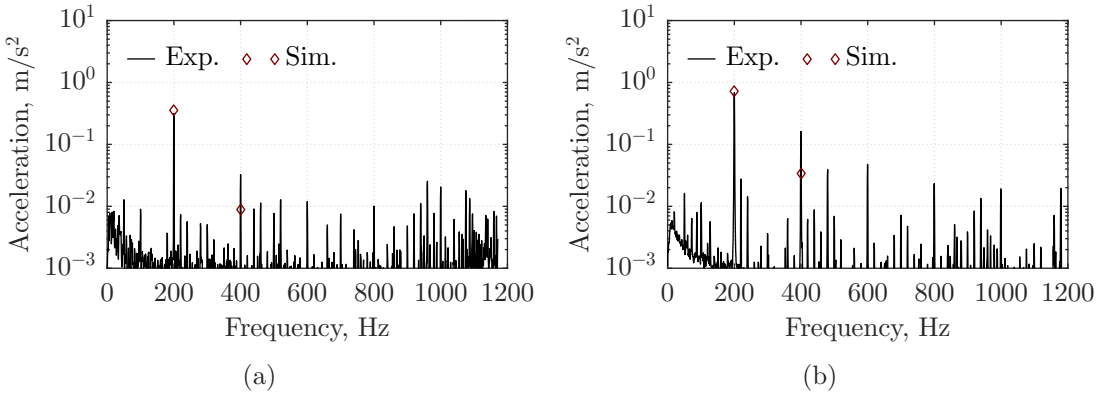

Figure 5.32: Vibration experimental validation of the time-stepping method: (a) no-load condition, (b) flux weakening condition. (Exp. - Experimental result, Sim. - Simulation result

5.6 Summary

Based on the air-gap magnetic field model given in the previous chapter, the universal principle of the ERFD in PMSMs is introduced first in this chapter. Then, the stator tooth modulation effect on the ERFD components is demonstrated by 3-D FEA simulation and experimental results. An analytical symmetrical tooth modulation effect model is developed based on the assumption of equal force distribution over the shoe surface of each individual stator tooth for prompt assessment. Moreover, the analytical model is further extended to an asymmetrical model to include the uneven force distribution characteristics so that the prediction errors can be effectively mitigated. Based on the stator tooth modulation models, the slot flux permeance can be omitted during ERFD calculation as it is inherently integrated in the models. Meanwhile, the stator tooth modulation effect is essential for stator radial vibration analysis in the corresponding mechanical model. On the other hand, the conventional comprehensive stator radial vibration analysis involves rather com-

plex transient electromagnetic FEA simulations and both radial and circumferential components of the air-gap magnetic field are required to achieve accurate prediction. Moreover, 2-D FFT is indispensable to decouple the spatial and temporal orders of the ERFD components. As a consequence, new methods are proposed based on multi-physics coupled with the stator tooth modulation effect model to significantly simplify the analysis without considerable compromise on the accuracy. Finally, experimental tests on prototype I are carried out to underpin the validity of the proposed method.

The experimental platforms involved in this chapter include:

- An surface-mounted ferrite machine (prototype III) driven by $i_d = 0$ vector control is employed for the experimental demonstration of the stator tooth modulation phenomenon;
- Vector control scheme is developed for prototype I to validate the proposed multi-physics analysis methods for stator radial vibration;
- The flux weakening control algorithm is implemented for prototype I to study the effect of armature reaction on stator radial vibration.

The new contributions in this area include:

- The stator tooth modulation effect on the ERFD is demonstrated by experimental tests with the assistance of FEA results in Section 5.2;
- An analytical symmetrical stator tooth modulation effect model is developed for the stator radial vibration prediction based on the assumption of even radial force distribution over individual tooth shoe surface in Section 5.3;
- By considering the uneven radial force distribution characteristics, an improved asymmetrical stator tooth modulation effect model is further derived in Section 5.4;
- Simple yet effective multi-physics analysis methods are proposed based on the stator tooth modulation effect to promptly predict stator radial vibration characteristics with negligible sacrifice on accuracy in Section 5.5.

The stator tooth modulation effect of ERFD generally occurs in PMSMs due to the existence of stator teeth and slots. Based on the proposed stator tooth modulation effect models, the characteristic of stator radial vibration can be more accurately and effectively illustrated. Meanwhile, the influences of the design parameters on the stator radial vibration characteristics can also be insightfully revealed by the corresponding analytical models. The proposed stator radial vibration analysis procedure based on the stator tooth modulation effect can be further developed for other types of machine drives. It is worth mentioning that all the air-gap magnetic field components induced by the rotor structure should be properly acknowledged in the model, including the rotor slot harmonic components in an induction machine.

Chapter 6

Sideband Vibration Analysis in PMSMs

The sideband magnetic field components will interact with other magnetic fields to produce high frequency ERFD components. The resultant ERFD components will further act on the stator to produce vibration, which could lead to high frequency electromagnetic noise. This is one of the main sources of acoustic noise in PMSM drive systems when controlled by PWM schemes. This chapter inherits the analytical model of sideband flux density from Chapter 4 to further develop the sideband ERFD model in SVPWM driven motors. The characteristics of sideband vibration in both integral-slot and FSCW PMSMs are analytically investigated, and experimentally validated. The vibration in the FSCW model is much more complex due to the rich spatial interharmonics, which introduce more sideband components. The corresponding components in SPWM are also developed to predict and analyze the vibration in the machine. In addition, the random PWM technique is also involved in the noise comparison with normal SVPWM. Without loss of generality, the acoustic noise investigation is replaced by a vibration investigation in this chapter, as acoustic noise measurement are heavily influenced by the testing environment. Vibration measurement, on the other hand, can be undertaken reliably in a normal laboratory environment.

6.1 Analytical Model of Sideband ERFD

6.1.1 Introduction

Recently, the vibration in PMSMs has been widely investigated for low frequency components. However, the existing literature studying high-frequency ERV and acoustic noise associated with PWM techniques are quite limited and mainly devoted to IM drive systems. A noise versus harmonic current characteristic function obtained based on the corresponding experimental results is defined to predict

the acoustic noise of IM drives [191]. The acoustic characteristics of an IM drive with SPWM and SVPWM techniques are investigated and compared experimentally [192]. Meanwhile, an experimental procedure is proposed to determine the acoustic and vibration behaviors in IM drive with SVPWM schemes [193]. Moreover, novel PWM techniques which employ trapezoidal modulator with fixed [194], variable frequency triangular [195] and sinusoidal [196] carrier signal, as well as random switching frequency [197, 198], are presented and investigated in order to mitigate the acoustic noise in IM drives. A simplistic switching frequency strategy to avoid approximations of natural frequencies is implemented to reduce the vibration and noise [199]. However, great disparity between the excitation and natural frequencies does not necessarily guarantee low audible noise. Nevertheless, the mechanism of high-frequency sideband ERV and acoustic noise in PMSM drives is more complex than that in IMs as a result of the interactions which arise from the saliency effect. Therefore, this research on IMs may not be valid and hence cannot be directly applicable for PMSM drives. Random PWM schemes are also developed to minimize the acoustic noise in PMSM drives [200, 201].

In general only qualitative, semi-quantitative, or experimental methods are implemented for the aforementioned studies and optimizations on ERV and acoustic noise related to PWM techniques. Therefore they could not offer direct insight into the problems. In this chapter, based on the universal sideband flux density model proposed in Chapter 4, the analytical model of sideband ERFD components in both integral-slot and FSCW PMSMs are systematically investigated. Furthermore, the associated characteristics of vibration are comprehensively studied.

6.1.2 Sideband ERFD Components from SVPWM Technique

The fundamental magnetic field components are the main components in integral-slot machines. There are abundant of interharmonics in FSCW PMSMs, besides the fundamental components, which have to be taken into account in the ERFD model. Hence, based on the proposed analytical flux density model, the universal sideband ERFD model can be derived accordingly and expressed as,

$$p_r(\theta_m,t) = -\frac{(b_0(\theta_m,t)+b_v(\theta_m,t))(b_{p\_\omega_\mu}(\theta_m,t)+b_{v\_\omega_\mu}(\theta_m,t))}{\mu_0} \tag{6.1}$$

As proposed in Chapter 3, $\omega_\mu = (\omega_s \pm 2\omega_e), (\omega_s \pm 4\omega_e), (2\omega_s \pm \omega_e)$ are the main components for the first and second switching band of SVPWM. By substituting the critical sideband air-gap flux density components proposed in Section 4.5 into (6.1), the corresponding sideband ERFD components can be calculated. The associated spatial orders, frequencies and amplitudes are demonstrated in Table 6.1.

It can be found that abundant ERFD components exist with the frequencies near the sideband frequency of ω_μ, which may be quite close to certain spatial mode eigenvalues of the machine stator. This particular spatial order ERFD component

Table 6.1: The main Sideband ERFD components

No.	Order	Frequency	Initial phase	Amplitude
1	0	$\mp(\omega_s \pm 3\omega_e)$	$\varphi_{p\_12} - \delta$	$\mp K_{12} B_0 B_{\mu 1}/2\mu_0$
2	$2p$	$\mp(\omega_s \pm \omega_e)$	$\varphi_{p\_12} + \delta$	
3	0	$\pm(\omega_s \pm 3\omega_e)$	$\varphi_{p\_14} - \delta$	$\mp K_{14} B_0 B_{\mu 1}/2\mu_0$
4	$2p$	$\pm(\omega_s \pm 5\omega_e)$	$\varphi_{p\_14} + \delta$	
5	0	$\pm 2\omega_s$	$\varphi_{p\_21} - \delta$	$\mp K_{21} B_0 B_{\mu 2}/2\mu_0$
6	$2p$	$\pm(2\omega_s \pm 2\omega_e)$	$\varphi_{p\_21} + \delta$	
7	$\upsilon_2 - p$	$\mp(\omega_s \pm 3\omega_e)$	$\varphi_{a\_12} - \delta$	$\mp K_{\upsilon_2} K'_{12} B_0 B_{\mu 1}/2\mu_0$
8	$\upsilon_2 + p$	$\mp(\omega_s \pm \omega_e)$	$\varphi_{a\_12} + \delta$	
9	$\upsilon_2 - p$	$\pm(\omega_s \pm 3\omega_e)$	$\varphi_{a\_14} - \delta$	$\mp K_{\upsilon_2} K'_{14} B_0 B_{\mu 1}/2\mu_0$
10	$\upsilon_2 + p$	$\pm(\omega_s \pm 5\omega_e)$	$\varphi_{a\_14} + \delta$	
11	$\upsilon_2 - p$	$\pm 2\omega_s$	$\varphi_{a\_21} - \delta$	$\mp K_{\upsilon_2} K'_{21} B_0 B_{\mu 2}/2\mu_0$
12	$\upsilon_2 + p$	$\pm(2\omega_s \pm 2\omega_e)$	$\varphi_{a\_21} + \delta$	
13	$p - \upsilon_1$	$\mp(\omega_s \pm 3\omega_e)$	$\varphi_{p\_12} - \varphi_s$	$\mp K_{\upsilon_1} K_{12} B_a B_{\mu 1}/2\mu_0$
14	$p + \upsilon_1$	$\mp(\omega_s \pm \omega_e)$	$\varphi_{p\_12} + \varphi_s$	
15	$p - \upsilon_1$	$\pm(\omega_s \pm 3\omega_e)$	$\varphi_{p\_14} - \varphi_s$	$\mp K_{\upsilon_1} K_{14} B_a B_{\mu 1}/2\mu_0$
16	$p + \upsilon_1$	$\pm(\omega_s \pm 5\omega_e)$	$\varphi_{p\_14} + \varphi_s$	
17	$p - \upsilon_1$	$\pm 2\omega_s$	$\varphi_{p\_21} - \varphi_s$	$\mp K_{\upsilon_1} K_{21} B_a B_{\mu 2}/2\mu_0$
18	$p + \upsilon_1$	$\pm(2\omega_s \pm 2\omega_e)$	$\varphi_{p\_21} + \varphi_s$	
19	$\upsilon_2 - \upsilon_1$	$\mp(\omega_s \pm 3\omega_e)$	$\varphi_{a\_12} - \varphi_s$	$\mp K_{\upsilon_1} K_{\upsilon_2} K'_{12} B_a B_{\mu 1}/2\mu_0$
20	$\upsilon_2 + \upsilon_1$	$\mp(\omega_s \pm \omega_e)$	$\varphi_{a\_12} + \varphi_s$	
21	$\upsilon_2 - \upsilon_1$	$\pm(\omega_s \pm 3\omega_e)$	$\varphi_{a\_14} - \varphi_s$	$\mp K_{\upsilon_1} K_{\upsilon_2} K'_{14} B_a B_{\mu 1}/2\mu_0$
22	$\upsilon_2 + \upsilon_1$	$\pm(\omega_s \pm 5\omega_e)$	$\varphi_{a\_14} + \varphi_s$	
23	$\upsilon_2 - \upsilon_1$	$\pm 2\omega_s$	$\varphi_{a\_21} - \varphi_s$	$\mp K_{\upsilon_1} K_{\upsilon_2} K'_{21} B_a B_{\mu 2}/2\mu_0$
24	$\upsilon_2 + \upsilon_1$	$\pm(2\omega_s \pm 2\omega_e)$	$\varphi_{a\_21} + \varphi_s$	

can potentially cause resonance, which can result in high ERV and acoustic noise. Therefore, it is highly recommended to investigate the sideband ERFD components together with corresponding natural frequencies in PMSM drives. However, the damping factors contribute to high-frequency resonance and these resonant effects will be less significant than low-frequency resonance [202]. Overall, the sideband ERFD components with large spatial orders, high natural frequencies and small amplitudes can be appraised and ignored accordingly to simplify the investigation.

As aforementioned, the low-frequency p^{th} spatial air-gap magnetic field component is contributed by both the PMs and armature reaction. The spatial interharmonic components of both the high-frequency sideband and the low-frequency armature air-gap magnetic field can be derived from the corresponding p^{th} spatial order components. For the convenience of ERFD derivation, the spatial orders of the low-frequency air-gap magnetic field components and the high-frequency sideband are classified into p^{th} and υ_1^{th} ($\upsilon_1^{th} \neq p$) components as well as p^{th} and υ_2^{th} ($\upsilon_2^{th} \neq p$) components respectively.

All the spatial air-gap magnetic field components induced by the main sideband

current harmonic components in first and second carrier domains have frequencies of $(\omega_s \pm 2\omega_e)$, $(\omega_s \pm 4\omega_e)$, and $(2\omega_s \pm \omega_e)$, while the corresponding main low-frequency components have a frequency of ω_e. Therefore, the interactions between the components with the same spatial order p engender two sets of main sideband ERFD components with respective spatial orders of 0 and $2p$ and frequencies of $(\omega_s \pm \omega_e)$, $(\omega_s \pm 3\omega_e)$, $(\omega_s \pm 5\omega_e)$, $(2\omega_s)$ and $(2\omega_s \pm 2\omega_e)$, which are given as the first six items in Table 6.1. These items are the main sideband ERFD components in integral-slot PMSMs.

However, apart from the fundamental flux density components, there is an abundance of interharmonics, which will introduce extra sideband ERFD components in FSCW PMSMs. The p^{th} spatial low-frequency air-gap magnetic field component interacts with the υ_2^{th} sideband components to produce two sets of main sideband ERFD components with respective spatial orders of $(\upsilon_2 - p)$ and $(\upsilon_2 + p)$. Whereas the interactions of the p^{th} spatial sideband air-gap magnetic field component and the υ_1^{th} armature reaction components bring another two sets with respective spatial orders of $(p - \upsilon_1)$ and $(p + \upsilon_1)$. They are listed as items 7-12 and 13-18 in Table 6.1 respectively. With $\upsilon_1 = \upsilon_2$, items 8, 10, and 12 will have the same spatial order number, rotational direction, and respective frequencies as items 14, 16, and 18. Whilst items 7, 9 and 11 will have the same spatial order number and respective frequencies as items 13, 15 and 17, but opposite rotational direction. As a consequence, the corresponding pair can be vectorially synthesized based on the given amplitudes and phases. However, the vector synthesis will result in very complex analytical derivations and the disparity of contributions from the components are rather great. Besides, the interactions of the υ_2^{th} spatial sideband air-gap magnetic field component and the υ_1^{th} armature reaction interharmonics also incur two sets of sideband ERFD components with respective spatial orders of $(\upsilon_2 - \upsilon_1)$ and $(\upsilon_2 + \upsilon_1)$, which are presented as the last six items in Table 6.1. Items 19, 21, and 13 contain respective 0^{th} spatial order components which can also be synthesized with items 1, 3, and 5 accordingly.

As discussed, the sideband vibration characteristics in integral-slot machines are of great difference to FSCW PMSMs. Hence two case studies are employed in this chapter for the sideband vibration investigation of integral and fractional slot PMSMs, which are demonstrated in Section 6.2 and 6.3 respectively.

6.2 Sideband Vibration Analysis in Integral-Slot PMSM

The sideband ERFD model will be derived first according to the feature of integral-slot machine. The associated vibration will qualitatively validated by both no-load and load conditions. Comprehensive experimental validations are carried out based on the characteristic investigation of different speed conditions. A new mechanical damping measurement method is also proposed by the sideband vibration model.

6.2.1 Analytical ERFD Model in Integral-Slot Machine

Since the items of 1-6 in Table 6.1 are the main sideband ERFD components in integral-slot PMSMs, the associated amplitude, frequency and initial phase for such components can be further simplified. Due to the negligible leakage inductances in integral-slot machines, it can be approximated that $\sigma_3 \approx 2$, $\sigma_4 \approx 0$, and hence it can be derived from Equation (4.132) that

$$K_{12} \approx 2C_{12}, \quad K_{14} \approx 2C_{14}, \quad K_{21} \approx -C_{21} \tag{6.2}$$

The $2p^{th}$ spatial order ERFD with frequencies of $\mp(\omega_s \pm \omega_e)$, $\pm(\omega_s \pm 5\omega_e)$, and $\pm(2\omega_s \pm 2\omega_e)$ can therefore be approximated as

$$P_{2p\_\omega_s\pm\omega_e} = \frac{C_{12}B_0B_{\mu1}}{\mu_0}, \quad P_{2p\_\omega_s\pm5\omega_e} = \frac{C_{14}B_0B_{\mu1}}{\mu_0}, \quad P_{2p\_2\omega_s\pm2\omega_e} = -\frac{C_{21}B_0B_{\mu2}}{2\mu_0} \tag{6.3}$$

All the 0-order components of the first and third items in Table 6.1 have the same frequency of $(\omega_s \pm 3\omega_e)$ and therefore they need to be synthesized. By substituting the sideband magnetic field model expressed in (4.128) into ERFD model, the resultant $(\omega_s \pm 3\omega_e)$ frequency components can be expressed as

$$\begin{aligned} p_{0\_\omega_s\pm3\omega_e}(\theta_m, t) =& \frac{\sigma_3(C_{12}+C_{14})B_0B_{\mu1}}{2\mu_0}\sin((\omega_s \pm 3\omega_e)t) \\ &+ \frac{\sigma_4 C_{12}B_0B_{\mu1}}{2\mu_0}\sin((\omega_s \pm 3\omega_e)t \mp 2\delta) \\ &+ \frac{\sigma_4 C_{14}B_0B_{\mu1}}{2\mu_0}\sin((\omega_s \pm 3\omega_e)t \pm 2\delta) \end{aligned} \tag{6.4}$$

By neglecting σ_4 associated items on the right hand side, the corresponding ERFD amplitude can be approximated as

$$P_{0\_\omega_s\pm3\omega_e}(\theta_m, t) = \frac{(C_{12}+C_{14})B_0B_{\mu1}}{\mu_0} \tag{6.5}$$

Similarly, the 0-order components of the fifth item in Table 6.1 share the same frequency of $(2\omega_s)$, and the synthesized result can be derived as

$$p_{0\_2\omega_s} = -\frac{\sigma_4 C_{21}B_0B_{\mu2}}{2\mu_0}\sin(2\delta)\sin(2\omega_s t) \tag{6.6}$$

The amplitude of this particular component is small because of $\sigma_4 \approx 0$ and therefore can be neglected for further vibration analysis.

The major sideband ERFD components of integral-slot PMSMs are listed in table 6.2, together with their orders, frequencies and amplitudes. By incorporating the tooth-effect Equation (5.18) and vibration Equation (5.3) of the stator, the corresponding vibration in integral-slot PMSMs can be analytically calculated.

Table 6.2: Sideband ERFD components in integral-slot PMSMs

No.	Order	Frequency	Amplitude
1	$2p$	$\omega_s \pm \omega_e$	$C_{12}B_0B_{\mu1}/\mu_0$
2	$2p$	$\omega_s \pm 5\omega_e$	$C_{14}B_0B_{\mu1}/\mu_0$
3	$2p$	$2\omega_s \pm 2\omega_e$	$(C_{12}+C_{14})B_0B_{\mu1}/\mu_0$
4	0	$\omega_s \pm 3\omega_e$	$-C_{21}B_0B_{\mu2}/(2\mu_0)$

6.2.2 Qualitative Validations in No-load Condition

In order to validate the analytical derivations developed in the foregoing sections, the experimental investigations on an integral-slot PMSM drive system of prototype IV under different operational conditions are comprehensively carried out. PMSMs with two slots per pole per phase, which can be facilitated with two-layer overlapping windings, are widely employed for various high-performance drive systems. Prototype IV for experimental validations possesses such configuration with 6 rotor poles and 36 stator slots. The prototype IV is driven by a conventional two-level VSI with SVPWM technique and MTPA control strategy. Since the SVPWM switching

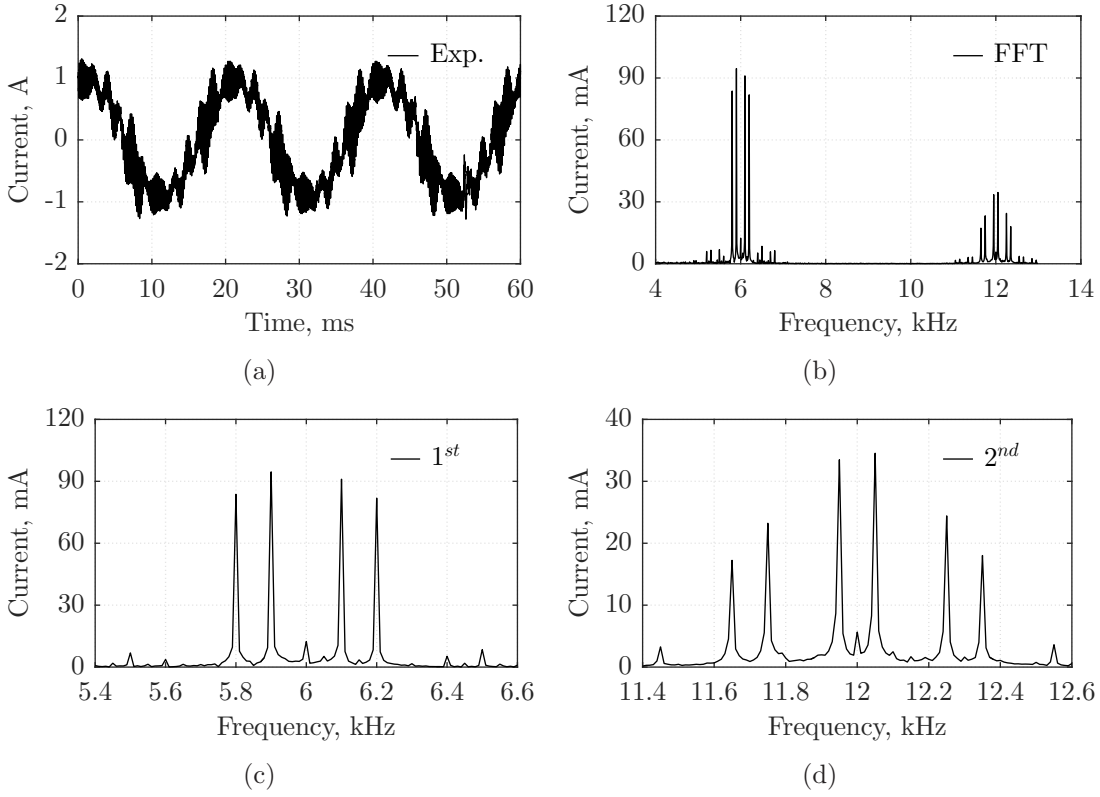

Figure 6.1: Experimental phase current waveform and its harmonic spectra: (a) phase current waveform, (b) current harmonic spectra, (c) first sideband harmonics, (d) second sideband harmonics. (Exp. - Experimental result)

frequency for the prototype drive system is 6kHz, the frequencies of the first and second sideband components will reach up to near 6kHz and 12kHz respectively. ERV and acoustic noise for higher frequencies such as 18kHz are normally insignificant and negligible. Thus only the first and second sideband components need to be investigated for the proposed prototype integral-slot PMSM drive system.

The experiment test on the prototype integral-slot PMSM drive system is first carried out at operational speed of 1000rpm under no-load condition from the dynamometer. The corresponding phase current waveform is captured and illustrated with its spectra at the first and second carrier frequency domain in Figure 6.1, which reveal the evident sideband current harmonic components. It is well validated from the figure that the $(\omega_s \pm 2\omega_e)$- and $(\omega_s \pm 4\omega_e)$-order current harmonics are the dominant components near the first carrier frequency while the $(2\omega_s \pm \omega_e)$-order components are the main harmonics in the second carrier frequency domain. The $(2\omega_s \pm 5\omega_e)$- and $(2\omega_s \pm 7\omega_e)$-order components can be quite close to $(2\omega_s \pm \omega_e)$-order harmonics with a large modulation index. However, the amplitudes are comparatively small in general.

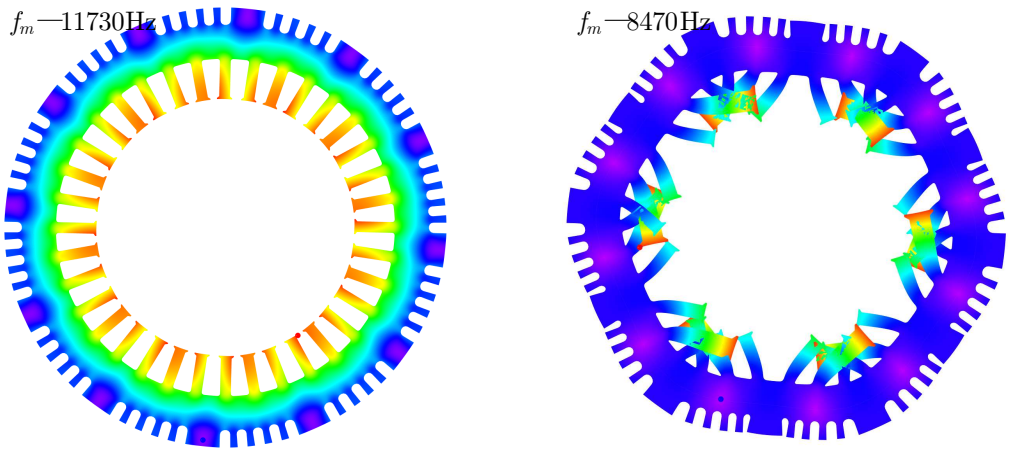

(a) (b)

Figure 6.2: 0^{th} and $2p^{th}$ vibration modes of the stator system from mechanical modal analysis: (a) 0^{th} spatial order, (b) $2p^{th}$ spatial order.

From the analytical derivations, those current components will generate corresponding 0^{th} and $2p^{th}$ spatial order sideband ERFD components on the stator by interacting with the main low-frequency magnetic field, and hence lead to sideband ERV and undesirable high-frequency acoustic noise. The natural frequencies of 0^{th} and $2p^{th}$ spatial order modes for the stator system of the prototype are essential to analytically evaluate the respective electromagnetic vibration. Consequently, a 2-D structural FEA model together with an eigenvalue subroutine is employed to get the corresponding natural frequencies of the 0^{th} and $2p^{th}$ spatial order modes. When the eigenvalues of those modes are around the first and second carrier frequencies, serious sideband ERV and acoustic noise will occur. The two mode shapes and their natural frequencies are obtained and illustrated in Figure 6.2, which reveals 11730Hz and 8470Hz for 0^{th} and $2p^{th}$ spatial order modes respectively. There are usually dis-

tant deviations between the switching frequency and natural frequency advised to avoid potential resonances. However, evident audible noise can still be generated even though the carrier frequency is far away from these natural frequencies.

Furthermore, an accelerometer is attached to the centre of the machine case surface along the axial direction in order to measure the vibration of the stator. The stator vibration of the prototype PMSM at 1000rpm under no-load condition is captured and the spectra near the first and second carrier frequency domain are then compiled and illustrated in Figure 6.3. The figures show vibrations occur at frequencies of 5950Hz/6050Hz, 5850Hz/6150Hz, 5750Hz/6250Hz, and 11900Hz/12100Hz labeled with circle, which are the $(\omega_s \pm \omega_e)$, $(\omega_s \pm 3\omega_e)$, $(\omega_s \pm 5\omega_e)$ and $(2\omega_s \pm 2\omega_e)$ respectively. The results qualitatively validate those are the main sideband electromagnetic vibration components in the first and second carrier frequency domains. Although the natural frequency of 0^{th} spatial order mode is much larger, the vibrations associated with the 0^{th} spatial orders with frequencies of 5850Hz/6150Hz are more severe than the $2p^{th}$ spatial orders due to their larger ERFD amplitudes.

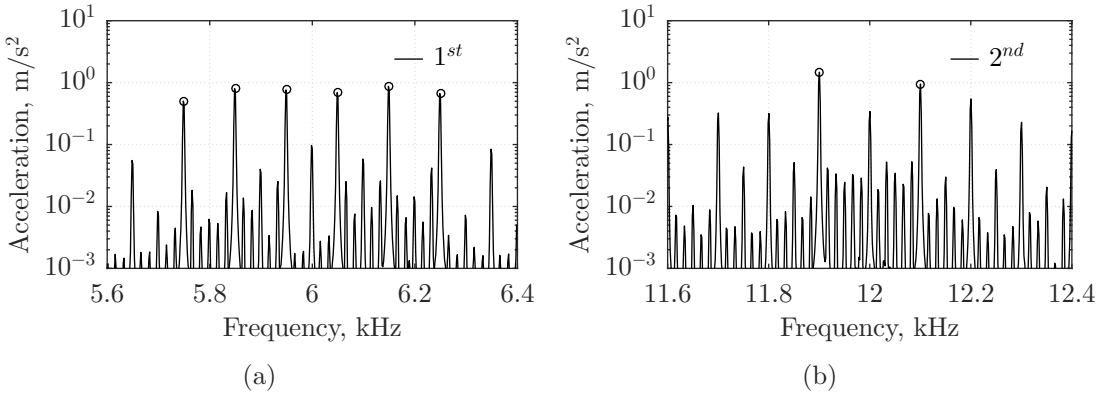

Figure 6.3: Stator system vibration spectra at 1000rpm with no-load condition: (a) first sideband components, (b) second sideband components.

6.2.3 Load Influence on Sideband Vibration

The PMSM with interior PM configuration will be in severe magnetic saturation under high load conditions. The magnetic saturation will reduce the inductance values, introduce cross-coupling effect and hence increase the sideband current harmonics significantly as revealed in Section 3.5. However, the relevant parameters σ_3 and σ_4 given in Equation (4.127) are almost unaffected by load and magnetic saturation for integral-slot PMSMs. Therefore, the impact of magnetic saturation on the sideband ERFD components is negligible. However, the load will increase the fundamental armature current component and hence the associated low-frequency armature reaction air-gap flux density. That may require a rise on the modulation index. The torque angle, which has a mild effect on the sideband ERFD components from the analytical models, will be also adjusted under the load condition.

Therefore, an experimental test on the prototype integral-slot PMSM drive with a load of 10N·m at 1000rpm is carried out in order to investigate the influence of torque angle on sideband electromagnetic vibration. With the MTPA control algorithm and the same operational speed, the modulation index with a 10N·m load is similar to the no-load condition and changes slightly from 0.769 to 0.789. Meanwhile, the torque angle is adjusted from about 0 to 22 degrees. The corresponding phase current waveform is captured and illustrated with its spectra in Figure 6.4.

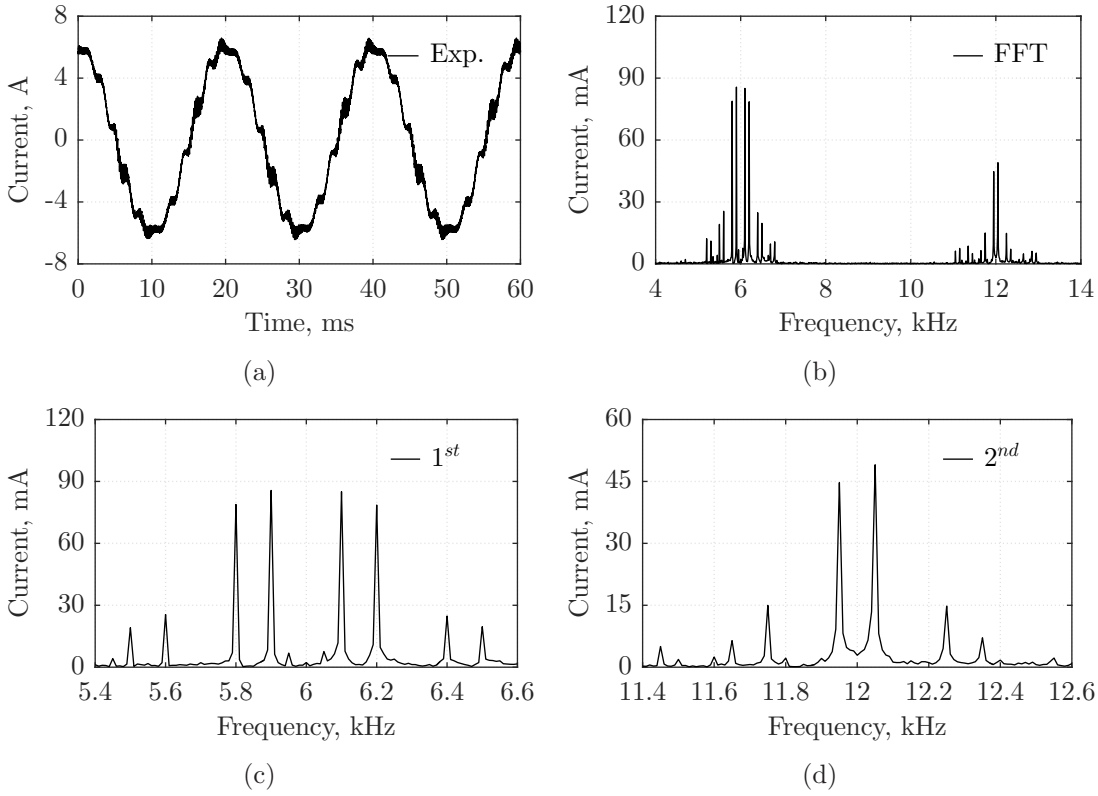

Figure 6.4: Current waveform and spectra at 1000rpm with 10Nm load: (a) current waveform, (b) current harmonic spectrum, (c) first sideband harmonics, (d) second sideband harmonics. (Exp. - Experimental result)

By comparing Figure 6.4 with Figure 6.1, it can be observed that the sideband harmonic components at both first and second carrier frequency domains have the same frequencies under no-load and load conditions. With load condition, the negligible variation on modulation index but significant increase on torque angle make the first sideband current harmonic components decrease sightly but the second components with frequencies of $(2\omega_s \pm \omega_e)$ increase significantly. Meanwhile, the corresponding stator vibrations are measured and the spectra near the first and second carrier frequency domain are derived and shown in Figure 6.5. As expected from the analytical models, Figure 6.5 shows that the amplitudes of the sideband ERV components, mainly the $(\omega_s \pm \omega_e)$, $(\omega_s \pm 3\omega_e)$, $(\omega_s \pm 5\omega_e)$ and $(2\omega_s \pm 2\omega_e)$ components are very close to the components from the no-load condition. Therefore, the simplified analytical models in table 6.1 are valid for sideband ERV analysis of integral-slot PMSM in most cases.

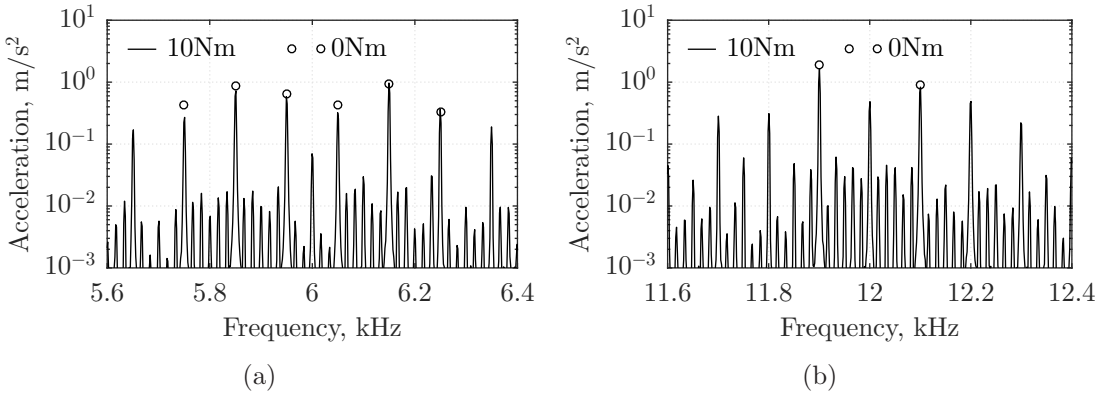

Figure 6.5: Stator system vibration spectra at 1000rpm with 10N·m load: (a) first sideband harmonics, (b) second sideband harmonics.

There are inevitable test errors of vibration caused by the connection of the load, the test point selection, and the acceleration installation. However, the vibration spectra involved in Figure 6.5 are obtained under the same situation as the no-load condition except that a different load was used to minimize test errors. A load of approximately 1.0N·m, mainly contributed from the friction of the mechanical transmission and dynamometer, exists in no-load condition, even without infliction of load from the dynamometer.

6.2.4 Quantitative Validations of Sideband Vibration

In order to sufficiently validate the sideband vibration model, comprehensive quantitative verification is carried out similar to the sideband current components. From the analytical models, the sideband ERFD components are mainly determined by the modulation index and torque angle. However, the vibration amplitudes are nearly independent to the torque angle for integral-slot PMSMs, which has been validated by both analytical model and experimental results. As a consequence, the inclusion of modulation index is efficient for the quantitative validation of the model. The modulation index of SVPWM is approximately proportional to its rotational speed when the prototype is operated under no-load condition (small friction load). Therefore, the amplitudes of the sideband ERFD components in the prototype drive under no-load conditions with different speed ranging from 0 to 1200rpm are evaluated based on the analytical models and depicted in Figure 6.6. The characteristics of those three sideband ERFD components generally comport well with corresponding current components. As expected, the amplitudes of all three components will gradually increase as the rotational speed and modulation index rise. It can also be observed from the figures that the 0^{th} spatial order harmonics with frequencies of $(\omega_s \pm 3\omega_e)$ are the largest. The $(\omega_s \pm \omega_e)$ components are generally larger than $(\omega_s \pm 5\omega_e)$ components for the $2p^{th}$ spatial order components. The tooth effect coefficients involved for the 0^{th} and $2p^{th}$ spatial order components are 0.75 and 0.72 respectively.

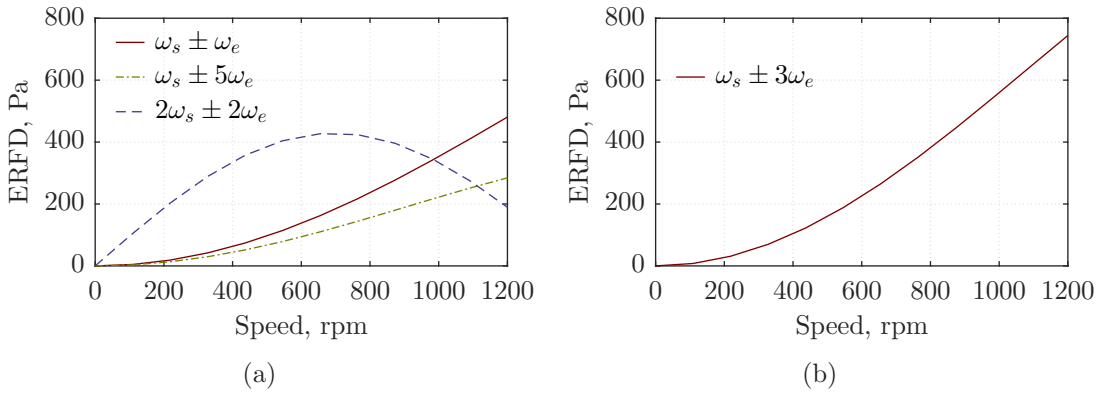

Figure 6.6: Sideband ERFD components under no-load conditions: (a) $2p^{th}$ spatial order components, (b) 0^{th} spatial order components.(Ana. - Analytical model, Exp. - Experimental result)

In order to validate the analytical models quantitatively, the amplitudes of the corresponding electromagnetic vibration components can be analytically evaluated by the analytical model with the results from Figure 6.6. Moreover, comprehensive experimental tests are carried out to capture the stator vibrations of the machine with no-load condition at different speeds. The corresponding amplitudes of the main vibration components in first and second carrier frequency domains are derived by taking the mean value of the amplitudes from five experimental samples in order to minimize the test error.

The amplitudes of the $2p^{th}$ spatial order components with frequencies of $(\omega_s \pm \omega_e)$, $(\omega_s \pm 5\omega_e)$ and $(2\omega_s \pm 2\omega_e)$ are compiled and compared with the analytical counterparts in Figure 6.7(a), 6.7(b) and 6.7(c) respectively, with close agreement achieved for $(\omega_s \pm \omega_e)$ and $(\omega_s \pm 5\omega_e)$ components. Whilst, the 0^{th} spatial order components with frequencies of $(\omega_s \pm 3\omega_e)$ are obtained and compared in Figure 6.7(d).

There are noticeable deviations between some analytical and experimental results, which reveals that the analytical models overestimate the $(2\omega_s \pm 2\omega_e)$-order components but underestimate the $(\omega_s \pm 3\omega_e)$-order components. However, the analytical results have demonstrated the tendency of such sideband electromagnetic vibration versus machine speed (modulation index) successfully. The analytical derivations of the sideband current harmonic components and the associated sideband ERFD components do not take into account the impact of magnetic saturation which is unavoidable in the prototype machine with interior PM configuration. The analytical equation, which is employed to evaluate the vibration amplitude, neglects the influence of actual complex geometry of the stator. The natural frequencies of the 0^{th} and $2p^{th}$ spatial order vibration modes are obtained from 2-D FEA, which ignores the axial effects and the impact of the phase windings. More importantly the modal damping ratios are estimated based on the low-fidelity empirical formula which will potentially introduce considerable error. In addition, there are always some inevitable experimental errors. By considering all those factors, it is reason-

able to conclude that experimental results are closely comparable with the analytical predictions.

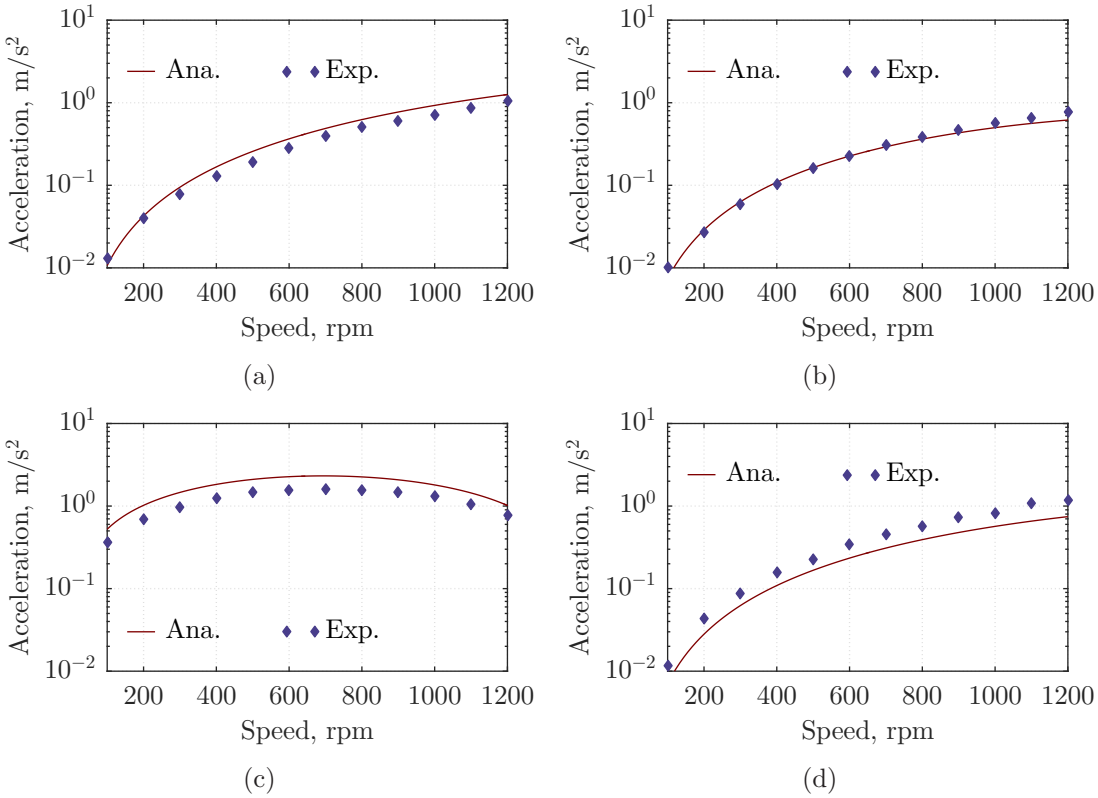

Figure 6.7: Machine vibration experimental validation with no-load condition at different speeds: (a) $2p^{th}$ spatial $(\omega_s \pm \omega_e)$ temporal order, (b) $2p^{th}$ spatial $(\omega_s \pm 5\omega_e)$ temporal order, (c) $2p^{th}$ spatial $(2\omega_s \pm 2\omega_e)$ temporal order, (d) 0^{th} spatial $(\omega_s \pm 3\omega_e)$ temporal order. (Ana. - Analytical model, Exp. - Experimental result)

6.2.5 Damping Ratio and Sideband Resonance

The damping ratio and natural frequencies of a stator system are the two key components in stator vibration. The derivations of these parameters from simulation and empirical method can introduce inevitable errors for the proposed analytical models. This will therefore compromise the validation and prediction, especially when the switching frequency and natural frequency of stator system are quite close. Hence accurate parameters are essential to support the model validation. The accurate prediction of stator natural frequency can also benefit the selection of appropriate switching frequency. The sweep frequency vibration method is employed for the stator system test as illustrated in Section 5.3.2. By exploiting the sideband vibration components, this method is further extended to measure the mechanical damping factors.

It can be derived that the analytical sideband ERFD of $2p^{th}$ spatial $(\omega_s \pm \omega_e)$ temporal order components are proportional to $B_{\mu 1}$, which is inversely proportional to

$(\omega_s \pm 3\omega_e)$ in the constant speed condition according to Equation (4.127). On the other hand, the vibration velocity is proportional to $(\omega_s \pm \omega_e)$. As a result, the relationship between such sideband vibration and corresponding natural frequency can be shown as

$$\begin{aligned} v_m = (\omega_s \pm \omega_e)A_m &\propto \frac{(\omega_s \pm \omega_e)}{(\omega_s \pm 3\omega_e)\sqrt{(\omega_{2p}^2 - (\omega_s \pm \omega_e)^2)^2 + 4\zeta^2\omega_{2p}^2(\omega_s \pm \omega_e)^2}} \\ &\approx \frac{1}{\sqrt{(\omega_{2p}^2 - (\omega_s \pm \omega_e)^2)^2 + 4\zeta^2\omega_{2p}^2(\omega_s \pm \omega_e)^2}} \end{aligned} \tag{6.7}$$

Consequently, the damping and resonant characteristics can be derived from the vibration velocity measurements by sweeping through all switching frequencies. An experimental test on the prototype IV is conducted at the operational speed of 1000rpm and no torque with different switching frequencies to acquire the mechanical parameters. Figure 6.8(a) depicts the amplitudes of $2p^{th}$ spatial order $(\omega_s \pm \omega_e)$ frequency components. The nature frequency can be obtained directly from the figure with the value of 8100Hz, while the damping ratio can also be approximately calculated by

$$\zeta_m = \frac{\Delta f}{2f_m} \tag{6.8}$$

where Δf is the band width when vibration amplitudes reduce into $1/\sqrt{2}$. The resonance test result can be fitted to calculate the corresponding damping ratio for $2p^{th}$ mode as about 0.12, while the empirical Equation (5.4) offers a much smaller result of 0.045. Obviously, the significant underestimation of the damping parameter will introduce large prediction errors near the resonant point. The stator system vibration spectra near the first carrier frequency at 1000rpm under no-load condition and switching frequency of 8kHz are captured and depicted in Figure 6.8(b). The results from analytical model are shown in the figure. It demonstrates noticeable deviations in all $2p^{th}$ spatial order components in the empirical parameters and the experimental tests. These frequencies are 7750Hz, 7950Hz, 8050Hz and 8250Hz. Whereas, such prediction errors have been effectively narrowed by the more accurate prediction of damping ratio. On the other hand the 0^{th} spatial order components, which are 7850Hz and 8150Hz, are far away from the resonance frequency. Therefore the damping factor has trivial effect on the vibration of these components. Consequently, the results from all these sources are nearly identical for those two frequencies.

The natural frequency of $2p^{th}$ spatial order mode of the stator system of the prototype PMSM is close to 8kHz. Therefore the stator will resonate and large sideband ERV is expected by the switching frequency of 8kHz. Compared with the results in Figure 6.5, it is evident that the $2p^{th}$ spatial order components with frequencies of $(\omega_s \pm \omega_e)$ and $(\omega_s \pm 5\omega_e)$ are significantly aggravated by the resonance phenomenon. Meanwhile, the 0^{th} spatial orders with frequencies of $(\omega_s \pm 3\omega_e)$ do not change significantly due to their distance from the natural frequency of 0^{th} spatial order mode. Consequently, it is always of particular importance to keep the switching frequency

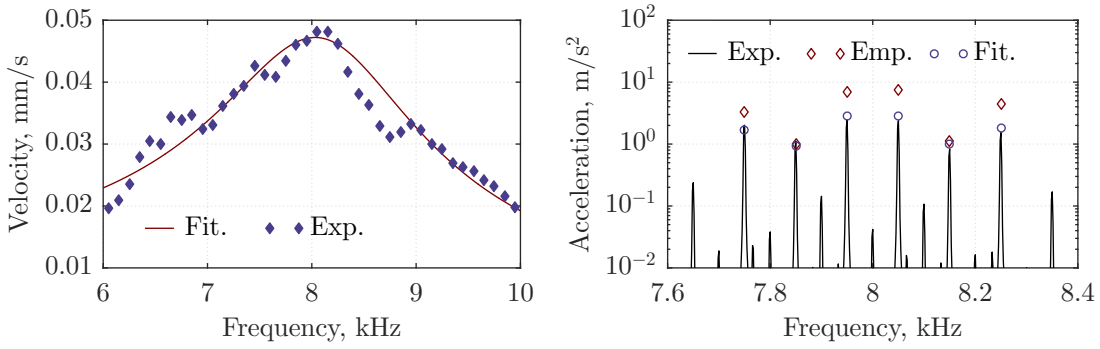

Figure 6.8: Mechanical parameters extraction and resonant analysis: (a) mechanical parameters test, (b) vibration spectrum at 1000rpm with switching frequency of 8kHz. (Exp. - Experimental result, Emp. - Empirical parameters based model, Fit. - Fitting parameters based model)

far away from the natural frequency of the main spatial order modes so that potential resonance from sideband ERFD can be effectively avoided. Otherwise, severe piercing and unpleasant acoustic noise is more likely to be produced by the sideband harmonic components.

6.3 Sideband Vibration Analysis in FSCW PMSM

Similar to the integral-slot PMSM, the analytical investigation on sideband ERFD of FSCW machines is carried out, followed by qualitative and quantitative validation in this section. The experiments under the no-load condition with different rotational speed are first carried out to reveal the effect of modulation index, and then flux weakening technique is implemented to study the impacts of armature reaction. The synthesis of the sideband ERFD components is further examined.

6.3.1 Sideband ERFD Analysis in FSCW PMSM

The 10-pole 12-slot FSCW PMSM prototype I is employed for the sideband ERV analysis and validation. A switching frequency of 4kHz is chosen for the SVPWM technique to observe the vibration components. As aforementioned, the critical high-frequency sideband and low-frequency air-gap magnetic field components will interact with each other to produce a great deal of sideband ERFD components. Examined from the analytical model of the interharmonic magnetic flux density coefficient K_v, it can be derived that $-t_0^{th}$ (first), p^{th} (fifth), and $(p-Z)^{th}$ (seventh) spatial harmonic components have the most significant amplitudes in the prototype I. Although there are some other evident harmonic components, they are of a much larger spatial order and hence can be neglected for ERV investigation. As a result, only the components involving three main spatial harmonic components of armature-

reaction and sideband air-gap magnetic field are suitable for the proposed machine ($\upsilon = -1, 5, -7$). The rotational directions of $-t_0^{th}$ and $(p-Z)^{th}$ spatial components are always opposite to the fundamental p^{th} components in the proposed FSCW PMSM. Based on Equation (4.121), the corresponding K_{-t_0} and K_{p-Z} are derived as 0.2531 and -0.7745 respectively.

Table 6.3: The 0^{th} spatial order sideband ERFD

No.	Frequency	Phase	Amplitude
1	$\mp(\omega_s \pm 3\omega_e)$	$\varphi_{p\_12} - \delta$	$\mp K_{12}B_0B_{\mu1}/(2\mu_0)$
2	$\pm(\omega_s \pm 3\omega_e)$	$\varphi_{p\_14} - \delta$	$\mp K_{14}B_0B_{\mu1}/(2\mu_0)$
3	$\pm(2\omega_s)$	$\varphi_{p\_21} - \delta$	$\mp K_{21}B_0B_{\mu2}/(2\mu_0)$
4	$\pm(\omega_s \pm 3\omega_e)$	$\varphi_s - \varphi_{a\_12}$	$\mp K_{p-Z}^2K'_{12}B_aB_{\mu1}/(2\mu_0)$
5	$\mp(\omega_s \pm 3\omega_e)$	$\varphi_s - \varphi_{a\_14}$	$\mp K_{p-Z}^2K'_{14}B_aB_{\mu1}/(2\mu_0)$
6	$\mp(2\omega_s)$	$\varphi_s - \varphi_{a\_21}$	$\mp K_{p-Z}^2K'_{21}B_aB_{\mu2}/(2\mu_0)$
7	$\pm(\omega_s \pm 3\omega_e)$	$\varphi_s - \varphi_{a\_12}$	$\mp K_{-t_0}^2K'_{12}B_aB_{\mu1}/(2\mu_0)$
8	$\mp(\omega_s \pm 3\omega_e)$	$\varphi_s - \varphi_{a\_14}$	$\mp K_{-t_0}^2K'_{14}B_aB_{\mu1}/(2\mu_0)$
9	$\mp(2\omega_s)$	$\varphi_s - \varphi_{a\_21}$	$\mp K_{-t_0}^2K'_{21}B_aB_{\mu2}/(2\mu_0)$

The abundant sideband ERFD components can potentially lead to significant sideband ERV and acoustic noises in the prototype PMSM drive. The interactions between the components with the same spatial order υ will incur two sets of sideband ERFD components with respective spatial orders of 0 and 2υ. Therefore, the p^{th}, $(p-Z)^{th}$ and $-t_0^{th}$ spatial order sideband air-gap magnetic field components, which all have main frequencies of $(\omega_s \pm 2\omega_e)$, $(\omega_s \pm 4\omega_e)$ and $(2\omega_s \pm \omega_e)$ with the corresponding low-frequency components, will generate 9 items in total of 0^{th} spatial order sideband ERFD components. Based on analytical results in Chapter 4, the frequencies, phases and amplitudes of those items are obtained and given in Table 6.3.

Table 6.4: The $2p^{th}$ spatial order sideband ERFD components

No.	Frequency	Phase	Amplitude
1	$\mp(\omega_s \pm \omega_e)$	$\varphi_{p\_12} + \delta$	$\mp K_{12}B_0B_{\mu1}/(2\mu_0)$
2	$\pm(\omega_s \pm 5\omega_e)$	$\varphi_{p\_14} + \delta$	$\mp K_{14}B_0B_{\mu1}/(2\mu_0)$
3	$\pm(2\omega_s \pm 2\omega_e)$	$\varphi_{p\_21} + \delta$	$\mp K_{21}B_0B_{\mu2}/(2\mu_0)$

On the other hand, the interactions will also produce 3 items each of $2p^{th}$, $(2p-2Z)^{th}$, and $(-2t_0)^{th}$ spatial order sideband ERFD components. For the sake of simplicity, the $(2p-2Z)^{th}$ and $(-2t_0)^{th}$ spatial order components are directly converted into the corresponding positive $(2Z-2p)^{th}$ and $2t_0^{th}$ components by simple mathematical manipulation. The corresponding frequencies, phases and amplitudes are listed in Table 6.4, 6.5 and 6.6 respectively.

Table 6.5: The $(2Z-2p)^{th}$ spatial order sideband ERFD components

No.	Frequency	Phase	Amplitude
1	$\pm(\omega_s \pm \omega_e)$	$-\varphi_{a\_12} - \varphi_s$	$\mp K_{p-Z}^2 K'_{12} B_a B_{\mu 1}/(2\mu_0)$
2	$\mp(\omega_s \pm 5\omega_e)$	$-\varphi_{a\_14} - \varphi_s$	$\mp K_{p-Z}^2 K'_{14} B_a B_{\mu 1}/(2\mu_0)$
3	$\mp(2\omega_s \pm 2\omega_e)$	$-\varphi_{a\_21} - \varphi_s$	$\mp K_{p-Z}^2 K'_{21} B_a B_{\mu 2}/(2\mu_0)$

Table 6.6: The $(2t_0)^{th}$ spatial order sideband ERFD components

No.	Frequency	Phase	Amplitude
1	$\pm(\omega_s \pm \omega_e)$	$-\varphi_{a\_12} - \varphi_s$	$\mp K_{-t_0}^2 K'_{12} B_a B_{\mu 1}/(2\mu_0)$
2	$\mp(\omega_s \pm 5\omega_e)$	$-\varphi_{a\_14} - \varphi_s$	$\mp K_{-t_0}^2 K'_{14} B_a B_{\mu 1}/(2\mu_0)$
3	$\mp(2\omega_s \pm 2\omega_e)$	$-\varphi_{a\_21} - \varphi_s$	$\mp K_{-t_0}^2 K'_{21} B_a B_{\mu 2}/(2\mu_0)$

The interactions between the components with the different spatial orders will also incur two sets of sideband ERFD components. As the p^{th} spatial air-gap magnetic field component will interact with the $(p-Z)^{th}$ and $-t_0^{th}$ spatial sideband components to generate 4 items each of $(2p-Z)^{th}$, $-Z^{th}$, $(p-t_0)^{th}$ and $(-p-t_0)^{th}$ spatial sideband ERFD components. The conversions from $(2p-Z)^{th}$, $-Z^{th}$ and $(-p-t_0)^{th}$ spatial components to the positive $(Z-2p)^{th}$, Z^{th} and $(p+t_0)^{th}$ components are directly carried out. The resultant frequencies, phases and amplitudes of those items form the first half of Table 6.7, 6.8, 6.9 and 6.10 respectively. The interactions between the p^{th} spatial sideband, the $(p-Z)^{th}$ and $-t_0^{th}$ spatial armature reaction air-gap magnetic field components will also result in sideband ERFD components with the same $(Z-2p)^{th}$, Z^{th}, $(p-t_0)^{th}$ and $(p+t_0)^{th}$ spatial orders and frequencies but different amplitudes and phases. The analytical characteristics of those components are acquired to complete the rest of Table 6.7, 6.8, 6.9 and 6.10.

Finally, $(Z-p-t_0)^{th}$ and $(p-Z-t_0)^{th}$ spatial sideband ERFD components will originate from the interaction between the $(p-Z)^{th}$ armature reaction and $-t_0^{th}$ sideband air-gap magnetic field components while $(p-Z+t_0)^{th}$ and $(Z-p+t_0)^{th}$

Table 6.7: The $(Z-2p)^{th}$ spatial order sideband ERFD components

No.	Frequency	Phase	Amplitude
1	$\pm(\omega_s \pm \omega_e)$	$-\varphi_{a\_12} - \delta$	$\mp K_{p-Z} K'_{12} B_0 B_{\mu 1}/(2\mu_0)$
2	$\mp(\omega_s \pm 5\omega_e)$	$-\varphi_{a\_14} - \delta$	$\mp K_{p-Z} K'_{14} B_0 B_{\mu 1}/(2\mu_0)$
3	$\mp(2\omega_s \pm 2\omega_e)$	$-\varphi_{a\_21} - \delta$	$\mp K_{p-Z} K'_{21} B_0 B_{\mu 2}/(2\mu_0)$
4	$\pm(\omega_s \pm \omega_e)$	$-\varphi_s - \varphi_{p\_12}$	$\mp K_{p-Z} K_{12} B_a B_{\mu 1}/(2\mu_0)$
5	$\mp(\omega_s \pm 5\omega_e)$	$-\varphi_s - \varphi_{p\_14}$	$\mp K_{p-Z} K_{14} B_a B_{\mu 1}/(2\mu_0)$
6	$\mp(2\omega_s \pm 2\omega_e)$	$-\varphi_s - \varphi_{p\_21}$	$\mp K_{p-Z} K_{21} B_a B_{\mu 2}/(2\mu_0)$

Table 6.8: The Z^{th} spatial order sideband ERFD components

No.	Frequency	Phase	Amplitude
1	$\pm(\omega_s \pm 3\omega_e)$	$-\varphi_{a\_12} + \delta$	$\mp K_{p-Z} K'_{12} B_0 B_{\mu 1}/(2\mu_0)$
2	$\mp(\omega_s \pm 3\omega_e)$	$-\varphi_{a\_14} + \delta$	$\mp K_{p-Z} K'_{14} B_0 B_{\mu 1}/(2\mu_0)$
3	$\mp(2\omega_s)$	$-\varphi_{a\_21} + \delta$	$\mp K_{p-Z} K'_{21} B_0 B_{\mu 2}/(2\mu_0)$
4	$\mp(\omega_s \pm 3\omega_e)$	$-\varphi_s + \varphi_{p\_12}$	$\mp K_{p-Z} K_{12} B_a B_{\mu 1}/(2\mu_0)$
5	$\pm(\omega_s \pm 3\omega_e)$	$-\varphi_s + \varphi_{p\_14}$	$\mp K_{p-Z} K_{14} B_a B_{\mu 1}/(2\mu_0)$
6	$\pm(2\omega_s)$	$-\theta_s + \varphi_{p\_21}$	$\mp K_{p-Z} K_{21} B_a B_{\mu 2}/(2\mu_0)$

Table 6.9: The $(p - t_0)^{th}$ spatial order sideband ERFD components

No.	Frequency	Phase	Amplitude
1	$\mp(\omega_s \pm \omega_e)$	$\delta + \varphi_{a\_12}$	$\mp K_{-t_0} K'_{12} B_0 B_{\mu 1}/(2\mu_0)$
2	$\pm(\omega_s \pm 5\omega_e)$	$\delta + \varphi_{a\_14}$	$\mp K_{-t_0} K'_{14} B_0 B_{\mu 1}/(2\mu_0)$
3	$\pm(2\omega_s \pm 2\omega_e)$	$\delta + \varphi_{a\_21}$	$\mp K_{-t_0} K'_{21} B_0 B_{\mu 2}/(2\mu_0)$
4	$\mp(\omega_s \pm \omega_e)$	$\varphi_{p\_12} + \varphi_s$	$\mp K_{-t_0} K_{12} B_a B_{\mu 1}/(2\mu_0)$
5	$\pm(\omega_s \pm 5\omega_e)$	$\varphi_{p\_14} + \varphi_s$	$\mp K_{-t_0} K_{14} B_a B_{\mu 1}/(2\mu_0)$
6	$\pm(2\omega_s \pm 2\omega_e)$	$\varphi_{p\_21} + \varphi_s$	$\mp K_{-t_0} K_{21} B_a B_{\mu 2}/(2\mu_0)$

components will arise from the interaction between $-t_0^{th}$ armature reaction and $(p - Z)^{th}$ sideband components. By converting to the corresponding positive spatial order, their frequencies, phases and amplitudes are given in Table 6.11 and 6.12 respectively.

It is evident that there are sideband ERFD items with the same frequencies but different amplitudes and phases in each individual table. However, such items rotate in either the same or opposite direction from one another. It can be seen that Table 6.6 and 6.7 also share the same spatial order of two and the all three items with same frequencies are of same direction. Table 6.10 and 6.11 have the same spatial order of six and two opposite-direction pairs of items with same frequencies and

Table 6.10: The $(p + t_0)^{th}$ spatial order sideband ERFD components

No.	Frequency	Phase	Amplitude
1	$\pm(\omega_s \pm 3\omega_e)$	$\delta - \varphi_{a\_12}$	$\mp K_{-t_0} K'_{12} B_0 B_{\mu 1}/(2\mu_0)$
2	$\mp(\omega_s \pm 3\omega_e)$	$\delta - \varphi_{a\_14}$	$\mp K_{-t_0} K'_{14} B_0 B_{\mu 1}/(2\mu_0)$
3	$\mp(2\omega_s)$	$\delta - \varphi_{a\_21}$	$\mp K_{-t_0} K'_{21} B_0 B_{\mu 2}/(2\mu_0)$
4	$\mp(\omega_s \pm 3\omega_e)$	$\varphi_{p\_12} - \varphi_s$	$\mp K_{-t_0} K_{12} B_a B_{\mu 1}/(2\mu_0)$
5	$\pm(\omega_s \pm 3\omega_e)$	$\varphi_{p\_14} - \varphi_s$	$\mp K_{-t_0} K_{14} B_a B_{\mu 1}/(2\mu_0)$
6	$\pm(2\omega_s)$	$\varphi_{p\_21} - \varphi_s$	$\mp K_{-t_0} K_{21} B_a B_{\mu 2}/(2\mu_0)$

Table 6.11: The $(Z-p-t_0)^{th}$ spatial order sideband ERFD components

No.	Frequency	Phase	Amplitude
1	$\mp(\omega_s \pm 3\omega_e)$	$\varphi_{a\_12} - \varphi_s$	$\mp K_{p-Z} K_{-t_0} K'_{12} B_a B_{\mu 1}/(2\mu_0)$
2	$\pm(\omega_s \pm 3\omega_e)$	$\varphi_{a\_14} - \varphi_s$	$\mp K_{p-Z} K_{-t_0} K'_{14} B_a B_{\mu 1}/(2\mu_0)$
3	$\pm(2\omega_s)$	$\varphi_{a\_21} - \varphi_s$	$\mp K_{p-Z} K_{-t_0} K'_{21} B_a B_{\mu 2}/(2\mu_0)$
4	$\pm(\omega_s \pm 3\omega_e)$	$\varphi_s - \varphi_{a\_12}$	$\mp K_{p-Z} K_{-t_0} K'_{12} B_a B_{\mu 1}/(2\mu_0)$
5	$\mp(\omega_s \pm 3\omega_e)$	$\varphi_s - \varphi_{a\_14}$	$\mp K_{p-Z} K_{-t_0} K'_{14} B_a B_{\mu 1}/(2\mu_0)$
6	$\mp(2\omega_s)$	$\varphi_s - \varphi_{a\_21}$	$\mp K_{p-Z} K_{-t_0} K'_{21} B_a B_{\mu 2}/(2\mu_0)$

Table 6.12: The $(Z-p+t_0)^{th}$ spatial order sideband ERFD components

No.	Frequency	Phase	Amplitude
1	$\pm(\omega_s \pm \omega_e)$	$-\varphi_s - \varphi_{a\_12}$	$\mp K_{p-Z} K_{-t_0} K'_{12} B_a B_{\mu 1}/\mu_0$
2	$\mp(\omega_s \pm 5\omega_e)$	$-\varphi_s - \varphi_{a\_14}$	$\mp K_{p-Z} K_{-t_0} K'_{14} B_a B_{\mu 1}/\mu_0$
3	$\mp(2\omega_s \pm 2\omega_e)$	$-\varphi_s - \varphi_{a\_21}$	$\mp K_{p-Z} K_{-t_0} K'_{21} B_a B_{\mu 2}/\mu_0$

directions.

The above items can be divided into two categories which are associated with either B_0 or B_a. By substituting the sideband air-gap magnetic field expressions into the corresponding sideband ERFD components, the amplitude ratio of the components from the two groups with the same orders and frequencies primarily involving in B_0/B_a and K_μ/K'_μ ($\mu = 12, 14, 21$) can be calculated. B_a can be rewritten as

$$B_a = \frac{K_L \psi_a}{\alpha \tau_p N K_{wp} L_{ef}}, \quad K_L = \frac{L_p}{\sum L_\upsilon + L_\sigma} \tag{6.9}$$

K_L is the percentage of the fundamental inductance component over the overall inductance. The involved leakage inductance, mainly contributed by the slot leakage can be quite significant in FSCW PMSMs [159]. The correlate inductance components could be derived by either the proposed analytical model in Section 4.4.4 or numerical analysis [203]. To further investigate the influence of the armature reaction, it is assumed that the saliency effect and leakage inductance are ignored in Equation (6.9). Thus K_L can be approximated as

$$K_L = \begin{cases} \frac{1}{2}(\frac{Z K_{wp}}{\pi p})^2, & \text{for single layer winding} \\ (\frac{Z K_{wp}}{\pi p})^2, & \text{for double layer winding} \end{cases} \tag{6.10}$$

It can be inspected that K_L is around 0.4 for most double-layer winding FSCW PMSMs even under ideal condition. For single-layer winding configuration, it will be even smaller. Hence, the ERFD components associated with B_a can be normally neglected under normal conditions of $\psi_a < \psi_f$. The resultant severe magnetic

saturation under heavy-load conditions will significantly mitigate the rotor saliency effect so that $L_{ad} \approx L_{aq} \approx L_p$, and hence $K_\mu \approx K'_\mu$ and $\varphi_{a\_\mu} \approx \varphi_{p\_\mu}$ can be obtained. Hence, the phase difference between the two groups of sideband ERFD components can be approximated as $\varphi_s - \delta$. Normally, FSCW PMSMs are operated with power factor close to unity for most load cases so that the phase difference $(\varphi_s - \delta)$ will be close to $\pi/2$. This particular phase difference will minimize the contribution of the sideband ERFD component associated with B_a to the resultant vectorial synthesis. Therefore, it is still practically reasonable to neglect those components even under heavy-load conditions of $\psi_a \approx \psi_f$, but essential to take these into account under extreme conditions of $\psi_a > \psi_f$. Furthermore, B_a can be quite close to B_0 under deep flux-weakening conditions, which will nonetheless result in much smaller sideband ERFD amplitudes than the no-load condition. However, those particular conditions can be employed to examine the influence of the armature reaction on sideband ERV characteristics as the spatial interharmonic components of armature reaction magnetic field are independent of φ_s, and hence the demagnetizing current can introduce abundant interharmonics in the machine.

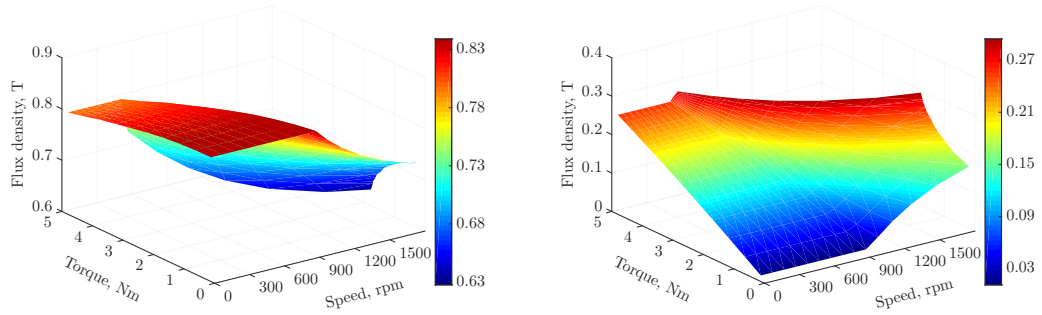

(a) (b)

Figure 6.9: The fundamental air-gap flux density: (a) air-gap flux density (B_0), (b) armature-reaction air-gap flux density without rotor saliency consideration (B_a).

To examine the armature reaction on the ERFD more specifically, B_0 and B_a are demonstrated in Figure 6.9(a) and 6.9(b) for the prototype FSCW PMSM. The maximum ratios between B_a and B_0 below and above the based speed are derived based on the results as 0.3275 and 0.4804. It is noteworthy that these ratios are usually much lower than the corresponding maximum ratios for most cases. Therefore, the items associated with B_0 are the dominant contributors of the corresponding sideband vibration in the prototype FSCW PMSM.

In general, only the sideband ERFD items with the same spatial orders, frequencies and directions can be vectorially synthesized based on their given amplitudes and phases. However the analytical formulae of such vector synthesis are too complex to provide apparent insights and hence not further provided here. Instead, actual evaluations on the vector syntheses of the items are performed for the prototype FSCW PMSM. The respective items associated with B_0 and B_a in Table 6.3 to 6.11 are synthesized based on the amplitudes and phases evaluated. As a result, the amplitude ratios between items associated with B_0 and synthesized values can be easily obtained and the corresponding ratio ranges are presented in Table 6.13.

Although the armature reaction generally results in more severe impacts on the sideband ERFD in the second carrier frequency domain than the first frequency domain below the base speed, they are mostly negligible even under heavy load conditions. Moreover, deep flux weakening effects far above the base speed can significantly reduce the corresponding amplitudes of the synthesized sideband ERFD components. Despite the same spatial orders and frequencies, there are respective items associated with B_0 and B_a in Table 6.3, 6.8, 6.10 and 6.11 with opposite rotational directions. The syntheses of such items result in the same frequencies but varying amplitudes of ERFD components with the circumferential positions. On the whole, considerations of the items associated with B_0 are sufficient for sideband ERFD investigation for the proposed FSCW PMSM from the actual results.

Table 6.13: The ranges of amplitude ratios between the dominant and synthesized sideband ERFD components

Spatial Order	Frequency	Ratio Range (below|above)
$(2t_0)^{th}$ and $(Z-2p)^{th}$	$\pm(\omega_s \pm \omega_e)$	0.93-1.01 | 0.91-1.41
	$\pm(\omega_s \pm 5\omega_e)$	1.00-1.07 | 0.88-1.65
	$\pm(2\omega_s \pm 2\omega_e)$	0.84-1.00 | 0.84-1.34
$(p-t_0)^{th}$	$\pm(\omega_s \pm \omega_e)$	0.91-1.01 | 0.89-1.47
	$\pm(\omega_s \pm 5\omega_e)$	1.01-1.06 | 0.85-1.72
	$\pm(2\omega_s \pm 2\omega_e)$	0.83-1.00 | 0.83-1.39
0^{th}	$\pm(\omega_s \pm 3\omega_e)$	0.83-1.00 | 0.83-1.50
	$\mp(\omega_s \pm 3\omega_e)$	0.97-1.00 | 0.98-1.18
Z^{th}	$\pm(\omega_s \pm 3\omega_e)$	0.90-1.00 | 0.89-1.15
	$\mp(\omega_s \pm 3\omega_e)$	0.82-1.00 | 0.67-1.88
$(p+t_0)^{th}$ and $(Z-p-t_0)^{th}$	$\pm(\omega_s \pm 3\omega_e)$	0.90-1.00 | 0.89-1.15
	$\mp(\omega_s \pm 3\omega_e)$	0.92-1.00 | 0.76-0.99
	$\pm 2\omega_s$	0.95-1.03 | 0.70-1.03

6.3.2 Qualitative Validations Under the No-load Condition

As discussed in the previous section, the B_0 associated 0^{th}, $(Z-2p)^{th}$, $(p-t_0)^{th}$, $(p+t_0)^{th}$, $2p^{th}$ and Z^{th} spatial orders are the main ERFD components of significant amplitude in the prototype. To analyze the corresponding vibration in the stator, the natural frequencies of these components are further to be calculated. The frequency sweep method with FEM for frequency response analysis is employed for the eigenvalue prediction.

The resultant eigenvalues of 0^{th} and $(p+t_0)^{th}$ modes are depicted in Figure 6.10. Based on the simulation result, the natural frequency of the 0^{th} spatial order stator mode is 13.78kHz, which is much higher than the frequencies of the second sideband ERFD components. The large eigenvalue and damping ratio significantly mitigate the induced sideband ERV and acoustic noise of 0^{th} spatial order components so

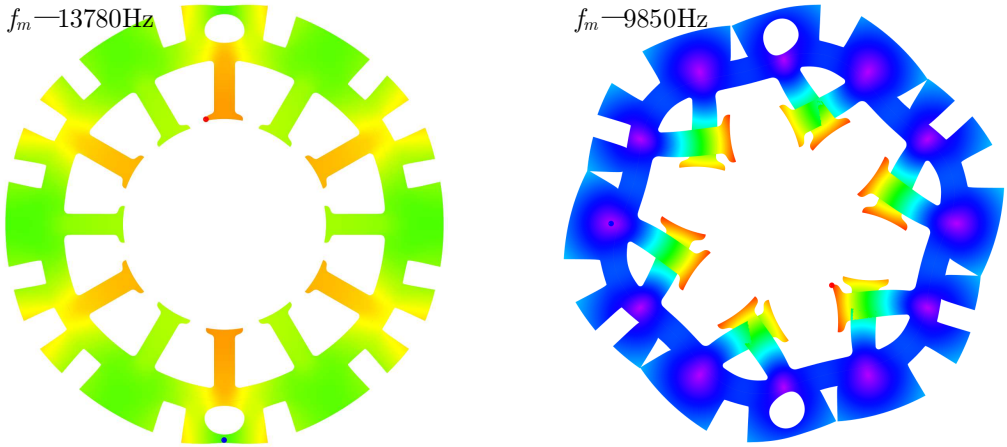

Figure 6.10: Stator system natural frequency analysis of different modes: (a) 0, (b) $(p + t_0) = 6$.

that they are negligible. The natural frequencies of higher order ERFDs, such as the $2p^{th}$ and Z^{th} components, are also well above 13kHz. Consequently the corresponding sideband ERV and acoustic noise can be ignored as well. Sometimes it is essential to include the modulated $(Z - 2p)^{th}$ items from $2p^{th}$ components by tooth effect during the investigation. However the $(Z - 2p)^{th}$ and $2p^{th}$ spatial order ERFD components are close in amplitudes for the prototype. The tooth effect coefficient of $2p^{th}$ spatial order is much smaller than its $(Z - 2p)^{th}$ counterpart. Hence the resultant $(Z - 2p)^{th}$ spatial order vibration from $2p^{th}$ components is somewhat too insignificant to be important in sideband vibration analysis. The eigenvalue of $(p+t_0)^{th}$ spatial order mode is 9.85kHz from the simulation, as shown in Figure 6.10(b), which is considerably higher than the frequencies of its first sideband components. As a result, these $(p+t_0)^{th}$ spatial sideband ERFD components in the first carrier frequency domain can be practically excluded from the investigation for the prototype drive. However the eigenvalue is relatively close to the frequencies of its second sideband components (around 8kHz) so that noticeable sideband ERVs in the second carrier frequency domain may be produced.

Furthermore, the natural frequencies of $(Z-2p)^{th}$ and $(p-t_0)^{th}$ spatial order stator modes have been given in Figure 5.29. Their eigenvalues are much smaller, with values of 2.4kHz and 7.19kHz. They are respectively close to the frequencies of the first and second sideband ERFD components, which are around 4kHz and 8kHz. Consequently it is essential to investigate these spatial components, which are the main contributors to sideband ERV and acoustic noise for the prototype FSCW PMSM based on the analytical results in details.

In order to validate the proposed analytical model, the experimental tests on the prototype FSCW PMSM drive system are first carried out at operational speed of 600rpm with no-load attached. The corresponding phase current waveform is captured and illustrated with its spectra at the first and second carrier frequency domains in Figure 6.11. This reveals the evident first and second sideband current

harmonic components. From Figure 6.11, the sideband current harmonic components with frequencies of $(\omega_s \pm 2\omega_e)$ (3.9kHz and 4.1kHz) and $(\omega_s \pm 4\omega_e)$ (3.8kHz and 4.2kHz) are the main harmonics near the first carrier frequency while the components with frequencies of $(2\omega_s \pm \omega_e)$ (7.95kHz and 8.05kHz) are the main harmonics near the second carrier frequency.

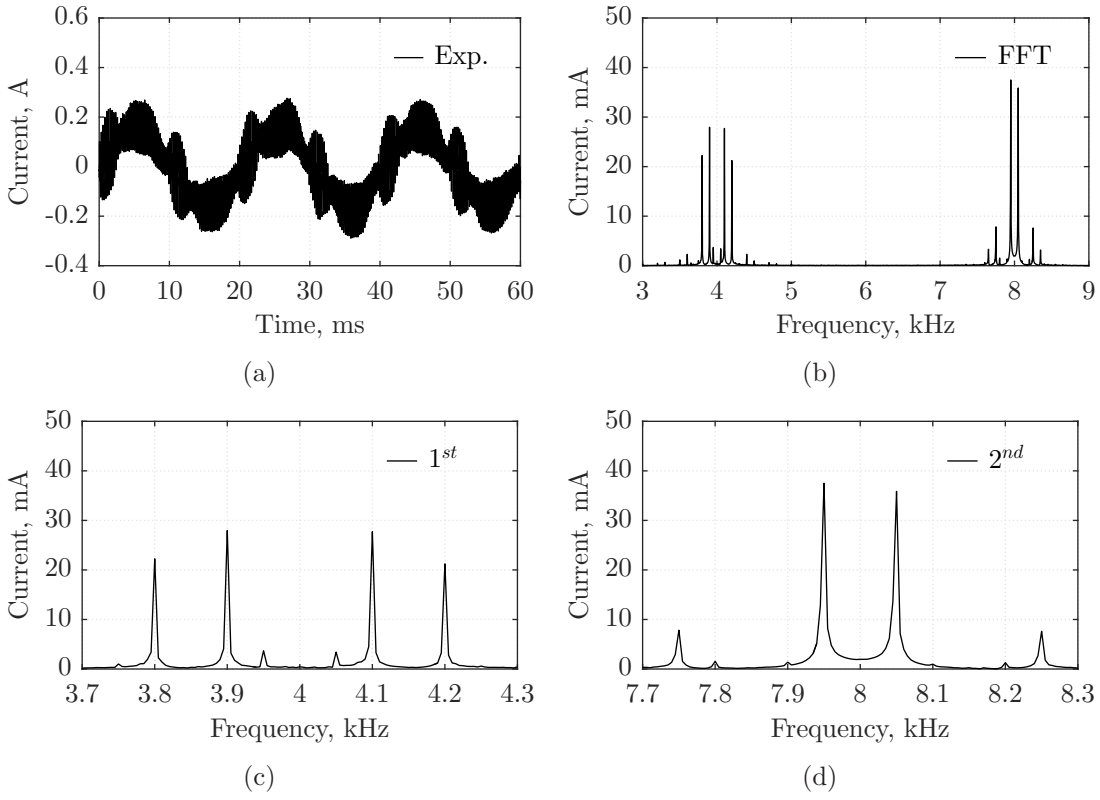

Figure 6.11: Phase current waveform and spectra at 600rpm under no-load condition: (a) phase current waveform, (b) current harmonic spectrum, (c) first sideband harmonics, (d) second sideband harmonics.

As proposed, those harmonic components will potentially cause severe sideband ERV and undesirable high-frequency acoustic noise in the prototype drive under operational conditions. Hence, the corresponding stator radial vibration waveform is also captured during the experiment. The associated spectra are compiled and illustrated in Figure 6.12. The figure reveals that the most severe vibrations occur at frequencies of 3.95kHz/4.05kHz $(\omega_s \pm \omega_e)$, 3.75kHz/4.25kHz $(\omega_s \pm 5\omega_e)$ and 7.9kHz/8.1kHz $(2\omega_s \pm 2\omega_e)$, which are introduced by $(Z - 2p)^{th}$, $2p^{th}$ and $(p - t_0)^{th}$ spatial sideband ERFD components in first and second carrier frequency domains. It can be further inspected from the figure that the vibrations at frequencies of $(\omega_s \pm 3\omega_e)$ (3.85kHz/4.15kHz), which can be contributed by 0^{th}, $(p + t_0)^{th}$ and Z^{th} spatial order sideband ERFD components, are quite trivial due to their large eigenvalues. Noticeable but small vibration with frequency of $(2\omega_s)$ can also be identified in the second switching frequency domain, which is mainly induced by the $(p + t_0)^{th}$ spatial order ERFD components. Moreover, evident vibrations are also detected at frequencies of 7.8kHz/8.2kHz $(2\omega_s \pm 4\omega_e)$ in the second carrier frequency domain.

These components originate from the sideband current components with frequencies of $(2\omega_s \pm 5\omega_e)$ in Figure 6.11. The $(2\omega_s \pm \omega_e)$ sideband current harmonic components will decrease considerably but the $(2\omega_s \pm 5\omega_e)$ components will increase substantially as the modulation index reaches nearly its maximum value. Such components can be even more significant and become the major harmonics in second carrier frequency domain. Nevertheless, they are still much smaller than the maximum vibrations of $(2\omega_s \pm 2\omega_e)$-order components and can be neglected for the prototype FSCW PMSM. In conclusion, all the vibration components predicted by the proposed model have been qualitatively validated by the experimental result.

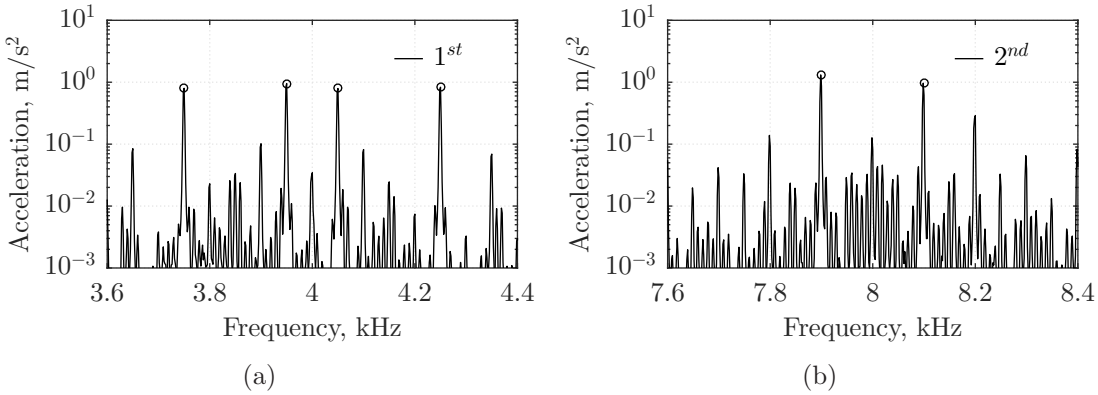

Figure 6.12: Machine vibration spectra at rotational speed of 600rpm: (a) first sideband components, (b) second sideband components.

6.3.3 Armature Reaction on Sideband Vibration

The armature reaction will complicate the sideband ERFD model, mainly from the interharmonic components. Based on the magnetic field model proposed in Section 4.4, significant interharmonic magnetic field components can be introduced by large demagnetizing current in FSCW PMSMs. Consequently, the flux weakening control is developed in the prototype drive to further examine the influence of armature reaction on sideband ERV instead. As a result, the load connection can be omitted to avoid the test error introduced by the load and mechanical connection. For the sake of fair comparison, the modulation index maintains maximum value of 1.12 during this experiment. The vibration under the maximum speed condition without demagnetizing current is captured and presented as well. The large speed difference between the operating points with no-load and flux weakening conditions will induce significant deviations from the frequency of same spatial ERFD components. This will result in very different vibration characteristics from the same spatial ERFD component with similar amplitude. A DC link voltage of 21V instead is employed in order to minimize such difference. Therefore the prototype drive under no-load condition can reach a maximum speed of 445rpm and extended speed of 1150rpm with flux weakening technique implemented. The frequency deviations on the $(\omega_s \pm \omega_e)$- and $(\omega_s \pm 5\omega_e)$-order components are 58Hz and 290Hz, respectively. As those differences are much smaller than the corresponding carrier frequency and eigenvalues,

they will not produce a significant difference on the stator mechanical behavior for sideband components.

The experimental tests on the prototype with rotational speeds of 445rpm and 1150rpm are carried out to reveal the influence of the armature reaction on sideband ERV characteristics. The corresponding current waveforms and first sideband spectra are obtained and compared in Figure 6.13. The associated current amplitude under flux weakening operation is about 8.0A, which can produce similar interharmonic components to the same active current from normal MTPA operation. In fact, it produces even larger interharmonic components as the magnetic saturation in the prototype gets ameliorated under flux weakening operation. Although modulation index maintains the same for the two cases, there is still tiny variation on the amplitudes of first sideband current harmonic components observed from Figure 6.13(c) and 6.13(d) due to the torque angle difference.

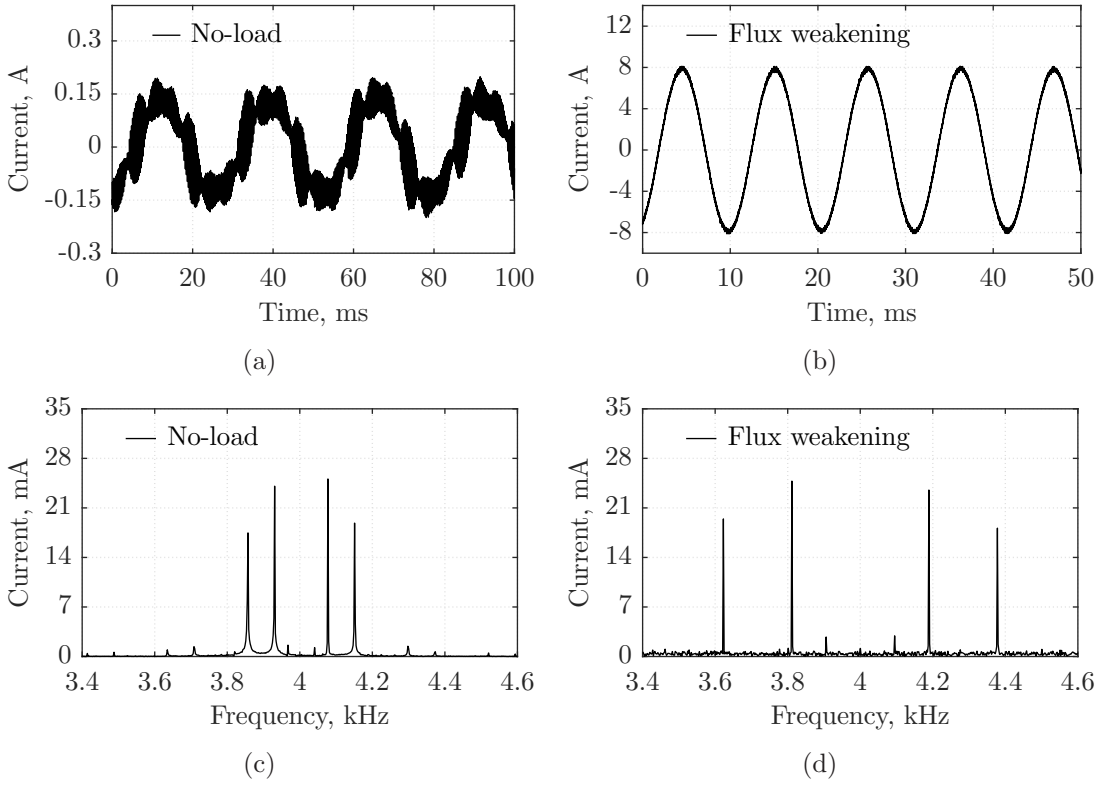

Figure 6.13: Current characteristics under maximum operational speed with and without flux weakening: (a) current waveform without flux weakening, (b) current waveform with flux weakening, (c) first sideband current spectrum without flux weakening, (d) first sideband current spectrum with flux weakening.

Moreover, the stator ERV of the prototype is also captured for such two cases and corresponding spectra in the first carrier frequency domain are compiled and compared in Figure 6.14. It can be observed that the main first sideband vibration components with the frequencies of 3.963kHz/4.037kHz ($\omega_s \pm \omega_e$), 3.815kHz/4.185kHz ($\omega_s \pm 5\omega_e$) without flux weakening condition, and frequencies of 3.905kHz/4.095kHz

($\omega_s \pm \omega_e$), 3.525kHz/4.475kHz ($\omega_s \pm 5\omega_e$) with flux weakening condition, have very similar amplitudes. Hence, it is experimentally validated that the sideband ERFD components associated with low-frequency armature reaction magnetic field components can be practically neglected in most cases. On the other hand, the large modulation index in these two cases makes the ($2\omega_s \pm 2\omega_e$)-order ERFDs in the second carrier frequency domain quite trivial and hence not discussed. However, similar results are also expected for those components. Consequently, the proposed analytical model of ERFD in the FSCW machine can be significantly simplified by omitting all B_a associated components in Table 6.3-6.12 for most cases.

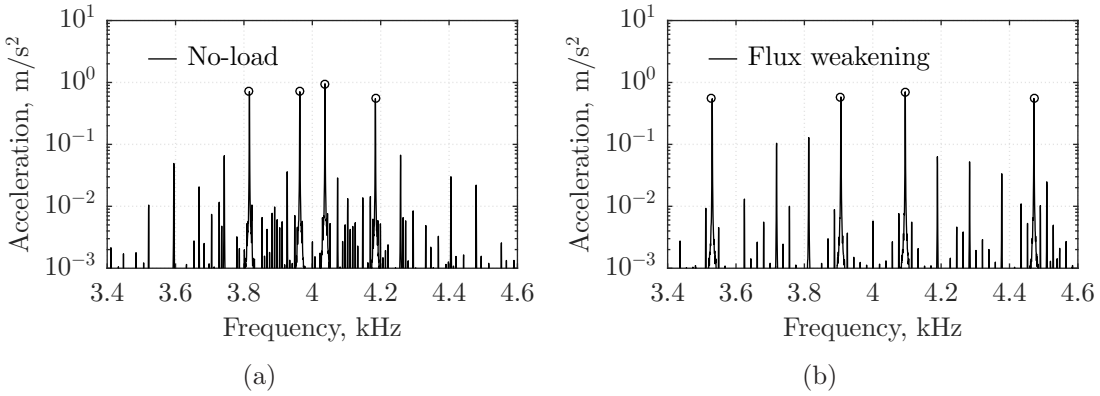

Figure 6.14: Influence of armature reaction on vibration: (a) first sideband ERVs without flux weakening, (b) first sideband ERVs with flux weakening.

6.3.4 Quantitative Validations of Sideband Vibration

As aforementioned, the armature reaction on sideband vibration can be neglected in most cases. Hence, for the sake of simplicity, comprehensive experimental tests on the prototype FSCW PMSM drive with no-load condition at different speeds are carried out to validate the analytical models. As discussed, $(Z-2p)^{th}$, $(p-t_0)^{th}$ and $2p^{th}$ spatial order components are the main contributors to the overall sideband ERV and will be verified quantitatively. Whilst, the $(p+t_0)^{th}$ spatial order ERFDs will be investigated separately. Without loss of generality, the investigations and validations for the machine under load conditions can be easily carried out by following exactly the same procedure and approach.

Under no-load conditions, correlation between the rotational speed and modulation index of SVPWM for the prototype FSCW PMSM is identified. The $(p-t_0)^{th}$ spatial ERFD components can be directly obtained from the analytical model in Table 6.9. Together with associated tooth effect coefficient, the amplitudes of the corresponding sideband ERFD components are demonstrated in Figure 6.15(b). Meanwhile, the $2p^{th}$ spatial ERFD can introduce $(Z-2p)^{th}$ components due to tooth effect so that the vector synthesis is required for the overall $(Z-2p)^{th}$ components. As a result, the resultant amplitudes of the $(Z-2p)^{th}$ spatial sideband ERFD components are evaluated and depicted in Figure 6.15(a). The characteristics of those sideband

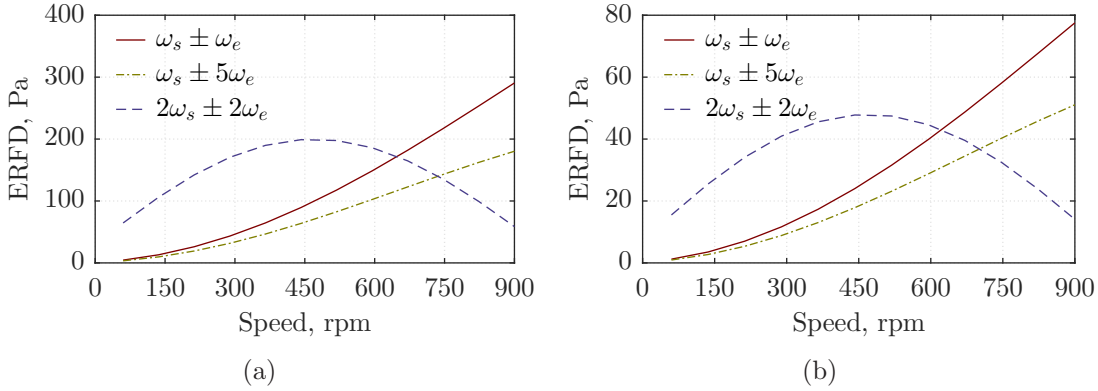

Figure 6.15: The ERFD components at different speeds: (a) $(Z-2p)^{th}$ spatial order, (b) $(p-t_0)^{th}$ spatial order.

ERFD components generally comport well with the features of the corresponding current components. It can be observed from the figure that the $(Z-2p)^{th}$ and $(p-t_0)^{th}$ spatial orders with the same frequency share the same profile. The amplitudes of all the components from first carrier frequency domain will gradually increase as the rotational speed (modulation index) rises, while the components from second carrier frequency domain will first increase and reach their peaks, and then start to decrease. Moreover, the $(\omega_s \pm \omega_e)$-order ERFDs are generally more significant than the corresponding $(\omega_s \pm 5\omega_e)$-order components over the whole rotational speed range, while the $(2\omega_s \pm 2\omega_e)$-order ERFDs are the largest as the rotational speed is below about 620rpm and turn into the smallest as the rotational speed exceeds around 700rpm. Meanwhile, the amplitudes of the $(Z-2p)^{th}$ spatial orders are nearly four times the $(p-t_0)^{th}$ counterparts. Consequently, it can be expected that electromagnetic vibration with frequencies of $(\omega_s \pm \omega_e)$ and $(\omega_s \pm 5\omega_e)$ would be primarily contributed by $(Z-2p)^{th}$ spatial ERFD components. However, $(2\omega_s \pm 2\omega_e)$ are quite close to the eigenvalue of $(p-t_0)^{th}$ spatial stator mode, and the electromagnetic vibration and acoustic noise with frequencies of $(2\omega_s \pm 2\omega_e)$ induced by the $(p-t_0)^{th}$ spatial orders can no longer be ignored.

Furthermore, the amplitudes of the key ERV components with frequencies of $(\omega_s \pm \omega_e)$, $(\omega_s \pm 5\omega_e)$ and $(2\omega_s \pm 2\omega_e)$, are analytically evaluated based on the sideband ERFD results given in Figure 6.15 for $(Z-2p)^{th}$ and $(p-t_0)^{th}$ spatial orders. Meanwhile, experimental tests are performed to capture the stator vibrations of the prototype FSCW PMSM with no-load condition at the speed ranged from 50 to 900rpm. The corresponding amplitudes of the main vibration components in first and second carrier frequency domains are derived by taking the mean of the results from five experimental samples in order to minimize the test error. The amplitudes of the components with frequencies of $(\omega_s \pm \omega_e)$ and $(\omega_s \pm 5\omega_e)$ are compiled and compared with the respective analytical counterparts in Figure 6.16(a), while the results with frequencies of $(2\omega_s \pm 2\omega_e)$ are obtained and compared in Figure 6.16(b). Figure 6.16(b) firmly confirms that the $(p-t_0)^{th}$ spatial order ERFDs, together with $(Z-2p)^{th}$ components, are the major causes of the second sideband electromagnetic vibration. However, the $(Z-2p)^{th}$ spatial components are the

predominant contributor of the first sideband electromagnetic vibration, while the $(p - t_0)^{th}$ components are negligible and hence not shown in the figure. Moreover, the analytical and experimental results demonstrate exactly the same tendency of the sideband ERV versus rotational speed.

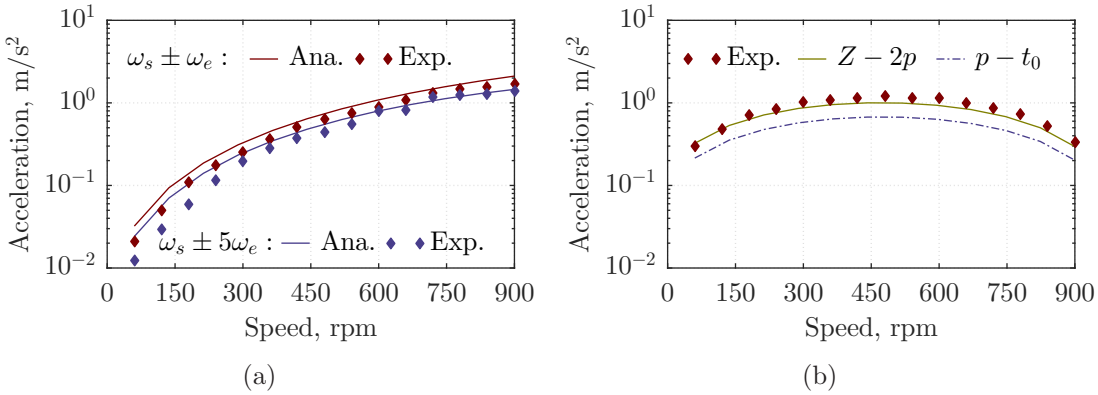

Figure 6.16: Experimental validations of the ERVs with different speeds: (a) $(\omega_s \pm \omega_e)$- and $(\omega_s \pm 5\omega_e)$-order components, (b) $(2\omega_s \pm 2\omega_e)$-order components.

However, the experimental results slightly deviate from the analytical predictions of the dominant components in Figure 6.16, which reveals that the analytical models generally overestimate the vibrations with frequencies of $(\omega_s \pm \omega_e)$ and $(\omega_s \pm 5\omega_e)$ but underestimate the components with frequencies of $(2\omega_s \pm 2\omega_e)$. The impacts of rotor position on inductance and ending leakage are normally neglected during inductance prediction from analytical and 2-D FEA models, and the prediction errors of the inductances partially contribute to such deviations. Meanwhile, some errors will be also introduced in the predictions of sideband magnetic field through the proposed interharmonic analytical model, which assumes ideal magnetic circuit and ignores the harmonic permeance. Moreover, the tooth effect models developed cannot fully depict the actual effect of the teeth on the sideband ERFD components. Besides, only the sideband ERFD components produced by $-t_0^{th}$, p^{th} and $(p - Z)^{th}$ spatial order magnetic field components are considered. Furthermore, the analytical vibration equation employed to evaluate the corresponding vibration amplitude, cannot take the full mechanical behavior of the rather complex stator into consideration. On the other hand, there are always some inevitable instrumental errors during the experimental tests. By considering all those factors, it is fair to conclude that the analytical and experimental results are in good agreements. Consequently, the validity of the proposed universal analytical methodology on sideband ERV has been experimentally verified.

6.3.5 Synthesis of Opposite Rotational Components

Although the frequency of $2\omega_s$ (8kHz) from $(p + t_0)^{th}$ spatial order sideband ERFD component is in the close vicinity of the corresponding natural frequency (9.85kHz)

from Figure 6.10(b), its resultant sideband ERV in the prototype at 600rpm with no-load condition is comparatively small as shown in Figure 6.12(b). However, notable vibration still can be expected in specific position as a result of vibration synthesis.

Under no-load condition, the third item of Table 6.10 is the absolute dominant $(p+t_0)^{th}$ spatial sideband ERFD components in the second carrier frequency domain. It can be inspected that such components share the same amplitude and frequency but have opposite rotational directions. As a result, the corresponding synthesis of such sideband ERFD components can be presented as

$$P_{(p+t_0)\_(2\omega_s)} = \frac{K_{-t_0} K'_{21} B_0 B_{\mu 2}}{\mu_0} \sin((p+t_0)\theta_m - (\delta - \varphi_{a\_21})) \sin(2\omega_s t) \tag{6.11}$$

It can be inspected from Equation (6.11) that the amplitude of the $(p+t_0)^{th}$ spatial vibration from second sideband ERFD components varies with circumferential position in the form of sinusoidal waveform with $(p+t_0) = 6$ cycles in total along the circumference. It implies that the resultant second sideband $(2\omega_s)$-order ERFD component and its induced vibration will be neutralized in some positions while doubled in terms of amplitude in the positions 15° away.

The experiment is carried out to validate the characteristics of $(p+t_0)^{th}$ spatial order components. Tests on two positions with 15° circumferential displacement are performed to measure the vibrations of the prototype FSCW PMSM for comparison. Since the maximum vibration of the $(2\omega_s \pm 2\omega_e)$-order components is captured around 480rpm as revealed in Figure 6.16(b), corresponding maximum vibration of $(p+t_0)^{th}$ in second carrier frequency domain can be achieved at this speed according to the proposed analytical model. Hence, the condition of 480rpm with no-load is employed for the experimental verification. The measured two positions are identified as near the minimum and maximum points for the $(p+t_0)^{th}$ spatial vibration from second sideband ERFD components.

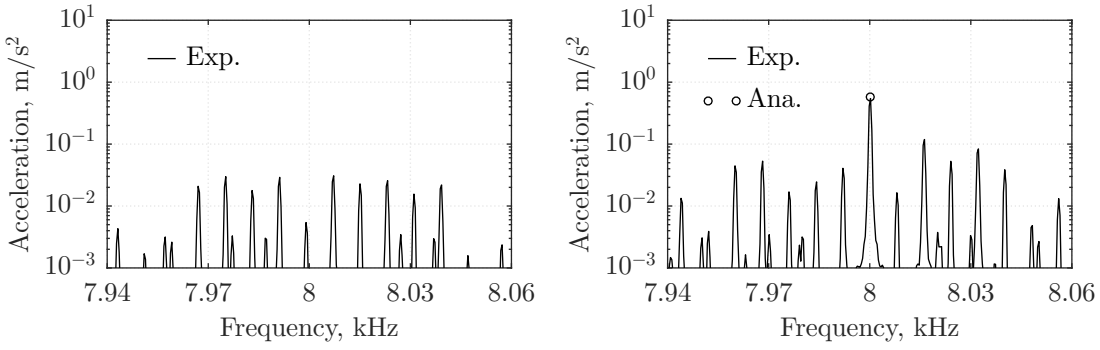

Figure 6.17: $(p+t_0)^{th}$-order vibration in different position: (a) position of 0°, (b) position of 15°.

The corresponding spectra of the vibrations measured from the two positions are compiled and demonstrated the near $2\omega_s$ range in Figure 6.17, which comport well

with Equation (6.11). The nearly maximum and minimum vibration amplitudes are obtained with 15° circumferential displacement in the experiments, which adequately validates the vibration synthesis model. The corresponding maximum value is also derived by the proposed analytical model, which is in great agreement with the experimental result as shown in Figure 6.17(b). Furthermore, the measured minimum value is more than two order of magnitude smaller than the maximum vibration. It is with the same level of test noise in Figure 6.17(a) and hence can be considered as zero. On the whole, the resonant effect of the $(p + t_0)^{th}$ spatial vibration is not that significant thanks to its large damping factor. In addition, such weakening and strengthening phenomena from vibration synthesis also exist in other spatial orders which have components with opposite rotational direction, such as 0^{th} and Z^{th} spatial order ERFDs.

6.4 Discussion of different PWM Schemes

Similar to the SVPWM technique, the vibration of SPWM is also studied in this section based on prototype I. The sideband ERFD components can be derived exactly by the same procedure based on the corresponding analytical magnetic field model. Meanwhile, the associated sideband vibration model can also be qualitatively and quantitatively validated by the experiments carried out in no-load conditions with different speed. Furthermore, the acoustic noise from random switching PWM scheme, which is commonly employed for noise reduction, is also investigated and compared with SVPWM scheme.

Table 6.14: The main sideband ERFD components of SPWM

No.	Order	Frequency	Phase	Amplitude
1	0	$\mp(\omega_s \pm 3\omega_e)$	$\varphi_{p\_12} - \delta$	$\mp K_{12}B_0B_{\mu1}/(2\mu_0)$
2	0	$\pm 2\omega_s$	$\varphi_{p\_21} - \delta$	$\mp K_{21}B_0B_{\mu2}/(2\mu_0)$
3	$Z-2p$	$\pm(\omega_s \pm \omega_e)$	$-\varphi_{a\_12} - \delta$	$\mp K_{p-Z}K'_{12}B_0B_{\mu1}/(2\mu_0)$
4	$Z-2p$	$\mp(2\omega_s \pm 2\omega_e)$	$-\varphi_{a\_21} - \delta$	$\mp K_{p-Z}K'_{21}B_0B_{\mu2}/(2\mu_0)$
5	$p-t_0$	$\mp(\omega_s \pm \omega_e)$	$\delta + \varphi_{a\_12}$	$\mp K_{-t_0}K'_{12}B_0B_{\mu1}/(2\mu_0)$
6	$p-t_0$	$\pm(2\omega_s \pm 2\omega_e)$	$\delta + \varphi_{a\_21}$	$\mp K_{-t_0}K'_{21}B_0B_{\mu2}/(2\mu_0)$
7	$p+t_0$	$\pm(\omega_s \pm 3\omega_e)$	$\delta - \varphi_{a\_12}$	$\mp K_{-t_0}K'_{12}B_0B_{\mu1}/(2\mu_0)$
8	$p+t_0$	$\mp 2\omega_s$	$\delta - \varphi_{a\_21}$	$\mp K_{-t_0}K'_{21}B_0B_{\mu2}/(2\mu_0)$
9	$2p$	$\mp(\omega_s \pm \omega_e)$	$\varphi_{p\_12} + \delta$	$\mp K_{12}B_0B_{\mu1}/(2\mu_0)$
10	$2p$	$\pm(2\omega_s \pm 2\omega_e)$	$\varphi_{p\_21} + \delta$	$\mp K_{21}B_0B_{\mu2}/(2\mu_0)$
11	Z	$\pm(\omega_s \pm 3\omega_e)$	$-\varphi_{a\_12} + \delta$	$\mp K_{p-Z}K'_{12}B_0B_{\mu1}/(2\mu_0)$
12	Z	$\mp(2\omega_s)$	$-\varphi_{a\_21} + \delta$	$\mp K_{p-Z}K'_{21}B_0B_{\mu2}/(2\mu_0)$

6.4.1 The Sideband Vibration with SPWM Scheme

As a resemblance to SVPWM technique, there will be abundant of sideband ERFD components with different spatial orders with SPWM technique as well. As aforementioned, only considerations of the sideband ERFD components associated with B_0 suffice most cases with SVPWM technique. That will be also valid for other PWM techniques so that only 0^{th}, $2p^{th}$, $(Z-2p)^{th}$, $(p-t_0)^{th}$, $(p+t_0)^{th}$ and Z^{th} spatial order sideband ERFD components are discussed for SPWM technique. As discussed in Section 3.5, the $(\omega_s \pm 4\omega_e)$-order sideband current harmonics are much smaller than the $(\omega_s \pm 2\omega_e)$-order components for SPWM technique so that the associated $(\omega_s \pm 4\omega_e)$-order sideband magnetic field components can be disregarded. Consequently, the resultant main sideband ERFD components of SPWM technique are given in Table 6.14. The corresponding sideband magnetic field components involved are give in Section 4.5.

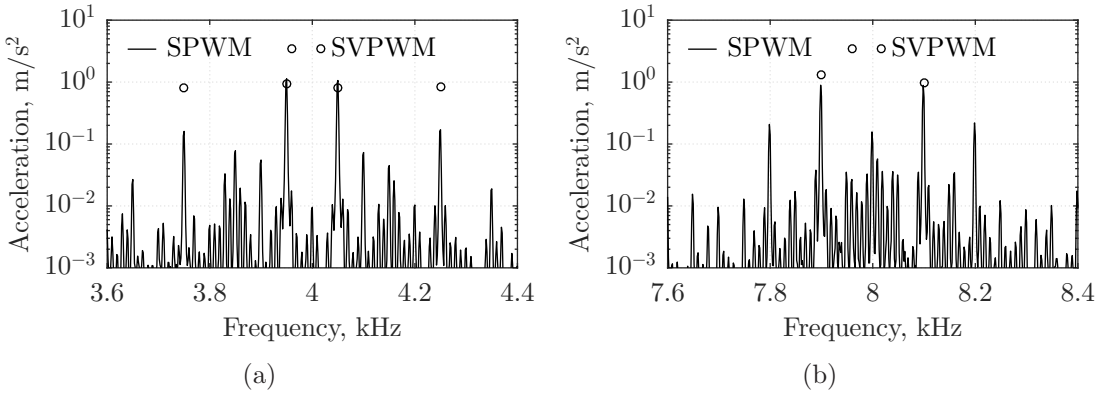

Figure 6.18: Machine vibration at 600rpm with SPWM: (a) first sideband components, (b) second sideband components.

The stator vibrations of the PMSM under 600rpm with no-load condition and SPWM technique are measured and their spectra are processed and illustrated in Figure 6.18. It can be easily observed that $(\omega_s \pm \omega_e)$- and $(2\omega_s \pm 2\omega_e)$-order components, which are 3950Hz/4050Hz, 7900Hz/8100Hz, are the main sideband ERV components of the prototype with SPWM technique in the first and second carrier frequency domains. There are also noticeable components such as $(\omega_s \pm 5\omega_e)$- and $(2\omega_s \pm 4\omega_e)$-order vibrations. They are usually associated with the $(\omega_s \pm 4\omega_e)$- and $(2\omega_s \pm 5\omega_e)$-order sideband current components in the prototype and normally negligible. Very mild $(\omega_s \pm 3\omega_e)$-order components, which are introduced by 0^{th} spatial order sideband ERFD components, can be also identified in the figure. The large eigenvalue of such stator mode makes the amplitudes of the corresponding accelerations insignificant. Moreover, the experimental results of the main sideband vibration components with SVPWM technique are also demonstrated for comparison in Figure 6.18. Compared with SVPWM, SPWM technique has slightly larger $(\omega_s \pm \omega_e)$-order vibration but mildly smaller $(2\omega_s \pm 2\omega_e)$-order component. Most importantly, the $(\omega_s \pm 5\omega_e)$-order vibrations are drastically reduced in SPWM technique. Such vibration results are in good correlation with the corresponding current

characteristics.

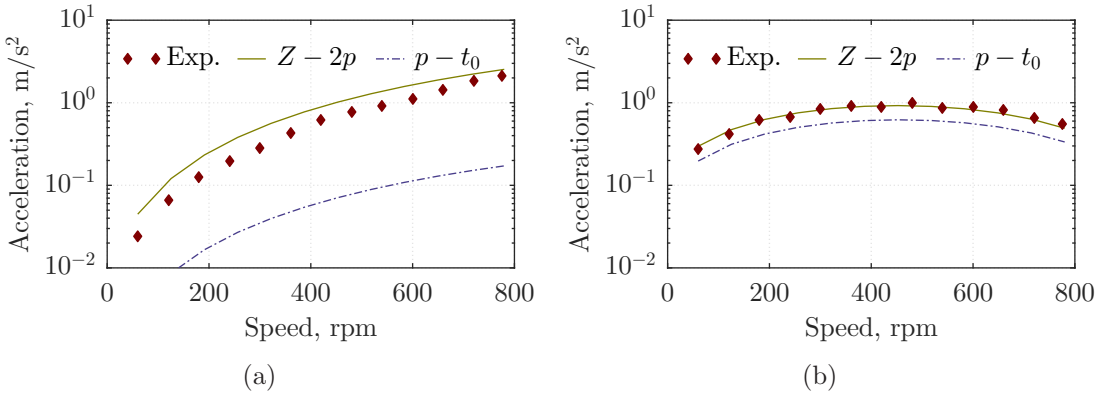

Figure 6.19: Vibrations experimental validations of SPWM at different speed: (a) frequencies of $(\omega_s \pm \omega_e)$, (b) frequencies of $(2\omega_s \pm 2\omega_e)$.

Moreover, the experiments on the prototype drive with SPWM technique with different speed are further carried out to validate analytical models. The amplitudes of the main sideband vibration frequencies of $(\omega_s \pm \omega_e)$ and $(2\omega_s \pm 2\omega_e)$ are derived from analytical models and experimental results, and compared in Figure 6.19. Without loss of generality, only the $(Z-2p)^{th}$ and $(p-t_0)^{th}$ spatial order components are included in the figure. The $(Z-2p)^{th}$ spatial orders are the predominant components in the first sideband, while $(p-t_0)^{th}$ spatial order components also become one of the major components in second sideband as associated frequencies are quite close to the eigenvalue. Rather satisfactory agreements between the analytical and experimental results for all these sideband components have been successfully demonstrated. With the consideration of numerous assumptions made for the analytical models, it is reasonable to conclude the validation of the proposed models and method.

6.4.2 The Acoustic Noise in Random PWM

In order to reduce the unpleasant acoustic noise in the drives, random PWM technique has become one of the common practices. The sideband harmonic components from random PWM technique will be continuously distributed over certain frequency range instead of being concentrated on certain discrete frequency points. In this part, the acoustic noise of the prototype I with the random switching SVPWM technique is investigated in comparison with normal SVPWM scheme. The range of the random switching frequency is set up as 3.5kHz-4.5kHz and 7.5kHz-8.5kHz respectively, for the experimental tests. For the sake of fair comparison, experimental tests with fixed frequencies of 4kHz and 8kHz are also performed. The spectra of measured current at 600rpm with no-load from random SVPWM scheme are obtained and demonstrated in Figure 6.20. The sideband harmonic components distribute randomly over the switching frequency range and multiple. As a result, the peak values of the $(\omega_s \pm 2\omega_e)$- and $(\omega_s \pm 4\omega_e)$-order components are significantly curtailed in contrast to regular-sampled SVPWM in Figure 6.11(c).

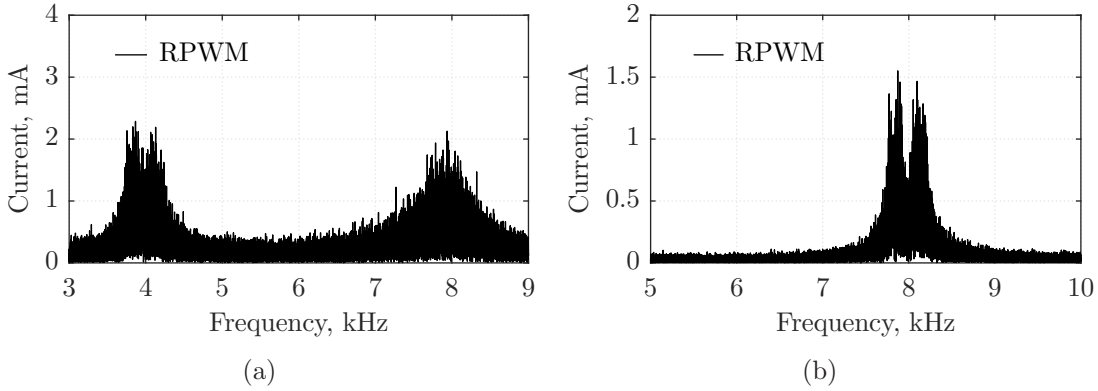

Figure 6.20: Current spectra of random SVPWM scheme: (a) switching frequency of 3.5-4.5kHz, (b) switching frequency of 7.5-8.5kHz.

Furthermore, a free-field microphone is placed one meter away from the prototype machine to measure the corresponding electromagnetic acoustic noise. The acoustic noise generated by the machine at 600rpm with no-load condition is recorded and its spectra at the first and second carrier frequency domains are compiled and shown in Figure 6.21(a) and 6.21(c), respectively, for fixed frequencies of 4kHz and 8kHz. Meanwhile, the results of random SVPWM technique with switching frequency range of 3.5kHz-4.5kHz and 7.5kHz-8.5kHz are depicted in Figure 6.21(b) and 6.21(d). It can be easily observed that evident acoustic noises are detected at exactly the same frequencies of the corresponding vibrations in normal SVPWM technique, with frequencies of $(\omega_s \pm \omega_e)$ (3.95kHz/4.05kHz or 7.95kHz/8.05kHz), $(\omega_s \pm 5\omega_e)$ (3.75kHz/4.25kHz or 7.75kHz/8.25kHz) and $(2\omega_s \pm 2\omega_e)$ (7.9kHz/8.1kHz or 15.9kHz/16.1kHz). Generally, humans are much less sensitive to the acoustic noise with frequency above 16kHz so that they are not included in Figure 6.21(c).

Like the sideband current components, the peak noise components have been successfully mitigated by the random SVPWM technique. However, the sound pressure over the frequency range actually increases due to the continuous switching distribution. As a consequent, the overall sound pressure level between 3kHz and 10kHz is 55.74dBA for regular SVPWM technique with switching frequency of 4kHz, while it is slightly larger with the value of 57.16dBA for random SVPWM technique with switching frequency range from 3.5kHz to 4.5kHz. On the other hand, carrier frequency of 8kHz delivers an overall sound pressure level between 5kHz and 10kHz of 44.88dBA for regular SVPWM technique. But the random SVPWM technique with switching frequency range from 7.5kHz to 8.5kHz produces slightly smaller sound pressure of 44.12dBA. Although the peak value of SPL can be effectively reduced by random SVPWM technique, the attenuation of the overall SPL cannot be guaranteed. Consequently, the switching frequency range should be carefully designed based on the mechanical and electromagnetic characteristics of the machine to maximize the benefits and minimize the demerits of random SVPWM technique simultaneously.

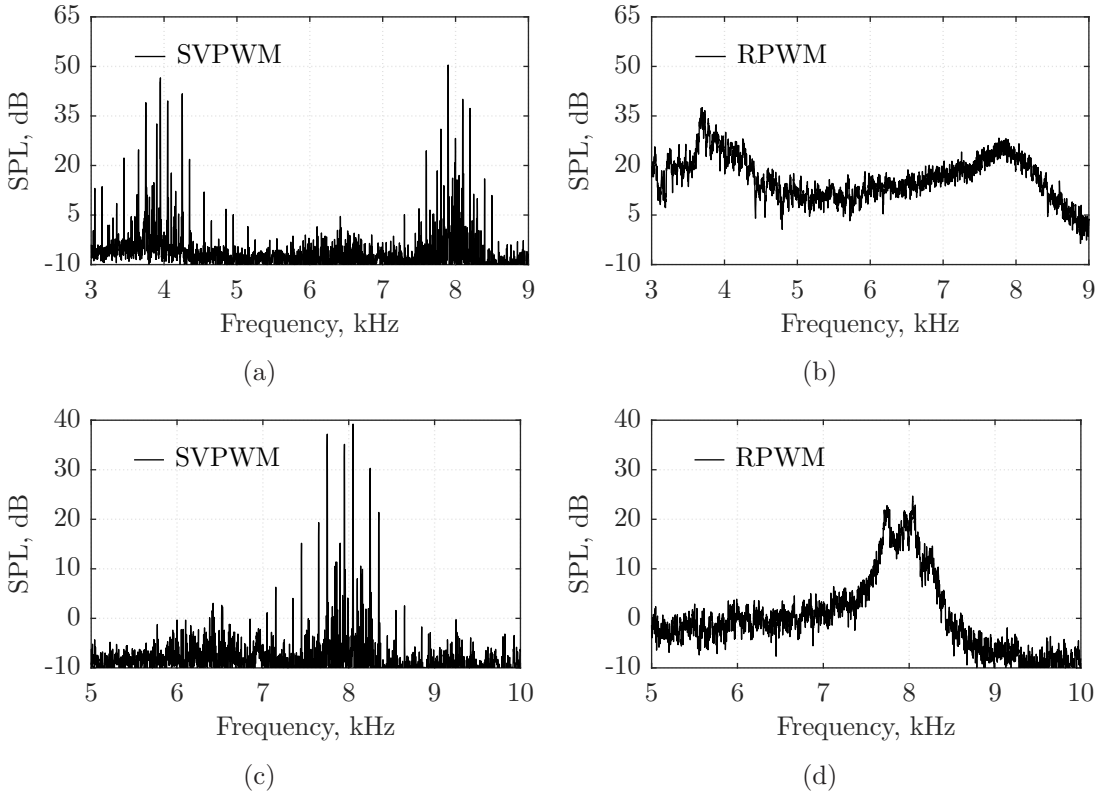

Figure 6.21: Comparison of noise spectra: (a) SVPWM with 4kHz switching frequency, (b) RPWM with 3.5-4.5kHz switching frequency, (c) SVPWM with 8kHz switching frequency, (d) RPWM with 7.5-8.5kHz switching frequency.

6.5 Summary

This chapter concentrates on the analytical investigations of main sideband ERV and corresponding experimental validations. Based on the universal sideband magnetic field component model, the analytical sideband ERFD models, with associated amplitudes, spatial orders, frequencies, initial phases and rotational directions are accordingly derived for both integral-slot and FSCW PMSMs. The influences of the rotational speed and armature reaction on sideband ERV have been comprehensively investigated. The rather rich interharmonic magnetic field components in FSCW PMSM result in much more complex sideband ERFD composition than its integral-slot counterpart. Consequently, FSCW PMSMs are generally much more susceptible to ERV including high frequency sideband vibrations and hence acoustic noise. Moreover, the mechanical damping factors, which place significant effects on the corresponding high frequency components, are also studied based on proposed sideband ERV model. Comprehensive experiments are carried out on two prototypes for the qualitative and quantitative validations of the proposed analytical models.

The experimental platform involved in this chapter include:

- The drive system based on an integral-slot PMSM (prototype IV) controlled by MTPA with SVPWM technique is developed for the corresponding sideband vibration investigation and validation;
- The SVPWM technique with variable switching frequency scheme is developed for mechanical damping and natural frequency measurement of prototype IV by proposed method based on sideband components;
- The drive system based on prototype I driven by both SVPWM and SPWM techniques is employed for the sideband vibration validation for the FSCW PMSM. Moreover, the flux weakening control is employed for the armature reaction investigation;
- The random SVPWM technique is developed for prototype I to compare the acoustic noise characteristics with regular-sampled SVPWM scheme;

The new contributions in this chapter include:

- The analytical sideband ERFD model of integral-slot PMSMs is proposed, and the characteristics of speed, load and resonance have been discussed based on the model in Section 6.2;
- A new method for mechanical damping and natural frequency measurement is proposed based on sideband vibration model in Section 6.2.5;
- The analytical sideband ERFD model in a FSCW PMSM with 10-pole 12-slot configuration is proposed and comprehensively discussed in Section 6.3;
- The characteristics of sideband acoustic noise components from SPWM and RPWM techniques are also investigated and compared with the regular-sampled SVPWM scheme in Section 6.4.

The proposed theoretical method allows prompt identification of the critical components from the abundant sideband ERFD components in PMSMs. Meanwhile, the analytical models developed can insightfully reveal the key factors of the ERFD components responsible for sideband ERV. Therefore, it offers an intuitive and effective tool of the sideband vibration assessment and optimization for PMSM drive system design and analysis. Moreover, the procedure involved in this chapter can be further employed for the sideband acoustic noise prediction in other drives controlled by PWM techniques.

Chapter 7

Conclusions and Future Work

The electromagnetic radial force and associated vibration of both low frequency and high frequency components in PMSM drives are investigated in this study. The survey is based on the investigation of the fundamental current, phase belt harmonics and sideband harmonics, followed by the investigation of corresponding air-gap magnetic field components. The low frequency vibration modeling scheme is developed with a new tooth effect model. Moreover, the sideband electromagnetic radial force densities are accordingly derived based on the magnetic field models. Comprehensive experiments, magnetic and structural FEM simulation results are employed for relevant current, electromagnetic field and vibration model validation. Further discussions on each part is carried out based on the proposed model, together with both simulation and experimental results.

7.1 Conclusions

Based on the conducted investigations, the following conclusions can be drawn in this study:

- The coupled circuit-field modeling scheme for machine steady-state and dynamic behavior prediction
  - The control strategies have been incorporated in the introduced steady-state performance assessment for PMSM drives. In addition, the saturation and cross coupling factors are also considered by the circuit-field coupling scheme. This method can offer a reliable performance prediction for PMSM drives.
  - The trigger time step method involved in the strong co-simulation can effectively reduce the computational load for VSI driven PMSMs to a reasonable level, and therefore the overall simulation time. It can also be employed for the machine performance assessment during the design

stage based on the integrated general control algorithm, as well as the current harmonics introduced by the drive.

  - The multi-loop based co-simulation scheme is developed by combining a circuit simulator with an FEA tool. The omitting of the controller source, either voltage or current, improves the convergence of numerical computation. As a result, multiple FEA machine models can be incorporated in the same schematic simulation model simultaneously. This method can be applied for modeling of versatile control algorithm.
  - The multi-loop based nonlinear harmonic modeling scheme offers another choice for more efficient calculation of the model. The parameters involved in the machine model are derived from a lookup table, which is extracted by FEA parametric sweeping. The significantly improved calculation efficiency and reasonable prediction accuracy makes it more suitable for the drive analysis and control investigation.

- The analytical sideband current model in SPWM and SVPWM

  - The proposed linear sideband current model can be employed to predict the main switching harmonic components in SVPWM. The relationship between the harmonics and associated parameters are insightfully revealed by the analytical model. The rotor saliency feature is incorporated by applying the Park transformation for the harmonics. Reasonable analysis accuracy can be achieved by this model.
  - The core saturation and *d*-*q* cross coupling factors are taken into account in a further improved sideband current model. The nonlinearity of the interior PMSM under heavy load would strongly influence the magnitudes of sideband current harmonics. This model can be used for the fast evaluation accounting the load affect.
  - The corresponding linear and improved nonlinear sideband current models are also proposed for SPWM technique. The comparative study with SVPWM is conducted based on the derived model. It is shown that in the first switching frequency band, the SPWM induces larger harmonic components. However in the second band, a slightly smaller amplitude would be exhibited by SPWM.

- The magnetic field analysis of open circuit and armature reaction condition

  - The analytical model of air-gap magnetic flux density in open circuit is developed for a single layer buried PM configuration. The effect of rotor flux leakage bridge is considered and the corresponding reluctance is derived. According to the harmonic model derived from flux density curve, the fundamental component is the principle component, and the harmonics can be effectively mitigated by feasible design.
  - A new permeance model is proposed for the calculation of interharmonic magnetic field components in FSCW machine. By identifying the magnetic path characteristics, the permeance of the main interharmonic MMF

orders are derived. Furthermore, the winding inductance model of FSCW PMSMs is accordingly improved.

- The presented permeance model can be employed to obtain the interharmonic magnetic field introduced by armature reaction in FSCW machine. A new flux density model is developed accordingly by involving a flux density coefficient. Additionally, the teeth flux leakage effect for low order harmonics are considered in the formulas.

- The low frequency electromagnetic radial force and tooth modulation effect on vibration

  - According to the simulation and experiments conducted based on a ferrite surface mounted machine, the effect of slot opening on the vibration is mainly exerted during the radial force transmission, rather than the process of introducing magnetic force from the slot magnetic field harmonics. Therefore, the slot opening factor can be neglected during the radial force analysis, while it is required in structural vibration analysis.
  - The analytical model of the tooth effect is proposed based on the study of tooth modulation phenomenon. Since the radial force distribution has a significant effect on the vibration, an asymmetrical tooth effect model has been developed. Not only can this model be utilized for the vibration assessment, but it can also be employed to examine the associated parameter characteristics.
  - New multi-physics vibration analysis methods are proposed by integrating the radial force tooth effect. The equivalent slot-less model can be employed for the electromagnetic radial force calculation to remove the slot opening effect. Both the analytical and the FEA method combined with tooth effect are developed to analyze the vibration. As an alternative, the ERFDs can be derived by 2-D FFT based on time-stepping method as well. The proposed methods can offer reasonable prediction for the vibration induced by the electromagnetic radial force in the machines.

- The high frequency electromagnetic radial force and associated acoustic noise

  - An analytical model of sideband radial force density in an integral slot PMSM is proposed and discussed. According to the analytical model and experimental validation, the core saturation has a small effect on the sideband vibration, while the angular speed is the principle variable. The sideband radial force can also be further developed to measure the mechanical damping ratio of the stator system.
  - The radial force component in a FSCW PMSM is further discussed. According to the developed model, there are many more radial force components than those in a integral slot machine, which makes it more complex to analyze. However, the ERFD components associated with fundamental armature reaction harmonics can be ignored in most cases, which will simplify the model. Extra attention must also be paid to the potential synthesis of opposite rotational components.

  - The similar derivation procedure can be applied for SPWM. Compared with SVPWM, there are few sideband radial force components responsible for the high frequency acoustic noise. However due to the larger magnitude in first sideband, more severe noise may be contributed in SPWM application. The random PWM is also employed to study the corresponding characteristics in which the peak components in the switching frequency domain can be effectively eliminated.

7.2 Proposed Future Work

Several suggestions on possible future work are summarized as follows:

- The co-simulation modeling scheme for machine steady-state and dynamic behavior prediction
  - Although the FEA model is employed for the parameter extraction, which is applied in the steady-state performance prediction to account for the core saturation, the torque pulsation still cannot be effectively included in this model, which will result in some prediction error in the output torque mean value. It can be addressed by employing the rotor position as another variable for the FEA model, but it would lead to tremendous burden in numerical computation. Therefore, a fast and effective prediction of average output torque and associated pulsation is still of great significance. A corresponding investigation will be conducted in the future.
  - The current ripple can be derived by the transient simulation coupled with control model. Since the phase belt component is normally induced by the back EMF harmonics, and may be affected by the control in addition to the torque pulsation. Consequently, to accurately assess the current harmonics, the co-simulation method is required for time consuming simulation. Based on the steady-state method, further investigation will be implemented to offer an more efficient and effective estimation method for current ripple.
  - The proposed multi-loop based nonlinear harmonic modeling scheme can be more efficient in system simulation compared with co-simulation method. However, as the model parameters are extracted from equivalent current vector to simulate the core saturation state in the machine, noticeable modeling error will be introduced due to the complexity of practical current distribution, especially in the dampers involved machine. Thus, the improvement of versatility of this model will be continued. Noticeably, the integration of core and magnet losses are also required for further improvement.
- The analytical sideband current model in SPWM and SVPWM

  - The analytical sideband current model in this study are carried out based on the two level inverter. The multi-level inverters are also applied in many applications. Due to the versatility of PWM scheme in multi-level inverter, the studies of sideband harmonics can be much more complex than its two level counterpart. Therefore, this will be further investigated.
  - Since the first and second sideband currents are principally responsible for the high frequency acoustic noise in most cases, only these components are discussed in the study. These models will be further extended to higher order sideband components to carry out the corresponding investigations of power losses and radio frequency interference in the system.
  - Based on the proposed sideband current model, the optimization schemes on both control and machine design will be discussed to minimize specific order or overall harmonics in the drive. The practical drive system will therefore be set up to implement corresponding experimental validation.

- The magnetic field analysis of open circuit and armature reaction condition

  - Only the average permeance model is discussed in the magnetic field study. Noticeable harmonics might exist in some order components, such as the $d-$axis component of interior PMSM. Therefore the assumption of neglect the permeance harmonics can introduce prediction error in the machine. To more accurately and comprehensively study the magnetic field characteristics, the key harmonic permeance model will be further developed.
  - The permeance model proposed is derived based on the assumption of uniform air gap, whereas, rotor shaping is a common scheme to achieve sinusoidal wave of back EMF in PMSM. The improvement of the permeance model, which is assumed to be an ideal square wave, can facilitate to analyze and optimize the magnetic field, and hence it will be further studied to obtain the non-uniform model.
  - Only the model with single PM layer is proposed for both open circuit and armature reaction magnetic field. However, the multi-layer buried structure is also widely applied for the purpose of flux focusing. Consequently, the existing model will be extended to the multi-layer occasion. The associated permeance model is also required to be improved simultaneously.

- The low frequency electromagnetic radial force and tooth modulation effect for vibration

  - According to the tooth modulation effect, the stator slot opening factor is considered during force transmission for PMSM drives. Similarly, the corresponding models for all machine types are required to be updated. In the induction machine, the slot harmonics in the rotor are still needed to be taken into account in the radial force calculation. Thus, further investigations on the induction machine would be carried out.

  - Based on the proposed tooth effect model, the corresponding improving schemes on vibration for PMSMs would be further discussed for the common configuration. Moreover, the skew technique also would be studied with a corresponding improved model.
  - The outer rotor PMSM exhibits its own characteristics in radial force. Different from the inner rotor PMSM, the PM introduced magnetic field maintains constant relative to the rotor, and the slot opening will produce slot harmonics which interacts with other harmonics to introduce radial force acting on the rotor. Consequently, the tooth effect model is required to be improved to adapt to the outer rotor machine and corresponding investigation will be implemented.
  - As discussed in the asymmetrical tooth effect model, the radial force acting on the teeth top is unequal. As a result, a torsional vibration would be introduced by the radial force on the teeth. This phenomenon has been validated by the simulation result during radial component analysis. Further investigation would be carried out to study the torsional vibration generated by the radial force.

- The high frequency electromagnetic radial force and associated acoustic
  - The following study on VSI driven induction machines will be conducted. The corresponding sideband magnetic field, radial force and vibration will be extended based on PMSM models. The acoustic noise studies of multilevel inverters also will be analytically carried out, and corresponding experimental platform will be set up to verify the associated model.
  - Corresponding acoustic noise optimization techniques will be further studied. According to the proposed radial force model, the acoustic noise can be affected by the machine design and the drive configurations. Therefore both analytical and experimental studies will be further undertaken to address the optimization schemes for sideband acoustic noise.

References

[1] H. S. Ko and K. J. Kim. Characterization of noise and vibration sources in interior permanent-magnet brushless DC motors. *IEEE Transactions on Magnetics*, 40(6):3482–3489, Nov 2004.

[2] H. J. Shin, J. Y. Choi, H. I. Park, and S. M. Jang. Vibration analysis and measurements through prediction of electromagnetic vibration sources of permanent magnet synchronous motor based on analytical magnetic field calculations. *IEEE Transactions on Magnetics*, 48(11):4216–4219, Nov 2012.

[3] T. J. E. Miller. *Brushless permanent-magnet and reluctance motor drives*. Monographs in electrical and electronic engineering. Clarendon Press, 1989.

[4] D. Polka. *Motors and Drives: A Practical Technology Guide*. ISA, 2003.

[5] A. Trzynadlowski. *Control of Induction Motors*. Academic Press series in engineering. Academic Press, 2001.

[6] J. F. Gieras and M. Wing. *Permanent Magnet Motor Technology: Design and Applications, Second Edition,*. Electrical and Computer Engineering. Taylor & Francis, 2002.

[7] P. Vas. *Sensorless Vector and Direct Torque Control*. Monographs in electrical and electronic engineering. Oxford University Press, 1998.

[8] J. R. Hendershot and T. J. E. Miller. *Design of Brushless Permanent-magnet Motors*. Magna Physics publications. Magna Pysics Pub., 1994.

[9] C. Xia. *Permanent Magnet Brushless DC Motor Drives and Controls*. Wiley, 2012.

[10] D. C. Hanselman. *Brushless Permanent-magnet Motor Design*. New Horizons in Comparative Politics. McGraw-Hill, 1994.

[11] J. F. Gieras, R. J. Wang, and M. J. Kamper. *Axial Flux Permanent Magnet Brushless Machines*. Springer Netherlands, 2008.

[12] J. F. Gieras, Z. J. Piech, and B. Tomczuk. *Linear Synchronous Motors: Transportation and Automation Systems*. Electric Power Engineering Series. CRC Press, 1999.

[13] R. Krishnan. *Permanent Magnet Synchronous and Brushless DC Motor Drives*. CRC Press, 2009.

[14] S. N. Vukosavic. *Digital Control of Electrical Drives*. Power Electronics and Power Systems. Springer US, 2007.

[15] S. E. Ryvkin and E. P. Lever. *Sliding Mode Control for Synchronous Electric Drives*. CRC Press, 2011.

[16] M. Cirstea, A. Dinu, M. McCormick, and J. G. Khor. *Neural and Fuzzy Logic Control of Drives and Power Systems*. Elsevier Science, 2002.

[17] A. Emadi. *Handbook of Automotive Power Electronics and Motor Drives*. Electrical and Computer Engineering. CRC Press, 2005.

[18] B. Wu. *High-Power Converters and AC Drives*. Wiley, 2007.

[19] A. Emadi, A. Khaligh, Z. Nie, and Y. J. Lee. *Integrated Power Electronic Converters and Digital Control*. Power Electronics and Applications Series. CRC Press, 2009.

[20] D. W. Kang and D. S. Hyun. Simple harmonic analysis method for multi-carrier PWM techniques using output phase voltage in multi-level inverter. *IEE Proceedings - Electric Power Applications*, 152(2):157–165, March 2005.

[21] B. P. McGrath, D. G. Holmes, and T. Meynard. Reduced PWM harmonic distortion for multilevel inverters operating over a wide modulation range. *IEEE Transactions on Power Electronics*, 21(4):941–949, July 2006.

[22] H. J. Ahn and D. M. Lee. A new bumpless rotor-flux position estimation scheme for vector-controlled washing machine. *IEEE Transactions on Industrial Informatics*, 12(2):466–473, April 2016.

[23] V. Utkin, J. Guldner, and J. Shi. *Sliding Mode Control in Electro-mechanical Systems*. Automation and Control Engineering. Taylor & Francis, 1999.

[24] T. M. Jahns and W. L. Soong. Pulsating torque minimization techniques for permanent magnet AC motor drives-a review. *IEEE Transactions on Industrial Electronics*, 43(2):321–330, Apr 1996.

[25] T. Li and G. Slemon. Reduction of cogging torque in permanent magnet motors. *IEEE Transactions on Magnetics*, 24(6):2901–2903, Nov 1988.

[26] Z. Q. Zhu and D. Howe. Influence of design parameters on cogging torque in permanent magnet machines. *IEEE Transactions on Energy Conversion*, 15(4):407–412, Dec 2000.

[27] L. Dosiek and P. Pillay. Cogging torque reduction in permanent magnet machines. *IEEE Transactions on Industry Applications*, 43(6):1565–1571, Nov 2007.

[28] L. Zhu, S. Z. Jiang, Z. Q. Zhu, and C. C. Chan. Analytical methods for minimizing cogging torque in permanent-magnet machines. *IEEE Transactions on Magnetics*, 45(4):2023–2031, April 2009.

[29] A. M. EL-Refaie. Fractional-slot concentrated-windings synchronous permanent magnet machines: Opportunities and challenges. *IEEE Transactions on Industrial Electronics*, 57(1):107–121, Jan 2010.

[30] P. N. Enjeti, P. D. Ziogas, and J. F. Lindsay. Programmed PWM techniques to eliminate harmonics: a critical evaluation. *IEEE Transactions on Industry Applications*, 26(2):302–316, Mar 1990.

[31] G. H. Lee, S. I. Kim, J. P. Hong, and J. H. Bahn. Torque ripple reduction of interior permanent magnet synchronous motor using harmonic injected current. *IEEE Transactions on Magnetics*, 44(6):1582–1585, June 2008.

[32] J. Holtz and L. Springob. Identification and compensation of torque ripple in high-precision permanent magnet motor drives. *IEEE Transactions on Industrial Electronics*, 43(2):309–320, Apr 1996.

[33] L. Tang, L. Zhong, M. F. Rahman, and Y. Hu. A novel direct torque controlled interior permanent magnet synchronous machine drive with low ripple in flux and torque and fixed switching frequency. *IEEE Transactions on Power Electronics*, 19(2):346–354, March 2004.

[34] Z. Q. Zhu and D. Howe. Analytical prediction of the cogging torque in radial-field permanent magnet brushless motors. *IEEE Transactions on Magnetics*, 28(2):1371–1374, Mar 1992.

[35] R. P. Deodhar, D. A. Staton, T. M. Jahns, and T. J. E. Miller. Prediction of cogging torque using the flux-MMF diagram technique. *IEEE Transactions on Industry Applications*, 32(3):569–576, May 1996.

[36] Z. Azar, Z. Q. Zhu, and G. Ombach. Influence of electric loading and magnetic saturation on cogging torque, back-EMF and torque ripple of PM machines. *IEEE Transactions on Magnetics*, 48(10):2650–2658, Oct 2012.

[37] K. Baoquan, L. Chunyan, and C. Shukang. Flux-weakening-characteristic analysis of a new permanent-magnet synchronous motor used for electric vehicles. *IEEE Transactions on Plasma Science*, 39(1):511–515, Jan 2011.

[38] X. Liu, H. Chen, J. Zhao, and A. Belahcen. Research on the performances and parameters of interior PMSM used for electric vehicles. *IEEE Transactions on Industrial Electronics*, 63(6):3533–3545, June 2016.

[39] A. Sarikhani and O. A. Mohammed. Demagnetization control for reliable flux weakening control in PM synchronous machine. *IEEE Transactions on Energy Conversion*, 27(4):1046–1055, Dec 2012.

[40] K. Atallah, D. Howe, P. H. Mellor, and D. A. Stone. Rotor loss in permanent-magnet brushless AC machines. *IEEE Transactions on Industry Applications*, 36(6):1612–1618, Nov 2000.

[41] D. Ishak, Z. Q. Zhu, and D. Howe. Eddy-current loss in the rotor magnets of permanent-magnet brushless machines having a fractional number of slots per pole. *IEEE Transactions on Magnetics*, 41(9):2462–2469, Sept 2005.

[42] A. Balamurali, C. Lai, A. Mollaeian, V. Loukanov, and N. C. Kar. Analytical investigation into magnet eddy current losses in interior permanent magnet motor using modified winding function theory accounting for pulsewidth modulation harmonics. *IEEE Transactions on Magnetics*, 52(7):1–5, July 2016.

[43] L. J. Wu, Z. Q. Zhu, D. Staton, M. Popescu, and D. Hawkins. Analytical modeling and analysis of open-circuit magnet loss in surface-mounted permanent-magnet machines. *IEEE Transactions on Magnetics*, 48(3):1234–1247, March 2012.

[44] L. J. Wu, Z. Q. Zhu, D. Staton, M. Popescu, and D. Hawkins. Analytical model for predicting magnet loss of surface-mounted permanent magnet machines accounting for slotting effect and load. *IEEE Transactions on Magnetics*, 48(1):107–117, Jan 2012.

[45] A. R. Tariq, C. E. Nino-Baron, and E. G. Strangas. Iron and magnet losses and torque calculation of interior permanent magnet synchronous machines using magnetic equivalent circuit. *IEEE Transactions on Magnetics*, 46(12):4073–4080, Dec 2010.

[46] S. S. Nair, J. Wang, L. Chen, R. Chin, I. Manolas, and D. Svechkarenko. Prediction of 3-D high-frequency eddy current loss in rotor magnets of SPM machines. *IEEE Transactions on Magnetics*, 52(9):1–10, Sept 2016.

[47] S. S. Nair, J. Wang, L. Chen, R. Chin, I. Manolas, and D. Svechkarenko. Computationally efficient 3-D eddy current loss prediction in magnets of interior permanent magnet machines. *IEEE Transactions on Magnetics*, 52(10):1–10, Oct 2016.

[48] P. Zhang, G. Y. Sizov, J. He, D. M. Ionel, and N. A. O. Demerdash. Calculation of magnet losses in concentrated-winding permanent-magnet synchronous machines using a computationally efficient finite-element method. *IEEE Transactions on Industry Applications*, 49(6):2524–2532, Nov 2013.

[49] H. A. Toliyat and G. B. Kliman. *Handbook of Electric Motors*. Taylor & Francis, 2004.

[50] Y. Lu and Y. Li. Tooth-slot cogging torque and noise analysis of permanent magnet motors. In *Electrical Machines and Systems, 2001. ICEMS 2001. Proceedings of the Fifth International Conference on*, volume 2, pages 860–862 vol.2, Aug 2001.

[51] D. Torregrossa, A. Khoobroo, and B. Fahimi. Prediction of acoustic noise and torque pulsation in PM synchronous machines with static eccentricity and partial demagnetization using field reconstruction method. *IEEE Transactions on Industrial Electronics*, 59(2):934–944, Feb 2012.

[52] J. Wang, Z. P. Xia, S. A. Long, and D. Howe. Radial force density and vibration characteristics of modular permanent magnet brushless AC machine. *IEE Proceedings - Electric Power Applications*, 153(6):793–801, November 2006.

[53] C. Ma and S. Zuo. Black-box method of identification and diagnosis of abnormal noise sources of permanent magnet synchronous machines for electric vehicles. *IEEE Transactions on Industrial Electronics*, 61(10):5538–5549, Oct 2014.

[54] C. Ma, Q. Liu, D. Wang, Q. Li, and L. Wang. A novel black and white box method for diagnosis and reduction of abnormal noise of hub permanent-magnet synchronous motors for electric vehicles. *IEEE Transactions on Industrial Electronics*, 63(2):1153–1167, Feb 2016.

[55] M. Baranski and T. Jarek. Analysis of PMSM vibrations based on back-EMF measurements. In *2014 International Conference on Electrical Machines (ICEM)*, pages 1492–1495, Sept 2014.

[56] J. F. Gieras, C. Wang, and J. C. Lai. *Noise of Polyphase Electric Motors*. Electrical and Computer Engineering. CRC Press, 2005.

[57] S. B. Chaudhury and S. Gupta. Online identification of AC motor misalignment using current signature analysis and modified K-mean clustering technique. In *2006 IEEE International Conference on Industrial Technology*, pages 2331–2336, Dec 2006.

[58] J. A. Rosero, J. Cusido, A. Garcia, J. A. Ortega, and L. Romeral. Broken bearings and eccentricity fault detection for a permanent magnet synchronous motor. In *IECON 2006 - 32nd Annual Conference on IEEE Industrial Electronics*, pages 964–969, Nov 2006.

[59] J. Rosero, J. Cusido, A. G. Espinosa, J. A. Ortega, and L. Romeral. Broken bearings fault detection for a permanent magnet synchronous motor under non-constant working conditions by means of a joint time frequency analysis. In *2007 IEEE International Symposium on Industrial Electronics*, pages 3415–3419, June 2007.

[60] H. Kim. On-line mechanical unbalance estimation for permanent magnet synchronous machine drives. *IET Electric Power Applications*, 3(3):178–186, May 2009.

[61] B. M. Ebrahimi and J. Faiz. Magnetic field and vibration monitoring in permanent magnet synchronous motors under eccentricity fault. *IET Electric Power Applications*, 6(1):35–45, January 2012.

[62] A. Takushima, Y. Shinobu, S. Tanaka, M. Eguchi, and K. Matsuki. Fan noise reduction of household refrigerator. *IEEE Transactions on Industry Applications*, 28(2):287–292, Mar 1992.

[63] J. Sopanen, V. Ruuskanen, J. Nerg, and J. Pyrhonen. Dynamic torque analysis of a wind turbine drive train including a direct-driven permanent-magnet generator. *IEEE Transactions on Industrial Electronics*, 58(9):3859–3867, Sept 2011.

[64] P. Beccue, J. Neely, S. Pekarek, and D. Stutts. Measurement and control of torque ripple-induced frame torsional vibration in a surface mount permanent magnet machine. *IEEE Transactions on Power Electronics*, 20(1):182–191, Jan 2005.

[65] Z. Q. Zhu, Y. Liu, and D. Howe. Minimizing the influence of cogging torque on vibration of PM brushless machines by direct torque control. *IEEE Transactions on Magnetics*, 42(10):3512–3514, Oct 2006.

[66] Z. Q. Zhu and J. H. Leong. Analysis and mitigation of torsional vibration of PM brushless AC/DC drives with direct torque controller. *IEEE Transactions on Industry Applications*, 48(4):1296–1306, July 2012.

[67] T. Su, S. Hattori, M. Ishida, and T. Hori. Suppression control method for torque vibration of AC motor utilizing repetitive controller with fourier transform. *IEEE Transactions on Industry Applications*, 38(5):1316–1325, Sep 2002.

[68] S. M. Hwang, J. B. Eom, G. B. Hwang, W. B. Jeong, and Y. H. Jung. Cogging torque and acoustic noise reduction in permanent magnet motors by teeth pairing. *IEEE Transactions on Magnetics*, 36(5):3144–3146, Sep 2000.

[69] A. Cavagnino, S. Saied, and S. Vaschetto. Experimental identification and reduction of acoustic noise in small brushed DC motors. *IEEE Transactions on Industry Applications*, 50(1):317–326, Jan 2014.

[70] A. Saxena and B. G. Fernandes. Noise and cogging torque reduction in brushless DC ceiling fan. In *2015 18th International Conference on Electrical Machines and Systems (ICEMS)*, pages 1334–1338, Oct 2015.

[71] S. P. Verma and A. Balan. Determination of radial-forces in relation to noise and vibration problems of squirrel-cage induction motors. *IEEE Transactions on Energy Conversion*, 9(2):404–412, Jun 1994.

[72] Z. Q. Zhu, Z. P. Xia, L. J. Wu, and G. W. Jewell. Analytical modeling and finite-element computation of radial vibration force in fractional-slot permanent-magnet brushless machines. *IEEE Transactions on Industry Applications*, 46(5):1908–1918, Sept 2010.

[73] W. Zhu, S. Pekarek, B. Fahimi, and B. J. Deken. Investigation of force generation in a permanent magnet synchronous machine. *IEEE Transactions on Energy Conversion*, 22(3):557–565, Sept 2007.

[74] G. Dajaku and D. Gerling. The influence of permeance effect on the magnetic radial forces of permanent magnet synchronous machines. *IEEE Transactions on Magnetics*, 49(6):2953–2966, June 2013.

[75] J. Le Besnerais, V. Lanfranchi, M. Hecquet, P. Brochet, and G. Friedrich. Prediction of audible magnetic noise radiated by adjustable-speed drive induction machines. *IEEE Transactions on Industry Applications*, 46(4):1367–1373, July 2010.

[76] R. Islam and I. Husain. Analytical model for predicting noise and vibration in permanent-magnet synchronous motors. *IEEE Transactions on Industry Applications*, 46(6):2346–2354, Nov 2010.

[77] C. Wang, J. C. S. Lai, and D. W. J. Pulle. Prediction of acoustic noise from variable-speed induction motors: deterministic versus statistical approaches. *IEEE Transactions on Industry Applications*, 38(4):1037–1044, Jul 2002.

[78] D. Braunisch, B. Ponick, and G. Bramerdorfer. Combined analytical-numerical noise calculation of electrical machines considering nonsinusoidal mode shapes. *IEEE Transactions on Magnetics*, 49(4):1407–1415, April 2013.

[79] O. A. Mohammed, T. Calvert, and R. McConnell. Coupled magnetoelastic finite element formulation including anisotropic reluctivity tensor and magnetostriction effects for machinery applications. *IEEE Transactions on Magnetics*, 37(5):3388–3392, Sep 2001.

[80] K. H. Yim, J. W. Jang, G. H. Jang, M. G. Kim, and K. N. Kim. Forced vibration analysis of an IPM motor for electrical vehicles due to magnetic force. *IEEE Transactions on Magnetics*, 48(11):2981–2984, Nov 2012.

[81] I. S. Jang, S. H. Ham, W. H. Kim, C. S. Jin, S. Y. Cho, K. D. Lee, J. J. Lee, D. Kang, and J. Lee. Method for analyzing vibrations due to electromagnetic force in electric motors. *IEEE Transactions on Magnetics*, 50(2):297–300, Feb 2014.

[82] H. Yang and Y. Chen. Influence of radial force harmonics with low mode number on electromagnetic vibration of PMSM. *IEEE Transactions on Energy Conversion*, 29(1):38–45, March 2014.

[83] D. Torregrossa, B. Fahimi, F. Peyraut, and A. Miraoui. Fast computation of electromagnetic vibrations in electrical machines via field reconstruction method and knowledge of mechanical impulse response. *IEEE Transactions on Industrial Electronics*, 59(2):839–847, Feb 2012.

[84] A. L. Rodriguez, D. J. Gomez, I. Villar, A. Lopez de Heredia, and I. Etxeberria-Otadui. Improved analytical multiphysical modeling of a surface PMSM. In *2014 International Conference on Electrical Machines (ICEM)*, pages 1224–1230, Sept 2014.

[85] Y. S. Chen, Z. Q. Zhu, and D. Howe. Vibration of PM brushless machines having a fractional number of slots per pole. *IEEE Transactions on Magnetics*, 42(10):3395–3397, Oct 2006.

[86] M. S. Islam, R. Islam, and T. Sebastian. Noise and vibration characteristics of permanent-magnet synchronous motors using electromagnetic and structural analyses. *IEEE Transactions on Industry Applications*, 50(5):3214–3222, Sept 2014.

[87] T. Sun, J. M. Kim, G. H. Lee, J. P. Hong, and M. R. Choi. Effect of pole and slot combination on noise and vibration in permanent magnet synchronous motor. *IEEE Transactions on Magnetics*, 47(5):1038–1041, May 2011.

[88] S. K. Lee, G. H. Kang, and J. Hur. Finite element computation of magnetic vibration sources in 100 kW two fractional-slot interior permanent magnet machines for ship. *IEEE Transactions on Magnetics*, 48(2):867–870, Feb 2012.

[89] J. Krotsch and B. Piepenbreier. Radial forces in external rotor permanent magnet synchronous motors with non-overlapping windings. *IEEE Transactions on Industrial Electronics*, 59(5):2267–2276, May 2012.

[90] D. Y. Kim, J. K. Nam, and G. H. Jang. Reduction of magnetically induced vibration of a spoke-type IPM motor using magnetomechanical coupled analysis and optimization. *IEEE Transactions on Magnetics*, 49(9):5097–5105, Sept 2013.

[91] J. Shen, J. A. Taufiq, and A. D. Mansell. Analytical solution to harmonic characteristics of traction PWM converters. *IEE Proceedings - Electric Power Applications*, 144(2):158–168, Mar 1997.

[92] J. F. Moynihan, M. G. Egan, and J. M. D. Murphy. Theoretical spectra of space-vector-modulated waveforms. *IEE Proceedings - Electric Power Applications*, 145(1):17–24, Jan 1998.

[93] H. W. van der Broeck, H. C. Skudelny, and G. V. Stanke. Analysis and realization of a pulsewidth modulator based on voltage space vectors. *IEEE Transactions on Industry Applications*, 24(1):142–150, Jan 1988.

[94] T. A. Sakharuk, A. M. Stankovic, G. Tadmor, and G. Eirea. Modeling of PWM inverter-supplied AC drives at low switching frequencies. *IEEE Transactions on Circuits and Systems I: Fundamental Theory and Applications*, 49(5):621–631, May 2002.

[95] J. Mathew, K. Mathew, N. A. Azeez, P. P. Rajeevan, and K. Gopakumar. A hybrid multilevel inverter system based on dodecagonal space vectors for medium voltage IM drives. *IEEE Transactions on Power Electronics*, 28(8):3723–3732, Aug 2013.

[96] G. Narayanan, D. Zhao, H. K. Krishnamurthy, R. Ayyanar, and V. T. Ranganathan. Space vector based hybrid PWM techniques for reduced current

ripple. *IEEE Transactions on Industrial Electronics*, 55(4):1614–1627, April 2008.

[97] C. M. Liaw, Y. M. Lin, C. H. Wu, and K. I. Hwu. Analysis, design, and implementation of a random frequency PWM inverter. *IEEE Transactions on Power Electronics*, 15(5):843–854, Sep 2000.

[98] K. Kamiev, J. Montonen, M. P. Ragavendra, J. Pyrhonen, J. A. Tapia, and M. Niemela. Design principles of permanent magnet synchronous machines for parallel hybrid or traction applications. *IEEE Transactions on Industrial Electronics*, 60(11):4881–4890, Nov 2013.

[99] G. Y. Sizov, D. M. Ionel, and N. A. O. Demerdash. Modeling and parametric design of permanent-magnet AC machines using computationally efficient finite-element analysis. *IEEE Transactions on Industrial Electronics*, 59(6):2403–2413, June 2012.

[100] T. M. Jahns, G. B. Kliman, and T. W. Neumann. Interior permanent-magnet synchronous motors for adjustable-speed drives. *IEEE Transactions on Industry Applications*, IA-22(4):738–747, July 1986.

[101] S. Morimoto, M. Sanada, and Y. Takeda. Wide-speed operation of interior permanent magnet synchronous motors with high-performance current regulator. *IEEE Transactions on Industry Applications*, 30(4):920–926, Jul 1994.

[102] S. Henneberger, U. Pahner, K. Hameyer, and R. Belmans. Computation of a highly saturated permanent magnet synchronous motor for a hybrid electric vehicle. *IEEE Transactions on Magnetics*, 33(5):4086–4088, Sep 1997.

[103] S. Kuttler, K. E. K. Benkara, G. Friedrich, F. Vangraefschepe, and A. Abdelli. Analytical model taking into account the cross saturation for the optimal sizing of IPMSM. In *2012 XXth International Conference on Electrical Machines*, pages 2779–2785, Sept 2012.

[104] R. Ni, D. Xu, G. Wang, L. Ding, G. Zhang, and L. Qu. Maximum efficiency per ampere control of permanent-magnet synchronous machines. *IEEE Transactions on Industrial Electronics*, 62(4):2135–2143, April 2015.

[105] J. A. Walker, D. G. Dorrell, and C. Cossar. Flux-linkage calculation in permanent-magnet motors using the frozen permeabilities method. *IEEE Transactions on Magnetics*, 41(10):3946–3948, Oct 2005.

[106] K. Hameyer, J. Driesen, H. De Gersem, and R. Belmans. The classification of coupled field problems. *IEEE Transactions on Magnetics*, 35(3):1618–1621, May 1999.

[107] F. Piriou and A. Razek. Finite element analysis in electromagnetic systems-accounting for electric circuits. *IEEE Transactions on Magnetics*, 29(2):1669–1675, Mar 1993.

[108] N. M. Abe, J. R. Cardoso, and A. Foggia. Coupling electric circuit and 2D-FEM model with Dommel's approach for transient analysis of EM devices. *IEEE Transactions on Magnetics*, 34(5):3487–3490, Sep 1998.

[109] S. Kanerva, S. Seman, and A. Arkkio. Inductance model for coupling finite element analysis with circuit simulation. *IEEE Transactions on Magnetics*, 41(5):1620–1623, May 2005.

[110] S. Seman, J. Niiranen, S. Kanerva, A. Arkkio, and J. Saitz. Performance study of a doubly fed wind-power induction generator under network disturbances. *IEEE Transactions on Energy Conversion*, 21(4):883–890, Dec 2006.

[111] F. Piriou and A. Razek. Coupling of saturated electromagnetic systems to nonlinear power electronic devices. *IEEE Transactions on Magnetics*, 24(1):274–277, Jan 1988.

[112] F. Hecht and A. Marrocco. A finite element simulation of an alternator connected to a nonlinear external circuit. *IEEE Transactions on Magnetics*, 26(2):964–967, Mar 1990.

[113] P. Zhou, W. N. Fu, D. Lin, S. Stanton, and Z. J. Cendes. Numerical modeling of magnetic devices. *IEEE Transactions on Magnetics*, 40(4):1803–1809, July 2004.

[114] E. Melgoza, C. A. Cruz, V. Venegas, R. Escarela-Perez, and J. L. Guardado. Strong coupling of electromagnetic transients and finite element magnetic field solvers. *IEEE Transactions on Magnetics*, 47(11):4574–4581, Nov 2011.

[115] S. C. Ahn, J. H. Lee, and D. S. Hyun. Dynamic characteristic analysis of LIM using coupled FEM and control algorithm. *IEEE Transactions on Magnetics*, 36(4):1876–1880, July 2000.

[116] J. F. Bangura. Directly coupled electromagnetic field-electric circuit model for analysis of a vector-controlled wound field brushless starter generator. *IEEE Transactions on Energy Conversion*, 26(4):1033–1040, Dec 2011.

[117] N. A. Demerdash, J. F. Bangura, and A. A. Arkadan. A time-stepping coupled finite element-state space model for induction motor drives. I. model formulation and machine parameter computation. *IEEE Transactions on Energy Conversion*, 14(4):1465–1471, Dec 1999.

[118] J. F. Bangura, F. N. Isaac, N. A. Demerdash, and A. A. Arkadan. A time-stepping coupled finite element-state space model for induction motor drives. II. machine performance computation and verification. *IEEE Transactions on Energy Conversion*, 14(4):1472–1478, Dec 1999.

[119] G. Bedrosian. A new method for coupling finite element field solutions with external circuits and kinematics. *IEEE Transactions on Magnetics*, 29(2):1664–1668, Mar 1993.

[120] P. Zhou, D. Lin, W. N. Fu, B. Ionescu, and Z. J. Cendes. A general cosimulation approach for coupled field-circuit problems. *IEEE Transactions on Magnetics*, 42(4):1051–1054, April 2006.

[121] S. L. Ho, S. Niu, and W. N. Fu. An equivalent parameter extraction method of transient electric circuit and magnetic field coupled problems based on sensitivity computation of system equations. *IEEE Transactions on Magnetics*, 47(8):2068–2075, Aug 2011.

[122] E. Lange, F. Henrotte, and K. Hameyer. An efficient field-circuit coupling based on a temporary linearization of fe electrical machine models. *IEEE Transactions on Magnetics*, 45(3):1258–1261, March 2009.

[123] T. Herold, E. Lange, and K. Hameyer. System simulation of a PMSM servo drive using field-circuit coupling. *IEEE Transactions on Magnetics*, 47(5):938–941, May 2011.

[124] P. Pillay and R. Krishnan. Modeling, simulation, and analysis of permanent-magnet motor drives. I. the permanent-magnet synchronous motor drive. *IEEE Transactions on Industry Applications*, 25(2):265–273, Mar 1989.

[125] P. Pillay and R. Krishnan. Modeling of permanent magnet motor drives. *IEEE Transactions on Industrial Electronics*, 35(4):537–541, Nov 1988.

[126] A. Gebregergis, M. H. Chowdhury, M. S. Islam, and T. Sebastian. Modeling of permanent-magnet synchronous machine including torque ripple effects. *IEEE Transactions on Industry Applications*, 51(1):232–239, Jan 2015.

[127] Y. Kano, K. Watanabe, T. Kosaka, and N. Matsui. A novel approach for circuit-field-coupled time-stepping electromagnetic analysis of saturated interior PM motors. *IEEE Transactions on Industry Applications*, 45(4):1325–1333, July 2009.

[128] G. Luo, R. Zhang, Z. Chen, W. Tu, S. Zhang, and R. Kennel. A novel nonlinear modeling method for permanent-magnet synchronous motors. *IEEE Transactions on Industrial Electronics*, 63(10):6490–6498, Oct 2016.

[129] D. G. Holmes and T. A. Lipo. *Pulse Width Modulation for Power Converters: Principles and Practice*. IEEE Press Series on Power Engineering. John Wiley & Sons, 2003.

[130] W. Liang, W. Fei, and P. C. K. Luk. Sideband torque ripple in direct drive permanent magnet wind power generator system. In *2014 IEEE Energy Conversion Congress and Exposition (ECCE)*, pages 4904–4910, Sept 2014.

[131] J. Holtz and S. Stadtfeld. A predictive controller for the stator current vector of AC machines fed from a switched voltage source. In *1983 International Power Electronics Conference: IPEC Tokyo*, pages 1665–1675, Mar 1983.

[132] S. Ogasawara, H. Akagi, and A. Nabae. A novel PWM scheme of voltage source inverters based on space vector theory. *Electrical Engineering*, 74(1):33–41, Jan 1990.

[133] J. T. Boys and P. G. Handley. Harmonic analysis of space vector modulated PWM waveforms. *IEE Proceedings B - Electric Power Applications*, 137(4):197–204, July 1990.

[134] A. M. Hava, R. J. Kerkman, and T. A. Lipo. Simple analytical and graphical methods for carrier-based PWM-VSI drives. *IEEE Transactions on Power Electronics*, 14(1):49–61, Jan 1999.

[135] G. Narayanan and V. T. Ranganathan. Analytical evaluation of harmonic distortion in PWM AC drives using the notion of stator flux ripple. *IEEE Transactions on Power Electronics*, 20(2):466–474, March 2005.

[136] F. Z. Peng. A generalized multilevel inverter topology with self voltage balancing. *IEEE Transactions on Industry Applications*, 37(2):611–618, Mar 2001.

[137] M. F. Escalante, J. C. Vannier, and A. Arzande. Flying capacitor multilevel inverters and DTC motor drive applications. *IEEE Transactions on Industrial Electronics*, 49(4):809–815, Aug 2002.

[138] K. A. Corzine, S. D. Sudhoff, and C. A. Whitcomb. Performance characteristics of a cascaded two-level converter. *IEEE Transactions on Energy Conversion*, 14(3):433–439, Sep 1999.

[139] R. L. Kirlin, S. Kwok, S. Legowski, and A. M. Trzynadlowski. Power spectra of a PWM inverter with randomized pulse position. *IEEE Transactions on Power Electronics*, 9(5):463–472, Sep 1994.

[140] V. Blasko. Analysis of a hybrid PWM based on modified space-vector and triangle-comparison methods. *IEEE Transactions on Industry Applications*, 33(3):756–764, May 1997.

[141] M. A. Rahman. History of interior permanent magnet motors. *IEEE Industry Applications Magazine*, 19(1):10–15, Jan 2013.

[142] B. Stumberger, G. Stumberger, D. Dolinar, A. Hamler, and M. Trlep. Evaluation of saturation and cross-magnetization effects in interior permanent-magnet synchronous motor. *IEEE Transactions on Industry Applications*, 39(5):1264–1271, Sept 2003.

[143] P. Ponomarev, I. Petrov, and J. Pyrhonen. Influence of travelling current linkage harmonics on inductance variation, torque ripple and sensorless capability of tooth-coil permanent-magnet synchronous machines. *IEEE Transactions on Magnetics*, 50(1):1–8, Jan 2014.

[144] D. Zarko, D. Ban, and T. A. Lipo. Analytical calculation of magnetic field distribution in the slotted air gap of a surface permanent-magnet motor using complex relative air-gap permeance. *IEEE Transactions on Magnetics*, 42(7):1828–1837, July 2006.

[145] A. Rahideh and T. Korakianitis. Analytical magnetic field calculation of slotted brushless permanent-magnet machines with surface inset magnets. *IEEE Transactions on Magnetics*, 48(10):2633–2649, Oct 2012.

[146] M. Rahman, T. Little, and G. Slemon. Analytical models for interior-type permanent magnet synchronous motors. *IEEE Transactions on Magnetics*, 21(5):1741–1743, Sep 1985.

[147] X. Jannot, J. C. Vannier, J. Saint-Michel, M. Gabsi, C. Marchand, and D. Sadarnac. An analytical model for interior permanent-magnet synchronous machine with circumferential magnetization design. In *2009 8th International Symposium on Advanced Electromechanical Motion Systems Electric Drives Joint Symposium*, pages 1–6, July 2009.

[148] E. C. Lovelace, T. M. Jahns, and J. H. Lang. A saturating lumped-parameter model for an interior PM synchronous machine. *IEEE Transactions on Industry Applications*, 38(3):645–650, May 2002.

[149] L. Fang, S. O. Kwon, and J. P. Hong. Conformal transformation technique for prediction of the magnetic field distribution in an IPM motor. In *2005 International Conference on Electrical Machines and Systems*, volume 3, pages 2124–2128 Vol. 3, Sept 2005.

[150] C. Mi, M. Filippa, W. Liu, and R. Ma. Analytical method for predicting the air-gap flux of interior-type permanent-magnet machines. *IEEE Transactions on Magnetics*, 40(1):50–58, Jan 2004.

[151] L. Zhu, S. Z. Jiang, Z. Q. Zhu, and C. C. Chan. Analytical modeling of open-circuit air-gap field distributions in multisegment and multilayer interior permanent-magnet machines. *IEEE Transactions on Magnetics*, 45(8):3121–3130, Aug 2009.

[152] Y. Guo, H. Lin, P. Jin, J. Yan, J. Wang, and Z. Jia. Analytical modeling of air-gap field distributions in permanent magnet embedded salient pole wind generator. *IEEE Transactions on Magnetics*, 49(12):5756–5760, Dec 2013.

[153] D. M. Ionel and M. Popescu. Finite-element surrogate model for electric machines with revolving field - application to IPM motors. *IEEE Transactions on Industry Applications*, 46(6):2424–2433, Nov 2010.

[154] D. M. Ionel and M. Popescu. Ultrafast finite-element analysis of brushless PM machines based on space - time transformations. *IEEE Transactions on Industry Applications*, 47(2):744–753, March 2011.

[155] G. Y. Sizov, P. Zhang, D. M. Ionel, N. A. O. Demerdash, and M. Rosu. Automated multi-objective design optimization of PM AC machines using computationally efficient FEA and differential evolution. *IEEE Transactions on Industry Applications*, 49(5):2086–2096, Sept 2013.

[156] Z. Q. Zhu and D. Howe. Instantaneous magnetic field distribution in brushless permanent magnet DC motors. III. effect of stator slotting. *IEEE Transactions on Magnetics*, 29(1):143–151, Jan 1993.

[157] Z. Q. Zhu, L. J. Wu, and Z. P. Xia. An accurate subdomain model for magnetic field computation in slotted surface-mounted permanent-magnet machines. *IEEE Transactions on Magnetics*, 46(4):1100–1115, April 2010.

[158] H. Chen, D. Li, R. Qu, Z. Zhu, and J. Li. An improved analytical model for inductance calculation of interior permanent magnet machines. *IEEE Transactions on Magnetics*, 50(6):1–8, June 2014.

[159] B. Prieto, M. Martinez-Iturralde, L. Fontan, and I. Elosegui. Analytical calculation of the slot leakage inductance in fractional-slot concentrated-winding machines. *IEEE Transactions on Industrial Electronics*, 62(5):2742–2752, May 2015.

[160] B. M. Wilamowski and J. D. Irwin. *Power Electronics and Motor Drives*. CRC Press, 2016.

[161] M. S. Islam, S. Mir, T. Sebastian, and S. Underwood. Design considerations of sinusoidally excited permanent-magnet machines for low-torque-ripple applications. *IEEE Transactions on Industry Applications*, 41(4):955–962, July 2005.

[162] N. Chen, S. L. Ho, and W. N. Fu. Optimization of permanent magnet surface shapes of electric motors for minimization of cogging torque using FEM. *IEEE Transactions on Magnetics*, 46(6):2478–2481, June 2010.

[163] W. Zhao, T. A. Lipo, and B. I. Kwon. Material-efficient permanent-magnet shape for torque pulsation minimization in SPM motors for automotive applications. *IEEE Transactions on Industrial Electronics*, 61(10):5779–5787, Oct 2014.

[164] R. Lateb, N. Takorabet, and F. Meibody-Tabar. Effect of magnet segmentation on the cogging torque in surface-mounted permanent-magnet motors. *IEEE Transactions on Magnetics*, 42(3):442–445, March 2006.

[165] B. Boukais and H. Zeroug. Magnet segmentation for commutation torque ripple reduction in a brushless DC motor drive. *IEEE Transactions on Magnetics*, 46(11):3909–3919, Nov 2010.

[166] M. Ashabani and Y. A. R. I. Mohamed. Multiobjective shape optimization of segmented pole permanent-magnet synchronous machines with improved torque characteristics. *IEEE Transactions on Magnetics*, 47(4):795–804, April 2011.

[167] N. Bianchi and S. Bolognani. Design techniques for reducing the cogging torque in surface-mounted PM motors. *IEEE Transactions on Industry Applications*, 38(5):1259–1265, Sep 2002.

[168] W. Fei and P. C. K. Luk. A new technique of cogging torque suppression in direct-drive permanent-magnet brushless machines. *IEEE Transactions on Industry Applications*, 46(4):1332–1340, July 2010.

[169] W. Fei and P. C. K. Luk. Torque ripple reduction of a direct-drive permanent-magnet synchronous machine by material-efficient axial pole pairing. *IEEE Transactions on Industrial Electronics*, 59(6):2601–2611, June 2012.

[170] K. Atallah, J. Wang, and D. Howe. Torque-ripple minimization in modular permanent-magnet brushless machines. *IEEE Transactions on Industry Applications*, 39(6):1689–1695, Nov 2003.

[171] S. H. Han, T. M. Jahns, W. L. Soong, M. K. Gven, and M. S. Illindala. Torque ripple reduction in interior permanent magnet synchronous machines using stators with odd number of slots per pole pair. *IEEE Transactions on Energy Conversion*, 25(1):118–127, March 2010.

[172] L. Parsa and L. Hao. Interior permanent magnet motors with reduced torque pulsation. *IEEE Transactions on Industrial Electronics*, 55(2):602–609, Feb 2008.

[173] R. Islam, I. Husain, A. Fardoun, and K. McLaughlin. Permanent-magnet synchronous motor magnet designs with skewing for torque ripple and cogging torque reduction. *IEEE Transactions on Industry Applications*, 45(1):152–160, Jan 2009.

[174] S. Huang, M. Aydin, and T. A. Lipo. Electromagnetic vibration and noise assessment for surface mounted PM machines. In *2001 Power Engineering Society Summer Meeting. Conference Proceedings*, volume 3, pages 1417–1426, July 2001.

[175] G. Dajaku and D. Gerling. Magnetic radial force density of the PM machine with 12-teeth/10-poles winding topology. In *2009 IEEE International Electric Machines and Drives Conference*, pages 1715–1720, May 2009.

[176] M. Valavi, A. Nysveen, and R. Nilssen. Characterization of radial magnetic forces in low-speed permanent magnet wind generator with non-overlapping concentrated windings. In *2012 XXth International Conference on Electrical Machines*, pages 2943–2948, Sept 2012.

[177] M. Valavi, A. Nysveen, and R. Nilssen. Effects of loading and slot harmonic on radial magnetic forces in low-speed permanent magnet machine with concentrated windings. *IEEE Transactions on Magnetics*, 51(6):1–10, June 2015.

[178] M. Valavi, J. Le Besnerais, and A. Nysveen. An investigation of zeroth-order radial magnetic forces in low-speed surface-mounted permanent magnet machines. *IEEE Transactions on Magnetics*, 52(8):1–6, Aug 2016.

[179] T. Ishikawa, H. Inaba, and M. Matsunami. Comparison of vibration characteristics of several interior permanent magnet synchronous motors. In *2008 International Conference on Electrical Machines and Systems*, pages 314–319, Oct 2008.

[180] H. Yang, Z. Han, and Y. Chen. Electromagnetic vibration of interior permanent magnet brushless motors under brushless DC and AC operation. In *2009 International Conference on Electrical Machines and Systems*, pages 1–6, Nov 2009.

[181] W. Fei and P. C. K. Luk. Investigation of radial electromagnetic force density and vibration in a fractional-slot interior permanent magnet synchronous machine. In *2013 IEEE Energy Conversion Congress and Exposition*, pages 4998–5005, Sept 2013.

[182] S. O. Kwon, J. J. Lee, T. Sun, and J. P. Hong. Characteristics and radial magnetic force of interior permanent magnet synchronous motor according to pole/slot combinations. In *2009 IEEE Vehicle Power and Propulsion Conference*, pages 1491–1495, Sept 2009.

[183] Z. Q. Zhu, Z. P. Xia, L. J. Wu, and G. W. Jewell. Influence of slot and pole number combination on radial force and vibration modes in fractional slot PM brushless machines having single- and double-layer windings. In *2009 IEEE Energy Conversion Congress and Exposition*, pages 3443–3450, Sept 2009.

[184] J. Hur, Y. D. Chun, J. Lee, and D. S. Hyun. Dynamic analysis of radial force density in brushless DC motor using 3-D equivalent magnetic circuit network method. *IEEE Transactions on Magnetics*, 34(5):3142–3145, Sep 1998.

[185] H. C. M. Mai, R. Bernard, P. Bigot, F. Dubas, D. Chamagne, and C. Espanet. Consideration of radial magnetic forces in brushless DC motors. In *2010 International Conference on Electrical Machines and Systems*, pages 1–6, Oct 2010.

[186] J. F. Gieras, C. Wang, C. S. L. Joseph, and N. Ertugrul. Analytical prediction of noise of magnetic origin produced by permanent magnet brushless motors. In *2007 IEEE International Electric Machines Drives Conference*, volume 1, pages 148–152, May 2007.

[187] M. Boesing and R. W. De Doncker. Exploring a vibration synthesis process for the acoustic characterization of electric drives. *IEEE Transactions on Industry Applications*, 48(1):70–78, Jan 2012.

[188] Y. Chen, H. Yang, and Z. Han. Investigation of electromagnetic vibration of permanent magnet brushless machines. In *2008 International Conference on Electrical Machines and Systems*, pages 621–626, Oct 2008.

[189] A. Cassat, C. Espanet, R. Coleman, L. Burdet, E. Leleu, D. Torregrossa, J. M'Boua, and A. Miraoui. A practical solution to mitigate vibrations in

industrial PM motors having concentric windings. *IEEE Transactions on Industry Applications*, 48(5):1526–1538, Sept 2012.

[190] S. J. Yang. *Low-Noise Electrical Motors*. Monographs in Electrical and Electronic Engineering. Oxford University Press, 1981.

[191] B. Kaku, I. Miyashita, and S. Sone. A novel prediction method of acoustic magnetic noise based on induction motor's NHCC function. *IEEE Transactions on Industrial Electronics*, 46(2):398–406, Apr 1999.

[192] W. C. Lo, C. C. Chan, Z. Q. Zhu, L. Xu, D. Howe, and K. T. Chau. Acoustic noise radiated by PWM-controllel induction machine drives. *IEEE Transactions on Industrial Electronics*, 47(4):880–889, Aug 2000.

[193] A. C. Binojkumar, B. Saritha, and G. Narayanan. Acoustic noise characterization of space-vector modulated induction motor drives - an experimental approach. *IEEE Transactions on Industrial Electronics*, 62(6):3362–3371, June 2015.

[194] A. Ruiz-Gonzalez, M. J. Meco-Gutierrez, F. Perez-Hidalgo, F. Vargas-Merino, and J. R. Heredia-Larrubia. Reducing acoustic noise radiated by inverter-fed induction motors controlled by a new PWM strategy. *IEEE Transactions on Industrial Electronics*, 57(1):228–236, Jan 2010.

[195] A. Ruiz-Gonzalez, F. Vargas-Merino, F. Perez-Hidalgo, M. J. Meco-Gutierrez, and J. R. Heredia-Larrubia. Low switching PWM strategy to reduce acoustic noise radiated by inverter-fed induction motors. In *2010 IEEE International Symposium on Industrial Electronics*, pages 1353–1358, July 2010.

[196] A. Ruiz-Gonzalez, F. Vargas-Merino, J. R. Heredia-Larrubia, M. J. Meco-Gutierrez, and F. Perez-Hidalgo. Application of slope PWM strategies to reduce acoustic noise radiated by inverter-fed induction motors. *IEEE Transactions on Industrial Electronics*, 60(7):2555–2563, July 2013.

[197] J. W. Chen. Design and analysis of low-acoustic noise motor drivers. In *2009 IEEE International Electric Machines and Drives Conference*, pages 1188–1193, May 2009.

[198] L. Accardo, M. Fioretto, G. Giannini, and P. Marino. Techniques of PWM space vector modulation for the reduction of magnetic acoustic noise in traction motor. In *International Symposium on Power Electronics, Electrical Drives, Automation and Motion, 2006. SPEEDAM 2006.*, pages 1084–1089, May 2006.

[199] J. Le Besnerais, V. Lanfranchi, M. Hecquet, and P. Brochet. Characterization and reduction of audible magnetic noise due to PWM supply in induction machines. *IEEE Transactions on Industrial Electronics*, 57(4):1288–1295, April 2010.

[200] J. Y. Chai, Y. H. Ho, Y. C. Chang, and C. M. Liaw. On acoustic-noise-reduction control using random switching technique for switch-mode rectifiers in PMSM drive. *IEEE Transactions on Industrial Electronics*, 55(3):1295–1309, March 2008.

[201] S. Bhattacharya, D. Mascarella, G. Joos, and G. Moschopoulos. A discrete random PWM technique for acoustic noise reduction in electric traction drives. In *2015 IEEE Energy Conversion Congress and Exposition (ECCE)*, pages 6811–6817, Sept 2015.

[202] W. Liang, P. Luk, and W. Fei. Analytical investigation of sideband electromagnetic vibration in integral-slot PMSM drive with SVPWM technique. *IEEE Transactions on Power Electronics*, PP(99):1–1, 2016.

[203] T. D. Strous, H. Polinder, and J. A. Ferreira. Inductance calculations for PM machines with concentrated windings. In *2011 IEEE International Electric Machines Drives Conference (IEMDC)*, pages 447–452, May 2011.

[204] W. Liang, J. Wang, and W. Fang. Analytical modeling of sideband current harmonic components in induction machine drive with voltage source inverter by an SVM technique. *IEEE Transactions on Power Electronics*, 28(11):5372–5379, Nov 2013.

Appendix A

Prototypes for Validation

Both low and high frequency vibration and associated electromagnetic components are analytically or numerically investigated in the study. While four different prototype machines are employed for experimental validation of models involved in vibration analysis. According to the requirement of each model, comprehensive experiments are carried out based on the corresponding machine. The key parameters of all these prototypes are illustrated in this section. Fundamentally, in order to set up corresponding platforms, kinds of control algorithm such as $i_d = 0$ control, MTPA control, flux weakening control, SVPWM, SPWM, random PWM, state observer, sliding mode observer, and feed forward current control are all developed based on the involved prototypes as well.

A.1 Prototype I

A concentrated interior PMSM, defined as Prototype I, of which the key configuration parameters are given in Table A.1, is involved in the drive system. The cross section and stator structure are demonstrated in Figure A.1, while the test platform is depicted in Figure A.2.

Table A.1: Structure specifications of Prototype I

Parameter	Value	Parameter	Value
Phase number	3	Pole pairs number	5
Slot number	12	Axial active length	70mm
Stator inner diameter	41mm	Stator outer diameter	76mm
Stator yoke height	3mm	Permanent magnet height	2mm
Air-gap height	0.5mm	Permanent magnet width	10.3mm

Due to its severe saturation characteristics and interior rotor structure, this machine is employed in Chapter 2 for modeling experimental validation of both steady and

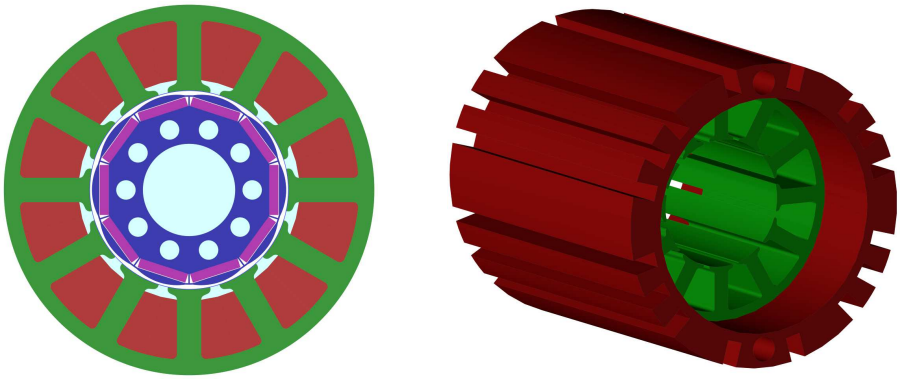

(a) (b)

Figure A.1: Prototype I: (a) cross section, (b) stator system.

dynamic performance assessment methods. The factors such as core saturation, cross coupling and control algorithm can be sufficiently demonstrated by the prototype. Experiments with $i_d = 0$ vector control, MTPA control, flux weakening control are comprehensively carried out under different load condition. Meanwhile, this machine is also involved in the improved nonlinear sideband current model verification. The nonlinear feature of sideband current induced by severe core saturation and $d - q$ coupling factor can be effectively reflected by the drive. Consequently, it makes the prototype extremely suitable for the nonlinear sideband current model validation. Corresponding measurements at different speed and output torque condition under $i_d = 0$ and MTPA control are conducted respectively with a switching frequency of 4kHz. Noticeably, the actual switching frequency of this machine is 8kHz, which is employed for the low frequency vibration experimental measurement. While in sideband investigation, in order to study the harmonic characteristics of both first and second order switching frequency domain components, the much lower 4kHz is involved for the experiments, which can makes the sideband components more significant for measurement.

(a)

Figure A.2: Experimental setup of Prototype I.

Moreover, due to its concentrated winding arrangement and significant armature reaction, this machine is also employed for the low frequency vibration investigation. The FSCW configuration would inevitably produce abundant of MMF harmonics,

while the significant armature reaction would further introduce noticeable flux density harmonics in the air gap, which would complicate the radial force model in the machine. By conducting experiment under flux weakening condition, the new proposed analysis procedure for vibration prediction based on tooth modulation effect is validated by prototype I. The advantage from flux weakening condition is that the interference from the mechanical connection at load condition can be avoided, while the spatial harmonic flux density components introduced by the interharmonic MMFs still can be effectively presented, even more significant due to the field weakening.

Table A.2: Key parameters of Prototype I

Parameter	Value	Parameter	Value
Phase resistance	0.57Ω	$d-$axis inductance	3.0mH
PM flux linkage	0.049Wb	$q-$axis inductance	4.2mH
DC link voltage	42V	Rated speed	300rpm
Rated torque	3Nm	Maximum speed	900rpm

On the other hand, this machine is also involved in the sideband vibration case study and analytical model verification for FSCW machine type. The different speed with no-load condition is employed for qualitative and quantitative investigation of high frequency vibration, while the flux weakening condition is applied for the affection analysis of winding armature reaction. Noticeably, the switching frequency of 4kHz is adopted, and hence, the characteristics of both first and second sideband vibration are investigated by the prototype. As for the third or even higher sideband components, the associated acoustic noise are normally less audible due to high switch frequency. Meanwhile, the recommended measurement range of the vibration accelerometer is from 1.5Khz to 10kHz, and noticeable test error might be introduced for higher frequency components. Consequently, the third and higher order components are all ignored during the experiments. However, similar sideband model derivation and measurements can be carried out with the same procedure of lower order components, if a smaller switching frequency is chosen and higher order sideband components are required to be considered. Additionally, this prototype is also employed to validate the SPWM associated harmonic characteristics of sideband current and vibration. And the random PWM is developed to compare the sideband acoustic noise feature with regular SVPWM technique as well.

The key electromagnetic parameters of the prototype are demonstrated in Table A.2. These parameters would be further employed for steady and transient performance prediction of the drive. Whilst, they are also involved in the sideband current and associated radial force density model. Specifically, the relevant modulation ratio and torque angle, are the major variables in sideband components. Therefore, the corresponding modulation ratio and torque angle are demonstrated in Figure A.3 for $i_d = 0$ and MTPA control respectively.

In fact, due to severe core saturation in the prototype, the PM flux linkage and

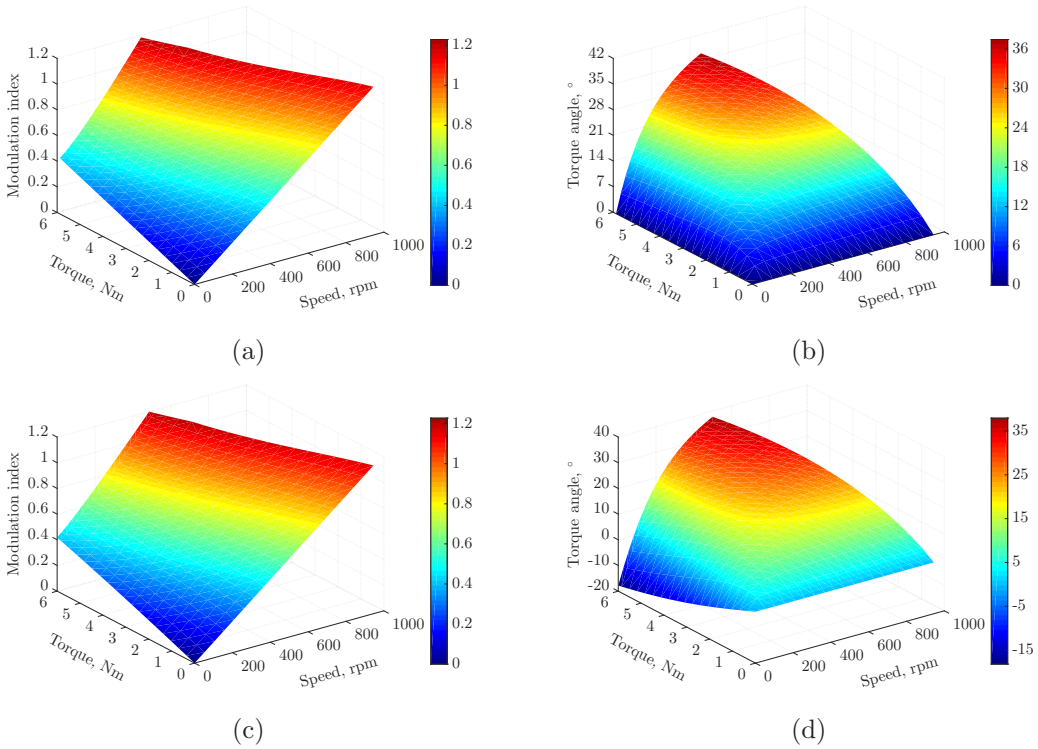

Figure A.3: Modulation and torque angle of Prototype I: (a) modulation in $i_d = 0$ control, (b) torque angle in $i_d = 0$ control, (c) modulation in MTPA control, (d) torque angle in MTPA control.

$d - q$ inductances would be significantly affected by current, which is determined by the output torque load. As a result, normally the FEA tool is necessary to be employed for accurate prediction, as discussed in Section 2.2 and 3.3. By considering the saturation and coupling effect, both electromagnetic parameters and output performance can be efficiently and precisely derived.

A.2 Prototype II

The prototype II, an 8-pole 36-slot PMSM, is employed for the linear sideband current model validation. The key configuration parameters are given in Table A.3, and the cross section, together with experimental platform are demonstrated in Figure A.4. Noticeably, the non-uniform air gap is employed to achieve sinusoidal back EMF in the winding, while the air-gap height given in the table is the minimum value and the maximum one is 2.4mm.

Although the magnet is surface mounted structure as revealed in the figure, the q-axis inductance is larger than the d-axis component due to the employed inset PM structure. The experiments, of which the output torque load from 0Nm to 10Nm, and the speed up to 1800rpm are carried out to investigate the sideband current characteristics. The PMSM is driven by a VSI with SVPWM technique and $i_d = 0$

Table A.3: Main configurations of Prototype II

Parameter	Value	Parameter	Value
Phase number	3	Pole pairs number	4
Slot number	30	Axial active length	70mm
Stator inner diameter	83mm	Stator outer diameter	133mm
Stator yoke height	8.5mm	Permanent magnet height	4.2mm
Air-gap height	1.2mm	Permanent magnet width	23mm

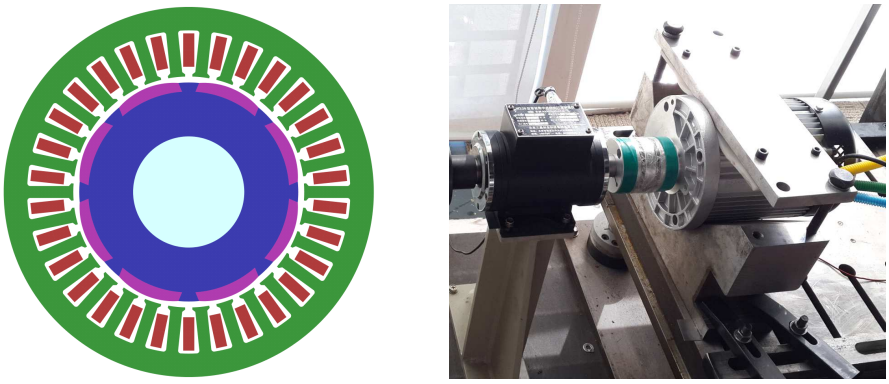

(a) (b)

Figure A.4: Prototype II: (a) cross section, (b) experimental setup of Prototype II.

vector control strategy during the experiments. Meanwhile, 3 hall sensors are involved in the controller for the machine angular speed and rotor position estimation. In order to collect the sideband components more accurately, similar to Prototype I, a low switching frequency of 4kHz is chosen for the power module instead of the actual 8kHz. Since the equivalent air-gap height in the prototype is comparatively huge, the magnetic field of armature reaction is insignificant. As a result, the affection of armature reaction on the core saturation is very trivial and negligible. Hence, it can be considered that the $d-q$ inductances and flux linkage parameters maintain constant, even in large output torque condition. Consequently, this machine can be employed for the linear analytical sideband current model validation.

The $d-q$ inductances and PM flux linkage are solved by FEM in no-load condition, and the obtained parameters are listed in Table A.4. As the air-gap height is relatively large, the winding inductance of this machine is very small, and hence induce remarkable sideband current components. Similar to Prototype I, the modulation ratio and torque angle are required for the sideband current analysis. Therefore, they are all derived based on analytical model Equation (2.10), and depicted in Figure A.5 as well. They would be further involved in the analytical sideband current harmonics prediction and model validation. It can be directly seen from the figure that the maximum torque angle is smaller than 11° due to the small armature reaction, while the whole modulation ratio range can be accomplished by the different speed from 0 to maximum value of 1800rpm.

Table A.4: Key parameters of Prototype II

Parameter	Value	Parameter	Value
Phase resistance	5.2mΩ	$d-$axis inductance	27.1μH
PM flux linkage	0.0179Wb	q-axis inductance	36.8μH
DC link voltage	24V	Rated speed	1200rpm
Rated torque	4Nm	Maximum speed	1800rpm

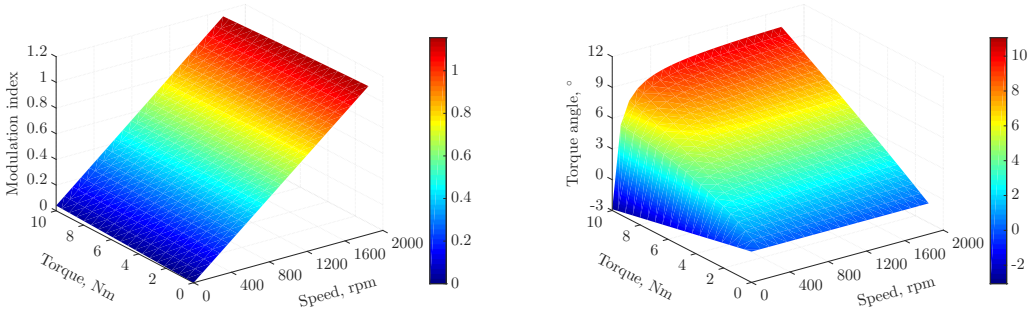

(a) (b)

Figure A.5: Modulation and torque angle of Prototype II: (a) modulation, (b) torque angle.

A.3 Prototype III

A 6-pole 9-slot surface mounted ferrite PMSM, which is defined as Prototype III, is involved for the tooth modulation effect demonstration. The main parameters of the machine, which is driven by sensor-less vector control, are given in Table A.5. While the cross section of the machine is depicted in Figure A.6(a), with stator system structure in Figure A.6(b). The platform together with vibration measurement instrument are shown in Figure A.7. As ferrite material is employed for the design, a large PM height of 9mm is required to offer the main flux density. Noticeably, this machine was originally designed as a brush-less DC motor application. In order to reduce the phase belt current component and further decrease the potential vibration components in the spectrum, the machine is driven by vector control strategy. However, noticeable harmonic current still can be introduced in the experimental result due to the flat topped back EMF.

The nearly close-slot structure makes the slot flux density harmonics very trivial in the air gap. In addition, the huge air-gap height ensures the armature reaction flux density at a very small level. Furthermore, the experiments are carried out at no-load condition, with high switching frequency of 12kHz to achieve reasonable steady performance with minimum current amplitude. As a result, only the PM introduced slot-less flux density components are necessary to be considered for low frequency radial force density items. This could facilitate to identify the modulation effect phenomenon of radial force transferring on teeth, because the spatial and temporal

order are identical for these components.

As only the low frequency vibration is investigated in the drive of Prototype III, the electromagnetic parameters are not necessary to be calculated. Instead, the FE model is involved for the flux density and associated radial force density analysis. The DC link voltage of the experimental drive is set as 160V to reach a maximum speed of 4000rpm.

Table A.5: Structure specifications of Prototype III

Parameter	Value	Parameter	Value
Phase number	3	Pole pairs number	3
Slot number	9	Axial active length	54mm
Stator inner diameter	46mm	Stator outer diameter	82mm
Stator yoke height	4.5mm	Height of permanent magnet	9mm
Air-gap height	0.75mm	Pole arc coefficient	1.0

Due to the small air-gap flux density introduced by the ferrite, the associated radial force density components are relatively small. As a result, the resultant vibration is insignificant in the experimental result. To mitigate the potential measurement interference and error, experiments at different speed of 2000rpm and 3000rpm are carried out respectively.

However, due to the small armature reaction in the machine, the corresponding magnetic field in load condition is insignificant. Consequently, this machine would not be employed for the vibration investigation of armature reaction, which is carried out based on Prototype I instead.

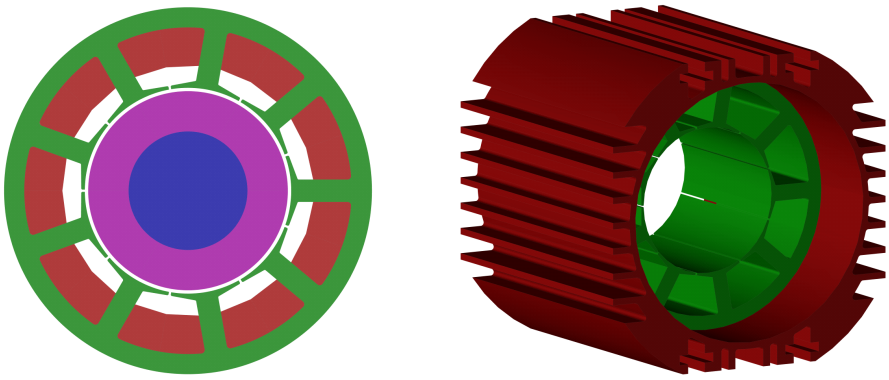

(a) (b)

Figure A.6: Prototype III: (a) cross section, (b) stator system.

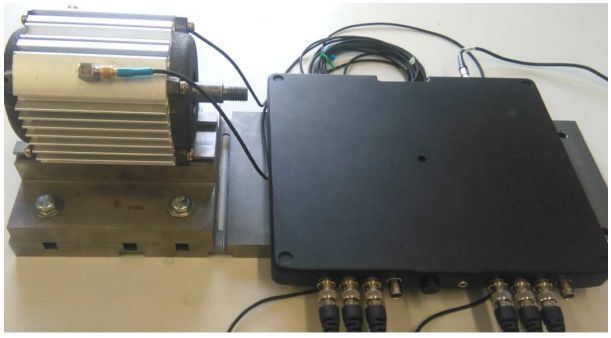

(a)

Figure A.7: Experimental setup of Prototype III.

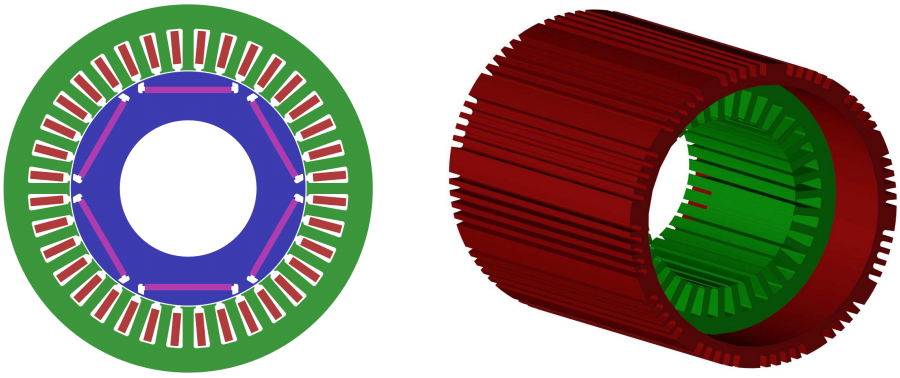

(a) (b)

Figure A.8: Prototype IV: (a) cross section, (b) stator system.

A.4 Prototype IV

According to the sideband radial force density investigation, there would be significant difference of characteristics between distributed-winding integral-slot and concentrated-winding fractional-slot machine. Consequently, an integral slot PMSM, defined as Prototype IV with 6-pole 36-slot configuration, is further employed for the sideband vibration investigation. The prototype, whose radial cross-section is depicted as Figure A.8, is driven by a conventional two-level VSI with SVPWM technique and maximum torque per ampere (MTPA) control strategy. The straight embedded PM structure can incorporate the saturation and cross coupling factors in the drive system to examine the reliability of the analytical model.

The main parameters of the drive system are given in Table A.6, and the experimental setup is shown in Figure A.9. Since the SVPWM switching frequency for the prototype drive system is 6kHz, the frequencies of the first and second sideband components will reach up to near 6kHz and 12kHz, respectively. All these components are investigated for the proposed prototype integral-slot PMSM drive system and corresponding analytical model is comprehensively validated.

The experimental measurement are implemented under different operational speed

Table A.6: Main configurations of Prototype IV

Parameter	Value	Parameter	Value
Phase number	3	Pole pairs number	3
Slot number	36	Axial active length	129mm
Stator inner diameter	104mm	Stator outer diameter	162mm
Stator yoke height	10.6mm	Permanent magnet height	2.8mm
Air-gap height	0.5mm	Permanent magnet width	38mm

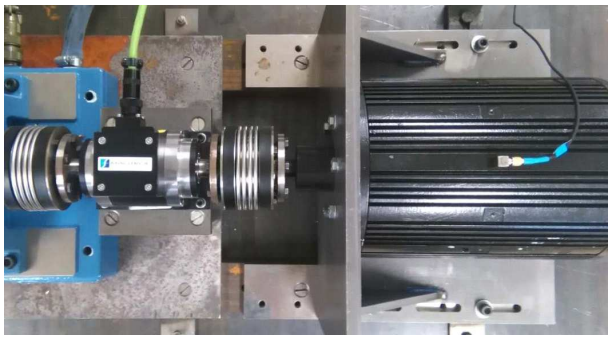

(a)

Figure A.9: Experimental setup of Prototype IV.

from to 100rpm to 1200rpm to validate the proposed analytical sideband vibration model. The electromagnetic parameters involved in the analytical model are list in Table A.7. While the sideband vibration variables, the modulation ratio and torque angle are depicted in Figure A.10. In order to study the load characteristic of sideband vibration, the experiment at 10Nm is conducted as well. Noticeably, in order to achieve similar modulation ratio of load condition with no-load one, an extra demagnetization current is injected in the winding based on MTPA control. As a result, the modulation ratio of load condition is around 0.789, which slightly increases from no-load condition of 0.769.

Moreover, the switching frequency sweeping method is also developed on Prototype IV, and corresponding vibration is measured to obtain the mechanical damping coefficient of the stator system by identifying the resonance frequency.

Table A.7: Main configurations of Prototype IV

Parameter	Value	Parameter	Value
Phase resistance	0.58Ω	$d-$axis inductance	6.26mH
PM flux linkage	0.412Wb	$q-$axis inductance	18.87mH
DC link voltage	280V	Rated speed	1000rpm
Rated torque	10Nm	Maximum speed	1200rpm

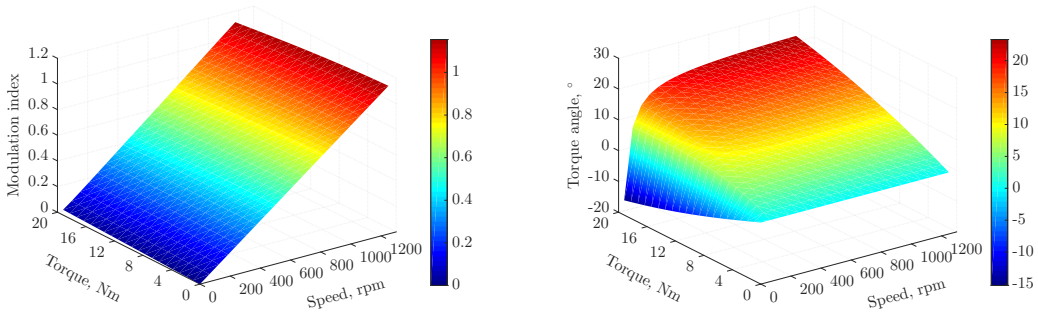

(a) (b)

Figure A.10: Modulation and torque angle of Prototype IV: (a) modulation, (b) torque angle.

Appendix B

Sideband Voltage Harmonic Components in SVPWM

B.1 Sideband Voltage Harmonic Coefficients Calculation in SVPWM

The coefficients of sideband harmonic components can be derived based on Fourier series expand by involving Bessel function. The main harmonic components are obtained and the detailed estimations are presented in this section.

B.1.1 Definition of Bessel function

The k^{th} order Bessel formula can be expressed as

$$J_k(x) = \sum_{n=0}^{\infty} \frac{(-1)^n}{n!} \frac{1}{\Gamma(k+n+1)} (\frac{x}{2})^{2n+k} \tag{B.1}$$

where

$$\Gamma(k+n+1) = (k+n)! \tag{B.2}$$

According to the characteristic of Bessel function, J_k is also the Laurent series coefficient of function $e^{jz\sin\theta}$, it can be presented as

$$e^{jz\sin\theta} = \sum_{k=-\infty}^{+\infty} J_k(z) e^{jk\theta}, |z| < \infty \tag{B.3}$$

Thus, it can be obtained that

$$\begin{cases} \cos(z\sin\theta) = J_0(z) + 2\sum_{k=1}^{\infty} J_{2k}(z)\cos(2k\theta) \\ \sin(z\sin\theta) = 2\sum_{k=0}^{\infty} J_{2k+1}(z)\sin((2k+1)\theta) \end{cases} \tag{B.4}$$

Then, the expression of equation (B.4) can be employed to analyze the harmonic coefficients proposed in Equation (3.10) for SVPWM.

B.1.2 Harmonic Coefficients Calculation

The amplitude of a_1 can be obtained from equation (3.10) directly and can be rewritten as

$$\begin{aligned} a_1 &= \frac{4}{\pi}\cos\left(\frac{M\pi}{2}(\sin(\omega_e t) + \xi\sin(3\omega_e t))\right) \\ &= \frac{4}{\pi}\Re\left\{e^{j\frac{M\pi}{2}(\sin(\omega_e t)+\xi\sin(3\omega_e t))}\right\} \\ &= \frac{4}{\pi}\Re\left\{e^{j\frac{M\pi}{2}\sin(\omega_e t)}e^{j\frac{M\pi}{2}\xi\sin(3\omega_e t)}\right\} \end{aligned} \tag{B.5}$$

According to equation (B.5), the right entries can be represented as

$$\begin{cases} e^{j\frac{M\pi}{2}\sin(\omega_e t)} = J_0\left(\frac{M\pi}{2}\right) + 2\sum_{k=1}^{\infty} J_{2k}\left(\frac{M\pi}{2}\right)\cos(2k\omega_e t) \\ \qquad\qquad + j2\sum_{k=0}^{\infty} J_{2k+1}\left(\frac{M\pi}{2}\right)\sin((2k+1)\omega_e t) \\ e^{j\frac{M\pi\xi}{2}\sin(3\omega_e t)} = J_0\left(\frac{M\pi\xi}{2}\right) + 2\sum_{k=1}^{\infty} J_{2k}\left(\frac{M\pi\xi}{2}\right)\cos(6k\omega_e t) \\ \qquad\qquad + j2\sum_{k=0}^{\infty} J_{2k+1}\left(\frac{M\pi\xi}{2}\right)\sin((6k+3)\omega_e t) \end{cases} \tag{B.6}$$

By neglecting the high order components, it can be approximated as

$$\begin{cases} e^{j\frac{M\pi}{2}\sin(\omega_e t)} \approx J_0\left(\frac{M\pi}{2}\right) + 2J_2\left(\frac{M\pi}{2}\right)\cos(2\omega_e t) + j2J_1\left(\frac{M\pi}{2}\right)\sin(\omega_e t) \\ e^{j\frac{M\pi\xi}{2}\sin(3\omega_e t)} \approx J_0\left(\frac{M\pi\xi}{2}\right) + j2J_1\left(\frac{M\pi\xi}{2}\right)\sin(3\omega_e t) \end{cases} \tag{B.7}$$

By substituting equation (B.7) into equation (B.5), it can be obtained that

$$\begin{aligned} a_1 =& \frac{4}{\pi}J_0\left(\frac{M\pi}{2}\right)J_0\left(\frac{M\pi\xi}{2}\right) + \frac{8}{\pi}J_1\left(\frac{M\pi}{2}\right)J_1\left(\frac{M\pi\xi}{2}\right)\cos(4\omega_e t) \\ &+ \frac{8}{\pi}\left(J_2\left(\frac{M\pi}{2}\right)J_0\left(\frac{M\pi\xi}{2}\right) - J_1\left(\frac{M\pi}{2}\right)J_1\left(\frac{M\pi\xi}{2}\right)\right)\cos(2\omega_e t) \end{aligned} \tag{B.8}$$

Similarly, a_2 can be rewritten as

$$a_2 = -\frac{2}{\pi}\sin\left(M\pi(\sin(\omega_e t) + \xi\sin(3\omega_e t))\right) = -\frac{2}{\pi}\Im\left\{e^{jM\pi\sin(\omega_e t)}e^{M\pi\xi\sin(3\omega_e t)}\right\} \tag{B.9}$$

By the same procedure, a_2 can be approximately derived as

$$\begin{aligned} a_2 = &-\frac{4}{\pi}(J_1(M\pi)J_0(M\pi\xi) + J_2(M\pi)J_1(M\pi\xi) - J_4(M\pi)J_1(M\pi\xi))\sin(\omega_e t) \\ &-\frac{4}{\pi}(J_3(M\pi)J_0(M\pi\xi) + J_0(M\pi)J_1(M\pi\xi))\sin(3\omega_e t) \\ &-\frac{4}{\pi}J_2(M\pi)J_1(M\pi\xi)\sin(5\omega_e t) - \frac{4}{\pi}J_4(M\pi)J_1(M\pi\xi)\sin(7\omega_e t) \end{aligned} \tag{B.10}$$

Noticeably, a_2 is relate to the imaginary part of the complex exponential function. Additionally, the higher order Bessel function J_4 is also involved for the $(7\omega_e)$-order harmonic calculation, which is neglected in Equation (B.7). It can be taken into account for $(4\omega_e)$ component in Equation (B.8) to achieve higher accuracy as well. All other sideband harmonic components can be derived exactly with the same procedure. By substituting the coefficients into the sideband voltage expressions, corresponding components can be derived.

B.2 Park Transformation of Sideband Voltage Harmonics

The sideband voltage components cannot be directly employed to analyse the current components as the effect of time varying winding inductances due to the saliency characteristic of rotor structure in interior PMSM. However, the *d-q* components of inductances can be considered to be constant by neglecting the affection of spatial harmonics. Thus the *d-q* equivalent circuit can be involved for the sideband current components analysis based on the Park transformation of sideband voltage harmonic components.

B.2.1 Principle of Park Transformation

Park transformation is a mathematical calculation that transforms three AC quantities, such as voltages, currents, flux linkages into DC quantities, as shown in Figure B.1(a). As for three phase voltages, It can be presented as

$$\begin{cases} u_d = \frac{2}{3}\left(u_a\cos\theta + u_b\cos\left(\theta - \frac{2\pi}{3}\right) + u_c\cos\left(\theta - \frac{4\pi}{3}\right)\right) \\ u_q = -\frac{2}{3}\left(u_a\sin\theta + u_b\sin\left(\theta - \frac{2\pi}{3}\right) + u_c\sin\left(\theta - \frac{4\pi}{3}\right)\right) \end{cases} \tag{B.11}$$

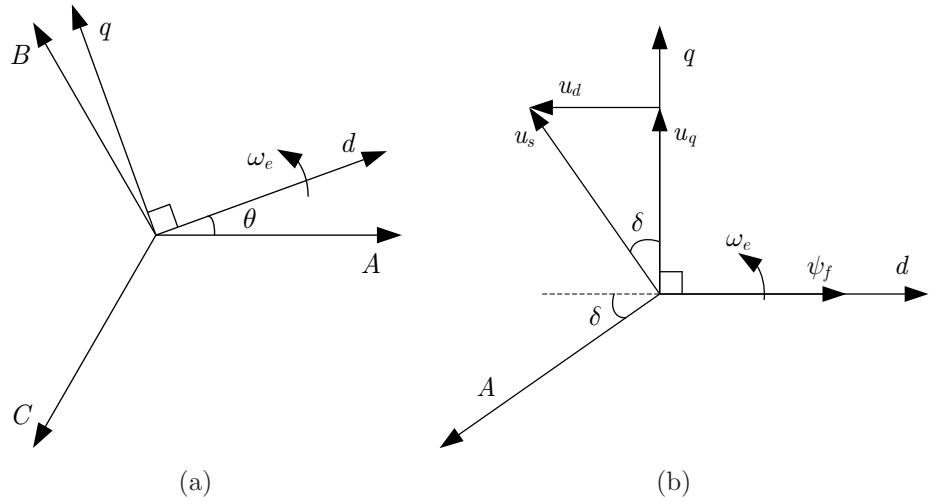

Figure B.1: The Park transformation coordinate demonstration: (a) Rotating reference frame; (b) Initial phase angle of d-axis.

where,

$$\theta = \omega_e t - \varphi_0 \tag{B.12}$$

φ_0 is the initial phase angle derivation between d-axis and phase A-axis. The relationship of two axis is demonstrated in Figure B.1(b). Apparently, d-axis lags voltage vector with a degree of $(\pi/2+\delta)$ in steady state. It depends on the required electromagnetic torque and implemented control strategy. Meanwhile, according to the fundamental component part in a_0 proposed in Equation (3.10), the initial phase of voltage vector is $-\pi/2$ relative to Phase A-axis. Consequently, it can be derived that

$$\varphi_0 = \pi + \delta \tag{B.13}$$

B.2.2 Sideband Voltage Harmonics in Rotating Frame

The main phase voltage harmonic components are proposed in Equation (3.13) and (3.16) analytically. Since the three-phase windings are normally symmetric with specific phase difference for each harmonic, the model of harmonics can be directly derived for other two phases based on the proposed equations. As for the ω_s-order sideband harmonic, there is no phase difference in three phase and the harmonics can be written as

$$\begin{cases} u_{a\_\omega_s} = \dfrac{U_{dc}}{2} C_{10} \cos(\omega_s t) \\ u_{b\_\omega_s} = \dfrac{U_{dc}}{2} C_{10} \cos(\omega_s t) \\ u_{c\_\omega_s} = \dfrac{U_{dc}}{2} C_{10} \cos(\omega_s t) \end{cases} \tag{B.14}$$

It should be noted that the phase difference is only relevant with harmonic order of ω_e, while independent with ω_s. Because the same carrier wave is involved for

the pulse width modulation of three phase output signal, while the phase angle difference only exists between the modulation wave of three phases. By applying Equation (B.11), the *d*-*q* components of ω_s order can be obtained

$$u_{\omega_s\_d} = 0, u_{\omega_s\_q} = 0 \tag{B.15}$$

As for $(\omega_s + 2\omega_e)$-order items, there is a lagging phase difference of $4\pi/3$. Consequently, the corresponding phase harmonic model can be presented as

$$\begin{cases} u_{a\_(\omega_s+2\omega_e)} = \dfrac{U_{dc}}{2} C_{12} \cos((\omega_s + 2\omega_e)t) \\ u_{b\_(\omega_s+2\omega_e)} = \dfrac{U_{dc}}{2} C_{12} \cos\left((\omega_s + 2\omega_e)t - \dfrac{4\pi}{3}\right) \\ u_{c\_(\omega_s+2\omega_e)} = \dfrac{U_{dc}}{2} C_{12} \cos\left((\omega_s + 2\omega_e)t - \dfrac{8\pi}{3}\right) \end{cases} \tag{B.16}$$

Accordingly, the associated *d*-*q* components can be derived as

$$\begin{cases} u_{(\omega_s+2\omega_e)\_d} = -\dfrac{U_{dc}}{2} C_{12} \cos((\omega_s + 3\omega_e)t - \delta) \\ u_{(\omega_s+2\omega_e)\_q} = +\dfrac{U_{dc}}{2} C_{12} \sin((\omega_s + 3\omega_e)t - \delta) \end{cases} \tag{B.17}$$

By similar procedure, all other main harmonics in first sideband can be obtained by the Park transform, and the derived items are list in Table B.1. It can be found the main components $(\omega_s \pm 2\omega_e)$ and $(\omega_s \pm 4\omega_e)$-order components are transferred into $(\omega_s \pm 3\omega_e)$-order items in the rotor frame. As a result, further synthesis is required for these the same order items.

Table B.1: Voltage harmonics of first sideband in rotor frame

Frequency	Axis	Expression
ω_s	d	0
	q	0
$\omega_s + 2\omega_e$	d	$-0.5U_{dc}C_{12}\cos((\omega_s + 3\omega_e)t - \delta)$
	q	$+0.5U_{dc}C_{12}\sin((\omega_s + 3\omega_e)t - \delta)$
$\omega_s - 2\omega_e$	d	$-0.5U_{dc}C_{12}\cos((\omega_s - 3\omega_e)t + \delta)$
	q	$-0.5U_{dc}C_{12}\sin((\omega_s - 3\omega_e)t + \delta)$
$\omega_s + 4\omega_e$	d	$-0.5U_{dc}C_{14}\cos((\omega_s + 3\omega_e)t + \delta)$
	q	$-0.5U_{dc}C_{14}\sin((\omega_s + 3\omega_e)t + \delta)$
$\omega_s - 4\omega_e$	d	$-0.5U_{dc}C_{14}\cos((\omega_s - 3\omega_e)t - \delta)$
	q	$+0.5U_{dc}C_{14}\sin((\omega_s - 3\omega_e)t - \delta)$

Moreover, the second sideband components are derived accordingly, and demonstrated in Table B.2. As shown in the table, the main components are $(2\omega_s)$ and $(2\omega_s \pm 6\omega_e)$-order harmonics, while the $(2\omega_s \pm 3\omega_e)$-order components are eliminated

in rotor frame. Similarly, all the same order components are needed to be synthesized by the trigonometric operation. Due to comparative small amplitude, the $(2\omega_s)$-order components are used to be the predominant items in second sideband domain.

Table B.2: Voltage harmonics of second sideband in rotor frame

Frequency	Axis	Expression
$\omega_e + 2\omega_s$	d	$-0.5U_{dc}C_{21}\sin(2\omega_s t + \delta)$
	q	$+0.5U_{dc}C_{21}\cos(2\omega_s t + \delta)$
$\omega_e - 2\omega_s$	d	$+0.5U_{dc}C_{21}\sin(2\omega_s t - \delta)$
	q	$+0.5U_{dc}C_{21}\cos(2\omega_s t - \delta)$
$3\omega_e \pm 2\omega_s$	d	0
	q	0
$5\omega_e + 2\omega_s$	d	$-0.5U_{dc}C_{25}\sin((2\omega_s + 6\omega_e)t - \delta)$
	q	$-0.5U_{dc}C_{25}\cos((2\omega_s + 6\omega_e)t - \delta)$
$5\omega_e - 2\omega_s$	d	$+0.5U_{dc}C_{25}\sin((2\omega_s - 6\omega_e)t + \delta)$
	q	$-0.5U_{dc}C_{25}\cos((2\omega_s - 6\omega_e)t + \delta)$
$7\omega_e + 2\omega_s$	d	$-0.5U_{dc}C_{27}\sin((2\omega_s + 6\omega_e)t + \delta)$
	q	$+0.5U_{dc}C_{27}\cos((2\omega_s + 6\omega_e)t + \delta)$
$7\omega_e - 2\omega_s$	d	$+0.5U_{dc}C_{27}\sin((2\omega_s - 6\omega_e)t - \delta)$
	q	$+0.5U_{dc}C_{27}\cos((2\omega_s - 6\omega_e)t - \delta)$

Appendix C

Sideband Harmonic Components in SPWM

The SPWM technique would also inevitably generate clusters of sideband voltage harmonics in the stator windings. The analytical derivations of those sideband voltage harmonic components are proposed for induction machine drive [204]. In this section, the corresponding sideband harmonics, including voltage and current, are derived for SPWM with the same procedure of SVPWM derivation.

C.1 Sideband Harmonics of SPWM Technique

The modulation function $y(t)$ in SPWM can be expressed as

$$y(t) = M\sin(\omega_e t), \quad 0 \leq M \leq 1 \tag{C.1}$$

As a resemblance to SVPWM scheme, the same harmonic expression proposed in Equation (3.9) can be adopted with associated coefficients presented as

$$\begin{cases} a_0 = 2M\sin(\omega_e t) \\ a_n = \dfrac{4}{n\pi}\sin\left(\dfrac{n\pi}{2} + \dfrac{nM\pi}{2}(\sin(\omega_e t))\right) \end{cases} \tag{C.2}$$

By involving the Bessel function, the main first and second sideband voltage harmonic components with SPWM technique can be expressed as

$$\begin{cases} H_1 \approx \dfrac{U_{dc}}{2}(C'_{10}\cos\omega_s t + C'_{12}\cos(\omega_s \pm 2\omega_e)t) \\ H_2 \approx \dfrac{U_{dc}}{2}(C'_{21}\sin(\omega_e \pm 2\omega_s)t + C'_{23}\sin(3\omega_e \pm 2\omega_s)t) \end{cases} \tag{C.3}$$

Noticeably, there are $(5\omega_e \pm 2\omega_s)$ and $(7\omega_e \pm 2\omega_s)$ components as well, however, they are comparatively trivial and hence negligible here. C'_{10}, C'_{12}, C'_{21} and C'_{23} can be

approximated as

$$C'_{10} = \frac{4}{\pi} J_0(\frac{M\pi}{2}), \quad C'_{12} = \frac{4}{\pi} J_2(\frac{M\pi}{2}), \quad C'_{21} = -\frac{2}{\pi} J_1(M\pi), \quad C'_{23} = -\frac{2}{\pi} J_3(M\pi) \tag{C.4}$$

By applying Park transformation, the sideband voltage harmonic components can be analytically rearranged in rotor synchronous reference frame. The ω_s, and $(3\omega_e \pm 2\omega_s)$-order components in the right side of (C.3) will be eliminated and disappear in the rotor synchronous frame by the transformation, while the $(\omega_s \pm 3\omega_e)$, and $(2\omega_s)$-order harmonics can be obtained from $(\omega_s \pm 2\omega_e)$ and $(\omega_e \pm 2\omega_s)$-order ones respectively. Therefore, the main harmonic components at first and second carrier frequency domains in the rotor synchronous frame can be presented as

$$\begin{cases} u_{d\_(\omega_s \pm 3\omega_e)} = -\dfrac{U_{dc}}{2} C'_{12} \cos(\omega_s t \pm 3\omega_e t \mp \delta) \\ u_{q\_(\omega_s \pm 3\omega_e)} = \pm\dfrac{U_{dc}}{2} C'_{12} \sin(\omega_s t \pm 3\omega_e t \mp \delta) \end{cases} \tag{C.5}$$

$$\begin{cases} u_{d\_(2\omega_s)} = -U_{dc} C'_{21} \sin\delta \cos(2\omega_s t) \\ u_{q\_(2\omega_s)} = U_{dc} C'_{21} \cos\delta \cos(2\omega_s t) \end{cases} \tag{C.6}$$

By substituting the main first and second sideband voltage harmonic expressions (C.5) and (C.6) into (3.27), the corresponding sideband current harmonic components can be derived as

$$\begin{cases} i_{d\_(\omega_s \pm 3\omega_e)} = \dfrac{-U_{dc} C'_{12} \sin(\omega_s t \pm 3\omega_e t \mp \delta)}{2(\omega_s \pm 3\omega_e) L_d} \\ i_{q\_(\omega_s \pm 3\omega_e)} = \dfrac{\mp U_{dc} C'_{12} \cos(\omega_s t \pm 3\omega_e t \mp \delta)}{2(\omega_s \pm 3\omega_e) L_q} \end{cases} \tag{C.7}$$

$$\begin{cases} i_{d\_(2\omega_s)} = -\dfrac{-U_{dc} C'_{21} \sin\delta \sin(2\omega_s t)}{2\omega_s L_d} \\ i_{q\_(2\omega_s)} = \dfrac{U_{dc} C'_{21} \cos\delta \sin(2\omega_s t)}{2\omega_s L_q} \end{cases} \tag{C.8}$$

By applying inverse Park transformation, the $(\omega_s \pm 3\omega_e)$-order current harmonics in the rotor synchronous frame can be turned into $(\omega_s \pm 2\omega_e)$ and $(\omega_s \pm 4\omega_e)-$order phase current harmonics in the stator stationary frame. Whilst, the $(2\omega_s)-$order one could be transformed into $(2\omega_s \pm \omega_e)-$order harmonics. The harmonics can be derived as the same expressions of SVPWM, which are proposed in Equation (3.31) and (3.36). While, the respective amplitudes and initial phases of those harmonics can be proposed as

$$I_{s\_12} = \frac{U_{dc}\sigma_1 C'_{12}}{4(\omega_s \pm 3\omega_e)}, \quad I_{s\_14} = \frac{U_{dc}\sigma_2 C'_{12}}{4(\omega_s \pm 3\omega_e)} \tag{C.9}$$

$$\begin{cases} \cos\varphi_{s\_12} = \sin\delta, & \sin\varphi_{s\_12} = -\cos\delta, \\ \cos\varphi_{s\_14} = \sin\delta, & \sin\varphi_{s\_14} = \cos\delta \end{cases} \tag{C.10}$$

And

$$I_{s\_21} = -\frac{U_{dc}C'_{21}}{4\omega_s}\sqrt{\frac{\sin^2\delta}{L_d^2} + \frac{\cos^2\delta}{L_q^2}} \tag{C.11}$$

$$\cos\varphi_{s\_21} = \frac{L_d\cos\delta}{\sqrt{L_d^2\cos^2\delta + L_q^2\sin^2\delta}}, \quad \sin\varphi_{s\_21} = \frac{L_q\sin\delta}{\sqrt{L_d^2\cos^2\delta + L_q^2\sin^2\delta}} \tag{C.12}$$

One of the implications from (3.9) is that the $(\omega_s \pm 4\omega_e)$-order sideband current harmonics in PMSM drive with SPWM technique stem from the difference between the $d-$axis and $q-$axis inductances (saliency). Therefore, they almost do not exist in the machine with small saliency such as surface mounted PMSMs but have nearly the same amplitudes as the $(\omega_s \pm 2\omega_e)$-order ones in the machine with large saliency. Another one is that the initial phase of $(2\omega_s \pm \omega_e)$-order ones are exactly the same as SVPWM components.

C.2 Magnetic Saturation and Cross Coupling Effect

By substituting the voltage models (C.5) and (C.6) into (3.42), the main current harmonic models in SPWM accounting the magnetic saturation and $d-q$ cross-coupling effects can be derived as

$$\begin{cases} i_{d\_(\omega_s\pm3\omega_e)} = \dfrac{U_{dc}C'_{12}(-L_q\sin((\omega_s\pm3\omega_e)t\mp\delta) \pm M_{dq}\cos((\omega_s\pm3\omega_e)t\mp\delta))}{2(\omega_s\pm3\omega_e)(L_dL_q - M_{dq}^2)} \\ i_{q\_(\omega_s\pm3\omega_e)} = \dfrac{U_{dc}C'_{12}(\mp L_d\cos((\omega_s\pm3\omega_e)t\mp\delta) + M_{dq}\sin((\omega_s\pm3\omega_e)t\mp\delta))}{2(\omega_s\pm3\omega_e)(L_dL_q - M_{dq}^2)} \end{cases} \tag{C.13}$$

$$\begin{cases} i_{d\_(2\omega_s)} = \dfrac{-U_{dc}C'_{21}\left(L_q\sin\delta + M_{dq}\cos\delta\right)\sin(2\omega_s t)}{2\omega_s\left(L_dL_q - M_{dq}^2\right)} \\ i_{q\_(2\omega_s)} = \dfrac{U_{dc}C'_{21}\left(L_d\cos\delta + M_{dq}\sin\delta\right)\sin(2\omega_s t)}{2\omega_s\left(L_dL_q - M_{dq}^2\right)} \end{cases} \tag{C.14}$$

The respective amplitudes of corresponding sideband current harmonics in stator stationary frame can be obtained by applying inverse Park transformation on (C.13) and (C.14) and expressed as

$$\begin{cases} I_{s\_12} = \dfrac{U_{dc}\sigma_1 C'_{12}}{4(\omega_s\pm3\omega_e)\left(1-\sigma_M^2\right)} \\ I_{s\_14} = \dfrac{U_{dc}C'_{12}}{4(\omega_s\pm3\omega_e)\left(1-\sigma_M^2\right)}\sqrt{\sigma_2^2 + \dfrac{4\sigma_M^2}{L_dL_q}} \end{cases} \tag{C.15}$$

$$I_{s\_21} = -\frac{U_{dc}C'_{21}}{4\omega_s\left(1-\sigma_M^2\right)}\sqrt{\frac{\sin^2\delta}{L_d^2} + \frac{\cos^2\delta}{L_q^2} + R_{21}} \tag{C.16}$$

It can be found that the $(\omega_s \pm 2\omega_e)$ components wouldn't be influenced by the cross-coupling effect, while $(\omega_s \pm 4\omega_e)$ ones would be affected by the coupling factor, as well as $(2\omega_s \pm \omega_e)$ harmonics. R_{21} is the same as the coupling component in SVPWM, which is given in Equation (3.58).

Appendix D

Prototypes for Simulation Validation

The key parameters of the simulation models involved for the validation of armature reaction magnetic field are demonstrated in this part. To extensively examine the proposed interharmonic model, different stator slot rotor pole combinations are used to construct the corresponding simulation models. 8 different typical combinations are employed for each type with either surface or interior PM and either single- or double-layer winding configurations.

D.1 Stator and Rotor Structure in Simulations

Both stator and rotor structures of the PMSMs, which are involved in the simulation validation in Section 4.4, are circumferentially expanded and demonstrated in Figure D.1. The slot structure of the stator is depicted in Figure D.1(a). The outer and inner radii of the stator are indicated as R_o and R_i respectively. The air-gap height is expressed as δ_g. The surface-mounted and surface-inset rotor structures are shown in Figure D.1(b), while the interior structure is depicted in Figure D.1(c).

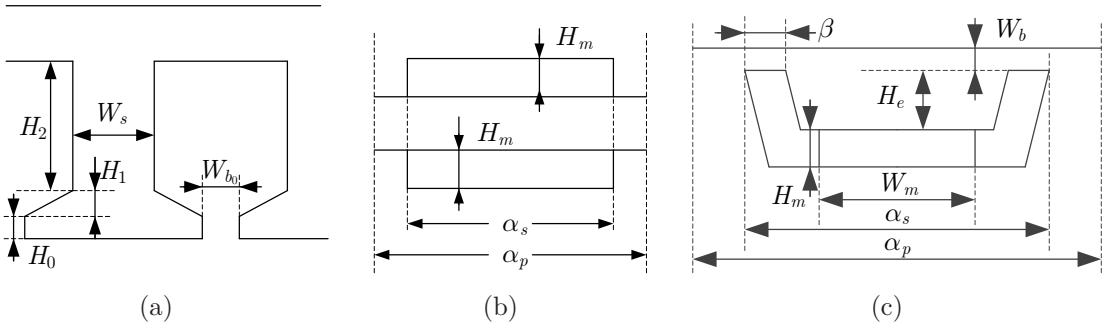

Figure D.1: Structure parameters of machine model: (a) slot structure, (b) surface and inset PM structure, (c) interior PM structure.

D.2 Main Configurations of Simulation Models

Table D.1: Key Parameters of Surface-Mounted and Surface-Inset PMSMs with Double-Layer Winding Configuration

Items	1	2	3	4	5	6	7	8	Unit
p	8	10	14	20	22	26	26	38	-
Z	9	12	15	21	24	27	30	42	-
R_o	136.3	120.8	111.6	101	98	95.5	93.5	88.3	mm
W_s	23.61	17.25	13.57	9.5	8.27	7.3	6.56	4.64	mm
H_0	2.67	2	1.6	1.14	1	0.89	0.8	0.6	mm
H_1	6.67	5	4	2.86	2.5	2.22	2	1.43	mm
H_2	36	27	21.6	15.4	13.5	12	10.8	7.7	mm
W_{b_0}	10.9	8.1	6.46	4.59	4	3.55	3.2	2.28	mm
H_m	5.63	5	4.29	3.75	3.64	3.46	3.46	3.16	mm

Table D.2: Key Parameters of Interior PMSMs with Double-Layer Winding Configuration

Items	1	2	3	4	5	6	7	8	Unit
p	8	10	14	20	22	26	26	38	-
Z	9	12	15	21	24	27	30	42	-
R_o	136.3	118	111.6	101.2	98	95.5	93.5	88	mm
W_s	23.56	15.06	13.54	9.48	8.25	7.3	6.54	4.62	mm
H_0	2.67	2	1.6	1.14	1	0.89	0.8	0.6	mm
H_1	6.67	5	4	2.86	2.5	2.22	2	1.43	mm
H_2	36	27	21.6	15.4	13.5	12	10.8	7.7	mm
W_{b_0}	5.44	5.67	3.22	2.29	2	3.55	3.18	1.8	mm
H_m	3.66	3.72	3.2	3.11	3.09	3.1	4.1	2.6	mm
W_m	35.6	26.5	18.8	12.03	10.58	10.8	9.76	6.6	mm
W_b	1.2	0.8	0.8	0.8	0.8	0.8	0.8	0.8	mm
H_e	4	5	4	4	4	4	4	3.5	mm
τ_s	0.85	0.85	0.85	0.85	0.85	0.85	0.85	0.9	-
τ_b	0.05	0.075	0.05	0.05	0.05	0.075	0.09	0.14	-

The key configuration parameters of the surface-mounted and surface-inset PMSMs employed for the $(p-Z)^{th}$ interharmonic analysis in Section 4.4.2 are given in Table D.1. The material DW360-50 is employed for the stator and rotor core laminations, while N30 is applied for the PM. The pole arc coefficients τ_s of surface-mounted and surface-inset PMSMs are 0.76 and 0.7 respectively. τ_s is defined in Equation (4.36). The corresponding parameters of the interior PMSMs are demonstrated in Table D.2. The double-layer concentrated winding configuration is employed for all these machines. The armature reaction magnetic field is derived by the frozen permeability method. For the surface-mounted PMSMs, only the armature

reaction component under d-axis is derived for the fundamental and interharmonic magnetic field analysis. For the surface-inset and interior PMSMs, both d- and q-axis magnetic fields are calculated. The excitation in each slot is one unit ampere turn for all models. The inner radii of the surface-mounted and surface-inset PMSMs are 75.5mm and the air-gap heights are 1mm. Whereas the corresponding parameters in the interior structure are 75.3mm and 0.6mm respectively.

Table D.3: Key Parameters of Surface-Mounted and Surface-Inset PMSMs with Single-Layer Winding Configuration

Items	1	2	3	4	5	6	7	8	Unit
p	10	14	22	26	34	38	46	50	-
Z	12	12	24	24	36	36	48	48	-
R_o	120.8	120.8	98	98	90.5	90.5	86.7	86.7	mm
W_s	17.25	17.25	8.27	8.27	5.43	5.43	4.04	4.04	mm
H_0	2	2	1	1	0.67	0.67	0.5	0.5	mm
H_1	5	5	2.5	2.5	1.67	1.67	1.25	1.25	mm
H_2	27	27	13.5	13.5	9	9	6.75	6.75	mm
W_{b_0}	7.9	7.9	4	4	2.66	2.66	1.98	1.98	mm
H_m	5	4.28	3.64	3.46	3.24	3.16	3.04	3	mm
τ_s	0.8	0.8	0.8	0.8	0.8	0.8	0.8	0.8	-

Table D.4: Key Parameters of Interior PMSMs with Single-Layer Winding Configuration

Items	1	2	3	4	5	6	7	8	Unit
p	10	14	22	26	34	38	46	50	-
Z	12	12	24	24	36	36	48	48	-
R_o	120.8	120.8	98	98	90.5	90.5	86.7	86.7	mm
W_s	17.2	17.2	8.25	8.25	5.42	5.42	4.03	4.03	mm
H_0	2	2	1	1	0.67	0.67	0.5	0.5	mm
H_1	5	5	2.5	2.5	1.67	1.67	1.25	1.25	mm
H_2	27	27	13.5	13.5	9	9	6.75	6.75	mm
W_{b_0}	6.07	6.07	3	3	1.99	1.99	1.5	1.5	mm
H_m	3.66	3.48	3.3	3.25	2.15	2.1	2.08	2.06	mm
W_m	32.33	20.95	10.5	7.64	8.1	7.2	5.88	5.38	mm
W_b	0.8	0.8	0.8	0.8	0.8	0.8	0.8	0.8	mm
H_e	4	4	4	4	3	3	3	3	mm
τ_s	0.93	0.93	0.93	0.93	0.96	0.96	0.96	0.96	-
τ_b	0.065	0.09	0.14	0.167	0.15	0.15	0.15	0.15	-

The key parameters of the surface-mounted and surface-inset PMSMs employed for the $(t_0/-t_0)^{th}$ interharmonic analysis in Section 4.4.3 are given in Table D.3. While the corresponding parameters for the interior PM structure are depicted in

Table D.4. To study the subharmonics in the FSCW PMSMs, the concentrated single-layer winding configuration is employed, in which the subharmonics can be significant. The same materials as the double-layer winding machines are applied for the single-layer winding configuration modeling. The same inner radius and air-gap height parameters are adopted from the double-layer winding configuration machines, which are 75.5mm and 1mm for the surface PMSMs, while 75.3mm and 0.6mm for the interior PMSMs. The same unit current excitation is set for the single-layer winding machines to obtain the magnetic field.